Energy Harvesting Dynamics of Ambient Stable Lead Halide Perovskite Nanocrystals

Thesis submitted in partial fulfillment

for the Award of Degree

Doctor of Philosophy

by

Suvadeep Panda

Department of Sciences & Humanities

RAJIV GANDHI INSTITUTE OF PETROLEUM TECHNOLOGY

JAIS, -229304

20BS0010   *2025*

CERTIFICATE

It is certified that the work contained in the thesis titled **"Energy Harvesting Dynamics of Ambient Stable Lead Halide Perovskite Nanocrystals" by "Suvadeep Panda"** has been carried out under my supervision and this work has not been submitted elsewhere for a degree.

It is further certified that the student has fulfilled all the requirements of Comprehensive, Candidacy, and SOTA.

_____

Supervisor
Dr. Debashis Panda

DECLARATION BY THE CANDIDATE

I, **"Suvadeep Panda"**, certify that the work embodied in this thesis is my own bona fide work and carried out by me under the supervision of **"Dr. Debashis Panda"** from "August 2020" to "December 2024", at Rajiv Gandhi Institute of Petroleum Technology, Jais.

The matter embodied in this thesis has not been submitted for the award of any other degree. I declare that I have faithfully acknowledged and given credits to the research workers wherever their works have been cited in my work in this thesis. I further declare that I have not willfully copied any other's work, paragraphs, text, data, results, etc., reported in journals, books, magazines, reports dissertations, thesis, etc., or available at websites and have not included them in this thesis and have not cited as my own work.

Place: RGIPT
Date:

_____
Suvadeep Panda
Roll No.-20BS0010

CERTIFICATE BY THE SUPERVISOR(S)

It is certified that the above statement made by the student is correct to the best of my knowledge.

_____
Dr. Debashis Panda
(Supervisor)

_____
Prof. Atul Sharma
(Head of Department, S&H)

CERTIFICATE

Certified that the work contained in the thesis titled **"Energy Harvesting Dynamics of Ambient Stable Lead Halide Perovskite Nanocrystals" by Mr. Suvadeep Panda** has been carried out under my supervision. It is also certified that he fulfilled the mandatory requirement of TWO quality publications arose out of his thesis work.

It is further certified that the two publications (copies enclosed) of the aforesaid   Mr. Suvadeep Panda have been published in the Journals indexed by —

    (a) SCI

    (b) SCI Extended

    (c) SCOPUS

  (Supervisor)   (Convenor, DPGC)
Dr. Debashis Panda   Dr. Praveen Kumar Srivastava

COPYRIGHT TRANSFER CERTIFICATE

Title of the thesis: "Energy Harvesting Dynamics of Ambient Stable Lead Halide Perovskite Nanocrystals"
**Name of the student:** Suvadeep Panda

Copyright Transfer

_____

Place: RGIPT   Suvadeep Panda
Date: Roll No. 20BS0010

Dedicated to My Parents

Acknowledgement

"Nearly everything is really interesting if you go into it deeply enough.''

Richard P. Feynman

It brings me immense pleasure to finally arrive at the moment when I can submit my doctoral thesis. But before I do, I take a special moment to thank 'GOD' for bestowing upon me all the favourable circumstances that allowed me to smoothly traverse this decisive path in my life. Additionally, there are several individuals whom I would like to express my gratitude to for their love, care, support, and efforts.

In particular, I extend my heartfelt appreciation to my doctoral thesis Supervisor, Dr. Debashis Panda, for his invaluable guidance, encouragement, academic stimulus, and generous assistance. I am deeply grateful for the numerous helpful discussions and suggestions I received during the thesis preparation process. I will always cherish his words, "A Ph.D. is not only a degree but a journey."

I will not forget those enjoyable and enlightening discussions with my supervisors at each stage of my writing, which often extended for several hours. These discussions have ultimately led me to the completion of this thesis.

Beyond my supervisor, I would like to express my gratitude to the rest of my RPEC committee: Prof. M S Balathanigaimani and Dr. Arshad Aijaz, for their insightful comments and encouragement, as well as for posing challenging questions that prompted me to broaden my research from various perspectives.

I would also like to extend my thanks to my lab mates who are also my friends: Surja, Prerna, Basab, Pooja, Utsav, Raman, Arvind Swapna, Ayush, Sachin, and Karan for the stimulating discussions and the positive lab environment we shared during our time working together over the past four years.

I would like to thank our BTP group and summer intern members Amritansh Vidhu, Atharva, Raghav, Prateek, Silvi, Imtiyaz, Mohammad Yasar, and Kritika for their support as helping hands in the experiments.

I warmly extend my appreciation to my seniors: Dr. Suman Debnath, Dr. Subhankar Mandal, Dr. Surja Kanta Pal, Dr. Puja Jaiswal, Dr Gargi Dey, Dr. Yogendra Yadwa, Dr. Vinamra Bhushan Sharma, Dr. Mohammad Belal Haider, Dr. Sadab Safi, and my friends Amit, Deepak, Sujeet, Sidharth, Angana, Anirudha, Gourav, Vidit, Chandan, Santosh, Pralay, Ashish, Aash Mohammad, Parvez, Ajeet, Amit, Prerna, for their help and support.

I would like to express my heartfelt gratitude to the teachers who have been instrumental in shaping my academic journey at various stages of my life – from school to bachelors and postgraduate studies. Their unwavering support and motivation have been invaluable. I extend my appreciation to Prof. Swati De, Prof. Tapas Majumder, Ratan Sir, Rajiv Sir.

I owe an immense debt to my beloved parents and family. Their enduring love, unwavering confidence, and constant support for my hard work have spurred me to

advance in my studies and career. The boundless affection and encouragement from my parents have consistently propelled me forward. My parents warmth has always filled me with peace and positivity. The support from my brother and sister has motivated me to reach unprecedented heights.

Last but certainly not least, my life is profoundly indebted to all my family members for their love, patience, support, and sacrifices. I would never have attained such heights without their blessing.

…. Suvadeep Panda

Contents

Chapter 5 *Electron Transfer in Ni-Doped CsPbBr3 Nanocrystal–Fluorophore Light Harvester*

Chapter 6 *Summary and Future Scope*

List of Abbreviations

NC	Nanocrystal
QD	Quantum Dot
PCE	Power Conversion Efficiency
PSC	Perovskite Solar Cell
PNC	Perovskite Nanocrystal
PLQY	Photoluminescence Quantum Yield
LED	Light-Emitting Diode
FRET	Förster Resonance Energy Transfer
DET	Dexter-type energy transfer
PET	Photoinduced Electron Transfer
OA	Oleic Acid
OLA	Oleylamine
PL	Photoluminescence
LARP	Ligand-Assisted Reprecipitation
MA	Methylammonium
FA	Formamidinium
ODE	Octadecene
HI	Hot Injection
FWHM	Full Width atHalf Maximum
MHPs	Metal Halide Perovskites
LHPs	Lead Halide Perovskites
PQDs	Perovskite Quantum Dots
SOC	Spin–Orbit Coupling
TET	Triplet Energy Transfer
ISC	Intersystem Crossing
CIGS	Copper Indium Gallium Selenide
EQE	External Quantum Efficiency
PeLED	Perovskite Light-Emitting Diode
OER	Oxygen Evolution Reaction
HER	Hydrogen Evolution Reaction
OIHP	Organic–Inorganic Hybrid Perovskite
IHPN	Inorganic Halide Perovskite Nanocrystal
DFB	Distributed Feedback (laser)
VCSEL	Vertical-Cavity Surface-Emitting Laser
PAN	Polyacrylonitrile
SBS	Styrene-Butadiene-Styrene
PVDF	Polyvinylidene Fluoride
PVP	Polyvinylpyrrolidone
CA	Cellulose Acetate
PVC	Polyvinyl Chloride
PDMS	Polydimethylsiloxane
DMF	N,N dimethyle formamide
DMSO	Dimethyl Sulphoxide

List of Figures

| | up-to 0.12 µM monitored at 493 nm. **[D]** Kinetics of the 496 nm bleach decay for Ni:PNC after successive addition of MV^{+2} up-to 0.12 µM (without RhB). | |

List of Schemes

List of Tables

Preface

SCOPE of THE THESIS:

Inorganic perovskite nanocrystals (PNCs) represent a rapidly advancing class of photoluminescent nanomaterials with significant potential in optoelectronic applications such as solar cells, light-emitting diodes (LEDs), and photodetectors. In particular, perovskite-based tandem solar cells (PSCs) have emerged as a transformative technology poised to outperform conventional silicon-based solar cells, achieving power conversion efficiencies (PCEs) exceeding 30%. The appeal of PNCs lies in their abundant elemental composition, exceptional defect tolerance, and long carrier diffusion lengths, which collectively enhance their performance in energy conversion, harvesting, and photocatalytic systems.

Structurally, the general formula ABX_3 of perovskites facilitates tunable optoelectronic properties: the A- and B-sites can accommodate various metal ions to modulate crystal structure and suppress non-radiative recombination, while the labile nature of the halide X-ion enables rapid halide exchange, allowing precise band gap engineering across the visible spectrum. Despite these advantages, a major limitation remains—their sensitivity to environmental conditions, which hinders real-world application. The scope of the thesis is to address the ambient stability issue through methodology development and thereafter deepen our understanding on energy harvesting properties of perovskite nanocrystals. The following questions have been selected to answer in this thesis are-

(i) How does hydrophilic-hydrophobic balance impact dimensional engineering of halide perovskite crystals?

(ii) Is it possible to synergize the defect tolerance with ambient stability of perovskite nanocrystals ?

(iii) Why does a facet of perovskite nanocrystal dictate the energy transfer dynamics of light-harvesting complex ?

(iv) How to resolve energy-transfer couple electron-transfer in PNC-based light harvesting system?

Chapter 1

Introduction

This chapter presents a comprehensive literature review of various types of perovskites, highlighting their historical development and key physical properties. It systematically explores emerging synthetic strategies, encompassing both top-down and bottom-up approaches, along with detailed discussions on purification methodologies. The photophysical dynamics of perovskite nanocrystals, particularly in the presence of different acceptor molecules, are examined using advanced spectroscopic techniques including steady-state fluorescence, time-correlated single-photon counting (TCSPC), and femtosecond transient absorption spectroscopy. Furthermore, the chapter explores the tunability of band gaps via ion exchange, and addresses critical issues related to ambient stability and toxicity through encapsulation techniques and metal ion doping. Finally, the diverse applications of perovskite materials are discussed, spanning solar cells, light-emitting diodes (LEDs), photodetectors, energy harvesting systems, as well as photocatalytic processes such as CO_2 reduction and water splitting.

1.1. Introduction:

In the pursuit of sustainable energy solutions, the advancement of highly efficient materials is pivotal to transitioning toward a resilient and renewable energy future. Over the years, fluorescent quantum dots have garnered significant interest in various domains, including energy conversion, catalysis, and energy harvesting.[1–3] However, their limited power conversion efficiencies, along with suboptimal absorption and emission coefficients, have posed substantial limitations to their broader application in high-performance optoelectronic devices. Consequently, the search for alternative materials with superior optical and electronic properties has intensified. Among the emerging candidates, metal halide perovskites have come out as transformative materials. With a general chemical formula of ABX_3—where A is a monovalent cation (e.g., methylammonium, formamidinium, or cesium), B is a divalent metal cation (commonly lead or tin), and X is a halide anion (Cl, Br, or I) — these materials exhibit a unique combination of properties that have revolutionized the field of optoelectronics[4–8].

Historically, the perovskite structure was first identified in the mineral calcium titanate ($CaTiO_3$) in the 19th century by Gustav Rose, who named it after the Russian mineralogist Lev

Perovski. However, it was not until the early 21st century that organic-inorganic hybrid metal halide perovskites gained widespread attention for photovoltaic applications.
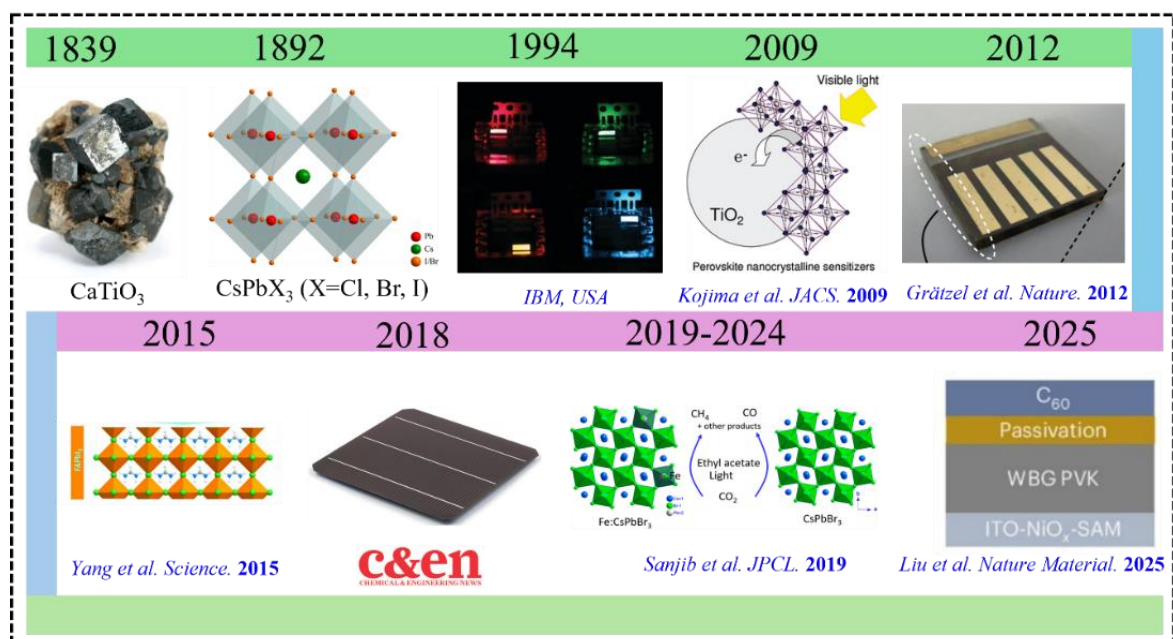
Figure 1.1: Important timeline of the perovskite research evolution. This includes the discovery of mineral perovskite ($CaTiO_3$) by Gustav Rose (1839); First synthesis of halide perovskite ($CsPbX_3$) and crystal structure determination by Horace L. Wells (1892); IBM USA first used the perovskite based light emitting device (1994); Miyasaka's group was the first to employ hybrid organic-inorganic halide perovskites (HOIPs) in photovoltaic devices, specifically as a visible-light sensitizer exhibiting PCE of 3.8% (2009); after that Grätzel's group showed that solid-state mesoscopic heterojunction solar cells employing methyl ammonium lead iodide (CH_3NH_3)PbI_3 nanocrystal as light harvesters with efficiency exceeding 9% (2012); furthermore yang et al. fabricated $FAPbI_3$-based PSCs with maximum power conversion efficiency greater than 20% (2015); perovskite silicon tandem solar cell achieved PCE over 26 % (2018); perovskite nanocrystals used as an efficient photocatalyst for the reduction of CO_2 to some value added products and water splitting to produce H_2 and O_2 (2019-2024); By now perovskite based solar cells achieved PCE over 30% (2025).

In 2009, Miyasaka and coworkers reported the use of methylammonium lead halide ($MAPbX_3$, where X = I or Br) as a light-harvesting material, achieving a power conversion efficiency (PCE) of 3.8%.[9] A major breakthrough came in 2012, when Snaith and colleagues demonstrated solid-state perovskite solar cells using a hole transport layer, achieving a dramatic improvement in both efficiency and stability.[10] Since then, the field has experienced exponential growth. By 2023, certified efficiencies of perovskite solar cells (PSCs) exceeded 26%. Parallel to the advancement in photovoltaics, perovskites were also investigated for

photocatalytic applications in the early 2020, such as artificial photosynthesis, CO_2 reduction, and water splitting, due to their strong light absorption, tunable band positions, and long carrier lifetimes. [11–14]

Beyond their photovoltaic and photocatalytic application, researchers began exploring low-dimensional and nanostructured perovskites. The development of quantum-confined nanocrystals (NCs), including 0D (e.g., Cs_4PbX_6), 1D (nanowires and nanorods), and 2D (Ruddlesden–Popper phase) materials, enabled fine-tuning of optical and electronic properties. Metal halide perovskite nanocrystals can be broadly classified into several categories based on their dimensionality and composition.

3D perovskite: 3D perovskite nanocrystals, characterized by their ABX_3 (X = Cl, Br, or I) crystal structure where A is an organic or inorganic cation, B a divalent metal ion (e.g., $MAPbI_3$ $CsPbBr_3$), have emerged as a transformative class of semiconductor materials due to their exceptional optoelectronic properties. These nanostructures exhibit high photoluminescence quantum yields (PLQYs), low exciton binding energy, high charge carrier diffusion length, narrow emission linewidths, and compositionally tunable bandgaps, enabling precise control over light emission across the visible and near-infrared spectra.[12–14] However, challenges such as instability under moisture, heat, and prolonged illumination hinder their commercialization. Recent advancements in surface ligand engineering, inorganic shell encapsulation, and lead-free alternatives (e.g., Sn^{2+}, Bi^{3+}-based perovskites) aim to address these limitations while retaining their optoelectronic performance.[15,16] Additionally, their solution-processability and compatibility with flexible substrates position them as a positive candidates for next-generation optoelectronic and photovoltaic technologies, though long-term stability and toxicity concerns necessitate further interdisciplinary research.[17,18]

2D layered perovskites: The structural design of two-dimensional (2D) metal-halide perovskite nanoplatelets originates from the Ruddlesden–Popper (R–P) phase, a family of layered perovskite materials characterized by alternating organic and inorganic layers.[19,20] During the 1990s, it was observed that incorporating larger organic cations—such as butylammonium (BA)—in place of the conventional small A-site cations like methylammonium (MA), formamidinium (FA), or cesium (Cs) facilitated the formation of these layered structures.[21–23] The introduction of bulky organic spacers disrupts the three-dimensional connectivity of the perovskite framework, resulting in the separation of inorganic $[BX_6]^{-4}$ octahedra into individual sheets.[24] This leads to the creation of quantum well-like structures with pronounced quantum and dielectric confinement effects. These 2D perovskite nanoplatelets not only exhibit improved environmental stability—owing to the protective hydrophobic nature of the organic layers—but also allow precise control over their optical and electronic properties by varying the number of inorganic layers (denoted by the n value).[25–27] As a result, they have attracted considerable attention for use in optoelectronic applications such as light-emitting diodes, photodetectors, and solar cells, where both stability and bandgap tunability are essential performance criteria.[28–31]

1D perovskites: One-dimensional (1D) nanostructured metal halide perovskites (MHPs), including nanowires (NWs) and nanorods (NRs) with diameters ranging from 1 to 100 nm and lengths extending to several hundred nanometers or even micrometers, have emerged as promising materials for a variety of photonic and optoelectronic applications. Their enhanced performance arises from several intrinsic advantages over their three-dimensional (3D) counterparts, such as extended charge-carrier diffusion lengths and lifetimes, high surface-to-volume ratios, increased charge confinement, and pronounced anisotropic geometries.[32,33] Stranks et al. reported charge diffusion lengths of approximately 100 nm in 3D MAPbI$_3$ and exceeding 1 μm in mixed-halide MAPbI$_{3-x}$Cl$_x$ systems.[34] Notably, single-crystalline MAPbI$_3$

NWs exhibit significantly longer carrier diffusion lengths, up to 21 μm, while MAPb$(I_{1-x}Br_x)_3$ NW arrays demonstrate values as high as 41 ± 3 μm.[35,36] These substantial enhancements in diffusion length are primarily attributed to the markedly prolonged charge-carrier lifetimes in 1D MHPs, thereby positioning them as superior candidates for high-performance optoelectronic devices.

0D perovskites: The emergence of "zero-dimensional" (0D) perovskite materials, particularly Cs_4PbX_6 (where X = Cl, Br, or I), as reported in 2016–2017, marked a significant turning point in the study of perovskite nanocrystals.[37,38] These discoveries spurred extensive research into the synthesis and application of Cs_4PbX_6 colloidal nanocrystals (NCs) in optoelectronic devices. When compared to their three-dimensional (3D) counterparts, $CsPbX_3$, 0D Cs_4PbX_6 NCs exhibit superior thermal and optical stability, most notably in their ability to maintain high photoluminescence quantum yields (PLQYs) for green emission in the solid state.[39] Structurally, Cs_4PbX_6 differs markedly from 3D perovskites. Instead of the extended corner-sharing network of $[PbX_6]^{4-}$ octahedra seen in $CsPbX_3$, the 0D variant consists of isolated $[PbX_6]^{4-}$ octahedra surrounded by Cs^+ cations, fully spatially decoupled in all three dimensions.[40,41] This structural dimensionality reduction gives rise to strong quantum confinement effects, resulting in molecule-like electronic behaviour. Therefore, Cs_4PbX_6 exhibits a wider bandgap, improved exciton binding energy, low charge carrier mobility, and diminished electrical conductivity relative to its 3D analogues. In addition to these intrinsic electronic characteristics, 0D Cs_4PbX_6 perovskites display intriguing photophysical properties, including small polaron absorption and broadband ultraviolet (UV) emission. These features make them attractive for a range of light-emitting and sensing applications.[40,42,43]
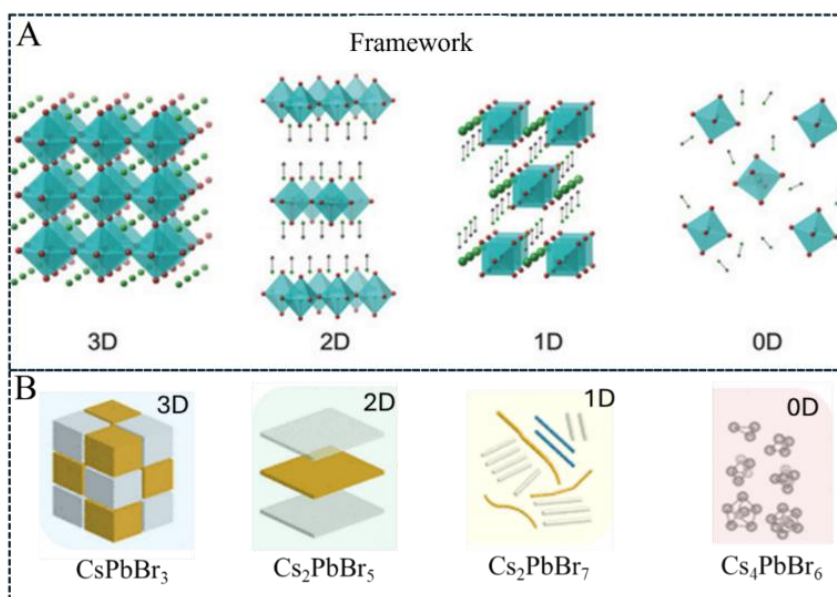
Figure 1.2: **[A]** Schematic representation of halide perovskite materials with different dimensionalities ranging from 3D to 0D.[44] Adapted from ref 44. Copyright 2022 Opto-Electronic Science **[B]** Schematic representation of perovskite materials with different degrees of confinement.[45] Adapted from ref 45. Copyright 2018 American Chemical Society.

Overall, these materials are characterized by exceptional features such as high absorption coefficients, tunable bandgaps across the visible spectrum, long charge carrier diffusion lengths, low exciton binding energies, and intrinsic defect tolerance. Such properties not only make them formidable contenders in solar photovoltaics but also potentiate their application in light-emitting diodes (LEDs), photodetectors, lasers, and even photocatalytic systems for energy conversion and artificial photosynthesis.[46–53]

Along with all the exceptional properties, one of the most compelling attributes of perovskite materials is their exceptional ability to mediate both energy transfer and electron transfer processes, which are critical for a wide range of optoelectronic and photocatalytic applications.[54–57] Owing to their high absorption cross-section and long exciton diffusion lengths, perovskites can efficiently harvest photon energy and transport excitons or free charge carriers over long distances without significant recombination losses.[50,52] This makes them ideal for facilitating Förster resonance energy transfer (FRET) in hybrid systems, where energy is non-radiatively transferred from perovskite donors to adjacent acceptor species such as

organic dyes, quantum dots, or catalytic molecules.[58–60] Similarly, Dexter-type energy transfer, which involves direct overlap of wavefunctions and requires short-range interaction, is also possible due to the delocalized nature of electronic states in perovskite nanocrystals.[61,62]

In terms of electron transfer, perovskites exhibit rapid charge injection and extraction properties, with well-aligned conduction and valence band edges that can be tuned through compositional engineering.[63] This enables efficient electron donation or acceptance in heterojunctions with semiconductors, metals, and molecular catalysts. Such properties are vital for the design of photoelectrochemical cells, solar fuels production, and sensitized devices, where the seamless transfer of photoexcited electrons or holes is required for high performance.[64,65] Furthermore, the strong light–matter interaction in perovskite materials promotes multi-exciton generation and hot-carrier dynamics, offering additional pathways for enhancing energy conversion efficiency. Collectively, these energy and electron transfer mechanisms underscore the multifunctional nature of perovskites and their suitability as active components in next-generation energy systems. In particular, the use of perovskites in photocatalytic processes, such as water splitting and carbon dioxide reduction to valuable chemicals like methane (CH_4), methanol (CH_3OH), and formic acid (HCOOH)—demonstrates their capacity to mimic and enhance natural photosynthetic pathways.[66–70] This positions them as promising materials for solar to chemical energy conversion, contributing significantly to the growth of a carbon-neutral energy economy.

Despite their remarkable potential, perovskite materials continue to face critical challenges that hinder their commercial viability. Their susceptibility to degradation under ambient conditions—including exposure to moisture,[71,72] thermal stress,[73,74] and ultraviolet radiation[75,76]—remains a major concern. Moreover, the widespread use of lead-based perovskites raises environmental and health-related issues, prompting efforts to develop lead-free alternatives such as tin- or bismuth-based compounds.[77–80] Instabilities arising from phase

transitions and poor crystallinity further compromise device performance. Addressing these challenges necessitates an interdisciplinary approach that combines insights from chemistry, materials science, and engineering. Advanced synthetic strategies to control nucleation and crystallization, development of phase-pure nanocrystals, and implementation of effective encapsulation techniques are crucial to enhancing long-term material stability.

This thesis aims to investigate the structural and optoelectronic properties of perovskite materials with a particular emphasis on enhancing ambient stability through experimental approaches. Furthermore, it explores the material's potential in energy transfer and harvesting systems, drawing inspiration from natural photosynthesis to establish pathways for sustainable energy technologies.

1.2. Emerging Synthetic Methods:

Over the past few decades, a lot of methods have been proposed for the synthesis of metal halide perovskites (MHPs). These synthetic routes are generally classified as "bottom-up method" or "top-down method". The ability to synthesize these MHPs with high quality and control over their various size, shape, and chemical composition has drawn huge attention. In this course I have elaborated some of the main techniques for the synthesis of MHPs.

A Bottom-up Method:

Depending on the type of synthesis, MHPs can typically be produced in three different ways using this method. These are (1) reprecipitation method (2) heat-up, and (3) in-situ synthesis. Among these methods hot injection method and ligand ligand-assisted reprecipitation method are used very often.
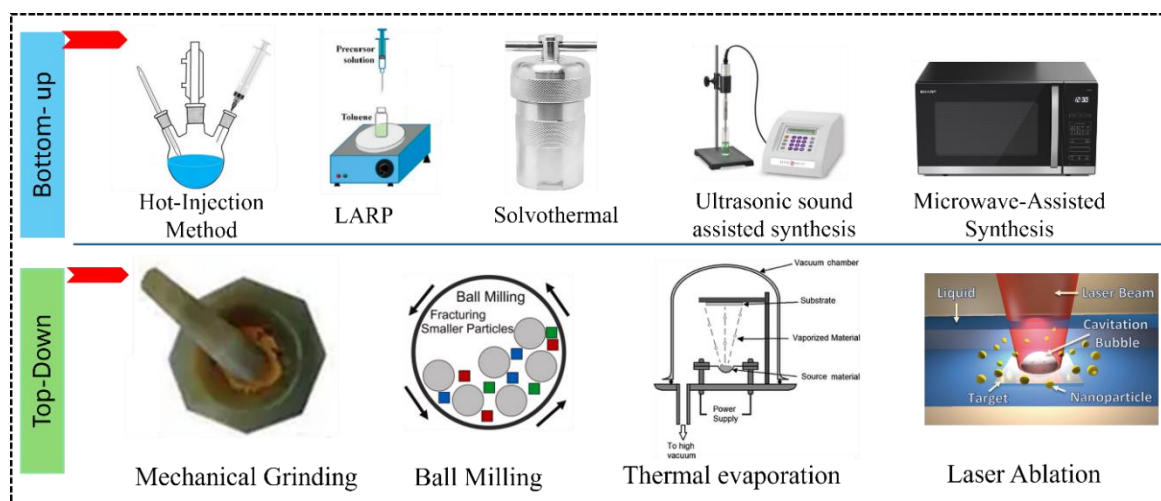
Figure 1.3: Different Synthetic methods for the preparation of Perovskite Nanocrystals. Methods under bottom-up categories are hot-injection method, Ligand assisted re-precipitation method (LARP), Solvothermal technique, Ultrasonic sound assisted synthesis, and Microwave sound assisted method. On the other hand, the Top-down method encompasses the mechanical grinding technique, Ball milling method, Thermal evaporation technique, and Laser Ablation approach respectively.

1.2.1 Hot Injection Method

Colloidal $CsPbX_3$ (X = Cl, Br, I) nanocrystals (NCs) have been synthesized via a hot-injection (HI) method, wherein Cs-oleate is swiftly injected into a hot solution (140–200 °C) containing PbX_2 salts dissolved in a nonpolar solvent such as octadecene (ODE), in the presence of carboxylic acids and primary amines.[49] The PbX_2 salts serve as a dual source of Pb^{2+} and halide ions (X^-). It has been observed that maintaining a 1:1 molar ratio of amines to acids facilitates the formation of monodisperse NCs, with size tunability achieved by adjusting the reaction temperature. Furthermore, mixed-halide perovskite NCs can be readily prepared by modulating the ratios of different lead halide salts (e.g., $PbCl_2/PbBr_2$ or $PbBr_2/PbI_2$), allowing precise control over the photoluminescence (PL) emission across the full visible spectrum (410–700 nm), either through halide composition tuning or NC size variation. The HI method has also been extended to organic-inorganic hybrid systems such as $MAPbX_3$ (X = Br, I) NCs, by substituting Cs-oleate with a methylamine solution. $MAPbBr_3$ and $MAPbI_3$ NCs were successfully synthesized through careful adjustment of the relative concentrations of

oleylamine (OLA) and oleic acid (OA) capping ligands.[81] In addition, the HI protocol has been adapted for the synthesis of perovskite-related lead halide phases. For instance, Cs_4PbX_6 (X = Cl, Br, I) NCs were obtained under Cs^+ and OLA-rich conditions, distinct from the stoichiometry used for $CsPbBr_3$ NCs, yielding monodisperse particles with size tunability from 9 to 25 nm.[82] Moreover, $CsPb_2Br_5$ NCs have been reported by several groups using octylamine and OA as surfactants in $PbBr_2$-rich reaction mixtures,[83] further demonstrating the versatility of the HI approach in producing various perovskite and perovskite-derived nanostructures.

1.2.2 Ligand Assisted Reprecipitation (LARP):

LARP technique is a very simple and scalable method for the synthesis of finest-quality perovskite NCs with tunable optical properties. In this method, lead halides or organic halides like methylammonium and formamidinium salts are dissolved in a polar solvent like DMF and DMSO, then at room temperature this precursor solution is rapidly added to a solvent (such as acetone, toluene, hexane) where the solubility of the substance is very low.[84–86] Now in presence of capping ligands which controls the nucleation and growth of the NCs and prevent the nanocrystal from aggregation the precipitation occurs. In 2012 Papavassiliou *et al*. first reports the LARP syntheses of hybrid organic−inorganic lead halide based perovskite NCs where they synthesized $MAPbX_3$, by solubilising (MA)-$(CH_3C_6H_4CH_2NH_3)_2Pb_2X_7$, or $(MA)(C_4H_9NH_3)_2Pb_2X_7$ (X = Br, Cl or I) salts in DMF (or acetonitrile) and dropped the corresponding solutions in toluene (or in a mixture of toluene and PMMA).[87] Huang et al. demonstrate that the size of the $MAPbBr_3$ can be adjusted by changing the temperature at which the LARP technique is operated..[88] This LARP method has also been stretched out to synthesise all inorganic PNCs, but it remains far behind than that of the hot-injection technique in controlling the shape of the NCs.

1.2.3 Solvent-Mediated Synthesis / Solvothermal Techniques:

It is a versatile method that depends on controlling the nucleation and growth of the NCs through solvent interaction. In this technique precursors (lead halides, organic halide salts) are dissolved in an appropriate solvent like DMF or DMSO. This solution mixture is then put through a controlled heating process either in a typical setup or within an autoclave for solvothermal synthesis.[89] The reaction kinetics, morphology of the NCs and the solubility of the precursor depends on the choice of the solvent. Additionally, use of capping ligands like oleic acid, oleylamine helps the formation of high quality NCs with tunable size and excellent optical properties. Solvent mediated synthesis is particularly profitable for producing uniform perovskite NCs which is extensively used for the application in solar cells, photodetectors, lasers and LEDs.

1.2.4 Ultrasound-Assisted Synthesis:

Ultrasound–assisted method is an innovative and efficient process to synthesize perovskite nanocrystals. This method uses high-frequency ultrasonic sound, which promotes rapid nucleation and growth of the nanocrystals. Due to the use of high-frequency waves, this process enhances the dispersion of precursor, reduces reaction time, and cuts down the need for high temperature, making it an environment-friendly and energy-efficient process. Kesari and Athawale employed ultrasonic irradiation to synthesize MAPbI$_3$ nanowires in isopropyl alcohol.[90] Similarly, Gedanken *et al*. reported the sonochemical synthesis of MAPbI$_3$ nanocrystals in isopropyl alcohol.[91] In addition to that, it provides precise control over the size, morphology and crystallinity of the nanocrystals, which is essential for the customisation of their applications in photovoltaics, optoelectronic devices, and LEDs. This technique is widely accepted due to its scalable and simple nature to produce high-quality NCs with improved stability and performance.

1.2.5 Microwave-Assisted Synthesis:

For the fabrication of perovskite nanocrystal with excellent opto-electronic properties, microwave assisted technique is also an energy efficient method. In this method microwave irradiation is used to provide uniform heating promoting controlled nucleation and growth of the nanocrystals.[92] This technique significantly reduces the duration of synthesis and consumption of energy compared to the conventional methods used for perovskite synthesis, while confirming high purity and reproducibility. By monitoring the microwave power, reaction time, and the concentration of the precursor one can control the size, shape, and crystallinity. Furthermore, this method reduces the use of hazardous chemicals and solvents making it an eco-friendly technique. Komarneni group initially reported the microwave hydrothermal synthesis of $BiFeO_3$ which crystalize at 467 K for 2 hours,[93] then Joshi *et al.* demonstrated a simple technique to synthesize single crystalline $BiFeO_3$ nanocubes for photoelectrode and photocatalytic applications.[94] Zhang et al. reported a rapid and efficient microwave-assisted process to produce $CsPbX_3$ NCs with controllable morphology and high quality.[95]

1.2.6 Template Based synthesis:

The template-assisted method offers a simple and effective approach to synthesize monodisperse perovskite nanocrystals (PNCs) by guiding crystallization within nanostructured templates, eliminating the need for capping ligands. Yamauchi *et al.* utilized mesoporous silica templates to grow $MAPbBr_xI_{x-3}$ nanocrystals, with pore size directly controlling the particle dimensions. This enabled modulation of optical properties via the quantum confinement effect.[96] Kaltenbrunner *et al.* further employed nanoporous alumina and silicon thin films as templates to produce PNCs without stabilizers or organic solvents.[97] Thereafter, Li et al. developed a solid-state confined growth strategy using mesoporous Al_2O_3 at elevated temperatures to synthesize highly emissive $CsPbBr_3$ nanocrystals. These NCs demonstrated

excellent optical performance, including a photoluminescence quantum yield (PLQY) of 70%, narrow emission linewidth (FWHM = 25 nm), and enhanced thermal stability.[98] Notably, this method avoids the use of expensive and toxic organic solvents, offering an environmentally friendly and scalable alternative for high-quality PNC production. This template-assisted approach thus provides precise size control, improved stability, and reduced environmental impact—key advantages for advancing PNC applications in optoelectronics.

1.2.7 Sol-Gel Technique:

The sol-gel Pechini method is the most useful and advantageous method due to its simplicity, cost effectiveness and versatility in synthesizing perovskite materials. This technique involves hydrolysis and condensation of organic or inorganic precursor in solution. Leading to the formation of sol and progressively converted into a gel-like network. By adjusting the reaction parameters like precursor concentration, pH, temperature, and the reaction time, this method offers precise tunning of the material morphology and the optical properties.[99,100] This sol-gel approach is widely used because it allows excellent control over the material structure as well as the purity and homogeneity, and requires lower synthetic temperature compared to the other solid state synthetic method. Initially Shlapa *et al*. synthesized very homogeneous $La_{1-x}Sr_xMnO_3$.nanocrystal with a very narrow particle size distribution between 30-35 nm.[101] Zhang *et al*. demonstrated a large variety of rare earth doped $La_4Ti_3O_{12}$ perovskite like structure which shows up and down conversion like emissive nature upon UV and NIR excitation.[102] Through a modified Pechini method Lima *et al*. showed the preparation of red emitting Eu^{+3} doped $LaAlO_3$ and a green emitting Tb^{+3} doped $LaAlO_3$.[103]

B Top-Down Method:

In this approach bulk materials are generally converted into nano-sized particle In Top-down method MHPs are mainly synthesized in three different ways depending on the nature of synthesis. These are (1) Ball milling (2) Thermal evaporation, (3) Laser ablation and. Despite

of their simple synthetic route this technique faces some challenges in controlling the proper particle size and morphology.

1.2.8 Wet Ball Milling:

Wet ball milling is the easiest top-down process for the synthesis of perovskite nanocrystals. Here bulk perovskite precursors are ground in a solvent filled container having stell balls. The high energy collision between the milling balls and the bulk materials is responsible for the synthesise of nano sized perovskite crystals,[104,105] while the solvents (toluene, or hexane) and surfactants (oleyl amine or oleic acid) prevents the agglomeration and stabilizes the formed nanoparticles. This method avoids the use of high temperature and complex synthetic route thereby offering scalability and simplicity than other bottom-up approaches.[105,106] However, controlling the size and shape of the nanocrystals and the structural defects generated by the extensive mechanical grinding is a big disadvantage of this process. Protesescu *et al* in 2018 synthesized colloidal $CsPbBr_3$ using wet ball milling method.[107] Furthermore, Mukasyan *et al*. in 2022 specifically synthesized methylammonium lead halide perovskite nanocrystal through wet ball milling technique.[108]

1.2.9 Thermal Evaporation:

Thermal evaporation is a vacuum assisted technique where heat is used to vaporise the precursor materials (metal halides or organic-inorganic salts) and subsequently condense onto a cooled surface. By altering the chamber pressure, temperature, and substrate evaporation rate isolated perovskite nanoparticles can be formed. This method does not require solvents or capping ligands and thereby advantageous for the synthesis of uniform and large size perovskite solar cells and LEDs.[109,110] This method has some demerits too like in presence of high temperature organic compounds could get degraded in case of hybrid perovskite synthesis and therefore increases the amount of impurity, and difficulties to achieve monodisperse nanoparticles. In 1997, Era *et al*. used a dual-source thermal evaporation approach to

successfully create 2-phenylethylammonium lead iodide and methylammonium lead iodide (MAPbI$_3$) thin films on quartz substrates.,[111] demonstrating one of the first instances of halide perovskite co-evaporation. Device application was only reported in 2013 when Liu and co-workers achieved over 15% PCE on PSCs based on thermally evaporated MAPbI$_3$ thin films.[112] In 2024 Wang *et al.* synthesized MHPs and their analogue through thermal evaporation method.[113]

1.2.10 Laser Ablation:

Because of its simplicity and little chemical requirements, laser ablation is an efficient top-down method for producing perovskite nanocrystals. With this technique, a bulk perovskite target, such as lead halide perovskites (like CsPbBr$_3$), is exposed to a high-intensity pulsed laser, immerged in a liquid, or placed in a controlled gaseous atmosphere. A plasma of vaporised particles is produced once the material is ablation by the laser energy, and these particles rapidly condense into nanocrystals. Laser wavelength, pulse duration, energy density, and ambient conditions are important factors that precisely control nanocrystal size, crystallinity, and photoluminescence characteristics.[114,115] In 2022 Liang *et al.* demonstrated patterning of CsPbBr$_3$ Perovskite Films using lamination-assisted femtosecond laser ablation technique.[116] Laser ablation has potential for usage in solar cells, LEDs, and photodetectors applications where high-quality nanocrystals are crucial due to its scalability and environmental adaptability.

1.3. Purification Techniques.

The crude perovskite nanocrystal obtained from different synthetic methods contains different sized particles, unreacted precursor and ligands. Thus, it should be well purified to remove the large size particles along with the unreacted products to have a monodisperse perovskite nanocrystal solution. Most of the common purification techniques that are generally used to separate perovskite nanocrystals are centrifugation-based purification, solvent washing, size selective precipitation, gel permeation chromatography, dialysis etc.[117–120]

centrifugation-based purification process is the most commonly used separation technique where nanoparticles are centrifuged at a high rotation rate (10,000 to 15,000 rpm) to get rid of the agglomeration and unreacted surfactants and precursors. In the solvent washing technique, perovskite nanocrystals have been repeatedly washed with a variety of selective solvents, including hexane and toluene, to dissolve and remove impurities while preserving the nanocrystal surface. Here solvent like methyl acetate and ethyl acetate are used to remove the excess capping ligands (such as oleic acid, oleyl amine).[118,121,122] In order to promote size selective separation, a poor solvent, such as acetone, is gradually added to the nanocrystal solution. This causes the larger particles to precipitate while the smaller particles stay in the supernatant. To obtain a monodisperse nanocrystal colloidal solution, this technique requires meticulous solvent ratio optimisation. Another efficient technique for separating the high-quality nanocrystal solution is gel permeation chromatography, which uses a column to separate the nanocrystals from aggregated materials at a specific flow rate. This technique can also be used to interchange ligands on a column to produce high-purity nanocrystals with improved stability.[117] The dialysis process involves sealing the nanoparticles in a semipermeable membrane and submerging them in a solvent bath. Pure nanoparticles are trapped inside the membrane while tiny contaminants like ions and ligands diffuse to the outside, but this process takes time and is only possible on a small scale.[123]

1.4. Stability of Perovskite Nanocrystal:

Lead halide perovskites (LHPs) possess remarkable optoelectronic characteristics, yet their ionic nature imparts a pronounced sensitivity to polar environments.[11] In particular, exposure to polar solvents or aqueous media often results in the rapid deterioration of their optical properties, detachment of surface-stabilizing ligands (especially in nanocrystalline forms), and in some cases, complete structural collapse. Even moderate moisture levels can induce degradation, thereby significantly hindering their practical deployment in real-world applications. This vulnerability is primarily attributed to the intrinsically low formation energy of LHPs, which renders them highly susceptible to extrinsic environmental stimuli such as light, oxygen, and thermal fluctuations. Among these, environmental stress is widely recognized as a principal factor compromising both the operational stability and longevity of LHP-based materials.[76,124–129]

1.4.1. Origin of instability in lead halide perovskite crystal structure:

Structural instability: The A-site cations in halide perovskites occupy 12-fold coordinated sites located within the interstitial voids formed by eight surrounding PbX_6 octahedra. As such, the incorporation of A-site cations is constrained by the geometric limitations of the three-dimensional PbX_6 framework.[127,130,131] If the A cation is excessively large, it cannot be accommodated within the available interstitial space, leading to lattice distortion or phase instability. Conversely, if the A cation is too small, it may fail to adequately fill the cavity, thereby compromising the structural cohesion and potentially resulting in the collapse of the three-dimensional perovskite structure. Hence, the ionic radius of the A-site cation plays a critical role in stabilizing the perovskite lattice. Goldschmidt tolerance factor, t is used to determine the structural stability and the distortion in perovskite nanocrystal. The Goldschmidt tolerance factor is expressed as the following equation (equation 1.1).[132]

$$t = \frac{(r_A + r_X)}{\sqrt{2}(r_B + r_X)} \quad\quad\quad (1.1)$$

where r_A, r_B and r_X correspond to the radius of the component A, B, and X, respectively. In general, perovskite materials retain three-dimensional structural connectivity when the Goldschmidt tolerance factor (t) falls within the approximate range of 0.813 to 1.107. Recent studies suggest that a more optimal range of $0.9 \leq t \leq 1.0$ is associated with the formation of ideal cubic perovskite structures, reflecting minimal octahedral distortion.[133,134] In contrast, when the tolerance factor lies between 0.71 and 0.9, the increased mismatch in ionic radii leads to distortions of the PbX_6 octahedra, favouring the emergence of lower-symmetry phases such as orthorhombic or rhombohedral structures. If the tolerance factor falls outside this range, the structural requirements for maintaining a stable 3D octahedral framework are not satisfied, often resulting in its collapse and the formation of lower-dimensional phases.[131,135]

Effect of environmental factors: Environmental stability remains a critical challenge for practical applications of Perovskite nanocrystals (NCs), particularly those based on lead halide compositions such as $CsPbX_3$. These nanocrystals are highly sensitive to external stimuli such as moisture, oxygen, heat, and ultraviolet (UV) irradiation.[127–129,136] Exposure to ambient humidity often results in rapid degradation due to the hygroscopic nature of the halide components and the dynamic ionic lattice, in presence of moisture the nanocrystal decomposes as per the reaction mechanism, $CsPbBr_3 + H2O \rightarrow PbBr_2 + CsBr + H_2O$ which facilitates hydrolysis and the formation of non-luminescent byproducts.[137] Similarly, thermal stress can induce phase transitions and lead to the decomposition of the perovskite structure into lead halides. Photo-induced degradation, particularly under UV illumination, is driven by the generation of halide vacancies, generating surface trap states, and phase segregation to adjacent nanoparticle, accelerating non-radiative recombination and structural instability.[125–129]

Interface induced instability: Due to their ionic composition, lead halide perovskites (LHPs) exhibit surface interactions that are largely governed by ionic forces. In a study, Roo[119] *et al.* first explored the surface dynamics of $CsPbBr_3$ perovskite nanocrystals (PNCs) using 1H NMR spectroscopy. They discovered that the ligands typically used for surface passivation oleic acid (OA) and oleylamine (OLA) are not firmly attached to the nanocrystal surface. In the absence of OLA, surface stabilization is primarily achieved through the formation of oleylammonium bromide from protonated OA. When both OA and OLA are present, the protonated OLA enhances OA's incorporation into the ligand shell, reinforcing surface stabilization through oleylammonium bromide. To further characterize the dynamic behavior of surface ligands, diffusion-ordered NMR spectroscopy (DOSY) was employed to measure the diffusion coefficient (D). The diffusion coefficient (D) is defined as the following equation (equation 1.2).

$$D = \frac{k_B T}{f} \hspace{3cm} (1.2)$$

The relatively small D values indicate rapid ligand exchange between the bound and unbound states, reflecting the weak and dynamic nature of ligand attachment.[138,139] This inherent instability at the nanocrystal–ligand interface renders $CsPbX_3$ nanocrystal particularly vulnerable to ligand desorption during purification procedures. The use of polar solvents, in particular, often results in substantial ligand loss, which can compromise the optical properties, colloidal stability, and, in some cases, the structural integrity of the nanocrystals.

1.4.2. Approach towards improving the stability of lead halide perovskite nanocrystal:

Improving the stability of perovskite nanocrystals (PNCs) has become a central focus in advancing their practical applications. Strategies to enhance their stability primarily involve surface passivation, ligand engineering, and compositional tuning. Surface passivation with robust and strongly binding ligands helps to prevent degradation caused by moisture, oxygen,

and heat.[140–148] Together, these approaches aim to mitigate the intrinsic instability of PNCs while preserving or enhancing their optoelectronic properties.

Compositional engineering: Compositional modifications, such as doping with metal ions or partially substituting halides, have also been effective in enhancing resistance to environmental stressors. Metal ion doping to the perovskite host lattice not only improves the ambient stability but also helps in augmenting the opto-electronic properties of the perovskite nanocrystals.

A-site doping: Modifying the A-site cation in perovskite nanocrystals (PNCs) with appropriate metal ions has proven to be an effective approach for enhancing both stability and optoelectronic performance. Substituting the smaller methylammonium (MA^+) with larger formamidinium (FA^+) or cesium (Cs^+) ions improves the structural compatibility within the perovskite lattice, thereby boosting thermal and environmental stability.[146,147] Etgar et al.[149] demonstrated that doping $CsPbX_3$ with rubidium (Rb^+) to form $Rb_xCs_{1-x}PbX_3$ quantum dots results in tunable fluorescence without significant structural disruption. These Rb/Cs mixed-halide PNCs showed improved long-term stability, evidenced by a slight redshift in absorption over time, while the chloride analogues were less stable. Similarly, the incorporation of potassium (K^+) ions into $CsPbBr_3$ PNCs substantially improved their resistance to photodegradation and environmental factors. This stability enhancement is linked to the formation of a K-rich surface phase that effectively inhibits halide ion migration and minimizes non-radiative recombination.[150,151] Overall, these studies emphasize the potential of A-site cation engineering, particularly through the inclusion of Rb^+ and K^+ ions, as a powerful strategy to enhance the durability and optical quality of perovskite nanomaterials.

B-site doping: Zhu *et al.*[152] reported that the substitution of A-site cations has a limited influence on the environmental stability and band-edge carrier dynamics of lead halide perovskites (LHPs), as demonstrated through comparative studies of $CsPbBr_3$, $FAPbBr_3$, and

MAPbBr$_3$ single crystals. In contrast, B-site doping has long been acknowledged as a successful method for tuning the optoelectronic characteristics and enhancing the structural robustness of LHPs.[152–156]

Among various dopants, Mn^{2+} has attracted considerable attention. Chen *et al.*[157] demonstrated that Mn^{2+}-doped CsPbBr$_3$ nanocrystals (PNCs) exhibited improved photoluminescence (PL) stability, retaining ~60% of their initial PL intensity after 120 days of air exposure, compared to only 30 days for undoped PQDs. Deng *et al.*[158] synthesized environmentally stable CsSnBr$_3$ hollow nanocages using stannous 2-ethylhexanoate at elevated temperatures. Sun *et al.*[159] achieved near-unity PL quantum yields in violet-emitting CsPbCl$_X$Br$_{1-X}$ PNCs via Ni^{2+} doping, which enhanced local lattice ordering and defect passivation. Meng *et al.*[160] reported the stabilization of blue-emitting PNCs through Al^{3+} doping. Furthermore, Song *et al.*[161] introduced rare-earth (RE) ions (e.g., Dy^{3+}, Eu^{3+}, Ce^{3+}, Sm^{3+}, Yb^{3+}, Tb^{3+}, Er^{3+}) in CsPbCl$_3$ PNCs, resulting in broadband emissions from the visible to near-infrared regions with enhanced PL efficiency and stability.

Encapsulation strategy:

The encapsulation of perovskite nanocrystals has appeared as a critical approach to address their inherent instability under ambient conditions, including exposure to moisture, oxygen, thermal stress, and ultraviolet radiation. Embedding nanocrystals within protective matrices, such as polymers, silica frameworks, inorganic shells, and metal-organic frameworks, establishes a physical barrier that effectively mitigates environmental degradation pathways.[162–165] This methodology not only preserves the optoelectronic and structural properties of perovskite nanocrystals but also substantially enhances their operational stability, thereby facilitating their practical deployment in optoelectronic devices. For example, Snaith *et al.*[144] incorporated MAPbX$_3$ nanocrystals into polystyrene (PS) and polymethyl methacrylate

(PMMA) beads, resulting in improved ambient stability. Similarly, Kuo *et al.*[166] encapsulated

CsPbX$_3$ perovskite nanocrystals (PNCs) within stretchable poly(styrene-butadiene-styrene)

(SBS) fibers via an electrospinning technique, producing waterproof, multicolor-converting

membranes for light-emitting diode (LED) applications. Chen and colleagues fabricated

uniform CsPbX$_3$/polyacrylonitrile (PAN) nanofibers through electrospinning, where the

hydrophobic nature of PAN conferred enhanced resistance to humidity.[167] Furthermore, Zhong

et al.[163] reported the synthesis of MAPbBr$_3$/polyvinylidene fluoride (PVDF) composite films,

where strong interactions between the –NH$_3^+$ groups of MAPbBr$_3$ and the –CF$_2$– groups of

PVDF led to an increase in photoluminescence quantum yield (PLQY). In addition to these

polymers, materials such as polyvinylpyrrolidone (PVP), cellulose acetate (CA), polyvinyl

chloride (PVC), and polydimethylsiloxane (PDMS) have also been employed to protect

perovskite nanocrystals from environmental degradation.
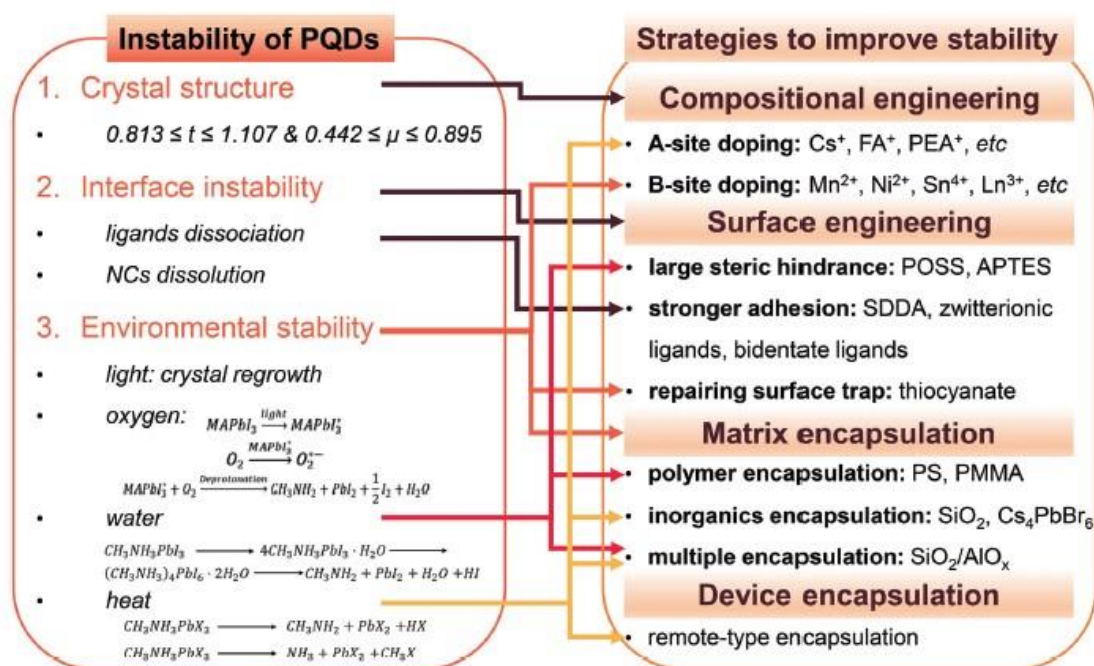
Figure 1.4 Schematic diagram summarizing the instability of PNCs and the corresponding solutions. Adapted from ref 134. Copyright 2019 Royal Society of Chemistry.

Despite the advantages of polymer-based encapsulation, particularly in moisture resistance, its limited thermal stability remains a significant limitation for high-temperature applications. Elevated temperatures often induce degradation of the polymer matrix alongside the detachment of organic ligands from the surface of PNCs, resulting in irreversible quenching of photoluminescence. In contrast, inorganic matrices exhibit superior mechanical strength and thermal resilience, making them highly suitable for enhancing the long-term stability of PNCs. For instance, Liu *et al.*[138] successfully incorporated pre-synthesized $CsPbBr_3$ PNCs into mesoporous silica (SiO_2) spheres with pore sizes ranging from 12 to 15 nm, achieving composites with enhanced thermal stability and photostability, which retained their optical properties after 40 days of ambient air exposure. Additionally, Zeng and co-workers demonstrated that, beyond conventional silica coatings, anchoring PNCs onto silica surfaces could further improve their environmental stability.[168] Other inorganic matrices, such as mesoporous Al_2O_3, TiO_2, ZnS, and CdS shells, have also been utilized effectively to safeguard perovskite nanocrystals against degradation.[169–171]

1.5. Metal Ion Doping in Perovskite Nanocrystals

1.5.1. Types of Metal Ion Doping in Perovskite Nanocrystals

Metal ion doping in halide perovskite nanocrystals involves deliberate substitution of lattice ions at the A-site (monovalent cation), B-site (divalent metal), or X-site (halide), which enables targeted tuning of optoelectronic properties, crystal phase behaviour, and environmental stability. A-site doping often utilizes ionic species such as Rb^+, K^+, or mixed cationic systems (e.g., $MA^+/FA^+/Cs^+$) to adjust the Goldschmidt tolerance factor and stabilize the 3D ABX_3 perovskite structure. For instance, mixing FA^+ and Cs^+ at the A-site ($FA_{1-x}Cs_xPbBr_3$) enables better structural rigidity and red-shifted photoluminescence with increasing FA^+ content due to lattice expansion.[172]

B-site doping is perhaps the most consequential, as it directly influences the conduction and valence band edges. Common dopants include Ni^{+2}, Mn^{+2}, Sn^{+2} Zn^{+2}, Cu^{+2},[153,155,157–159] , and Co^{+2}. These are introduced via isovalent or heterovalent substitution at the Pb^{+2} site. For example, Mn^{+2}-doped $CsPbX_3$ nanocrystals ($CsPb_{1-x}Mn_xX_3$) display dual emission due to energy transfer between host and dopant states.[157] Partial replacement of Pb^{2+} with Sn^{2+} or Zn^{2+} also reduces toxicity while retaining the desirable optical properties of the parent perovskite [158,172]

X-site doping refers to halide substitution—typically Cl^-, Br^-, or I^-—to modulate band gaps and emission colors across the visible spectrum. For example, by tuning the halide ratio in $CsPb(Br_{1-x}I_x)_3$, one can achieve emission shifts from green to red, though phase segregation remains a challenge in mixed-halide systems.

1.5.2. Property Enhancement Achieved through Doping

Doping has emerged as a key strategy to overcome several limitations inherent in pristine perovskite nanocrystals, particularly related to instability and toxicity. A-site cation engineering (e.g., FA^+/Cs^+ mixing) enhances phase stability by balancing lattice strain and minimizing phase transitions to non-perovskite δ-phases. For example, $FA_{1-x}Cs_xPbI_3$ nanocrystals exhibit significantly improved photostability and retain their near-IR emission under ambient conditions for extended periods.[172]

B-site doping with divalent or heterovalent cations not only reduces Pb content but also enhances thermal and photochemical stability. Sn^{+2} or Zn^{+2} substitution at the Pb-site has shown to increase the formation energy of the perovskite phase and suppress ion migration and degradation.[158] However, care must be taken, as certain dopants (e.g., Ge^{+2}, Sn^{+2}) may oxidize easily, negatively affecting device performance.

Optoelectronic properties also benefit from doping-induced improvements in carrier dynamics. Dopants can passivate nonradiative recombination centers, extend exciton lifetime, and enhance charge extraction efficiency. For example, Mn^{+2} doping in $CsPbCl_3$ enhances PL lifetime and creates spin-polarized excitonic emission, offering advantages in spintronic applications. Additionally, doping is a promising strategy to achieve defect-tolerant band structures, maintain high PLQY, and stabilize perovskites without requiring complex surface passivation strategies.[173]

1.5.3. Applications of Metal-Ion-Doped Perovskite Nanocrystals

The improved properties achieved through doping make perovskite nanocrystals suitable for a wide range of applications. In light-emitting diodes (LEDs), doped perovskites offer narrow, high-brightness emission with enhanced thermal and operational stability. For instance, Mn^{+2}-doped $CsPbCl_3$ nanocrystals have been used in color-tunable LEDs with suppressed blinking and high efficiency.

In photovoltaics, doping enables energy band alignment, phase stabilization, and defect passivation, contributing to enhanced power conversion efficiency (PCE) and reduced hysteresis. Mixed-cation and mixed-halide perovskites have shown remarkable improvements in moisture and thermal stability, which is crucial for long-term device operation.[8,10]

Doped perovskites are also increasingly applied in photodetectors due to their enhanced light sensitivity and wavelength selectivity. In photocatalysis, doping introduces active sites for redox reactions, improves charge separation, and enables visible-light-driven processes like CO_2 reduction and water splitting.[64,66] Moreover, doped perovskites have found use in biomedical imaging, chemical sensing, and anti-counterfeiting due to their bright, tunable luminescence and functional surface chemistry.

1.6. Properties of Perovskite Materials.

1.6.1. Linear absorption and fluorescence properties

Metal halide perovskite (MHP) is a potential material for low-cost optoelectronic devices because of its exceptional optical and electrical properties. These characteristics include a narrow bandwidth, high absorption coefficient, high PLQY, tunable photoluminescence across the visible spectrum and beyond, and defect tolerance.[12–14] Lead-based MHPs have a p-type electrical conduction band, which is made up of σ-antibonding between the np orbital of the halide (where n =3 to 5 for Cl to I) and the 6p orbital of lead.[174,175] The valence band exhibits a partial s-type feature since it consists of halide np orbitals and Pb 6s. The band's colour is determined by its orbital properties; I 5p, Pb 6p, and Pb 6s orbitals are represented by green, red, and blue, respectively. As the valence band of MHPs has the dominant contribution from the halide p orbitals, the position of the valence band becomes extremely sensitive towards the selection of halide ions. The band gap can be readily controlled by changing the halide ions from I^{-1} to Br^{-1} to Cl^{-1}. By altering the I and Br ion compositions, Noh *et al.*[176] showed optical band gap tuning in mixed-halide $MAPb(I_{1-x}Br_x)_3$ perovskite nanocrystal. Furthermore, Kumawat *et al*. used the Sommerfeld model to compute the band gap in $MAPb(Br_{1-x}Cl_x)_3$ while taking the excitonic contribution at the band-edge into account. It is important to keep in mind that, although the A-site cations such as Cs, FA, or MA do not directly contribute to the electrical band gap, but can influence the crystal structure through Pb-X-Pb rotation and thereby modify the band gap.[177–179] Furthermore, surface modification and the quantum confinement effect also have a significant impact on tuning the optical characteristics of these MHP nanocrystals.
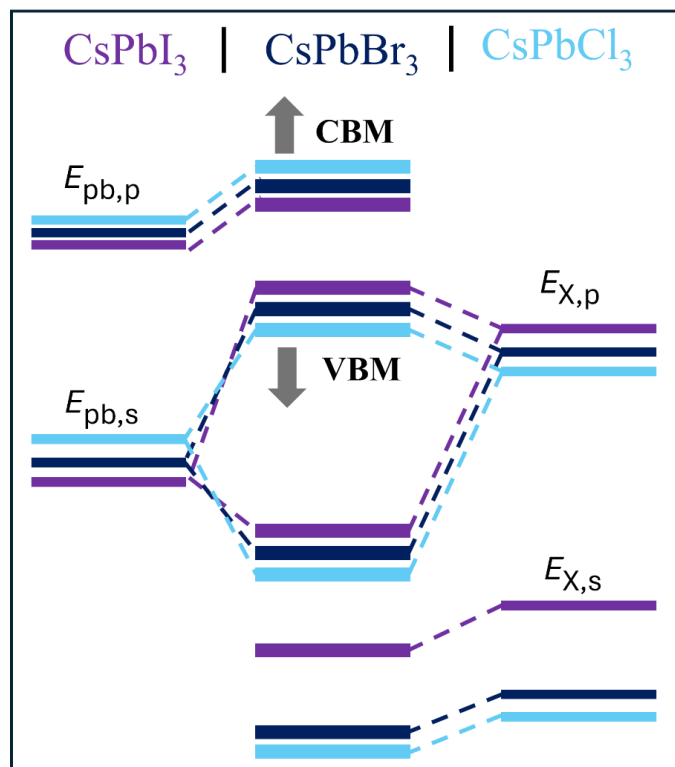
Scheme 1.1: Absolute energy level positions of lead-based halide perovskites. Arrows indicate the shift in energy levels upon atom substitution.[180]

1.6.2. High charge carrier diffusion length:

The performance of perovskite materials in a variety of optoelectronic devices is greatly improved by their renowned high charge carrier mobility.[34,181,182] The high charge carrier mobility observed in perovskite materials, particularly in hybrid organic-inorganic lead halide perovskites, originates from their unique crystallographic and electronic properties.[181] A fundamental contributor is the favourable band structure, in which both the conduction and valence bands are highly dispersive due to strong orbital overlap between the B-site metal cation (e.g., Pb^{+2}) and the halide anions (X^-), resulting in low effective masses for both electrons and holes shown by Motta *et al.*, in 2015.[183] This facilitates rapid charge transport with reduced scattering. Additionally, the soft and polar lattice of perovskites allows for dynamic screening of charged defects, meaning that local lattice distortions can adapt to and stabilize charge carriers, thereby minimizing recombination and trap-assisted scattering.

Another key factor is the relatively weak electron–phonon coupling in these materials, in 2016 Herz *et al*, this weak electron–phonon coupling limits energy losses due to lattice vibrations and maintains high mobility even at room temperature.[184] Moreover, the presence of strong spin–orbit coupling (SOC) in lead-based perovskites further modifies the band structure by splitting energy levels, effectively reducing non-radiative recombination and enhancing carrier transport (Brivio et al., 2014). Additionally, the perovskite structure exhibits tolerance to point defects, as many do not introduce deep energy levels in the bandgap, allowing for long carrier lifetimes and diffusion lengths (Yin et al., 2014). These characteristics allow perovskite-based devices to achieve high power conversion efficiencies, rivalling or even surpassing those of traditional semiconductor materials.

1.6.3. Photophysical dynamics of perovskite nanocrystal:

Perovskite nanocrystals (NCs) exhibit a range of excited-state processes that critically influence their optoelectronic properties. Upon photoexcitation, carrier dynamics span from femtoseconds to microseconds, governed by processes such as hot carrier cooling, exciton formation, carrier trapping, and radiative or non-radiative recombination.[184,185] Immediately after photon absorption, hot carriers with excess energy relax rapidly (<1 ps) to band-edge states through phonon scattering. Depending on confinement effects, either free carriers or bound excitons may form, influencing charge transport and separation. Carrier trapping at surface or defect sites occurs on a 1–10 ps timescale, often leading to non-radiative recombination and reduced luminescence efficiency. Under high excitation fluence, Auger recombination—where energy from electron-hole recombination is transferred to a third carrier—dominates, typically within 10–100 ps. Radiative recombination of band-edge carriers, responsible for photoluminescence (PL), occurs over 1–100 ns. Delayed emission, observed over 100 ns to microseconds, is attributed to trap states or biexcitonic recombination.
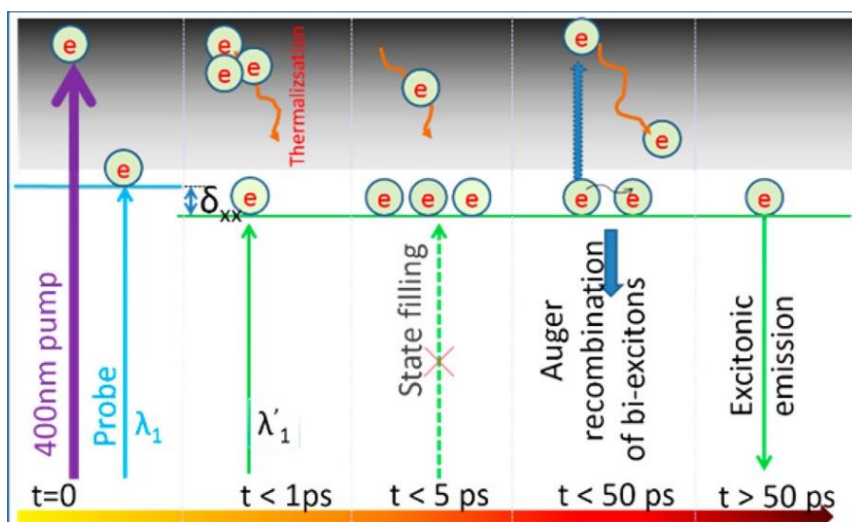
Scheme 1.2: Schematic representation of the excited-state processes happening upon photoexcitation of perovskite nanocrystals.[186] Adapted from ref 186. Copyright 2017 American Chemical Society.

Table 1.1: A concise summary of these excited-state processes and their characteristic timescales.

Phenomenon	Timescale	Process type	Functional relevence
Hot carrier cooling	<100 fs – 1 ps	Phonon-mediated relaxation	Limits hot carrier harvesting
Exciton formation/dissociation	<1 ps	Carrier correlation	Affects charge separation and transport
Carrier trapping	1–10 ps	Surface/defect interaction	Leads to non-radiative recombination
Auger recombination	10–100 ps	Multicarrier non-radiative loss	Decreases PL at high excitation densities
Radiative recombination	1–100 ns	Band-edge emission	Enables light emission in LEDs and lasers
Delayed emission	100 ns – μs	Trap- or multiexciton-mediated	Reveals trap state occupation and dynamics
Energy transfer	10–1000 ps	FRET/Dexter mechanism	Enables hybrid photonic or catalytic systems
Charge transfer	100 fs – 10 ps	Electron/hole extraction	Critical in photovoltaics and photocatalysis

Energy and charge transfer processes are also vital: Förster or Dexter energy transfer (10–1000 ps) facilitates exciton migration in hybrid systems, while ultrafast charge transfer (100 fs–10 ps) to acceptor materials dictate device functions such as photovoltaics and photocatalysis.[184–187] These dynamics are highly sensitive to crystal composition, size, and surface chemistry.

Techniques like transient absorption spectroscopy and time-correlated single-photon counting (TCSPC) provide valuable insights into these phenomena, enabling the design of perovskite NCs with tailored properties for light-emitting, harvesting, and catalytic applications.

1.6.4. Defect tolerance of perovskite nanocrystal:

The disordered distribution of uncoordinated atoms and ions on the surfaces of nanocrystals (NCs) often leads to the formation of surface defects, which can act as non-radiative recombination centers for charge carriers. These defects significantly influence the photoelectric properties of NCs by quenching photoluminescence and reducing charge carrier lifetimes. However, lead halide perovskite NCs are known for their exceptional defect tolerance. Owing to the low formation energies of intrinsic point defects, they predominantly form shallow trap states rather than deep-level traps that strongly hinder optoelectronic performance.[188–190] Importantly, antisite defects, which typically introduce deep states in other semiconductors, are energetically unfavourable in perovskite lattices. Through theoretical modelling, Brinck *et al.*[191] demonstrated that even the removal of surface ligands has only a minimal effect on the electronic structure of perovskite NCs. This behaviour is attributed to the material's structural resilience and defect tolerance, allowing perovskite NCs to retain high photoluminescence quantum yield (PLQY) despite incomplete surface passivation.

1.6.5. Light-harvesting ability of perovskite nanocrystal:

Perovskite materials exhibit exceptional light-harvesting properties, which are integral to their outstanding performance in a wide array of solar energy conversion optoelectronic applications, including solar cells, light-emitting diodes (LEDs), lasers, and photodetectors.[192–194] These capabilities are primarily driven by highly efficient energy transfer mechanisms, wherein photoexcited energy is relayed from perovskite nanocrystals to nearby acceptor molecules. The two principal pathways facilitating this transfer are Förster resonance energy

transfer (FRET) and Dexter energy transfer (DET). FRET is a long-range, non-radiative dipole–dipole interaction, typically effective over distances of 10–12 nm, and its efficiency is critically dependent on the spectral overlap between donor emission and acceptor absorption.[195–197] In contrast, DET is a short-range mechanism, operative over 1–2 nm, requiring direct orbital overlap between the donor and acceptor species.[197,198] In addition to spatial and spectral factors, the spin state of the excitons also plays a critical role in the energy transfer dynamics. Both singlet and triplet energy transfer processes can occur, governed by the nature of the donor–acceptor system and the perovskite matrix. In a notable study, DuBose *et al*. (2021) demonstrated that modulation of the spectral overlap integral $J(\lambda)$ via chloride ion exchange in $CsPbBr_3$ nanocrystals allows precise control over both the rate and efficiency of singlet energy transfer to Rhodamine B.[199] Their findings indicated that increased chloride content enhances the contribution of the DET pathway relative to FRET as upon Cl-alloying the spectral overlap gradually decreases. Furthermore, subsequent investigations have underscored the importance of donor–acceptor separation in modulating FRET efficiency, suggesting that nanoscale spatial tuning is a viable strategy for optimizing energy transfer in perovskite-based assemblies.

Triplet energy transfer (TET) refers to the process by which the triplet excited state of an acceptor molecule is populated via energy transfer. The direct excitation of a chromophore into its triplet excited state is a spin-forbidden process due to the requirement for a change in spin multiplicity. However, triplet states can be accessed indirectly through processes such as intersystem crossing (ISC) from the singlet excited state or singlet fission in suitable molecular systems.[200–205] An alternative and increasingly explored strategy involves the use of semiconductor nanocrystals as sensitizers to facilitate direct triplet state population in molecular acceptors via triplet energy transfer. In this approach, photoexcitation of the nanocrystal generates an exciton that can transfer energy to a molecular acceptor. For this

energy transfer to be thermodynamically favourable, the nanocrystal's band gap must be lower in energy than the singlet excited state of the acceptor, yet higher than its triplet state energy. Under these conditions, the nanocrystal can selectively sensitize the triplet state of the acceptor without populating the singlet state. This method offers significant advantages, as triplet excited states generally exhibit extended lifetimes compared to singlet states, enhancing their utility in applications such as photochemical catalysis, photon up conversion, and photodynamic therapy. A recent study by Chemmangat et al.[206] revealed that increasing the Mn^{+2} doping concentration in a $CsPb(Cl_{0.7}Br_{0.3})_3$ host lattice significantly enhances the triplet character of energy transfer. This observation suggests that compositional engineering of the perovskite matrix can be employed to manipulate spin-dependent pathways and thereby tailor the photophysical behaviour of hybrid systems.
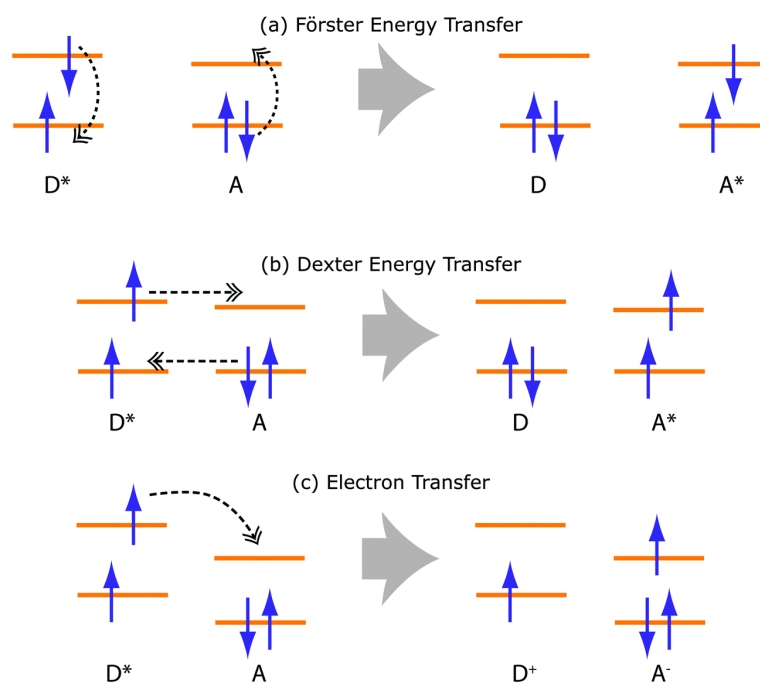
Scheme 1.3: **[a]** FÖRSTER and **[b]** DEXTER energy transfer mechanism. **[c]** electron transfer mechanism. Black arrows indicate excitation, relaxation and electron exchange during the energy and electron transfer process, respectively.[207] Adapted from ref 203. Copyright 2015 Royal Society of Chemistry.

In 2020, Luo et al. (2020) reported a two-step Dexter-type triplet energy transfer mechanism from CsPbBr₃ nanocrystals to surface-bound tetracene carboxylic acid ligands. In a follow-up study, the same group demonstrated that quantum confinement within the nanocrystals markedly improves TET efficiency, emphasizing the influence of nanocrystal size on transfer dynamics.[208] More recently, the development of low-dimensional and two-dimensional (2D) halide perovskites has emerged as a promising semiconductor material for the efficient sensitization of molecular triplet states.

1.6.6. Charge transfer dynamics in perovskite nanocrystal:

Perovskite nanocrystals (NCs) have garnered significant attention as efficient interfacial electron transfer agents due to their exceptional optoelectronic properties, tunable band structures, and high surface-area-to-volume ratios. These features position them as ideal candidates for facilitating charge transfer processes in hybrid systems such as photoelectrochemical cells, photocatalysts, and heterojunction-based optoelectronic devices.[209,210] Upon photoexcitation, perovskite NCs generate tightly bound electron–hole pairs (excitons) that are spatially confined within the nanocrystal, leading to a dynamic competition between interfacial charge transfer and radiative or nonradiative recombination. As a result, the kinetics of electron or hole transfer across the semiconductor interface become critically important in dictating the overall efficiency of these systems.

To enhance the efficiency of selective charge transfer, particularly for reductive applications requiring electron accumulation, sacrificial agents are typically introduced to quench one type of carrier—most commonly, holes. Commonly used sacrificial hole scavengers include solvents like ethanol and ethyl acetate or molecular donors such as triethanolamine (TEOA) and ascorbic acid, which help suppress hole-mediated recombination and facilitate sustained

electron flow.[211] In addition to these strategies, a wide range of redox-active probes—such as methyl viologen (MV^{+2}), ferrocene/ferrocenium couples, semiconductor heterojunctions, and metallic nanoclusters—have been employed to monitor and study the kinetics of interfacial electron transfer from perovskite NCs.[212,213]

Importantly, these materials are also capable of efficient hole transfer, underscoring their dual functionality in redox processes. Notably, in 2020, De et al.[214] demonstrated selective hole transfer from $CsPbBr_3$ nanocrystals to surface-anchored 4-mercaptophenol, emphasizing the role of specific molecular functionalization in directing charge separation pathways. The ability to control both electron and hole transfer at the nanoscale through interface engineering and ligand design opens up new opportunities for developing highly efficient photocatalytic and energy conversion systems based on perovskite nanocrystals.

Another critical factor influencing the efficiency of interfacial charge transfer in perovskite nanocrystals lies in their surface chemistry. Native surface ligands, typically introduced during colloidal synthesis to maintain nanocrystal stability and dispersibility, often serve as insulating barriers that hinder the diffusion and proper orientation of electron-accepting molecules at the nanocrystal surface. Consequently, effective charge transfer strongly depends on the molecular interactions between the semiconductor interface and the redox-active species.[215–217] Functional groups such as carboxylates and thiocyanates present on electron acceptors have been shown to bind preferentially to under-coordinated lead or halide sites on $CsPbBr_3$ nanocrystals, thereby facilitating close contact and favourable alignment for electron injection or extraction. These groups also play a critical role in passivating surface trap states, thereby enhancing photochemical stability and electronic coupling. In 2020, Prof. Kamat's research group demonstrated the profound influence of ligand binding mode and geometry on interfacial electron transfer. Their findings revealed that tightly bound ligands, such as didodecyldimethylammonium bromide (DDAB), create a physical barrier that limits the

approach of electron acceptor molecules to the nanocrystal surface, thereby hindering electron transfer efficiency. Conversely, $CsPbBr_3$ nanocrystals capped with more labile ligands, such as oleic acid (OA) and oleylamine (OAm), allow greater surface accessibility and facilitate more effective electron transfer at the interface.[218] The interplay between surface ligand engineering and charge-transfer kinetics continues to be a pivotal area of research in optimizing perovskite-based photocatalytic and optoelectronic systems.
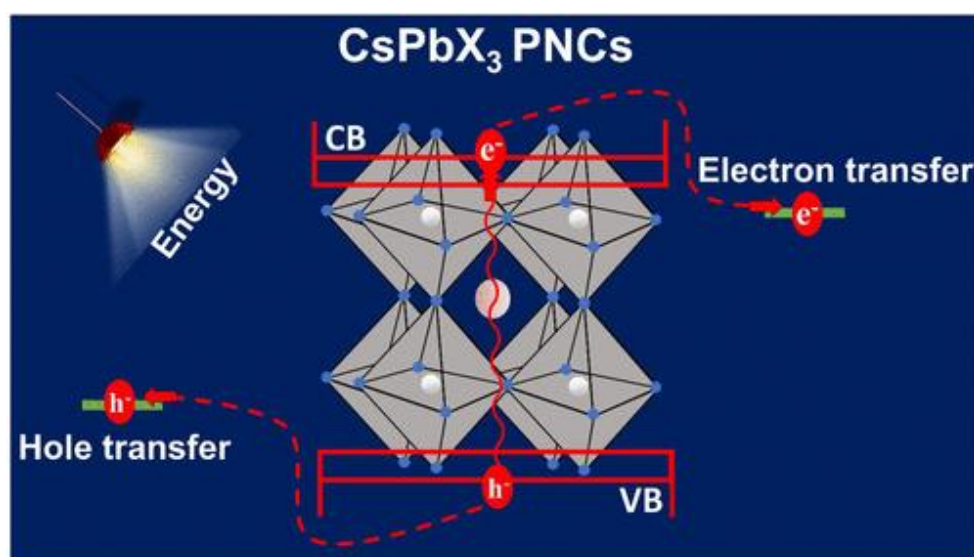
Scheme 1.4: Electron and Hole transfer mechanism from perovskite nanocrystal to the nearby acceptor molecule.[219] Adapted from ref 214. Copyright 2022 American Chemical Society.

1.6.7. Superfluorescence and superradiance of perovskite nanocrystals:

Perovskite nanocrystal (PNC) superlattices have emerged as promising systems for understanding the superradiance and superfluorescence—collective quantum emission phenomena driven by coherent excitonic interactions. Superfluorescence (SF) arises when an initially incoherent population of excitonic dipoles spontaneously establishes phase coherence, culminating in a delayed, intense pulse of coherent radiation. This collective emission is mediated by the spontaneous emergence of a macroscopic dipole moment within the system.[220] Conversely, superradiance proposed by Dicke in 1954 typically involves coherent excitation of dipoles into a common excited state via an external laser source, followed by rapid,

directional emission as the dipoles decay in phase.[221] The ordered, high-density arrangement of nanocrystals in PNC superlattices fosters strong interparticle dipole–dipole interactions and electronic coupling, enabling the formation of minibands and significantly enhancing radiative recombination while suppressing nonradiative pathways.[222,223] These features render perovskite superlattices an ideal medium for cooperative emission effects. Moreover, by tailoring the nanocrystal composition, interparticle spacing, and superlattice symmetry, the emission dynamics and coherence properties can be precisely tuned. Such control opens up new avenues for engineering quantum photonic devices, including on-demand coherent light sources, single-photon emitters, and components for quantum communication and computation platforms [224–226]

1.6.8. Ensemble to single particle journey of perovskite nanocrystal:

Over the years, advancements in the synthesis of perovskite nanomaterials have significantly enhanced control over size uniformity and reproducibility, enabling detailed investigations into their quantum-confined optical properties. These improvements have facilitated single-particle studies of perovskite quantum dots (PQDs) or nanocrystals (PNCs), uncovering phenomena typically unclear in ensemble measurements, such as photoluminescence blinking, single-photon emission, exciton fine-structure splitting, and the quantum-confined Stark effect.[227,228] In the single-particle regime, quantum confinement induces discrete energy levels, allowing direct observation of quantum phenomena like single photon emission and quantum entanglement. These effects are not only of fundamental interest but also critical for the development of quantum photonic technologies. Moreover, the self-assembly of PNCs into superlattices introduces collective quantum optical behaviours, including superfluorescence, driven by strong interparticle coupling and coherent excitonic interactions. These cooperative phenomena expand the functional potential of perovskite-based materials, making them attractive candidates for advanced optoelectronic applications such as quantum light sources,

high-resolution imaging systems, and low-threshold lasers. A comprehensive understanding of both ensemble-averaged and single-particle emission characteristics is essential for the rational design of perovskite materials for specific high-performance applications, spanning from efficient light-emitting diodes to next-generation quantum devices. Continuous investigation of these quantum optical properties is expected to accelerate innovation in perovskite optoelectronics, paving the way for next-generation technologies.

1.7. Applications of Perovskite Materials.

Perovskite materials have drawn immense interest over the past decade due to their extraordinary optoelectronic properties, compositional versatility, and cost-effective processability. Originally investigated in the context of oxide-based ceramics, the perovskite class now encompasses a broad range of hybrid organic–inorganic and fully inorganic halide perovskites, which have demonstrated promising potential across a variety of application domains. The multifunctional nature of perovskite materials, arising from their tunable band gaps, high absorption coefficients, long carrier diffusion lengths, and facile solution processability, underpins their utility in an expanding array of technological applications.[12–14]

1.7.1. Photovoltaics (Solar Cells).

Perovskite nanocrystals (PNCs) have emerged as a transformative material in photovoltaic technology, leveraging their unique nanoscale properties to advance solar cell applications. These nanocrystals exhibit quantum confinement effects, enabling precise tuning of their bandgap by adjusting their size and composition. Since the first report of a perovskite-based solar cell (PSC) in 2009 by Miyasaka group with a power conversion efficiency (PCE) of just 3.8%,[9] the field has witnessed a meteoric rise, with state-of-the-art devices now exceeding 26% efficiency in experimental setups.[229,230] Unlike bulk perovskites, PNCs can be synthesized via

low-cost, solution-processable methods, facilitating their integration into flexible, lightweight, and semi-transparent solar devices through techniques like spin-coating or inkjet printing. Their high absorption coefficients permit ultrathin, efficient active layers, reducing material usage while maintaining performance. Additionally, PNCs are promising for tandem solar cells, where they complement silicon or CIGS layers by capturing high-energy photons, potentially pushing PCEs beyond 30%. However, challenges persist in stability and toxicity; PNCs are susceptible to moisture, heat, and UV degradation, and lead content raises environmental concerns.[127–129] Recent advances address these via surface ligand engineering, encapsulation, and lead substitution with elements like tin or germanium. Furthermore, defect passivation and improved charge transport mechanisms mitigate recombination losses, enhancing durability.[15,17,231,232] As research progresses in nanostructural optimization and eco-friendly formulations, perovskite nanocrystals hold immense potential to drive scalable, high-efficiency, and low-cost renewable energy solutions, marking a pivotal shift in solar technology innovation.

1.7.2. Light-Emitting Devices (LEDs).

Perovskite nanocrystals (PNCs) have revolutionized light-emitting diode (LED) technology due to their exceptional optoelectronic properties, including high photoluminescence quantum yield (PLQY), narrow emission linewidths, and tunable bandgaps across the visible spectrum.[233] By adjusting the composition (e.g., halide mixing in $CsPbX_3$, where X = Cl, Br, I) and nanocrystal size, PNCs can emit precise, saturated colours spanning deep blue to near infrared, making them ideal for high-performance displays and lighting.[11,234,235] Their solution-processability enables low-cost fabrication of ultrathin, flexible LED devices via techniques such as spin-coating, inkjet printing, or blade-coating, aligning with next-generation applications in wearable electronics and rollable screens. In display technologies, PNC-based LEDs (PeLEDs) outperform conventional quantum dots and organic LEDs (OLEDs) in colour

purity and brightness, with recent red and green PeLEDs achieving external quantum efficiencies (EQEs) exceeding 20%,[236,237] rivalling commercial standards. For white-light illumination, PNCs can serve as down-conversion phosphors in blue LED chips, offering tunable correlated colour temperatures (CCTs) and high luminous efficacy. Additionally, their defect-tolerant nature and rapid radiative recombination rates minimize non-radiative losses.[188,189] Emerging applications include electrically driven single-photon sources for quantum communication and bio-integrated optoelectronics for medical imaging. As efforts in defect passivation, charge transport layer optimization, and scalable manufacturing intensify, perovskite nanocrystals are poised to redefine energy-efficient, vibrant, and adaptable lighting and display systems.[219,234,235]

1.7.3. Catalysis and Electrochemical Applications.

Perovskite nanocrystals (PNCs), particularly those based on halide compositions such as $CsPbX_3$ (X = Cl^-, Br^-, I^-), have recently emerged as promising materials for catalysis and electrochemical applications,[66,238,239] owing to their tunable surface chemistry, high surface-to-volume ratios, and favourable charge transport characteristics. While much attention has been directed toward their optoelectronic properties, the potential of PNCs in facilitating redox reactions and interfacial charge transfer processes has opened new frontiers in energy conversion and storage technologies. In photocatalysis, the strong light absorption and efficient generation of photoexcited charge carriers render these materials highly active for driving processes such as the photoreduction of CO_2,[66] photocatalytic water splitting,[64] and degradation of organic pollutants.[240] The composition-dependent band alignment of PNCs can be finely tuned to match the redox potentials required for these reactions, enabling tailored catalytic behaviour. Furthermore, surface passivation strategies and ligand engineering play a critical role in enhancing their catalytic activity by modulating charge transfer kinetics and minimizing recombination losses. Beyond photocatalysis, perovskite NCs are increasingly explored as

active materials in electrochemical devices, including batteries, fuel cells, and supercapacitors.[241–243] In particular, hybrid organic–inorganic and all-inorganic perovskite NCs have shown promise as electrode materials and ion conductors in lithium-ion and sodium-ion batteries due to their favourable ion mobility and electrochemical stability.[244] Moreover, the defect-rich surfaces and tunable ion vacancy concentrations in these nanostructures enable efficient catalysis in oxygen evolution (OER) and hydrogen evolution (HER) reactions, key steps in water electrolysis.[245–247] Despite these advantages, the long-term operational stability of PNCs under electrochemical conditions remains a significant challenge, primarily due to their sensitivity to moisture, oxygen, and thermal stress. Ongoing research is focused on developing robust encapsulation strategies, surface modifications, and heterostructure composites to mitigate degradation while preserving or enhancing catalytic performance. As these challenges are progressively addressed, perovskite nanocrystals are expected to play an increasingly central role in catalysis and electrochemical energy technologies.

1.7.4. Photodetectors and Imaging Devices.

Perovskite nanocrystals (NCs), particularly all-inorganic variants such as $CsPbX_3$ ($X = Cl^-$, Br^-, I^-), have emerged as highly promising materials for next-generation photodetectors and imaging devices due to their exceptional optoelectronic properties, including high absorption coefficients, tunable band gaps, narrow emission linewidths, and high photoluminescence quantum yields.[12–14,233] These nanocrystals exhibit fast photoresponse, low dark current, and high responsivity across a broad spectral range from ultraviolet to near-infrared, making them ideal candidates for photodetection applications. One of the critical advantages of perovskite NCs lies in their size- and composition-dependent tunability, which allows precise control over their spectral response and enables the fabrication of wavelength-selective detectors.[239] Furthermore, their solution processability and compatibility with flexible substrates support the development of low-cost, large-area, and mechanically robust imaging sensors. In imaging

41

applications, the high spatial resolution and sensitivity of perovskite NC-based photodetectors are particularly beneficial for biomedical imaging, low-light surveillance. Additionally, perovskite NCs have been integrated into photodiode and photoconductor architectures, achieving notable performance metrics such as high external quantum efficiency (EQE) and detectivity values comparable to or exceeding those of conventional semiconductor materials like silicon or InGaAs.[237] Moreover, their potential in multispectral and colour imaging systems is being actively explored by leveraging mixed-halide compositions and heterostructures to achieve pixel-level spectral resolution. As research continues to overcome challenges related to long-term operational stability, environmental sensitivity, and toxicity, perovskite nanocrystals are poised to revolutionize the landscape of photodetector and imaging device technologies, offering high-performance, low-cost, and versatile alternatives to traditional materials.

1.7.5. Lasers and Optical Amplifiers.

Perovskite nanocrystals (PNCs) have shown promise for high-performance laser applications from the initial demonstration of stimulated emission and lasing in colloidal perovskite quantum dots. These materials offer a compelling combination of features from both colloidal semiconductor NCs and halide perovskites, such as solution-based fabrication, adjustable band gaps, strong light absorption, and minimal non-radiative losses.[12–14,233] Halide perovskite NCs are generally classified into two types: organic–inorganic hybrid perovskites (OIHPs) and inorganic halide perovskite NCs (IHPNs). While OIHPs incorporate organic components that can degrade under ambient conditions, IHPNs are more robust, showing enhanced resistance to moisture and oxygen. Both types, however, have proven to be highly effective in achieving optical gain and have been utilized across a range of laser technologies. These include random lasing systems,[248] distributed feedback (DFB) lasers,[249] vertical-cavity surface-emitting lasers

(VCSELs),[250] and advanced laser arrays capable of multicolour and high-resolution output.[251,252]

1.8. Scope of the Thesis.

With their exceptional optoelectronic characteristics, perovskite nanocrystals (PNCs) have garnered considerable attention as next-generation materials for advanced energy and photonic technologies. Their applications span a broad spectrum, including high-efficiency solar cells, light-emitting diodes (LEDs), and photodetectors. Notably, perovskite-based tandem solar cells (PSCs) have emerged as a disruptive alternative to conventional silicon photovoltaics, achieving power conversion efficiencies (PCEs) beyond 30%. The widespread appeal of PNCs arises from their composition of abundant elements, remarkable tolerance to structural defects, and long carrier diffusion lengths—features that collectively enhance their capabilities in light harvesting, charge transport, and photocatalysis.

Despite their remarkable potential, perovskite materials suffer from key limitations that hinder commercial viability, including degradation under moisture, heat, and UV exposure. Their lead content raises environmental concerns, prompting interest in tin- and bismuth-based alternatives. Additionally, phase instability and poor crystallinity further compromise device performance and reproducibility.

This thesis aims to address the pressing issue of ambient instability in inorganic perovskite nanocrystals (PNCs) while advancing the fundamental understanding of their energy harvesting capabilities. By integrating polymer-directed synthesis, facet engineering, and strategic metal ion doping, the research explores the underlying structure–property relationships that govern the stability and optoelectronic behaviour of these materials. Particular attention is given to the role of surface chemistry and crystallographic facets in influencing energy and electron transfer processes within PNC-based light-harvesting

assemblies. In this context, the following research questions have been selected to guide the investigation: (i) How does the hydrophilic–hydrophobic balance impact the dimensional engineering of halide perovskite crystals? (ii) Is it possible to synergize the defect tolerance with ambient stability of perovskite nanocrystals? (iii) Why does a facet of the perovskite nanocrystal dictate the energy transfer dynamics of the light-harvesting complex? and (iv) How can the coupling between energy transfer and electron transfer be resolved in PNC-based light-harvesting systems?

Chapter 2

Materials and Methodology

This Chapter covers the different chemicals used throughout the research, providing detailed synthetic method for 0D/3D perovskite composite crystals, as well as the metal-doped perovskite nanocrystals. It further includes various equipment employed, purification techniques, polymeric film preparation, ion exchange method and different spectroscopic and microscopic characterization. Experimental set up for time-corelated single photon counting and transient absorption spectroscopy have also been shown here. Methods of spectroscopic and microscopic data analysis have been presented as well.

2.1. Materials

Cesium Bromide (CsBr,) is from Avra. Lead Bromide (PbBr2, 99%), Nickel acetate tetrahydrate [(CH3COO)2Ni·4H2O, 98%], Cobalt acetate tetrahydrate [(CH3COO)2Co·4H2O, 99%], hexane HPLC (95%,), toluene HPLC(99.8%), rhodamine B, N,N-Dimethylformamide (DMF, 99.8%) and Hydrobromic acid (HBr, 99%) are obtained from Molychem., Bovine Serum Albumin (BSA, 98%), Cesium Carbonate (Cs2CO3, 97%) are purchased from SRL Chem. Dimethyl sulfoxide (DMSO, 99.5%) is from FINAR, Polyvinylidene difluoride (PVDF) from Alfa Aesar, 1-Octadecene (ODE,90%), Oleic Acid (OA), Oleylamine (OAm, 95%) is from TCI Chemicals and acetonitrile HPLC (99.8%) is obtained from SDFCL. All reagents were used without any further purification.

2.2. Experimental Techniques:

2.2.1. UV-vis absorption spectrometry

All the absorption spectra have been recorded at ambient conditions on a LABINDIA UV 3200 spectrophotometer and an Agilent compact UV-VIS spectrophotometer. The absorbance (A) of an absorber is defined as –

$$A = \log\left(\frac{I_0}{I}\right) = \varepsilon \times C \times l \qquad (2.1)$$

where I_0 and I stand for the incident and transmitted light intensities, respectively. C is the molar concentration of the absorbing species, ε is the molar extinction coefficient at a specific

wavelength, and l is the transverse light's path length (in centimeters). The cuvette's route length in the solution phase was 1 cm throughout the duration of the experiment. For the baseline correction, two milliliters of solvents were added to each cuvette and put in the sample and reference chambers. The sample cuvette is then filled with the appropriate volume of nanocrystal solution, and the absorbance spectra is recorded. In case of polymer thin film baseline was corrected using a transparent glass slide placed in both sides, then the fluorescent film prepared through drop casting method was placed in the sample chamber and measured the absorbance spectra. The nanocrystals' absorbance is maintained below 0.1 in the solution phase and below 0.6 in the thin film.

2.2.2. Fluorescence measurement:

The photoluminescence spectra were recorded using a Varian Cary Eclipse fluorescence spectrophotometer. A pulsed Xe-lamp was used as the excitation source Corrections for the spectral sensitivity of the photomultiplier (Hamamatsu R928) were applied to the fluorescence spectra. Bandwidth ranging from 5 nm to 10 nm was utilized. Photoluminescence measurements were carried out at a right angle to the incident light direction, and the fluorescence intensity was monitored through the excitation slit gap.

2.2.3. Determination of the photoluminescence quantum yield (PLQY):

The PLQY is defined as the ratio of the number of photons emitted to the number of photons absorbed, given by the following equation (equation no 2.2).

$$(\varphi_s) = \frac{\text{number of photons emmited}}{\text{number of photons absorbed}} \qquad (2.2)$$

The change in absorption is also taken into consideration. The relative quantum yields the samples from which the absolute quantum yields to be determined were corrected by the following equation (equation no 2.3).

$$(\varphi_s) = \frac{\text{Area under the fluorescence spectrum}}{(1 - 10^{-absorbance})} \qquad (2.3)$$

Here absorbance of the sample corresponds to the excitation wavelength at which the samples were excited.to measure the fluorescence spectra. The absolute PLQY (ϕ_s) is defined as

$$\phi_s = \phi_f^{ref} \times \left(\frac{\phi_{ref}^{sample}}{\phi_{ref}^{ref}} \right) \qquad (2.4)$$

Where ϕ_{rel}^{sample}, and ϕ_{relref}^{ref} is the relative quantum yield of the sample and the reference respectively. ϕ_f^{ref} is the absolute quantum yield of the reference.

The absolute photoluminescence quantum yield (ϕ_f) is determined by the equation (equation no 2.5).

$$\phi_s = \phi_{ref} \times \left(\frac{I_s \, A_{ref} \, \eta_s^2}{I_{ref} \, A_s \, \eta_{ref}^2} \right) \qquad (2.5)$$

ϕ_s and ϕ_{ref} are the quantum yields of the unknown sample and the reference, respectively. I_s and I_{ref} are the integrated PL intensity of the sample and the reference, respectively. η_s and η_{ref} are the refractive index of the respective solvents. η_{ref} is 1.33 for water, whereas η_s for toluene and hexane are 1.49 and 1.37, respectively. Literature values of the PLQY of Coumarin-102 in water are 0.76. All the samples and references are excited at 400 nm, the other conditions are exactly the same for all the samples.

2.2.4. Time-resolved fluorescence measurements:

After excitation with a pulsed laser, the excited fluorophore depopulates to the ground state with emission, which is characteristic of an emissive state. In such a process, the change in

fluorescence intensity, I(t). With time (t) exponentially follows the following equation (equation no 2.6).

$$I(t) = I_0 e^{(-t/\tau)} \tag{2.6}$$

Where I_0 is the initial intensity and τ is fluorescence lifetime. The fluorescence lifetime is the time spent by the electron or the fluorophore in the excited state before coming to the ground state. However, the excitation pulse should be considered as a δ-pulse.

The Time-Correlated Photon Counting (TCSPC) technique measures the probability of a single emitted photon being detected at a time (t) after the excitation of the sample. This probability is calculated by sampling the emission resulting from a large number of excitation pulses. The probability of p(t) for the detection of a single photon is taken as the intensity distribution I(t) of all emitted photons as a result of excitation. The excitation pulse is triggered with an electronic pulse. The delay between the excitation pulse and the arrival of the emitted photon is back-calculated. The instrument response function (IRF) has been recorded using LUDOX as a scattering solution. All measurements are performed with the excitation polarizer in the vertical position and the emission polarizer at the magic angle (55 °) relative to the excitation polarizer. The number of counts at the peak of the time-resolved fluorescence is kept at 8000.
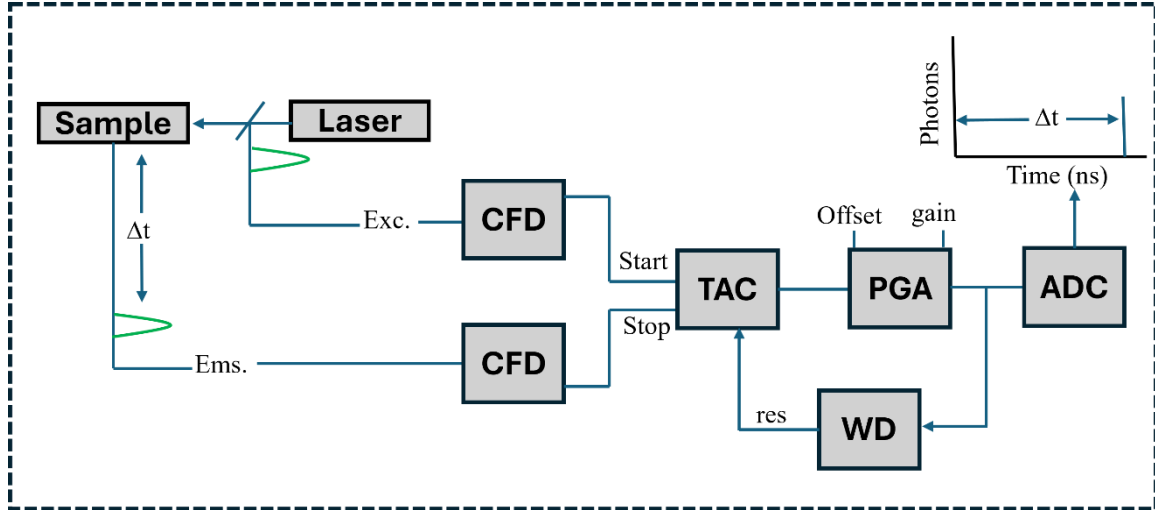
Scheme 2.1 Simplified schematic visualization of Time-Correlated Single Photon Counting (TCSPC) setup. Revised from ref 263.

2.2.5. Analysis of the fluorescence decay:

The time-resolved fluorescence intensity function I(t) is fitted as the sum of n-exponentials as shown in the following equation (equation no 2.7) where τ_i and α_i are the lifetime and the corresponding pre-exponential factor (amplitude) of the ith component.

$$I(t) = \sum_{i=1}^{n} \alpha_i \, e^{-t/\tau_0} \tag{2.7}$$

A major problem of analysis arises due to the fact that the excitation pulse is not a δ-function pulse; rather, it has a finite width. This complicates the decay profile considerably, especially for short fluorescence lifetimes. The observed time-resolved fluorescence N(t) can no longer be considered to be the true fluorescence response function I(t) from the sample, but is a convolution of the instrument response function R(t) and I(t), as is shown in the following equation (equation no 2.8).

$$N(t) = \int_0^t R(t' + \delta) I(t - t') dt \tag{2.8}$$

Where δ is the shift parameter. The instrument response function (IRF) of having finite width can be considered as a sequence of δ-functions, each producing its fluorescence decay. The

50

observed fluorescence profile is simply the sum of the responses to these δ-function responses. The shift is necessary because the instrument response function is measured at a wavelength near the excitation wavelength, whereas fluorescence is detected at a wavelength far away from the excitation. As the time response of the detector (photomultiplier) depends upon the wavelength (due to the wavelength dependence of the energies of the electrons ejected from the photocathode), the arrival of the signal at TAC from the PMT is wavelength dependent, and hence, the shift parameter is necessary in the analysis.

The deconvolution is done by an iterative deconvolution method to determine the pre-exponential factor and the lifetime. Ez-Time program first generates a set of guess values for the amplitudes and lifetime depending on the time scale of decay to be fitted. For each value of amplitudes and lifetimes, the program then yields the decay profile, convolutes it numerically with the instrument response function collected experimentally, and then, compared the generated curve with the experimentally observed decay, using non-linear regression. The values of the parameter are adjusted in successive iterations till a good fit is obtained, i.e. convergence is achieved. The goodness of the fits is judged by the closeness of the value of the reduced χ^2 to unity. χ^2 is defined as

$$\chi^2 = \frac{1}{n-p}\sum_{k=1}^{n}\frac{[N(t_k)-N_c(t_k)]^2}{\sigma_k^2} \approx 1.0 \qquad (2.9)$$

Where $N(t_k)$ and $N_c(t_k)$ are the experimental and calculated values of time-resolved fluorescence intensity at time t_k k being the number of data points fitted, and is the number of free parameters in the equation. σ_k is the standard deviation associated with the ith data and is defined as in the following equation (equation 2.10) (based on Poisson statistics)

$$\sigma_k = \sqrt{N(t_k)} \qquad (2.10)$$

51

The goodness of the fit is also judged by the randomness of the weighted residuals of the experimental data with those of the calculated data. The weighted residuals r(t$_k$) of the data are defined as

$$r(t_k) = \frac{N(t_k) - N_c(t_k)}{\sigma_K} \qquad (2.11)$$

For best-fitted experimental data, the weighted residuals r(t$_k$) should be distributed randomly at about zero.

2.2.6. Double Reciprocal Plot for the calculation of apparent binding constant (Kapp):

For the calculation of the apparent binding constant, we used the following equation (equation no 2.12) proposed by Benesi-Hildebrand using the PL emission data.

$$\frac{1}{\phi_0 - \phi_{obs}} = \frac{1}{\phi_0 - \phi'_{obs}} + \frac{1}{(\phi_0 - \phi'_{obs}) \times K'_{app}} \frac{1}{[Q]} \qquad (2.12)$$

$$K'_{app} = \frac{k_{app}}{(\phi_0 - \phi'_{obs})}$$

Where ϕ_0 is the PLQY of the perovskite nanocrystals in the absence of any acceptor, and ϕ_{obs} is the PLQY of the nanocrystals in the presence of a particular concentration of the acceptor (Rhodamine B). $\phi_{obs'}$ is the PLQY of the PNCs at the maximum concentration of the acceptor. [Q] is the acceptor concentration at each step. The equation suggests it's a linear plot, and from the slope we estimated the binding constant (Kapp) for the PNCs with Rhodamine B.

2.2.7. Fluorescence Resonance Energy Transfer Parameters:

R_0 is the Froster distance at which FRET efficiency is 50%. Which was estimated using the steady state PL Intensity, through the following equation (equation no 2.13).

$$R_0 = 0.211 \times \left[\frac{\{\kappa^2 \, \phi_D \, J(\lambda)\}}{\eta^4} \right]^{\frac{1}{6}} \tag{2.13}$$

Where κ^2 is the transition dipole orientation in space, we have taken it 2/3 for our case. ϕ_D is the PLQY of the Donor calculated using equation 2.5. η is the refractive index of the medium, in this case it is 1.49 for toluene. J(λ) is the overlap integral, which is expressed as the following equation (equation no 2.14).

$$J(\lambda) = \frac{\int_0^\infty F_D(\lambda)\varepsilon_A(\lambda)\lambda^4 d\lambda}{\int_0^\infty F_D(\lambda)d\lambda} \tag{2.14}$$

$F_D(\lambda)$ is the PL Intensity of the donor in the wavelength range λ to $\lambda + \Delta\lambda$, along with the total intensity normalized to 1. ε_A (λ) is the absorption coefficient of the acceptor at λ. The donor–acceptor distance (R_{D-A}) and the FRET efficiency (E_{FRET}) was calculated using the following equations respectively.

$$k_{FRET} = \frac{1}{\tau_A{}^{rise}} = \frac{1}{\tau_D}\left(\frac{R_0}{R_{DA}}\right)^4 \tag{2.15}$$

$$k'_{FRET} = \left(\frac{1}{\tau_{DA}} - \frac{1}{\tau_D}\right) = \frac{1}{\tau_D}\left(\frac{R_0}{R_{DA}}\right)^4 \tag{2.16}$$

$$E_{FRET} = \left(\frac{R_0^4}{R_0^4 + R_{DA}^4}\right) \tag{2.17}$$

where τ_{DA} is the donor's lifetime (in presence of acceptor), τ_D is the donor's lifetime (without acceptor), R_0 is the Förster distance, and R_{DA} is the D−A distance. k'_{FRET} is the rate of energy transfer for D−A pair without considering acceptor's rise time.

2.2.8. Transient Absorption Measurements:

800 nm light having a FWHM of 75 fs with an energy of 3.25 mJ and a repetition rate of 1 kHz has been obtained from an amplified laser (Libra, Coherent, USA). About 1.35 mJ of the output has been used to pump an optical parametric amplifier (OPA–TOPAS, Light Conversion, Lithuania) to get tunable pump pulses. All experiments are performed here; the pump wavelength used is 400 nm. A small fraction of 800 nm light is used to fall on the CaF_2 crystal to generate white light continuum (WLC) (350–750 nm), which is used as a probe to interrogate the system in the presence and absence of pump, and a delay is provided to the probe pulse w.r.t. pump pulse to get the time evolution of excited state processes. The white light has been divided into probe and reference beams using a beam splitter. The reference beam is used to correct for real-time intensity fluctuation of the white light continuum. The pump pulse is passed through a synchronized mechanical chopper to cut each alternative pump pulse, creating a succession of "pump" and "no pump" situations. Pump (400 nm) and probe pulses are spatially overlapped on the sample solution, kept in a rotating cell with a path length of 1 mm so that an intense pump pulse cannot damage the sample. The effect of rotational diffusion is corrected by adjusting the polarization to the magic angle (54.7°). The steady state absorbance of the sample before and after the transient absorption experiment has been recorded to check the effect of irradiation of pump light on the sample. All the extracted data are chirp corrected for the removal of the group velocity dispersion (GVD) and fitted using the IGOR Pro software.
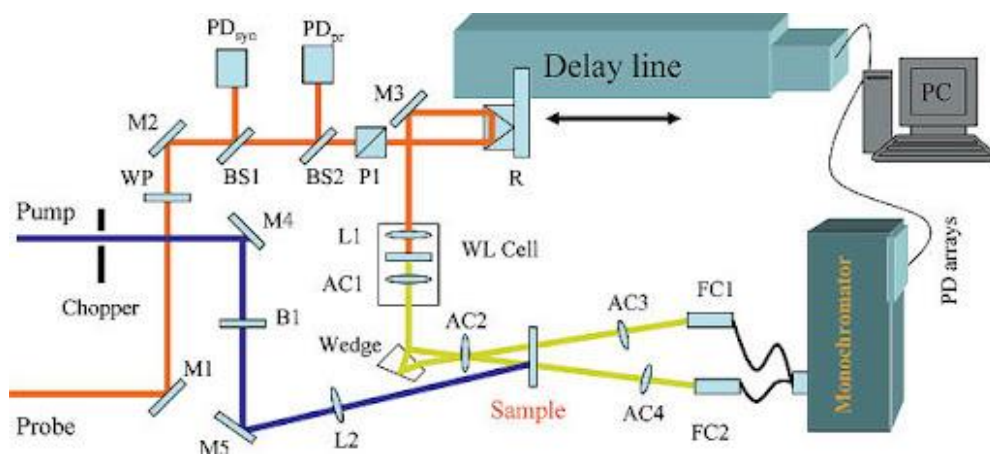
Scheme 2.2 Optical layout of femtosecond Transient Absorption spectrometer setup. Copyright 2025 Del Mar Photonics.

2.2.9. Fourier Transform Infrared (FT-IR) spectroscopy:

Thermo Scientific NICOLET Is20 FT-IR spectrometer equipped with DTG (Deuterated TriGlycine Sulfate) detector has been used to identify bond stretching frequencies of our sample in the range of 4000–500 cm^{-1}. For the data collection KBr pellet is prepared by adding a drop of the sample and vacuum dried it to remove the solvents. The apply of stretching and bending vibrational modes correlated to confirm the presence of functional group attached to the perovskite nanocrystal surface as N-H, COO-H, C-H, C=O, and C-O, etc.

2.2.10. X-ray Photoelectron Spectroscopy (XPS):

This technique was carried out by using a Thermo-ScientificK-Alpha X-ray photoelectron spectrometer with an Al Kα micro focus monochromatic X-ray source and ultra-low energy electron flood gun. The sample was drop-cast on a thin glass slide and vacuum dried before measurements. The pass energy of the survey spectra is 200 eV. A 50-eV pass energy was used for high-resolution, element-specific XPS spectra. The binding energy calibration was done using Gold metal (Au $4f_{7/2}$ at 84.0 eV), Silver metal (Ag3d$_{5/2}$ at 368.2 eV), and Copper metal (Cu2p$_{3/2}$ at 932.6 eV). The take-off angle is kept at 90º through the experiments. These spectra are analyzed with the advantage XPS software. This technique was used to investigate the

elemental composition, the oxidation state of the element as well as the chemical environment of each element of perovskite nanocrystal, like Pb (+II), Cs(+I), Br(-I), I(-I). This method was used to detect the doped elements like Ni(+II), Co(+II).

2.2.11. Transmission Electron Microscopy (TEM):

The samples were imaged by a transmission electron microscope (TEM) (HR-TEM FEI Titan G2 60) mounted with a field emission gun FEG TEM at 300 kV accelerating voltage. The samples for TEM were prepared on amorphous carbon films supported on a copper grid. The average diameter values were expressed as mean ± standard deviation. (SD) This technique was employed to identify the nano range of particles, average size below 20 nm and the corresponding lattice spacing between 0.35 nm to 0.50 nm.

2.2.12. Field Emission Scanning Electron Microscopy (FE-SEM):

FE-SEM images and Energy dispersive X-ray spectroscopy were performed using a JEOL model JSM-7900F (Japan) with a varied acceleration voltage. The samples were prepared by drop casting the sample in a pre-cleaned glass slide and dried in vacuum oven. This technique was used to determine the morphology of the nanocrystals and their elemental composition.

2.2.13. Dynamic Light Scattering (DLS):

This method was used to measure the hydrodynamic diameter of synthesized perovskite nanocrystals. Zetasizer Nano ZS (Malvern Instruments Limited, U.K.) was used to analyze the hydrodynamic diameter. A 633 nm He/Ne light source was used, and the scattered light is detected at an angle of 173°. Measurements are carried out at $25^{\circ}C$ using the appropriate sample dilution to minimize the undesired scattering events. The average value for each sample is obtained from 10 measurements.

2.2.14. X-Ray Diffraction (XRD):

The X-ray diffraction (XRD) measurement was carried out on PANalytical model EMPYREAN from 10° to 90° with a turning speed of 2.6°/min. The samples were prepared by drop casting nanocrystal solution on a pre-cleaned glass slide and vacuum dried before experiment. This method was used to identify the crystal planes associated with the perovskite nanocrystals as well as the lattice phases in which the crystal lattice exist. Crystal planes are identified by comparing with the standard reference (JCPDS no -73–2478, 18–0364, 075–0412).

2.2.15. Rietveld Refinement Process:

Rietveld refinement entails adjusting various parameters describing the diffraction pattern to align with observed data by fitting a calculated X-ray or neutron diffraction pattern. Initially, a theoretical diffraction pattern is computed using the initial structural model. To assess the fit quality between calculated and experimental patterns, statistical measures such as Rietveld refinement factors are employed, offering insights into the adequacy of the refined structural model. In a typical Rietveld refinement, individual scale factors pertaining to phase concentration as well as profile, background, and lattice parameters are variably adjusted. The refinement process is iterative, with parameters readjusted until convergence between the calculated and experimental patterns occurs, stabilizing refinement parameters. Upon achieving a satisfactory fit, the refined structural model furnishes precise information regarding the material's crystal structure, encompassing atomic positions, unit cell dimensions, bond lengths, bond angles, and other structural parameters. In Rietveld refinement, the $\chi 2$ statistic is a measure of the goodness of fit between the observed diffraction data and the calculated diffraction pattern.

In the Rietveld refinement process, a two-phase approach is adopted, considering the presence of both orthorhombic and cubic phases simultaneously. The orthorhombic phase belongs to the Pnma space group, while the cubic phase is classified under the $Pm\bar{3}m$ space group. During the refinement process, we have employed a background model based on "linear interpolation between set background points with refinable heights." Additionally, the peak shape was modeled using the "Thompson–Cox hastings pseudo-Voigt axial divergence symmetry" method; this includes a mixture Gaussian and Lorentzian broadening of the peak shape, consistent with our instrumental resolution. Based on the refined parameters, a physical representation of the crystal structure is created by using VESTA.

2.3. Synthetic Methods:

2.3.1. Anti-solvent method:

Synthesis of halide perovskite crystal (HPC): In a typical synthesis, lead bromide (0.05 g) and cesium bromide (0.03 g) were placed in a mortar pestle and ground for half an hour, then the paste was taken into a 100 mL round bottom flask, and 2 mL of DMSO was added into it. The solution was then heated at 90°C for 30 min, followed by the addition of 20 μL of HBr: DMF (3:1) solution. Pre-sonicated BSA (19 mg) in DMSO was added dropwise for halide perovskite crystal, HPC-1. 100 μL of 10% PVDF in DMSO solution was added along with the BSA solution for HPC-2. The solution was left for 15 min more. The perovskite crystals were then allowed to precipitate in toluene under vigorous stirring.
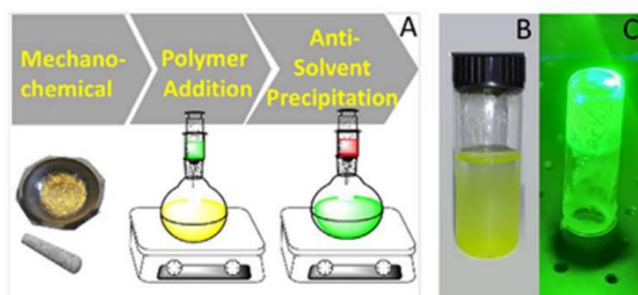
Scheme 2.3 Schematic representation of the Antisolvent method for the preparation of hybrid perovskite crystal (HPC 1 & HPC 2).

2.3.2. Hot Injection method:

Synthesis of pristine CsPbBr₃ nanocrystal: For the synthesis of Cesium−Oleate precursor, first, cesium carbonate (1.31 g), oleic acid (4 mL), and octadecene (16 mL) were mixed in a 100 mL three-neck round-bottom flask and degassed for 30 min under vacuum oven and then heated to 120 °C under vigorous stirring for 60 min under N_2 environment. Afterward, the mixture was heated to 150 °C until the solution became transparent.

In a typical synthesis of $CsPbBr_3$ nanocrystal, oleic acid (6 mL), oleylamine (6 mL), and octadecene (10 mL) were taken in a 100 mL three-neck round-bottom flask and dried under vacuum for 30 min at 120 °C to remove the moisture from the above chemicals. 0.5 g of $PbBr_2$ was dissolved completely by heating the solution at 150°C under N_2 environment. The temperature was then elevated to 180 °C and 5 mL of Cs−oleate precursor was swiftly injected under vigorous stirring. Within 10 s, the reaction mixture was transferred into an ice bath, then a greenish-yellow precipitate was obtained. The precipitate was first centrifuged at 10000 rpm for 5 min to discard oils and then redispersed solution was further centrifuged at 10000 rpm for 10 min to remove large-sized particles. The greenish yellow colored $CsPbBr_3$ nanocrystals were dispersed in toluene for further experimentation.

Synthesis of Metal (Ni, Co)-Doped Perovskite Nanocrystals: In a typical synthesis of metal-doped $CsPbBr_3$ nanocrystal, oleic acid (6 mL), oleylamine (6 mL), and octadecene (10 mL) are placed in a 100 mL three-neck round-bottom flask and dried under vacuum for 30 min at 120°C to remove the moisture content from the above chemicals. For synthesis of Ni:$CsPbBr_3$ (Ni:PNC)─1.0 g of $PbBr_2$ (2.8 mmol), 250 mg nickel(+II) acetate (1.0 mmol); for Co:PNC─1.0 g of $PbBr_2$ (2.8 mmol), 250 mg Cobalt(II) acetate (1.0 mmol) and for bimetallic doped, Ni:Co:PNC─1.0 g of $PbBr_2$ (2.8 mmol), 125 mg nickel(II) acetate, 125 mg cobalt(II) acetate (1.0 mmol) are dissolved completely by heating the solution at 150°C under nitrogen

environment. The temperature is then elevated to 180 °C, and 5 mL of the Cs–oleate precursor is swiftly injected under vigorous stirring. After 10 s, the reaction mixture is transferred into an ice bath, and then a greenish-yellow precipitate is obtained. The precipitate is first centrifuged at 10,000 rpm for 5 min to discard oils, and then, the redispersed solution is again centrifuged at 10,000 rpm for 10 min to remove large-sized particles.
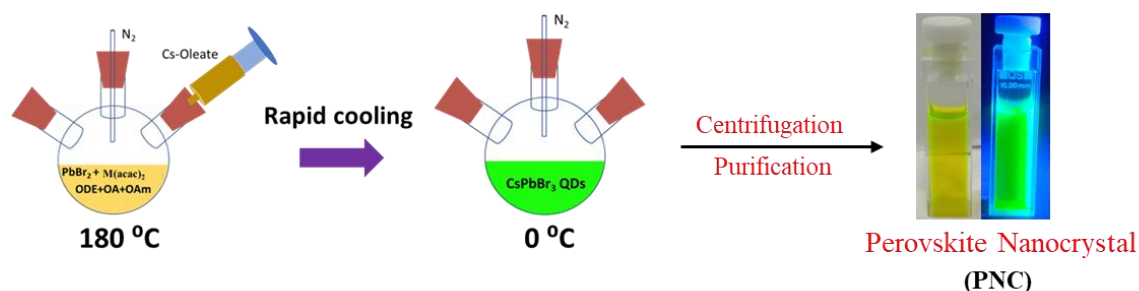
Scheme 2.4 Schematic representation of the Hot-injection method for the synthesis of perovskite nanocrystal and metal-doped perovskite nanocrystal (PNC & M:PNC).

2.3.3. Halide exchange of Polymer-encapsulated nanocrystal in aqueous solution

Briefly, 0.1 g of PVDF was added to 1 mL of the CsPbBr$_3$ nanocrystal solution. The polymer-encapsulated nanocrystals were placed on the glass surface and then heated at 120°C for 15 min to remove the toluene. NCs-doped polymer loaded on glass surface was dipped. into 3% aqueous HI solution for 1 min or so. After the ion exchange, polymer-encapsulated nanocrystal was heated at 180 °C for 15 min for fabrication of the film

2.3.4. Preparation of Rhodamine B (RhB)solution:

2.0 mg of RhB was taken in 10 ml of acetonitrile solvent to make it a 400µM stock solution. From that stock solution a 40 µM solution was prepared by dilution. A certain amount from that two-stock solution were gradually added to the donor system to make the final concentration of the acceptor dye as 0.5 µM, 1.0 µM, 2.0 µM, 5.0 µM, 10.0 µM, respectively.

2.3.5. Preparation of Thin film:

For the preparation of thin film at first solution were prepared by adding desired concentration of RhB into the donor system (Ni:PNC). Then a little amount of the solution was drop casted onto the glass surface.

2.3.6. Preparation of Methyl Viologen solution:

5.1 mg of MV^{+2} was taken in a mixture of acetonitrile (9600 µL) and ethanol (400 µL) solvent to make it a 2mM stock solution. From that stock solution 50 µL was added to a mixture of acetonitrile (4752 µL) and ethanol (198 µL) solvent prepared by dilution.to make it a 20 µM solution. A certain amount from that 20 µM solution were gradually added to the donor system to make the final concentration of MV^{+2} as 0.02 µM, 0.04 µM, 0.06 µM, 0.08 µM, 0.10 µM, and 0.12 µM respectively.

2.3.7. Calculation of molar concentration of Ni:PNC:

The NCs were precipitated out using 15 ml methyl acetate followed by centrifugation at 8000 rpm for 10 mins, then the precipitation was dried under vacuum to get the total weight of the NCs. From the HR TEM imaging the obtained shape of the nanocrystal is cube with average edge length (a) of 8.06 nm, weight of the single NC is calculated using $m = d \times V$, where m is the mass of the single NC, d is the bulk density of $CsPbBr_3$ (4.86 g/cm^3), and V is the volume of the NC ($V = a^3$). So, the no of NCs present in the sample was calculated by dividing the total mass of the NCs with the mass of a single NC. Now the number of NCs was divided with Avogadro's number (N_A) to obtain the mole of the NCs From that molar concentration (c, mol/L) was determined from the amount of methyl acetate was used for precipitation. In our case the mole of NCs was 9.80×10^{-2} µmol, so the molar concentration of the stock NC solution was 6.53 µM. For all the experiments in this current article we have taken 10 µL of the stock solution, so the final concentration of the NCs throughout the experiment was 32 nM.

Chapter 3

PVDF-Directed synthesis, Stability and Anion exchange of Cesium Lead Bromide Perovskite nanocrystal

Photoluminescent perovskite nanocrystals are mostly used along with base materials such as polymers for material processing and large-scale production purposes. However, the role of polymer in crystal structure engineering and thereby dictating the emission properties of lead halide perovskite nanocrystals has been poorly understood. First, we have developed a polymer-directed antisolvent method for synthesis of halide perovskite crystals at room temperature and observed that the thermodynamic stabilities of crystals drive the formation of perovskite composite crystal of orthorhombic Cs_4PbBr_6 and monoclinic $CsPbBr_3$. Surprisingly, hydrophobic polyvinylidene fluoride (PVDF) can reduce the size of perovskite crystals to nano dimensions even at room temperature. On the other hand, perovskite nanocrystals, $CsPbBr_3$ synthesized by modified hot-injection method undergo rapid encapsulation in PVDF matrices. The size of the encapsulated nanocrystal in PVDF matrices ranges in 88±32 nm. We have illustrated that there are three types of radiative recombination predominantly operative in nanocrystals-doped polymer- (i) surface defect caused radiative recombination (0.6–3ns), (ii) exciton recombination (3–15 ns), and (iii) shallow trap assisted recombination (10–50 ns). The interface created at nanocrystal and polymer plays a decisive role in populating the shallow trap states in perovskite-polymer nanocomposite. These nanocomposites undergo fast halide exchange in aqueous hydroiodic acid solution and possess remarkable enhancement of water/photo-stability. This research would pave the way for their greater use in hydrogen production and light-emitting devices.

3.1 Introduction:

Over the past decade, perovskite crystal remains the most sought-after photoluminescent nanomaterial for its record-breaking photoelectric conversion efficiency (PCE).[229,230] Following the pioneering work of Miyasaka group in 2009 on inorganic-organic halide perovskite, the research on the all-inorganic perovskites has gained significant momentum due to their superior performances in light-emitting diodes, photovoltaics, photodetectors, and lasing.[9,52,233] All inorganic Cesium lead halide perovskite (CsPbX$_3$, X=Cl, Br, I) nanocrystals (NCs) have been considered the most promising nanomaterials due to their unique optoelectronic properties- bright photoluminescence (PL), narrow spectral widths, and bandgap tunability over the entire visible spectrum.[4–7] The inherent challenges with these NCs are- the aggregation-caused photoluminescence quenching in the solid-state due to the loss of quantum confinement, high cost associated with anion exchange for color tunability, and extreme sensitivity toward reaction conditions leading to feeble photoluminescence

properties.[253–255] Moreover, the use of perovskite crystals for photocatalytic H_2 production has also been very limited due to their poor aqueous stability.[256]
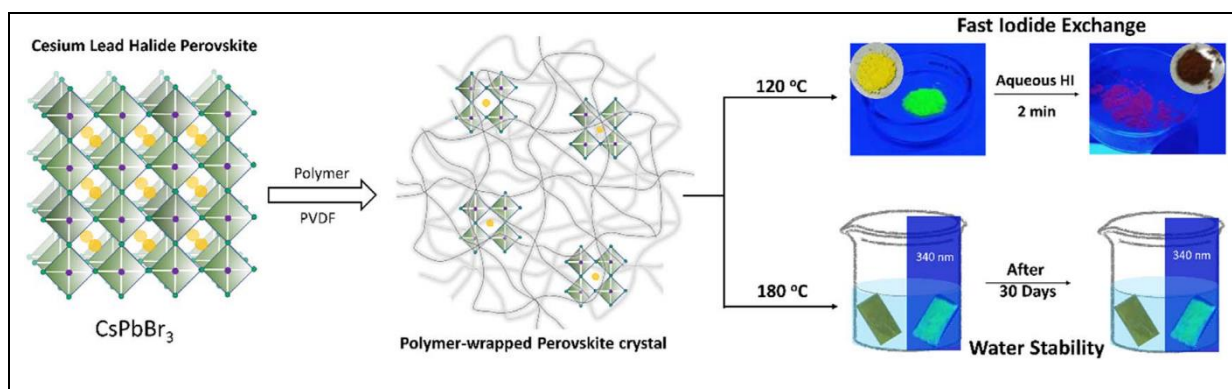
Scheme 3.1: Polymer-wrapping strategy for augmentation of photoluminescence properties of perovskite nanocrystals.

To improve the ambient stability of perovskite crystals, encapsulation approaches are becoming indispensable. Polymers are the most favored base material for encapsulation of perovskite crystals in comparison to Metal-Organic Frameworks due to their adaptability, processing, and self-healing abilities.[162,163,165,257] Moreover, polymers are much more flexible in comparison to rigid inorganic shells such as SiO_2, TiO_2, Al_2O_3, CdS, ZnS, and others for augmenting the optoelectronic properties of perovskite crystals.[169–171] However, there are reports where polymers, such as poly (lauryl methacrylate), and polystyrene have been used for successful encapsulation of inorganic-organic halide perovskite due to their better solubility in a common solvent, dimethylformamide (DMF). However, very limited reports exist on polymeric encapsulation of all-inorganic perovskites. Amphiphilic polymer encapsulated nanocrystals can undergo a switchable anion exchange in toluene.[258] Nevertheless, an instantaneous and reversible anion exchange of NCs by using an aqueous acidic solution remains far from reality.

On the other hand, primarily two synthetic strategies have been developed for the dimensional engineering of perovskite crystals - hot-injection method for nanocrystals and anti-

solvent method for microcrystals.[259,260] Mechanochemical methods such as wet ball milling, mortar pestle, and ligands-assisted reprecipitation (LARP) methods are becoming emerging methods for the cost-effective development of cesium lead halide nanocrystals at ambient condition.[107,261,262] In this work, our first objective is to offer a polymer-encapsulation strategy for both the synthetic methods of perovskites, because polymers are known to prevent agglomeration, and thus can stabilize nanocrystals. We have chosen a hydrophobic polymer, Polyvinylidene fluoride (PVDF), and a hydrophilic biopolymer, bovine serum albumin (BSA). PVDF is chosen over other hydrophobic polymers because of its insolubility and morphological retainment in a range of solvents such as arenes, chlorohydrocarbons, and aliphatic esters. Moreover, the low melting temperature (177 °C) of PVDF can be exploited for thermophysical properties of polymer-perovskite composites (scheme 3.1). BSA is selected as a biopolymer to extend the concept of biomolecular wrapping often used in quantum dots.

Nanocrystals obtained from hot-injection method reportedly show poor photoluminescence properties. Thus, post-synthetic modification of these synthesized nanocrystals becomes inalienable for boosting their photoluminescence properties. It has been hypothesized that excess lead atoms lead nanoparticles, and halide ions quench the photoluminescence of perovskite nanocrystals. Salt-treatment strategies in apolar media have been adopted by using Na/NH4 thiocyanate and sodium/ammonium tetrafluoroborate salts for removal of such quenchers (photoluminescence) from the surface of nanocrystals.[259,263] But water treatment of perovskite nanocrystals have been avoided due to their poor stability in aqueous medium. In this work, we have attempted the water treatment of polymer encapsulated nanocrystals for removal of excess metal ions and halides due to the better solubilities of these ions in aqueous medium.

We show here that polymers can direct synthesis of perovskite nanocrystal composite (Cs_4PbBr_6 and $CsPbBr_3$) in an anti-solvent method at room temperature. Polymer encapsulation

of NCs by a commonly used hydrophobic polymer PVDF is an effective strategy for enhancing the ambient stability of perovskites. Fast, and reversible anion exchange of NCs in aqueous hydroiodic acid (HI) solution have been demonstrated. The melting temperature of the polymer has been targeted to regulate the water-accessibility of PVDF encapsulated NCs. Unprecedentedly, perovskite-polymer nanocomposites are stable for more than 07 days. Upon incubation in water, the photoluminescence dynamics of NC-doped PVDF have been presented. We believe this study will draw the attention of researchers to explore photocatalytic hydrogen production by utilizing an encapsulation strategy for all inorganic NCs.

3.2 Results & Discussion:

3.2.1. Polymer-guided synthesis of perovskite nanocrystal at room temperature

The antisolvent precipitation method using dimethyl sulfoxide (DMSO) as a solvent and toluene as antisolvent has been employed to crystalize cesium lead halide perovskite (figure 3.1(A)). Prior to dissolving in DMSO, precursor salts- lead bromide and cesium bromide have been ground mechanically for boosting the formation of crystal network. Desired polymers— bovine serum albumin (BSA) and polyvinylidene fluoride have been premixed in the solution. Dropwise addition of solution in the toluene for crystallization of perovskite has yielded greenish-yellow crystals (figure 3.1(B)). These halide perovskite crystals (HPC) are found to be highly photoluminescent under UVlight (405nm) irradiation (figure 3.1(C)).
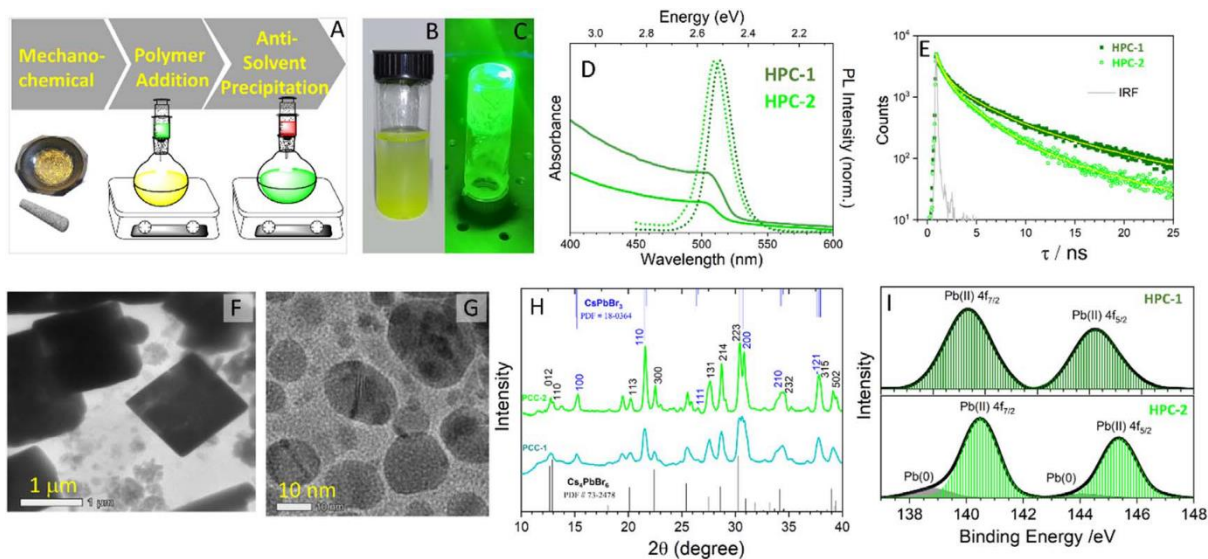
Figure 3.1. **[A]** Schematic representation of antisolvent method. **[B-C]** Photographs of halide perovskite crystals at ambient and under UVlight (405nm LED excitation) respectively. **[D]** Absorption (solid lines) and photoluminescence spectra (dotted lines) of perovskite crystals, HPC-1 (dark green) and HPC-2 (light green). **[E]** Time-resolved photoluminescence decays of perovskite crystals. HPC-1 (dark green) and HPC-2 (light green). Instrument response function (IRF) has been represented in grey line. **[F-G]** TEM images of the perovskite crystals, HPC-1, and HPC-2 respectively. **[H]** Powder XRD pattern of perovskite crystals, HPC-1 (green line) and HPC-2 (cyan line) with the standard reference of rhombohedral Cs_4PbBr_6, JCPDS no. 73–2478 (grey lines) and monoclinic $CsPbBr_3$, JCPDS no. 18–0364 (blue line). **[I]** High resolution XPS spectra of Pb (II) for HPC-1 (top panel) and HPC-2 (bottom panel).
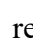
Emission features of green-emitting perovskite crystals are first characterized by full-width at half maxima (fwhm). The emission peak positions (λ_{max}) of these crystals are centered at 513 nm (fwhm=17 nm) with a band gap of 2.25 eV for HPC-1 and 509 nm (fwhm=22 nm) with a bandgap of 2.23 eV for HPC-2 (figure 3.1(D) and A 3.2). noticeable hypsochromic shift is suggestive of the reduced size of crystals due to the presence of hydrophobic PVDF. The quantum yields quantified by using a method used for powdered samples are found to be— 87% for HPC-1 and 37% for HPC-2 [34]. Time resolved photoluminescence (TRPL) studies show that the photoluminescence of HPC-2 decays at a much faster rate than that of HPC-1 (figure 3.1(E)). The decay traces are well fitted with triexponential for 405 nm excitation (table 1). Analysis of TRPL decay trace ofHPC-1 reveals the presence of- a shorter component with a

lifetime (τ_1) of 0.76 ns (65%), a short component (τ_2) of 3.37 ns (28%), and a long component (τ_3) 12.11 ns (7%). The component, τ_1 originates from the trap states arising from the surface defects of perovskite crystals. Whereas the components- τ_2 and τ_3 can be attributed to exciton recombination and shallow trap-mediated radiative recombination respectively. The long-lived states for perovskite crystals are assigned to shallow trap-mediated recombination due to the low exciton binding energy and trap density. These localized energy states originating from structural disorder or lattice defects of crystals lie within the band-edge. Similarly, photoluminescence decay trace of HPC-2 has three components- 0.61 ns (67%), 2.62 ns (29%) and 9.03 ns (3%). Since the decays are multiexponential, then it is pertinent to use an average decay time.[264] The average lifetime of HPC-1 is estimated to be 6.04 ns, whereas that of HPC-2 is 3.26 ns. Interestingly, the photoluminescence lifetime of perovskite crystal HPC-1 is closely matched with that of microcrystals.[265,266] The decrease in photoluminescence lifetime is often observed with size reduction (from micro to nano) of halide perovskite crystals.[41] Thus, at this stage, it can be hypothesized that hydrophobic PVDF has caused a dramatic reduction in the size of perovskite crystals and hydrophilic BSA promotes the formation of micron-sized crystals.

Table 3.1. Photoluminescence decay parameters of perovskite crystals.

Sample	τ_1 (ns)	τ_2 (ns)	τ_3 (ns)	a_1	a_2	a_3	$<\tau>$ (ns)	χ^2
HPC-1	0.76	3.37	12.11	0.65	0.28	0.07	**6.04**	1.13
HPC-2	0.61	2.62	9.03	0.67	0.29	0.03	**3.26**	1.11
Cs_4PbBr_6 Microcrystal	-	2.0	11.5	-	0.65	0.35	9.18	
Cs_4PbBr_6 Nanocrystal	-	1.4	8.6	-	0.56	0.44	7.36	

λ_{exc} = 405 nm; IRF= 180 ps; Luminescence lifetimes, $<\tau> = \Sigma a_i \tau_i^2 / \Sigma a_i \tau_i$

To test this hypothesis, we have imaged the synthesized perovskite crystals using high-resolution transmission electron microscopy (HR-TEM). TEM images of as-synthesized HPC-1 show micron-sized crystals (figure 3.1(F)). Unprecedentedly TEM image of HPC-2 reveals the formation of nanocrystals (figure 3.1(G)). The lattice spacing observed for HPC-2 (figure A 3.1) is 0.30 nm which is generally referred to as the [214] crystal plane for Cs_4PbBr_6.[267,268] Broad size distribution of HPC-2 has been noticed with an average size, 7.2±2.8 nm (figure A 3.1).

However, it is imperative to understand the degree of homogeneity present in synthesized crystals of hybrid perovskite crystals. And thus, we have performed XRD studies of these synthesized crystals (figure 3.1(H)). XRD peaks of perovskite crystals are well correlated with the characteristic interplanar planes of monoclinic $CsPbBr_3$ NCs (PDF#18-0364) and orthorhombic Cs_4PbBr_6 (PDF#73-2478). It can be noticed that the antisolvent precipitation at room temperature yields perovskite composite crystals- Cs_4PbBr_6/ $CsPbBr_3$. The existence of heterogeneity in crystal formation can thus be rationalized from the phase diagram of $PbBr_2$: CsBr compositions. It predicts the formation of thermodynamically stable crystals either the CsBr-rich Cs_4PbBr_6 or $PbBr_2$-rich $CsPb_2Br_5$. Since CsBr is less soluble than $PbBr_2$ in dimethyl sulfoxide, thus, formation of zero-dimensional Cs_4PbBr_6 is quite inevitable at room temperature.[269] We have analyzed Energy-dispersive x-ray spectra (EDS) of HPC-1 and HPC-2 (figure A 3.3). The atomic ratio of Cs:Pb:Br is suggestive of perovskite composite crystal- $Cs_4PbBr_6/CsPbBr_3$ as well.[270,271] Due to the high natural abundance of Br, the excess in the Br signal may come from the artifacts such as reabsorption of Pb and Cs x-ray emissions. High-resolution XPS spectrum of HPC-1 for Pb 4f yields two distinct gaussian-shaped peaks as shown in figure 3.1(I). The peaks are centered at 139.3 eV ($4f_{7/2}$) and 144.2 eV ($4f_{5/2}$). The 4.9 eV is the spin–orbit splitting of Pb^{+2}. The XPS spectrum of HPC-2 for Pb 4f shows additional weaker peaks at 138.8 and 144.1 eV and the two intense peaks are at 140.5 eV ($4f_{7/2}$)

and 145.4 eV ($4f_{5/2}$). Thus, it can be hypothesized that the size reduction of perovskite crystals may yield Pb (0) nanoparticles as a byproduct. This satisfactorily explains the observation of the low photoluminescence quantum yield of HPC-2 in comparison to HPC-1.[272,273]

3.2.2. PVDF-encapsulated Cesium lead bromide perovskite nanocrystal

Based on our understanding of dictating role of PVDF in dimensional engineering of perovskite crystals, we have extended the concept of polymer wrapping of perovskite nanocrystals. The colloidal perovskite nanocrystals (NCs) have been synthesized by a modified hot-injection method at ambient condition and purified NCs is dispersed in toluene for polymer doping studies. Solid PVDF has been directly added in toluene containing dispersed NCs. The white PVDF polymer turns greenish-yellow, and the toluene becomes colorless within a very short period of time, confirming a fast entrapment of nanocrystals in polymeric network (figure 3.2(A)). Perovskite-polymer nanocomposite films prepared by heating them at melting temperature, 180 °C of PVDF have been used for photoluminescence and material characterization studies. Photoluminescence spectrum of dispersed halide nanocrystals (HNC) shows a peak at 511 nm (fwhm=21 nm) with a bandgap of 2.99 eV (figures 3.2(B) and figure A 3.4). Whereas the emission peak position (λ_{max}) of polymer-encapsulated nanocrystal (PHNC-1) is centered at 525 nm (fwhm=19 nm) with a bandgap of 2.23 eV. A noticeable bathochromic shift is suggestive of structural reorganization of perovskite crystals in a polymer matrix.

Time-resolved photoluminescence decay of nanocrystals dispersed in toluene is shown in figure 3.2(C). It can be deconvoluted into three components: a shorter one with a lifetime (τ_1) of 1.83 ns (19%) for surface defects, a short component (τ_2) of 5.63 ns (69%) for exciton recombination, and a long component (τ_3) 14.81 ns (12%) for shallow trap-mediated radiative recombination. Interestingly, the average photoluminescence lifetime of PVDF-encapsulated nanocrystals dramatically increased to 35.52 ns (table 3.2). The amplitude of shallow-trap

mediated radiative recombination gets significantly increased at the expense of exciton recombination[263,274].
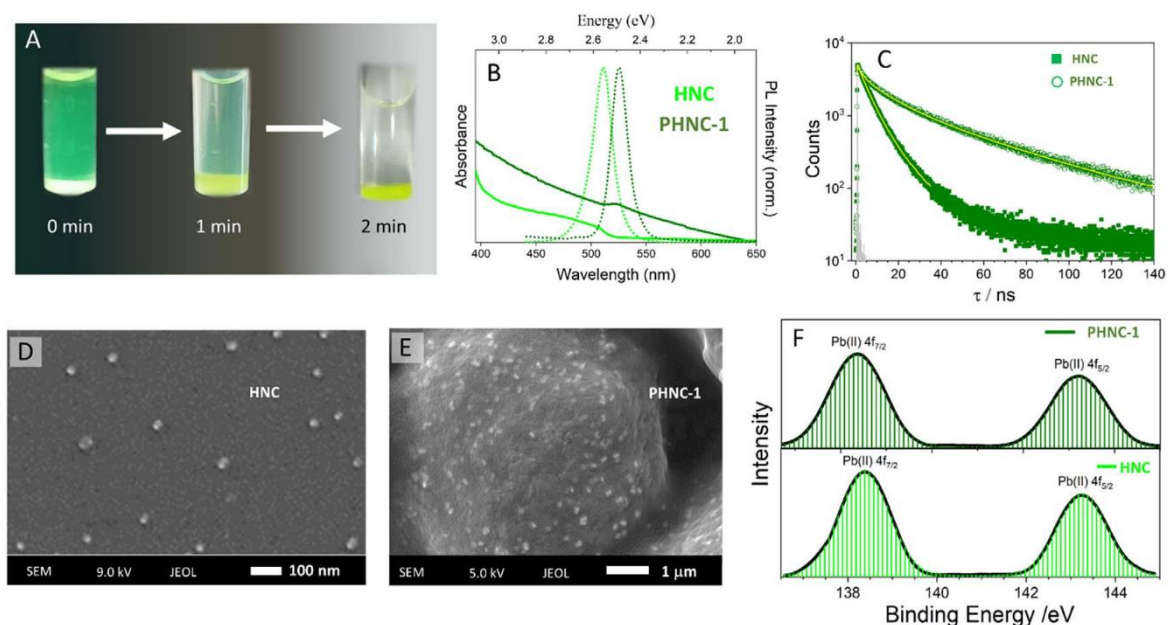
Figure 3.2. **[A]** Representative photographs showing instantaneous entrapment of perovskite nanocrystal in PVDF matrix. **[B]** Absorption (solid lines) and photoluminescence spectra (dotted lines) of dispersed nanocrystals (HNC) in toluene (light green) and polymer-entrapped nanocrystal, PHNC-1 (dark green). **[C]** Time-resolved photoluminescence decays of-HNC (solid green squares), and PHNC-1 (hollow light green circles). Instrument response function (IRF) represented in grey line. **[D-E]** SEMimages of -HNC and PHNC-1 respectively. **[F]** High-resolution XPS spectra of Pb (II) for PHNC-1 (top panel) andHNC(bottom panel).

We can thus summarize the radiative recombination of NC-doped PVDF (Scheme 3.2(A)). The surface defect caused radiative recombination takes place at a much faster time scale, 0.6–3 ns, whereas the time scale of exciton recombination lies between 3–15 ns and a much longer time-scale range, 10–50 ns is due to shallow trap assisted recombination. PVDF plays a decisive role in increasing the population of shallow trap states in perovskite-polymer nanocomposite (Scheme 3.2(B)). Hydrophobicity of PVDF does not allow polymeric encapsulation of large-sized perovskite crystals, thus these crystals get broken into smaller ones for nanofilling in polymer matrices. Mismatch in ionic characters and refractive indices between PVDF and lead halide perovskites cause greater structural disorder or lattice defects

in these nanocrystals. Upon polymeric encapsulation of nanocrystals, the trap levels get redistributed due to the

numerous interface regions generated by the interaction of crystalline perovskite and amorphous PVDF. Physical properties of the interfaces would be affected by chain mobility, chain conformation, crystallinity, and coulombic potential. The differences of these have caused the redistribution of the trap levels in the perovskite- polymer nanocomposites. According to the multi-layered core model, an interfacial layer of several tens nm is multi-layered and consists of three layers- a bonded layer, a bound layer, and a loose layer.[275] An electric double layer of several tens to 100 nm is also superimposed in the interfacial layer. Free volume becomes higher, and density becomes lower from the bonded layer to the loose layer. The loose layer is much larger in volume friction than the bound layer, the shallow traps become dominated traps in the NCs-doped PVDF.
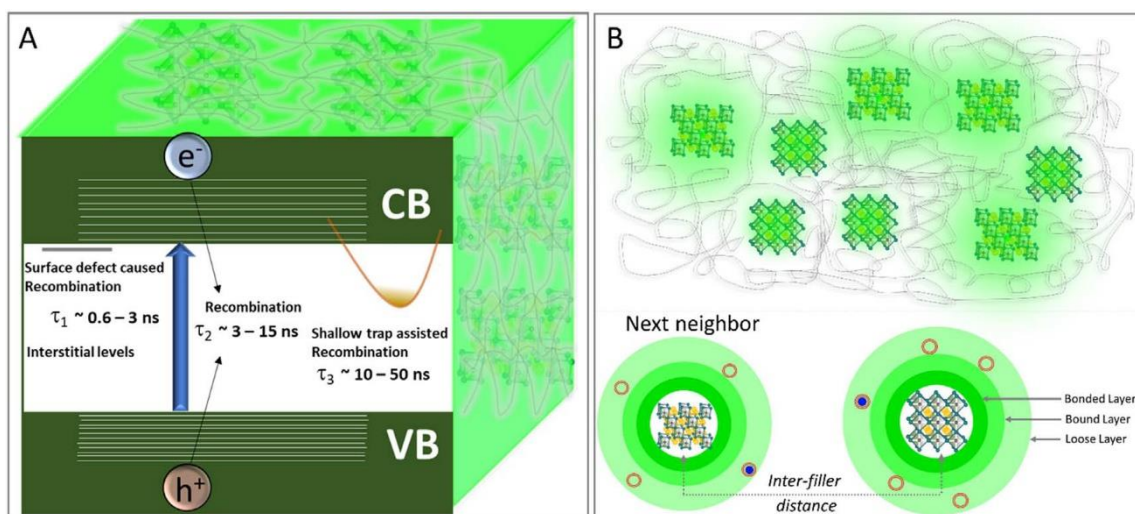
Scheme 3.2: Schematic illustration of – **[A]** radiative recombinations in nanocrystals-doped polymer, **[B]** perovskite-polymer interface (*top panel*), and formation of shallow traps at the loose layer (*bottom panel*). ⭕ represent shallow trap-states and 🔵 carrier-trapped by shallow traps.

To visualize the nanocrystals in PVDF matrix, scanning electron microscopy (SEM) has been employed (figures 3.2(D)–(E)). It can clearly be noticed from the SEM images that

nanocrystals are quite uniformly doped in the polymer matrix. However, the sizes of these crystals are relatively large, 88±32 nm than the reported sizes of halide perovskite nanocrystals. Analysis of EDS and XRD (figure A 3.5 & 3.7.) data suggests the existence of $CsPbBr_3$ nanocrystal in PVDF polymer matrix. Br is the most abundant element and its ability to absorb both the Cs and Pb x-rays has perhaps caused observation of its excess signal. High-resolution XPS spectrum of nanocrystal doped polymer for Pb 4f (figures 3.2(F)), yields two distinct peaks at 138.4 eV ($4f_{7/2}$) and 143.2 eV ($4f_{5/2}$) with a characteristic spin–orbit splitting, 4.9 eV of Pb^{+2}. No significant change in peak positions of XPS spectrum of dispersed nanocrystals (NC) for Pb 4f has been noticed.

3.2.3. Halide exchange of polymer-encapsulated nanocrystals

At ambient condition, $CsPbI_x$ perovskite is the thermodynamically least stable structure in comparison to $CsPbBr_x$.[276] Moreover, the halide exchange of these nanocrystals in an aqueous solution using hydrobromic acid or hydroiodic acid (HI) remains a challenge owing to their poor stability in water. Our strategy for selecting hydrophobic PVDF polymer for the entrapment of nanocrystals is because PVDF can stabilize the nanocrystals in an aqueous solution by reducing water accessibility of such nanocrystals. Halide exchange studies have been performed with dried perovskite-polymer nanocomposite at 120 °C that is lower than the melting temperature of polymer. Representative images illustrate the reversible anion exchange of perovskite-polymer nanocomposite. We could easily obtain red-emitting nanocrystals doped polymer (PHNC-2) via anion exchange in an aqueous medium of 3% HI. A film of PHNC-2 has been prepared by heating the crystal at 180 °C for further studies.

The photoluminescence spectrum of PHNC-2 displays a peak at 685 nm (fwhm=39 nm) with a bandgap of 1.8 eV (figures 3.3(B)). A spectral broadening has been noticed for PHNC-2 in compassion to PHNC-1 (fwhm=19 nm). Such broadening of spectral band is consistent with those reported in the literature.[274,277] The broad PL emission is most likely due to the- (i)

combination of two different halides self-assembling- possibly forming $CsPbBr_xI_{(1-x)}$ and (ii) structural heterogeneity caused by weaker binding of larger iodide ions to cesium ions.
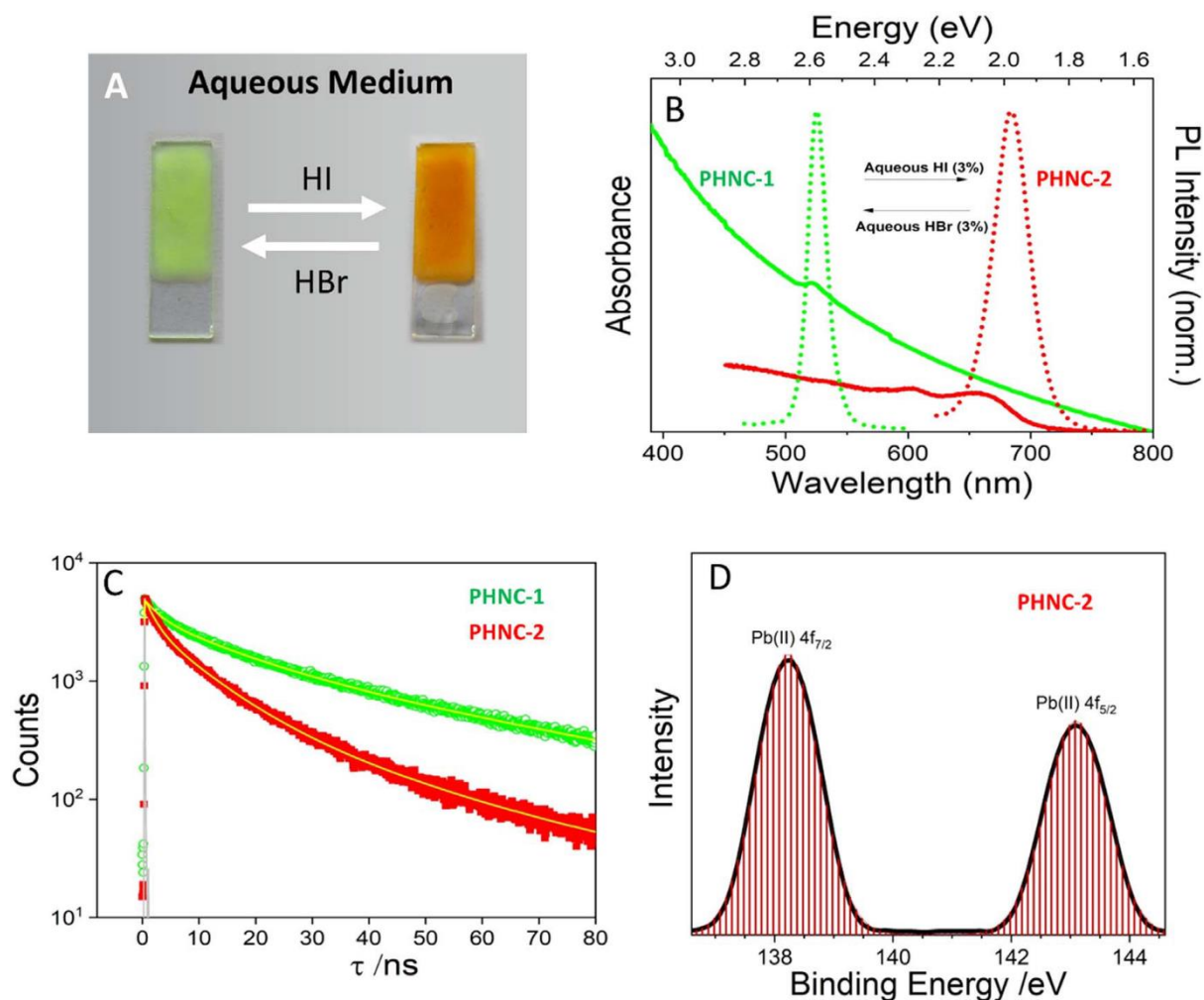
Figure 3.3. **[A]** Images polymer-encapsulated nanocrystal undergoing fast halide exchange. **[B]** Absorption (solid lines) and photoluminescence spectra (dotted lines) of green-emitting nanocrystal-doped polymer, PHNC-1 (green) and red-emitting nanocrystal-doped polymer, PHNC-2 (red). **[C]** Time-resolved photoluminescence decays of - PHNC-1 (green), and PHNC-2 (red). Instrument response function (IRF) represented in grey line. **[D]** High-resolution XPS spectra of Pb (II) for PHNC-2 respectively.

The photoluminescence decay of PHNC-2 shows faster kinetics than that of PHNC-1 (figure 3.3(B)). The average photoluminescence lifetime of PHNC-2 is 8.59 ns. A closer analysis of components and associated amplitude uncovers that the exciton recombination (τ_2) is the dominant one for PHNC-2.

Table 3.2. Photoluminescence decay parameters of nanocrystals doped polymer.

Sample	λ_{ems} (nm)	τ_1 (ns)	τ_2 (ns)	τ_3 (ns)	a_1	a_2	a_3	$<\tau>$ (ns)	χ^2
HNC	513	1.83	5.63	14.81	0.19	0.69	0.12	8.12	1.11
PHNC-1	525	2.39	13.06	44.5	0.27	0.39	0.34	35.52	1.02
PHNC-2	680	1.86	9.09	28.49	0.40	0.48	0.12	8.59	1.07

λ_{exc} = 405 nm; IRF= 180 ps; Luminescence lifetimes, $<\tau> = \Sigma a_i \tau_i^2 / \Sigma a_i \tau_i$

Expectedly, the high-resolution XPS spectrum of PHNC-2 for Pb 4f has two characteristic peaks at 138.2 eV ($4f_{7/2}$) and 143.1 eV ($4f_{5/2}$). The XPS spectrum for iodine 3d shows two distinct peaks at 618.9 eV ($3d_{5/2}$) and 630.4 eV ($3d_{3/2}$) with spin–orbit splitting of 11.5 eV. To understand the type of crystals structure of red-emitting nanocrystals we have performed XRD studies of PHNC-2. XRD peaks of red-emitting perovskite nanocrystals are well-matched with the characteristic interplanar planes of monoclinic $CsPbBr_3$ NCs (PDF#18-0364), suggesting the structure of $CsPbI_3$.

3.2.4. Water- and Photo-stability of PVDF-encapsulated Nanocrystals

We have performed the studies to understand the effect of polymeric encapsulation on the aqueous- and photo-stability of NCs. First, the perovskite-polymer nanocomposite films have been prepared by heating them at a melting temperature,180 °C of PVDF. Figures 3.4(A), (B) show that the emissivity of NCs doped polymer even remains intact after 07 days of incubation in water. It has been reported that the photoluminescence of core-shell $CsPbBr_3$/ZnS nanocrystals gets significantly quenched even after 2 days of incubation in water.[171]

To the best of our understanding, this is the first report where the photoluminescence of perovskite-polymer nanocomposite remains unaltered even after a month of incubation in water. The emission peak positions (λ_{max}) of PHNC-1 and PHNC-2 films remain unchanged. Interestingly, the photoluminescence intensity of films gets relatively increased. To decipher the origin of enhancement, we have performed TRPL studies of films before and after the incubation of polymer nanocomposite films. After incubation, the photoluminescence lifetime

of PHNC-1 increased to 45.79 ns (table 3.3). A similar increasing trend of photoluminescence

lifetime has also been observed for PHNC-2. The increase in radiative lifetime suggests that

solvent, water can passivate surface defects. Slow diffusion of quenchers (photoluminescence)

such as bromide and cesium ions from polymeric surface and interfacial area of

nanocomposites to bulk water has perhaps caused augmentation of radiative lifetime.
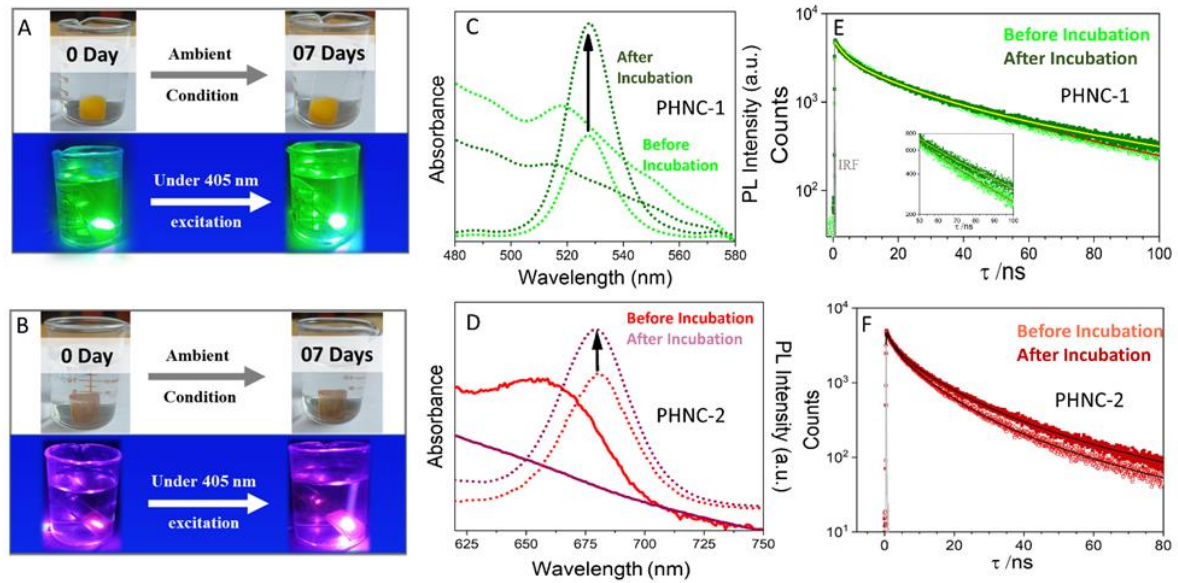
Figure 3.4. **[A-B]** Digital photographs of green and red-emitting NC-doped polymer films dipped in a beaker containing water respectively. **[C]** Absorption (solid lines) and photoluminescence spectra (dotted lines) of green-emitting NC-doped polymer films, PHNC-1, before incubation (light green) and after incubation (dark green) in distilled water. **[D]** Absorption (solid lines) and photoluminescence spectra of PHNC-2, before incubation (red) and after incubation in distilled water (violet) **[E-F]** Time-resolved photoluminescence decays of - PHNC-1 (green), and PHNC-2 (red) before and after incubation in distilled water. Inset (E): Highlighting differences in longer components.

Table 3.3. Photoluminescence decay parameters of perovskite-polymer nanocomposite before and after incubation in water.

PHNC-1									
	λ_{ems} (nm)	τ_1 (ns)	τ_2 (ns)	τ_3 (ns)	a_1	a_2	a_3	$<\tau>$ (ns)	χ^2
Prior incubation	525	2.39	10.59	40.29	0.22	0.37	0.41	33.79	1.02
After incubation	525	2.77	16.06	59.59	0.33	0.40	0.28	45.79	1.07
PHNC-2									
Prior incubation	680	1.86	9.09	28.49	0.4	0.48	0.12	8.59	1.07
After incubation	680	2.48	10.73	32.17	0.41	0.44	0.15	10.53	1.04

λ_{exc} = 405 nm; IRF= 180 ps; Luminescence lifetimes, $<\tau> = \Sigma a_i \tau_i^2 / \Sigma a_i \tau_i$

3.3 Conclusion:

We present here a polymer-directed antisolvent method for synthesis of perovskite composite crystals. $CsPbBr_3$ and zero-dimensional Cs_4PbBr_6 are found to be the constituents of composite crystals. PVDF does not only restrict the growth of the crystal, rather facilitate the synthesis of nanocrystals under ambient conditions. Freshly prepared perovskite nanocrystals instantaneously get entrapped in the PVDF polymer matrix. Upon polymeric entrapment, these crystals undergo aggregation as evident from their increased size, 88 ± 32 nm. We have resolved the types of radiative recombination present in polymer-encapsulated nanocrystals. The surface defect caused radiative recombination takes place at a much faster time scale (0.6–3 ns), whereas the exciton recombination lies in the time scale of 3–15 ns and a much longer time-scale range, 10–50 ns is due to shallow trap assisted recombination. PVDF perhaps contributes to the creation of more shallow trap states for perovskite-polymer nanocomposite. Polymer-encapsulated nanocrystals can undergo fast halide exchange in an aqueous HI solution. These polymer-encapsulated nanocrystals are highly stable, and their photoluminescence properties remain unaltered even after 07 days of incubation in water. In this work, we demonstrate the necessity of hydrophobicity caused by $–CF_2–$ network of PVDF in either synthesizing or providing stability to perovskite nanocrystals.

Chapter 4

Facet {100} Fosters Resonance Energy Transfer

in Ni/Co-doped CsPbBr$_3$ Nanocrystals

The design of an effective light harvester with metal-doped perovskite nanocrystals (M:PNCs) aims to achieve directional energy flow. The potential of crystal facets needs to be assessed for dictating the energy transfer dynamics of M:PNCs. Herein, we have engineered facets of amine-capped $CsPbBr_3$ perovskite nanocrystals by doping with a trace amount of Ni and Co ions. Ni-doped $CsPbBr_3$ (Ni:PNC) showcases structural heterogeneity with regular cubic shape, whereas bimetallic-doped $CsPbBr_3$ (Ni:Co:PNC) evolves to an elongated dodecahedron structure. Structural analysis using Rietveld refinement strongly corroborates the construction of a dodecahedron structure for Ni:Co:PNC through systematic displacement of Cs ions. Energy transfer from doped nanocrystals to rhodamine B (RhB) occurs through a dipole−dipole interaction, known as Förster resonance energy transfer (FRET). The emergence of the isoemissive point and rise time of RhB conclusively establishes the resonance energy transfer mechanism. Energy transfer in thin films occurs at a much faster rate than in the toluene medium. {100} facet-dominated Ni:PNC registers a FRET efficiency of 94%, whereas {111} and {002} facet-dominated Ni:Co:PNC is restricted at 21% FRET efficiency. The distance between the donor and acceptor, R_{DA}, dictates the dynamics of energy transfer, rather than spectral overlap and the photoluminescence quantum yield of these doped nanocrystals. The surface composition of facets, typically Cs ions, perhaps plays a decisive role in regulating the binding constant of the donor and acceptor. Our study demonstrates the importance of facets of nanocrystals in tuning the desired energy transfer processes for photocatalytic applications.

4.1 Introduction:

Colloidal cesium lead halide perovskite (CsPbX$_3$, X = Cl, Br, and I) nanocrystals (PNCs) are the most promising photoluminescent inorganic self-assemblies owing to their cutting edge applications in tandem-solar cell, light-emitting diodes, and photo(electro)catalysis.[233,278–280] However, these photoluminescent nanocrystals remain far from practical applicability due to their poor ambient stability.[46,119,281] The coulombic interaction guided dynamic binding between ammonium ions (of oleylamine) with bromide ions present in crystal lattice and oleate ions (of oleic acid) with lattice's cesium ions falls apart in the presence of water molecules, as oleate becomes oleic acid and leaves the hydroxide ion. This hydroxide ion readily forms lead hydroxide salt, Pb(OH)$_2$, with crystal's Pb(II) ion.[282] Very recently, Ma et al. have elucidated the intricacies of binding water molecules with formamidinium lead iodide (FAPbI$_3$) nanocrystals and demonstrated that its crystal facet {100} is substantially more vulnerable to

moisture-induced degradation than facet {111}.[283] To improve the ambient stability of PNCs, doping of metal ions into the perovskite crystal is the current focus of research.[155,284,285]

Metal ion-doped perovskite nanocrystals (M:PNCs) possess unique excellent photostability (PL), narrow spectral widths, and bandgap tunability. Very recently, doping of several alkaline-earth metals (e.g., Mg^{+2}, Ca^{+2}, and Ba^{+2}) into perovskite nanocrystals has been investigated for improvement of the photoluminescence quantum yield.[286–288] Transition metal ions have also been tested as dopants for achieving near unity photoluminescence quantum yield, band tuning, and improving stability.[153,155,156,289] The defect tolerance ability of PNCs remains the foundation behind such doping.[290] However, a greater emphasis on sustainability vis-à-vis net-zero carbon emission has also pushed researchers to harness the potential of metal-doped perovskite nanocrystals for photocatalytic applications, such as green hydrogen production and sustainable fuels/chemicals production by CO_2 reduction.[69,291–294]

Efficient energy transfer coupled with electron transfer remains the bottleneck in designing of a semiconductor photocatalysts with augmented photocatalytic efficiency.[295–297] In order to achieve so, doping of catalytically active transition metal ions (Pd, Fe, Cu, etc.) is done quite frequently with a presumption that these ions can facilitate electron (charge) transfer processes.[69,298,299] However, the complexity involved in excited state energy transfer processes of transition-metal ion doped nanocrystals has not been investigated in detail. Thus, it has intrigued us to investigate the photophysics and photochemistry of nickel(II) and cobalt(II) ions-doped cesium lead bromide nanocrystals (Scheme 4.1). Ni(II) ion-doped nanocrystals are found to retain intense emission and offer remarkable stability. The role of dopant Ni(II) ions having the smallest transition metal Shannon radii in modulating photoluminescence properties of perovskite nanocrystals has been attributed to structural rigidity of the crystal favoring carrier-dopant spin exchange interactions.[300,301]

Scheme 4.1. Highlighting the Research Gap and Scope of Our Work in Deciphering Facet-Directed Energy Transfer Dynamics of Transition Metal-Doped Cesium Lead Halide Perovskite Nanocrystal (M:PNC)
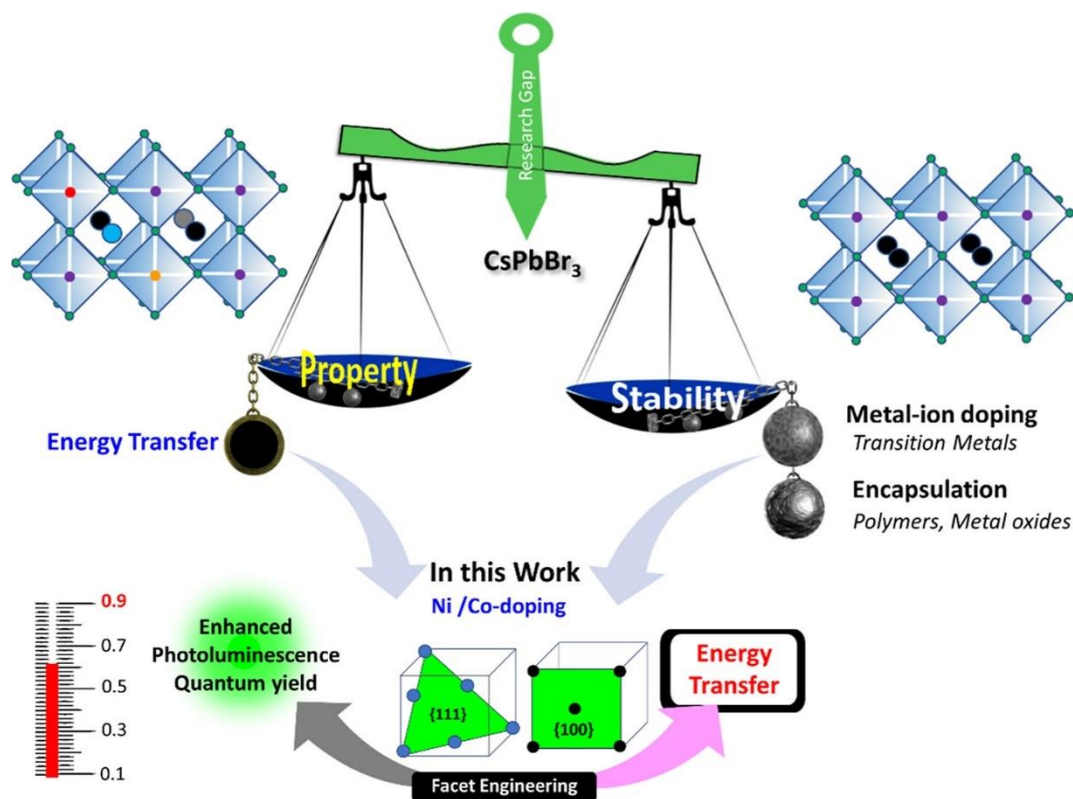
Scheme 4.2. **[A]** Spectral Overlap between Photoluminescence Spectra of Metal-Doped PNCs and Rhodamine B; Energy Transfer Processes Involved between M:PNCs and Rhodamine B, where hν′ Is the Emission from Metal-Doped PNC and hν″ Is the Emission from Rhodamine B and * Indicates the Excited State; **[B]** Schematic Representation of the Donor−Acceptor Pair for the Resonance Energy Transfer Process
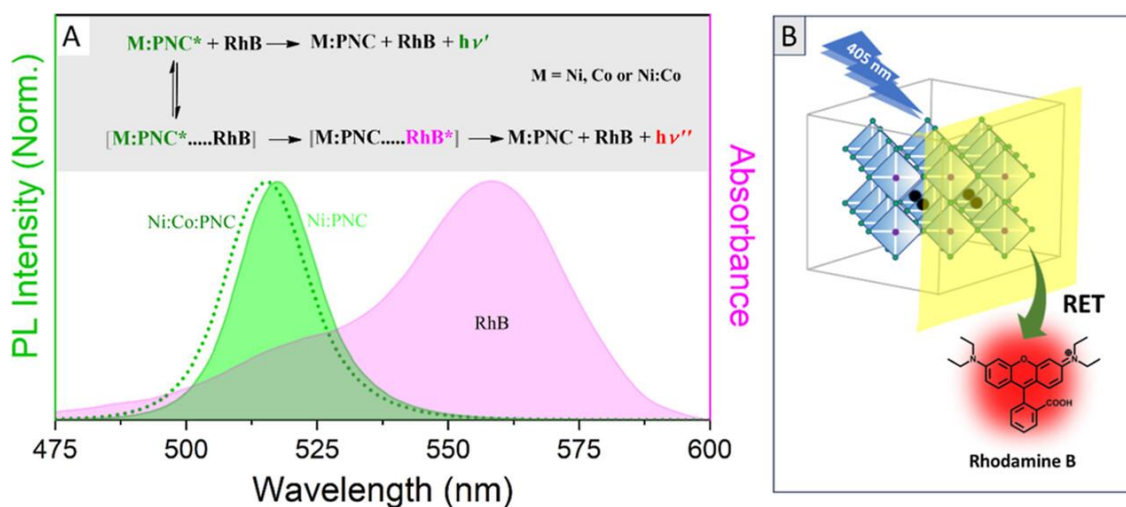
Here, we have selected a Ni/Co-doped nanocrystal as a donor and organic dye, rhodamine B as an acceptor for understanding the energy transfer processes. The basis of this donor−acceptor selection stems from the observation of photocurrent generation by organic dyes in quantum dot solar cells.[302,303] Moreover, recent studies on Förster resonance energy transfer (FRET) between pristine cesium lead bromide perovskite and organic fluorophores indicate that singlet energy transfer efficiency is dictated by (i) binding constant of the acceptor with nanocrystal's surface and (ii) overlap integral, $J(\lambda)$.[57,304,305] The binding constant of a donor−acceptor system is very intrinsic and thus plays a pivotal role in determining the efficiency of energy transfer, whereas the overlap integral, a theoretical concept, provides a rationale for the modulation of energy transfer efficiency for a set of systems. However, it has been presumed that donor acceptance remains unchanged. Thus, it is pertinent to understand the role of crystal facets in regulating the binding constant vis-à-vis energy transfer from transition metal-ion doped perovskite nanocrystal to organic fluorophore.[273]

In this work, we synthesized $Ni:CsPbBr_3$ (Ni:PNC) and $Co:CsPbBr_3$ (Co:PNC) and $Ni:Co:CsPbBr_3$ (Ni:Co:PNC) perovskite nanocrystals by using a modified hot-injection method. To decipher the role of crystal facets in energy transfer, we have selected an organic dye rhodamine B as an acceptor, whose photophysical properties are well characterized.[306] The reason for selection for this donor (D)−acceptor (A) pair is owing to nearly identical values of spectral overlap integral, $J(\lambda)$, between emission of metal-doped PNCs (M:PNCs) and absorption of rhodamine B (RhB).

Energy transfer from M:PNCs to rhodamine B is probed by the decrease in emission of PNCs and concurrent increased emission of RhB. The appearance of the isoemissive point is suggestive of equilibrium between two emissive species (Scheme 4.2). Herein, energy transfer from metal-doped perovskite nanocrystals to rhodamine B has been systematically investigated by using steady state and time-resolved photoluminescence measurements. Our detailed

structural studies document the crystal stiffening by a small doping of Ni/Co, which modifies the facet accordingly. We believe that this study will serve as a reference point for designing a transition metal-doped perovskite nanocrystals for tuning their photocatalytic activities.

4.2 Results & Discussion:

4.2.1. Structural Heterogeneity.

We first performed structural analysis of as-synthesized doped-PNCs to trace the origin of their enhanced optical properties and improved ambient stability. Full-survey and high-resolution XPS spectra of doped PNCs for Pb 4f, yield two distinct Gaussian-shaped peaks due to spin−orbit coupling of 4f-orbital, as shown in Figure 4.1 & Figure A 4.1.The Pb 4f peaks in the XPS spectrum of Ni:Co:PNC and Co:PNC appear at 142.7 eV ($4f_{5/2}$) and 137.8 eV ($4f_{7/2}$), nearly at the same position of the undoped- $CsPbBr_3$.[259] The Pb 4f peaks of Ni:PNC are shifted to higher binding energy, that is, at 143.4 eV ($4f_{5/2}$) and 138.6 eV ($4f_{7/2}$). The spin-orbit splitting of Pb(II) for both remains the same, 4.9 eV. XPS peak positions of core-level spectra are vastly affected by the chemical environment (surrounding electron-cloud) of that element. It therefore suggests that Ni(II) greatly impacts the chemical environment around Pb(II) in the nanocrystal.[307] Ni-doping might enhance the chemical bonding of Pb, with the neighboring bromide ion causing a peak in higher-binding energy.[308] Such an effect is minimal for doping of the Co(II) ion. Interestingly, insignificant shifting of Pb 4f peaks in Ni:Co:PNC compared to that of Co:PNC suggests a similar environment of Pb in both the combinations. It is possible that the combination of Co and Ni doping in Ni:Co:PNC may not affect the Pb−Br bond, but may affect the overall structure, i.e., distortion of the overall lattice structure. Notably, the XPS spectra of Ni(II) for Ni:Co:PNC greatly resembles those for Ni: PNC (figure A 4.3).
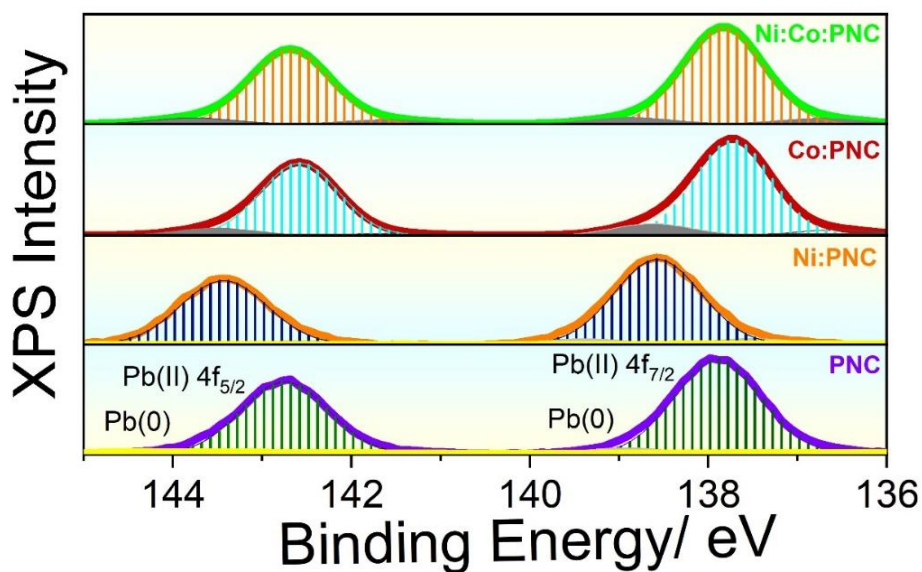
Figure 4.1: High resolution XPS spectra of Pb(II) for PNC (*violet line*), Ni:PNC (*orange line*), Co:PNC (*red line*) and Ni:Co:PNC (*green line*).
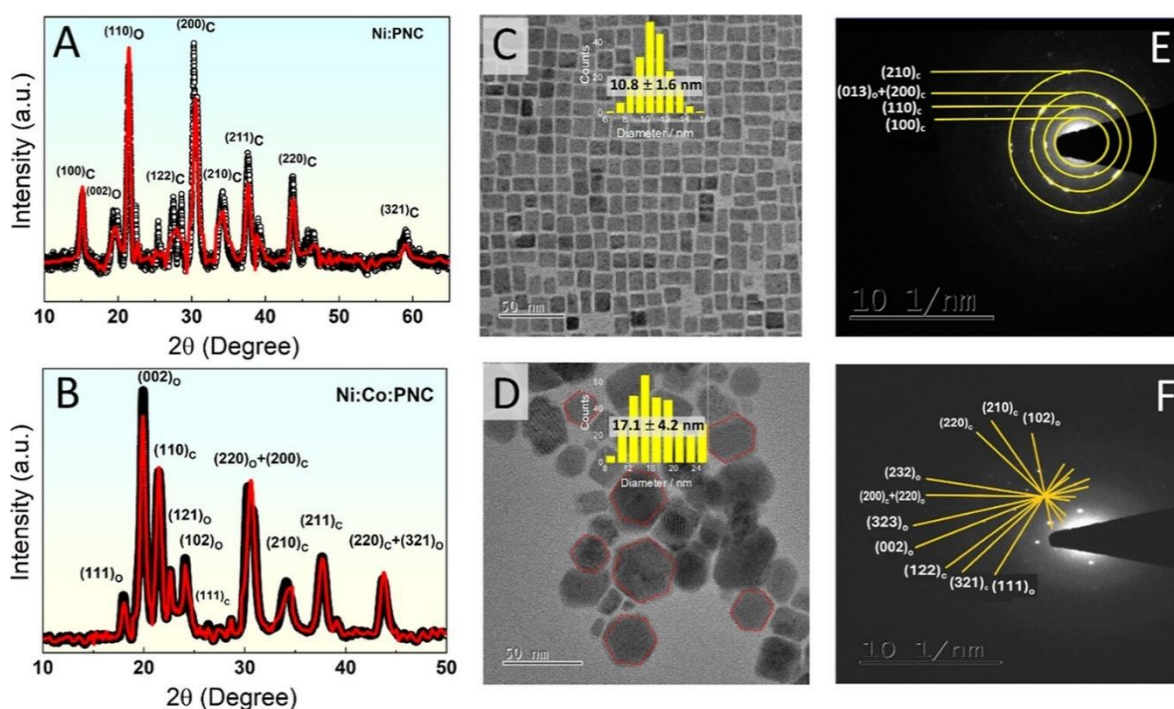
Figure 4.2. Rietveld refinement of the X-ray diffraction pattern of **[A]** Ni:PNC and **[B]** Ni:Co:PNC. The data are shown as circles and the result of the refinement as a solid line (red). We have used orthorhombic phase (space group: Pnma, no. 62) of $CsPbBr_3$ and added cubic phase (space group: Pm$\bar{3}$m, no. 221). **[C,D]** TEM images of Ni:PNC and Ni:Co:PNC respectively. **[E,F]** TEM-FFT pattern of Ni:PNC and Ni:Co:PNC respectively.
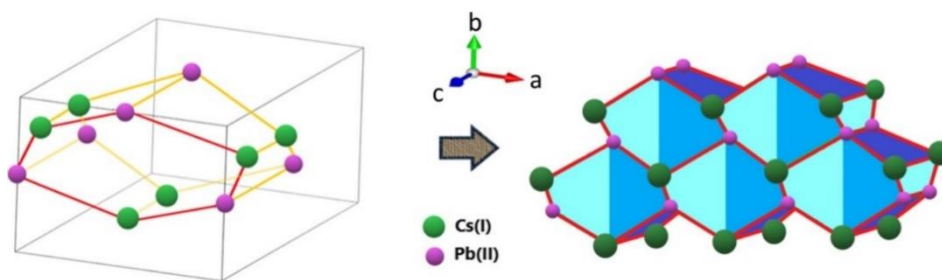
Figure 4.3. Front surface on the ab plane (solid red lines) of Ni:Co:PNC. Addition of adjacent trapezoid (solid yellow line) results in the formation of the dodecahedron structure. The Ni:Co:PNC crystal lattice having Cs(I) and Pb(II) ions only. On the front surface of the ab plane by connecting Pb−Cs−Pb−Cs−Pb−Cs−Pb, the front hexagonal is first sketched, then extending the whole structure in all directions to the elongated dodecahedron.

Thereafter, we have analyzed energy-dispersive X-ray spectra (EDS) of Ni:PNC, Ni:Co:PNC, and Co:PNC (figure A 4.3) to estimate the dopant concentration in metal-doped perovskite nanocrystals. The elemental ratio of Cs:Pb:Br of metal-doped PNCs is found to be 1:1:3, confirming the $CsPbBr_3$ composition. The atomic percentages of Ni(II) in Ni:PNC and Ni:Co:PNC are 2.3 and 0.8, respectively, whereas those of Co(II) in Ni:Co:PNC and Co:PNC are 1.0, and 2.4, respectively. Hence, the doping of about 2% metal ions in PNCs creates a strong impact in structural heterogeneity.

X-ray diffraction (XRD) studies have been performed to resolve facet engineering through metal-doping of perovskite nanocrystals. Our careful Rietveld refinement demonstrates that doped perovskite nanocrystals exist in two phases orthorhombic and cubic phases.[309,310] The Rietveld-refined XRD patterns of Ni:PNC and Ni:Co:PNC are shown in Figure 4.1 A, B. The percentage of orthorhombic and cubic phases vastly varies with doping. Unprecedentedly, facet engineering through metal doping has been noticed with observation of {100} facet only in Ni:PNC. Emergence of facet {111} for Ni:Co:PNC signals its significant structural change in comparison to that of Ni:PNC. The displacement of Cs-ion in the orthorhombic structure (maintaining same space group) in Ni:Co:PNC compared to that of Ni:PNC plays a crucial role in such facet engineering. A subtle change in the position of Cs

ions in the Ni:Co:PNC nanocrystal in comparison to that of the Ni:PNC nanocrystal has been observed, while negligible change of Br and no change of the Pb atom is noticed (figure A 4.4). The Cs atom in Ni:Co:PNC systematically shifts toward the surface of the orthorhombic structure, which forms an irregular hexagon (figure A 4.4A).[311] However, the Cs ions get displaced in one direction for Ni:PNC and therefore does not construct such a systematic dodecahedron structure (figure A 4.4B). Eventually, the one-directional movement of the Cs atom in Ni:PNC suggests the possibility of spatial inversion symmetry breakings. We have imaged the doped perovskite nanocrystals Ni:PNC and Ni:Co:PNC by using transmission electron microscopy (TEM) to further support such changes in the crystal structure.

Figure 4.2C shows the typical cubic (10.8 ± 1.6 nm) structures of Ni:PNC, while Figure 4.2D captures the elongated hexagon (17.1 ± 4.2 nm) for Ni:Co:PNC. In addition to that, we have also observed a perfect hexagon structure for Ni:Co:PNC. Lattice spacing observed for Ni:PNC is 0.39 nm, whereas that for Ni:Co:PNC is 0.42 nm (figure A 4.5). By analyzing the reciprocal crystal point in the TEM images (Figure 4.2D, E), we measured the d-spacing values and associated them with specific {hkl} planes. Facets {100}, {110}, and {200} of Ni:PNC correspond to the family of planes of cubic $CsPbBr_3$. The presence of facets {111}, {002}, and {211} signifies a predominant orthorhombic structure of Ni:Co:PNC. Our refined crystallographic analysis, combined with the creation of a physical structure based on the refinement parameters, reveals an intriguing pattern within the orthorhombic phase. The absence of atoms at the corners and the resulting formation of a trapezo-rhombic dodecahedral-like structure (elongated dodecahedron) closely correspond to the observed hexagonal pattern observed in the TEM image. Structural analysis using Rietveld refinement suggests that the ratio of the total integrated intensities between orthorhombic and cubic phases for Ni:Co:PNC is 55:45, whereas that for Ni:PNC becomes 25:75. Moreover, the plane {100} of Ni:PNC cuts four Cs(I) ions and a bromide ion, whereas plane {111} of Ni:Co:PNC consists of two Pb(II)

ions and one bromide ion (Figure 4.3). The consistency observed between our calculated d-spacing values and the refined crystallographic parameters validated the accuracy of our approach. The agreement between the predicted planes from the TEM-FFT pattern analysis and the refinement results from XRD contributes to a deeper understanding of the structural modifications induced by dopants Ni (II) and Co (II) in the $CsPbBr_3$ lattice.

4.2.2. Enhanced Photoluminescence and Ambient Stability.

Ni/Co-doped cesium lead bromide perovskite nanocrystals Ni:PNC, Co:PNC, and Ni:Co:PNC dispersed in hexane more or less retain the green-emissive features of pristine PNC. The emission peak positions (λ_{max}) are centered at 518 nm (fwhm = 18 nm) with a band gap of 2.30 eV for Ni:PNC (Figure 4.4A & A 4.6).. However, the emission peak of Ni:Co:PNC gets blue-shifted to 515 nm (fwhm = 19 nm) with a band gap of 2.32 eV. The photoluminescence quantum yield (PLQY) of Ni:Co:PNC is measured to be 0.70, whereas that of Co:PNC and Ni:PNC are relatively low, 0.54 and 0.33 respectively.
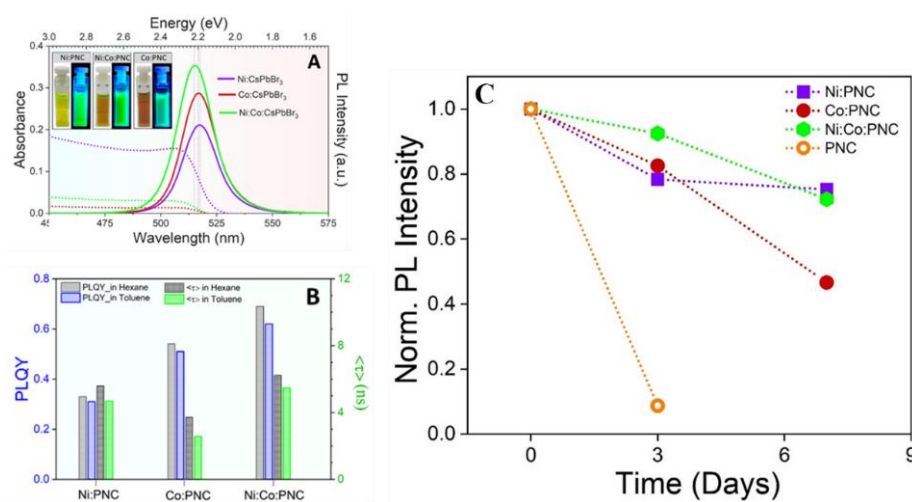
Figure 4.4. **[A]** Absorption (dotted line) and photoluminescence (solid lines) spectra of metal-doped perovskite nanocrystals in hexane. Ni:PNC (violet), Ni:Co:PNC (green), and Co:PNC (red) Inset: Photographs of perovskite nanocrystals at ambient and under 405 nm irradiation. **[B]** Comparison of PLQY and Average photoluminescence lifetime of doped-PNCs in two different solvent hexane (grey bar) and toluene (blue bar representing PLQY and green bar representing average photoluminescence lifetime). **[C]** Ambient stability of Ni:PNC (purple square), Co:PNC(brown sphere), and Ni:Co:PNC (green hexagon) respectively. This Norm PL intensity decreases substantially after only 3 days for undoped PNC.

The augmented photoluminescence properties of doped- PNCs may be accounted for by invoking either spin−orbit coupling (quantum hoping) or structural (facet) engineering.[307] We have found that Ni:PNC and Ni:Co:PNC are relatively more stable than Co:PNC. The stability of Ni:PNC is in agreement with reported results (Figure 4.4C).[301,308] Crystal stiffening caused by smaller ionic radii of the Ni(II) ion has been attributed to the improved stability of Ni:PNC as well. The average photoluminescence lifetimes, τ_{avg}, of Ni:PNC and Ni:Co:PNC in toluene are 4.68 and 5.47 ns, respectively, whereas that of Co:PNC is relatively low, 2.57 ns (Figure 4.4B). It can be mentioned that toluene acts as a photoluminescent quencher for doped- PNC. Solvent n-hexane is relatively less polar and viscous than toluene. Therefore, clustering of nanocrystals in toluene might have contributed to the decrease in PNC's photoluminescence. Hence, this photophysical study serves as a reference point for energy transfer studies in a toluene medium.

4.2.3. Crystal Facet-Directed Energy Transfer to Rhodamine B.

Energy transfer studies between organic fluorophores are often manipulated by regulating the binding affinity between acceptor and donor moieties.[264,312] However, an understanding of the role of structural heterogeneity of nanocrystals in its energy transfer process involving organic molecules is very limited. Recently, it has been suggested that pendant groups of acceptor molecules can also regulate their binding affinity toward perovskite nanocrystals.[305] An obvious question thus arises, how does the electronegative atom (e.g., iodine and chlorine) of the acceptor molecule influence its binding affinity to the perovskite nanocrystal? The role of crystal facets in doped-PNCs cannot be ignored, as it has also been shown that facet {100} FAPbI$_3$ strongly interacts with highly polar water molecules.[283]
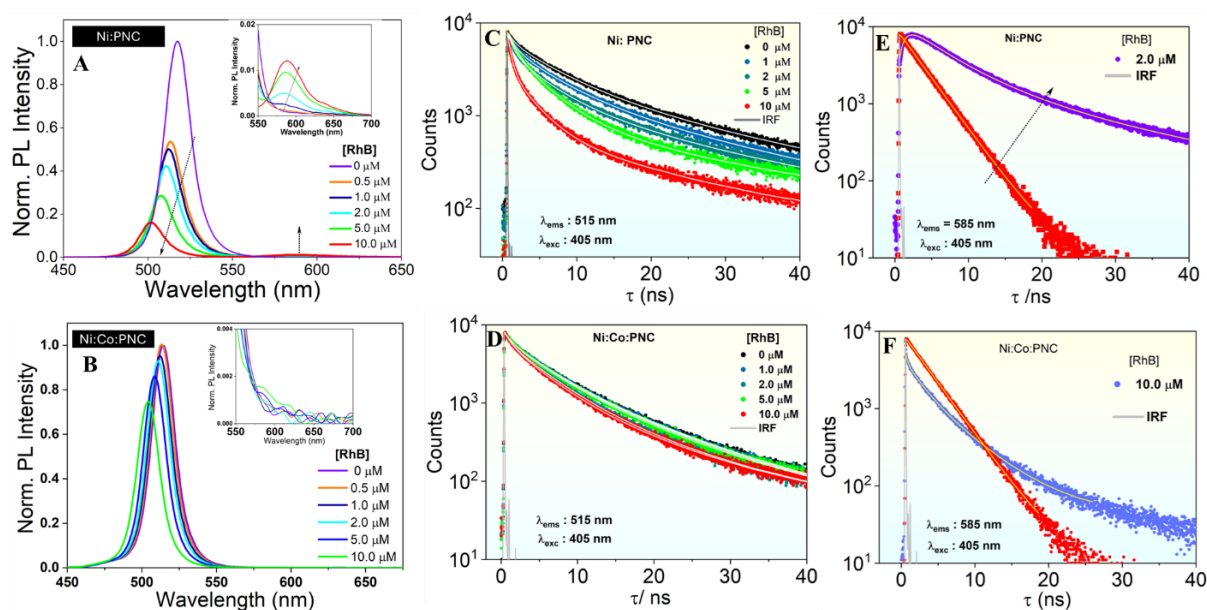
Figure 4.5. Photoluminescence quenching of donors **[A]** Ni:PNC and **[B]** Ni:Co:PNC with successive addition of acceptor, rhodamine B. Inset: Modulation of emission properties of the acceptor. Time-resolved photoluminescence decays at λ_{ems} = 515 nm. **[C]** Ni:PNC and **[D]** Ni:Co:PNC highlighting faster kinetics upon gradual addition of rhodamine B. **[E,F]** Time-resolved photoluminescence decays of the acceptor (λ_{ems} = 585 nm) for the Ni:PNC−RhB pair and Ni:Co:PNC−RhB pair, respectively. Instrument response function (IRF) at λ_{exc} = 405 nm represented by the gray line.

To interrogate the efficiency of energy transfer, we have measured steady-state and time-resolved emission spectra of donors Ni:PNC, Ni:Co:PNC, and Co:PNC in the presence and absence of acceptor rhodamine B (Figures 4.5 A, B). The photoluminescence of donors undergoes gradual quenching with the addition of rhodamine B (0−10 μM). However, the photoluminescence quenching for Ni:PNC is relatively sharper than that of Ni:Co:PNC (Figure 4.5 A, B). Interestingly, concurrent emission of acceptor is pronounced for the Ni:PNC−RhB pair (inset, Figure 4.5A), whereas hardly any emission originates from acceptor for the Ni:Co:PNC−RhB pair (inset, Figure 4.5B). The isoemissive point that appears at 560 nm is suggestive of the existence of two emissive species [Ni:PNC*] and [Ni:PNC−RhB*] in equilibrium. A hypsochromic shift in photoluminescence spectra of M:PNC is due to the

presence of a chloride ion in commercially available rhodamine B (empirical formula: $C_{28}H_{31}ClN_2O_3$).

Synchronicity between the decrease in donor emission and concurrent increase in acceptor emission is commonly observed for organic donor-acceptor systems. It seems that such synchronicity is missing for the doped PNC−RhB system, as evident by the low concurrent emission of fluorophore and the significant decrease in the emission of doped PNCs. To account for this observation, we have drawn its similarity with widely reported interactions of metal nanoparticles (such as Au and Ag nanoparticles) with organic fluorophores. The cause of significant photoluminescence quenching of doped PNC can thus be attributed to the specific interaction (such as adsorption and electron transfer) of rhodamine B with its surface. Moreover, to shed light on the molecular characteristics of rhodamine B in solvent toluene, we have performed photophysical studies of rhodamine B alone in toluene (figure A 4.8). It is found that RhB starts to form molecular aggregates at its increased concentration signaled by a decrease in its fluorescence lifetime. Such heterogeneity is thus expected to exhibit concentration-dependent energy transfer dynamics for the M:PNC−RhB system.

Time-resolved photoluminescence studies of D-A pairs are in direct agreement with steady-state photoluminescence studies. TRPL decay of Ni:PNC−RhB and Ni:Co:PNC−RhB pairs at 515 nm (λ_{exc} = 405 nm) with gradual addition of acceptor (0-10 μM) becomes faster (Figure 4.5 C, D) and the decay parameters are tabulated in table A 4.1 & A 4.2. However, the decrease in τ_{avg} for Ni:PNC−RhB is 83%, whereas that for Ni:Co:PNC−RhB remains at merely 20%. It is evident that the emission of RhB originates from the excitation of doped PNCs and direct energy transfer from perovskite nanocrystals to the organic fluorophore yields a singlet excited state of the acceptor. Involvement of triplet–triplet (T–T) annihilation has been recently contested by presenting the dependence of acceptor's singlet excited state formation on excited state decay of the donor, doped-PNC. To quantify the rate of energy transfer for the

90

Ni:PNC−RhB pair, we have recorded fluorescence decay of rhodamine B at 585 nm (λ_{exc} = 405 nm) in the presence and absence of the donor, Ni:PNC (Figure 4.5 E). Emergence of rise time in fluorescence decay of rhodamine B confirms the energy transfer from Ni:PNC table A 4.3. However, there is no rise time noticed for the Ni:Co:PNC−RhB pair even at a 10 µM concentration of rhodamine B (Figure 4.5 F table A 4.4).

To further substantiate the light-harvesting abilities of the doped Ni:PNC−RhB system, we have investigated their energy transfer dynamics in the thin film as well. The concentrations of acceptor RhB have been kept relatively low to avoid the formation of molecular aggregates. The photoluminescence of Ni:PNC drops dramatically even at 0.5 µM of rhodamine B. Thereafter, it follows a common trend observed for energy transfer decrease in Ni:PNC emission with concurrent increase in RhB emission (Figure 4.6 A). TRPL decay of Ni:PNC−RhB in thin films at 512 nm (λ_{exc} = 405 nm) with gradual addition of acceptor (to 1.0 µM) becomes faster (Figure 4.6 B table A 4.7). The rise time in fluorescence decay of RhB again bolsters the efficient energy transfer from Ni:PNC (Figure 4.6 C table A 4.8). The rate of energy transfer in the thin film is much faster than that in solution (Table 4.1). It therefore suggests that rhodamine B resides in close proximity to Ni:PNC in thin films owing to the arrested diffusion.
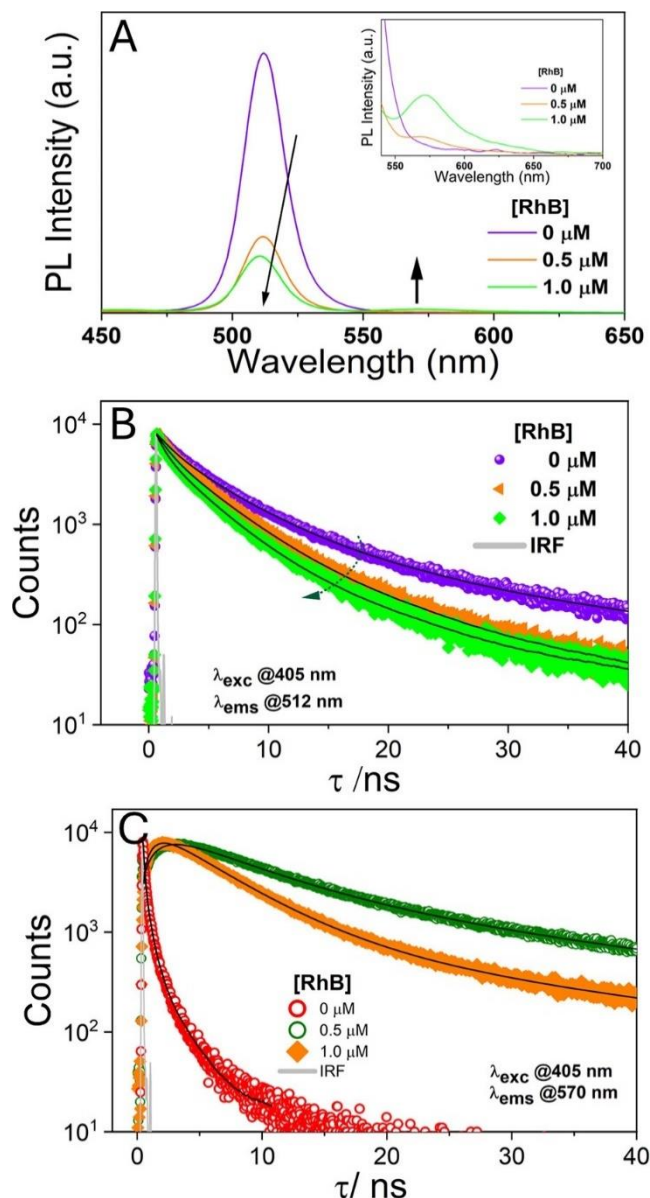
Figure 4.6 [A] Photoluminescence spectra of Ni:PNC in the presence of RhB in thin films. Inset: Concomitant increase in fluorescence of RhB. **[B]** Time-resolved photoluminescence decays at λems = 512 nm at varied concentrations of rhodamine B in thin films. **[C]** Timeresolved photoluminescence decays of the acceptor, RhB (λems = 570 nm), at its two different concentrations in thin films for the Ni:PNC− RhB pair. Time-resolved photoluminescence decay of the donor, Ni:PNC, at 560 nm in the absence of rhodamine B (red hollow circle).

Table 4.1. Efficiency of Energy Transfer and Associated Parameters for Different Donor-Acceptor Pairs[a].

	Donor	[RhB] (μM)	PLQY (Donor)	$<\tau_D>$ (ns)	J(λ) (M^{-1}cm^{-1}nm^4)	τ_A^{rise} (ns)	k_{FRET} (10^9 s^{-1})	R_0 (Å)	R_{DA} (Å)	E_{FRET} (%)
Toluene	Ni:PNC	2	0.32	4.68	2.10	0.90	1.11	30.49	20.19	**84**
		10				0.31	3.22		15.47	**94**
	Co:PNC	10	0.44	2.57	2.09	0.75	1.33	31.89	23.45	**77**
	Ni:Co:PNC	10	0.62	5.47	1.92	–	0.05[b]	33.53	46.36	**21**
Thin film	Ni:PNC	0.5	—	5.05	1.87	1.48	0.67	—	—	—
		1.0	—	5.05		0.93	1.07	—	—	—

$a_{k_{FRET}} = \dfrac{1}{\tau_A^{rise}}$ for the D–A pair with the appearance of rise time.

$b_{k'_{FRET}} = \left(\dfrac{1}{\tau_{DA}} - \dfrac{1}{\tau_D}\right)$ for the D–A pair with nonappearance of rise time.

Resonance energy transfer (RET) involves a nonradiative energy transfer from an electronic excited state of a donor molecule (D*) to the ground state of an acceptor molecule.[264,312] The Förster theory for energy transfer processes assumes dipole−dipole interactions and predicts that the rate of RET follows a $1/R^6$-type distance dependence, where R is the center-to-center distance between D and A. However, a significant deviation from the $1/R^6$ dependence is observed for donor−acceptor systems with increased asphericity. Bagchi and co-workers have formulated that the rate of RET follows $1/R^4$ dependence for nanoparticle−fluorophore systems.[313,314] To quantify the energy transfer for M:PNC−rhodamine systems, the rise time of the acceptor is being exploited. The excited state concentration of the acceptor, *A*(t)*, generated via FRET, is proportional to the time-resolved fluorescence intensity of the donor $I_{DA}(t)$ in the presence of the acceptor. Moreover, this donor−acceptor system is relatively homogeneous with no excluded volume. Considering the cubic and elongated dodecahedron structures for doped-PNCs, we have quantified the rate of

energy transfer and efficiency of energy transfer (E_{FRET}) by using formalism of $1/R^4$ dependence for FRET.

$$k_{FRET} = \frac{1}{\tau_A{}^{rise}} = \frac{1}{\tau_D} \left(\frac{R_0}{R_{DA}} \right)^4 \qquad (4.1)$$

for the D–A pair with the acceptor rise time.

$$k'_{FRET} = \left(\frac{1}{\tau_{DA}} - \frac{1}{\tau_D} \right) = \frac{1}{\tau_D} \left(\frac{R_0}{R_{DA}} \right)^4 \qquad (4.2)$$

for the D–A pair without acceptor rise time.

$$E_{FRET} = \left(\frac{R_0^4}{R_0^4 + R_{DA}^4} \right) \qquad (4.3)$$

Where $\tau_A{}^{rise}$ is the rise-time component of acceptor, τ_{DA} is the donor's lifetime with acceptor, τ_D is the donor's lifetime (without acceptor), R_0 is the Förster distance, and R_{DA} is the D−A distance.
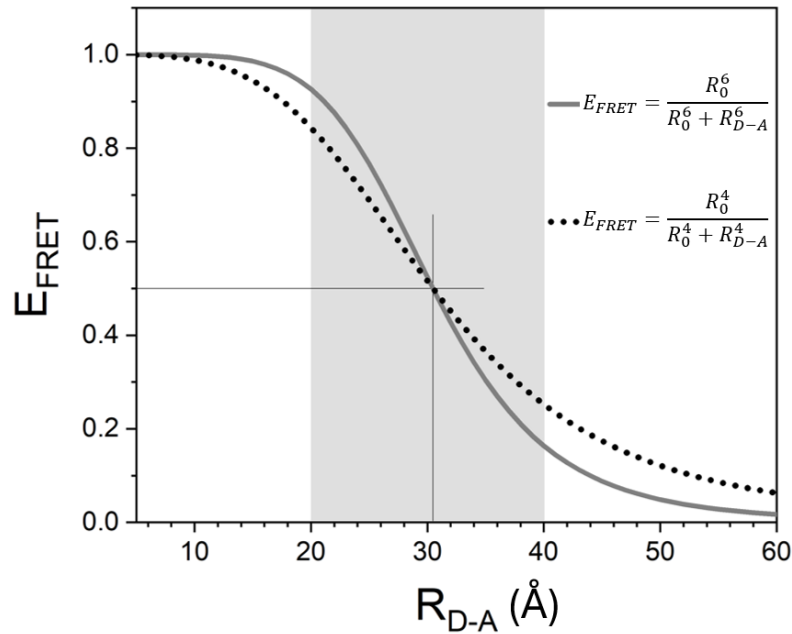
Figure 4.7: Dependence of efficiency of energy transfer (E_{FRET}) on distance between donor and acceptor, $R_{D\text{-}A}$

Table 4.1 summarizes all the quintessential parameters associated with FRET efficiency, E_{FRET}. FRET efficiency for Ni:PNC–RhB pair is estimated to be 94% (equation 4.3)

whereas that for Ni:Co:PNC–RhB pair remains just 21%. And FRET efficiency is found to be greatly influenced by the distance between donor and acceptor, R_{DA}. The rate of energy transfer of D–A pair is inversely related with photoluminescence quantum yield of donor. Moreover, the spectral overlap integral, $J (\lambda)$ is hardly impacting either k_{FRET} .or k'_{FRET} (Table 4.1).

It therefore raises a very pertinent question: what is the reason for variation of R_{DA}? Hence, to provide a rationale, we have performed binding studies of rhodamine B with metal-doped PNCs. Double-reciprocal plots have been constructed to measure the apparent association constants (K_{app}) of rhodamine B with metal-doped PNCs (figure A 4.10). The estimated K_{app} value for Ni:PNC−RhB pair is relatively high, 10.2×10^5 M^{-1}, whereas that for the Ni:Co:PNC−RhB pair, it is quite low, 0.38×10^5 M^{-1}. It therefore suggests preferential binding interactions of rhodamine B with metal-doped PNCs. Moreover, Figure 4.8 highlights the pivotal role of the association constant (K_{app}) in regulating the energy transfer dynamics of M:PNC−RhB pairs.

Such a huge variation in the binding constant cannot be obtained without either compositional variation of crystal facets or preferential interaction of oleylamine/oleic acid with facets. The basis of this hypothesis stems from the recent observation that cyclohexamine gets preferentially absorbed at the {111} facet of the FaPbI$_3$ perovskite.[283] However, accurate quantification of surface composition or stoichiometry of facets {100} and {111} is quite difficult; thereby, we have analyzed structural features through Rietveld refinement. Hence, facet {100} offers a conducive chemical environment for rhodamine B due to the presence of a number of cesium ions and thus fosters dipole−dipole interaction such as FRET.[283,304] However, the presence of Pb(II) in facet {111} enforces specific adhesion with oleyamine due to the chelation/metal−ligand type of interactions and hence blocks the access of rhodamine B to the Ni:Co:PNC nanocrystal.[315,316] To support this hypothesis, we have recorded FTIR spectra of RhB to resolveits mode of interaction with M:PNC systems.
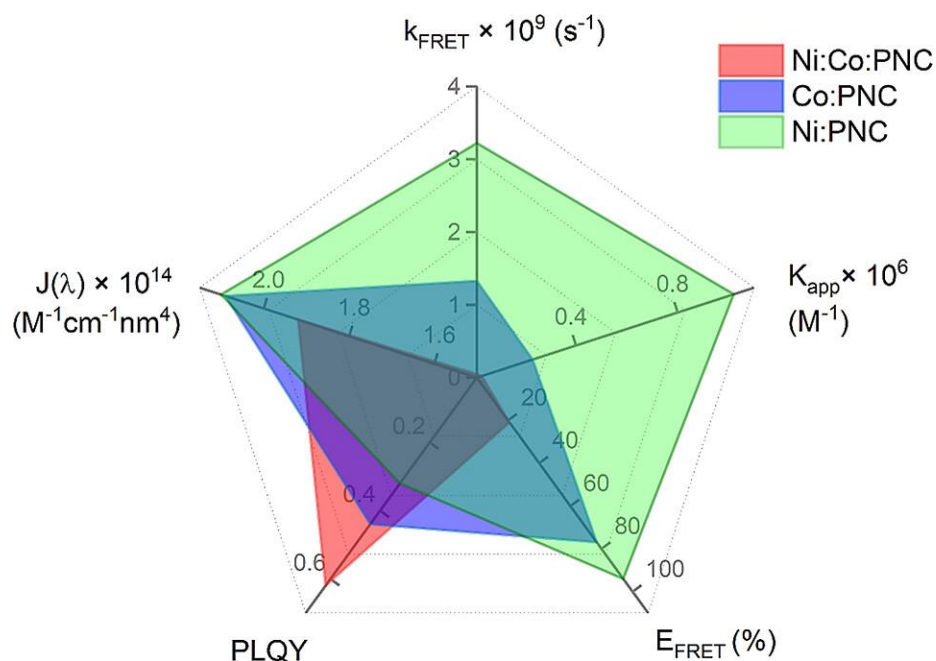
Figure 4.8: A radar plot highlighting dependence of rate of energy transfer, k_{FRET} and efficiency of energy transfer, E_{FRET} on spectral overlap integral, $J(\lambda)$, PLQY and apparent binding constant ($Kapp$) for M:PNC-RhB pairs.

The FTIR spectrum of rhodamine B (Figure 4.9) shows a broad peak in the $3700-3100$ cm^{-1} region, which can be ascribed to the $-$OH stretching of the carboxylic group and a strong band at 1660 cm^{-1} is ascribed to the C=O stretching of the carboxylic group. The FTIR spectrum of the Ni:Co:PNC$-$RhB system follows a more or less similar trend. In addition to that, a strong alkyl C$-$H stretching in the $2700-3000$ cm^{-1} region is clearly visible, indicating the presence of oleic acid and oleyamine. However, the FTIR spectrum of the Ni:PNC$-$RhB system exhibits a drastic decrease in the intensity of characteristic $-$OH stretching of the carboxylic group.
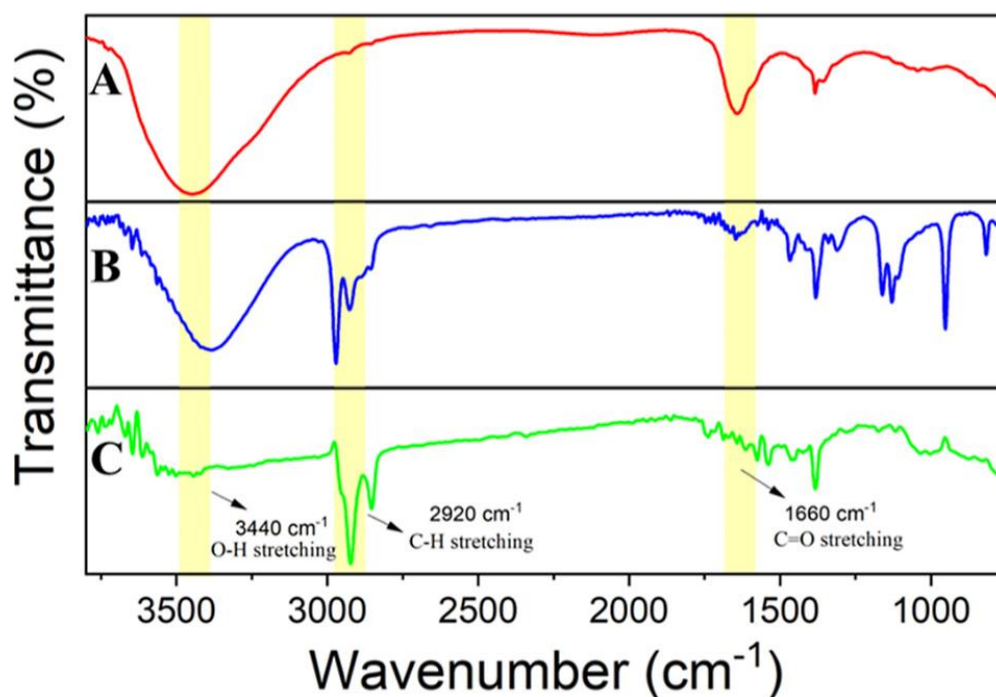
Figure 4.9: Fourier transform infrared (FTIR) spectra of **[A]** rhodamine B (red line), **[B]** Ni:Co:PNC–RhB (blue line), and **[C]** Ni:PNC–RhB (green line).

This can be attributed to the anchoring of rhodamine B to the cations at the NC surface via the carboxylate group. Strong evidence of the attachment of rhodamine B to the M:PNC surface is the disappearance of the band ascribed to the C=O stretching of the carboxylic group.

4.3 Conclusions:

We have demonstrated facet-engineering of CsPbBr$_3$ perovskite nanocrystals with doping of trace amounts of nickel(II) and cobalt(II) ions. Ni:PNC retains regular cubic structure, whereas Ni:Co:PNC evolves into an irregular dodecahedron structure. Doping of nickel ions in the CsPBBr$_3$ crystal lattice leads to crystal stiffening for Ni:PNC, while it distorts the crystal structure of Ni:Co:PNC via repositioning of atoms in the lattice. The ambient stability and photoluminescence property get significantly augmented for Ni:Co:PNC in comparison to those of Ni:PNC. We have identified that the mode of energy transfer remains Förster resonance energy transfer. Ni:PNC dominated with facet {100} records an impressive FRET

efficiency for rhodamine B, whereas Ni:Co:PNC dominated with facet {111} shows very poor efficiency to the same acceptor. Observation of regular and irregular structures with crystallographic termination and role of surface composition of facet {100} of metal-doped PNCs have been rationalized through structural analysis using Rietveld refinement. The size of metal-doped PNCs hardly plays any role in their energy transfer dynamics with organic fluorophore, RhB.

Chapter 5

Electron Transfer in Ni-Doped CsPbBr$_3$ Nanocrystal–Fluorophore Light Harvester

The design of multifunctional nanostructures capable of coupling energy and electron transfer processes is central to advancing artificial photosynthesis and optoelectronic applications. Herein, we report a comprehensive study on a triadic light-harvesting system consisting of Ni-doped CsPbBr₃ perovskite nanocrystals (Ni:PNCs), Rhodamine B (RhB), and methyl viologen (MV^{+2}), which enables sequential Förster resonance energy transfer (FRET) and photoinduced electron transfer (PET). Ni^{2+} doping enhances the structural rigidity and ethanol tolerance of the Ni:PNC, as confirmed by spectroscopic and morphological analyses. Efficient energy transfer from Ni:PNC to RhB is demonstrated through photoluminescence quenching and time-resolved lifetime analysis, with energy transfer efficiency reaching ~88%. Competitive binding experiments and Stern–Volmer analysis reveal preferential association of MV^{+2} over RhB at the nanocrystal surface, significantly influencing charge transfer geometry. Femtosecond transient absorption spectroscopy provides kinetic evidence for ultrafast electron transfer from the photoexcited PNC–fluorophore complex to MV^{+2}, leading to the formation of MV$^{+}\bullet$ radical species. The incorporation of RhB is shown to modulate both the rate and spatial dynamics of charge separation, suggesting a protective role at the nanocrystal interface. These findings offer new mechanistic insights into energy-transfer-coupled electron transfer (ECET) and establish Ni:PNC-based assemblies as a versatile platform for solar-to-chemical energy conversion.

5.1 Introduction:

Outstanding attributes of Cesium lead bromide, CsPbBr₃ perovskite nanocrystals (PNC) such as high absorption coefficients, defect tolerance and high photoluminescence quantum yields make them promising nanomaterials in the field of light-harvesting and photocatalysis.[199,304,317] Their abilities to participate in Resonance Energy Transfer (RET) and photoinduced electron transfer (PET) reactions further fuel to construct multicomponent donor–acceptor assemblies, especially in hybrid systems involving organic fluorophores and redox-active species for designing artificial photosynthetic systems.[318–322]

The mechanism of Energy transfer, particularly Förster Resonance Energy Transfer (FRET) has been investigated in detail. Fluorophores such as Rhodamine B, Coumarin derivatives, and BODIPY derivatives and Nile Red have been integrated with PNCs to form hybrid nanostructures for energy harvesting studies.[57,323,324] These organic dyes can relay intermediate

energy and charge transfer. The basis of this donor-acceptor selection stems from the observation of photocurrent generation by organic dyes. Moreover, recent studies on Förster Resonance Energy Transfer (FRET) between pristine cesium lead bromide perovskite and organic fluorophores indicate that singlet energy transfer efficiency is dictated by- (i) donor-acceptor distance, (ii) binding constant of acceptor with nanocrystal's surface, and (iii) overlap integral, J(λ).[57,317] These hybrid assemblies offer a unique platform to investigate exciton dynamics and enhance emission characteristics of the acceptor dyes, which is particularly useful in solar cell applications.[325,326]
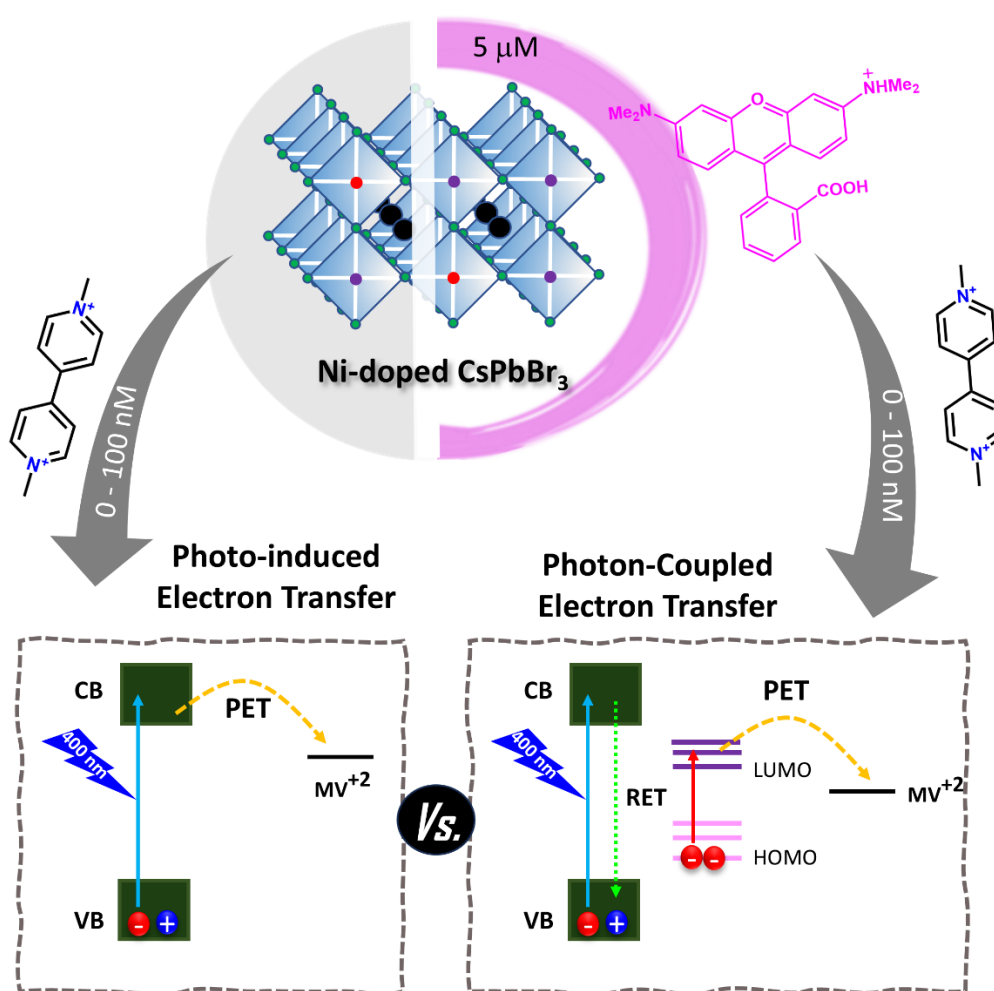
Scheme-5.1: Highlighting the scope of our work in metal-doped Cesium lead halide for deciphering energy transfer coupled electron transfer dynamics.

Methyl viologen (MV^{+2}), a well-known electron acceptor with a low reduction potential and stable radical cation form ($MV^{+\bullet}$), has been widely used as a redox probe to study photoinduced charge transfer reactions in semiconductor–molecule assemblies.[327–331] Photoinduced Electron transfer between PNCs and MV^{+2} serves as a model system for investigating directional electron transfer and charge separation dynamics. When photoexcited PNCs are brought into contact with MV^{+2}, electron transfer from the conduction band of the PNCs to MV^{+2} becomes thermodynamically favorable, leading to the formation of the reduced $MV^{+\bullet}$ species.[213,331,332] However, the PET for a metal-doped PNC, such Ni:PNC remains unexplored.

In a PNC–fluorophore– MV^{+2} triad, electron transfer can proceed through either sequential energy transfer from PNC to the fluorophore, followed by electron transfer to MV^{+2} or direct electron transfer from the photoexcited PNC to MV^{+2} depending on energetics (Scheme 5.1). Alejandro et al. demonstrated $CsPbBr_3$ NCs functionalized with BODIPY dyes show ~82% FRET while also exhibiting charge-mediated triplet energy transfer (TET) leading to charge-separated states.[324] Likewise, Sławski et al. investigated Competition between Photoinduced Electron Transfer and Resonance Energy Transfer in an Example of Substituted Cytochrome c-Quantum Dot Systems.[333] Herein the photoinduced electron transfer dynamics in a Ni:PNC– RhB– MV^{+2} triad system has been explored. We unravel the mechanism of electron transfer and the role of the fluorophore in modulating the charge transfer pathway using steady-state and time-resolved emission studies, and transient absorption measurements.

5.2 Results & discussion:

5.2.1 Ethanol Tolerance of Ni:PNC:

Synthesized pristine $CsPbBr_3$ (PNC) and Nickel-doped $CsPbBr_3$ perovskite nanocrystal (Ni:PNC) exhibit cubic phase, with an average edge length of 10.2 ±1.9 nm for PNC and 8.1 ±1.4 nm for Ni:PNC (Figure 5.1, Figure A5.1 & A5.4). The dose of metal dopant in $CsPbBr_3$ is about 2.5%. Deciphering the role of dopant metal ion in electron transfer dynamics of a triad, energy donor (Ni:PNC)—energy acceptor (RhB) —electron acceptor (MV^{+2}) is the subject of investigation here. Considering the solubility/dispersibility of individual components in solvents, we have identified a ternary solvent system, toluene—acetonitrile—ethanol for stabilizing for this triad system, Ni:PNC—RhB— MV^{+2}. Stability of PNCs in solvent becomes a bottleneck in understanding the optical dynamics of PNCs in wide range of solvent. Since PNCs are prone to degradation in ethanol, hence we have first investigated the ethanol tolerance of Ni:PNC (Figure 5.1C-D). The volume percentage of ethanol has been varied from 0 – 0.024 in a binary solvent of acetonitrile and ethanol.

A comparative stability study reveals improved ethanol tolerance of Ni:PNC over pristine PNC. This enhanced stability can be attributed to lattice contraction induced by the incorporation of Ni^{+2} ions, leading to reduction of surface defects and enhancement of the structural integrity of the nanocrystals.[308,334] The structural rigidity of Ni:PNC thus provides a protective shield for augmenting its ethanol tolerance.
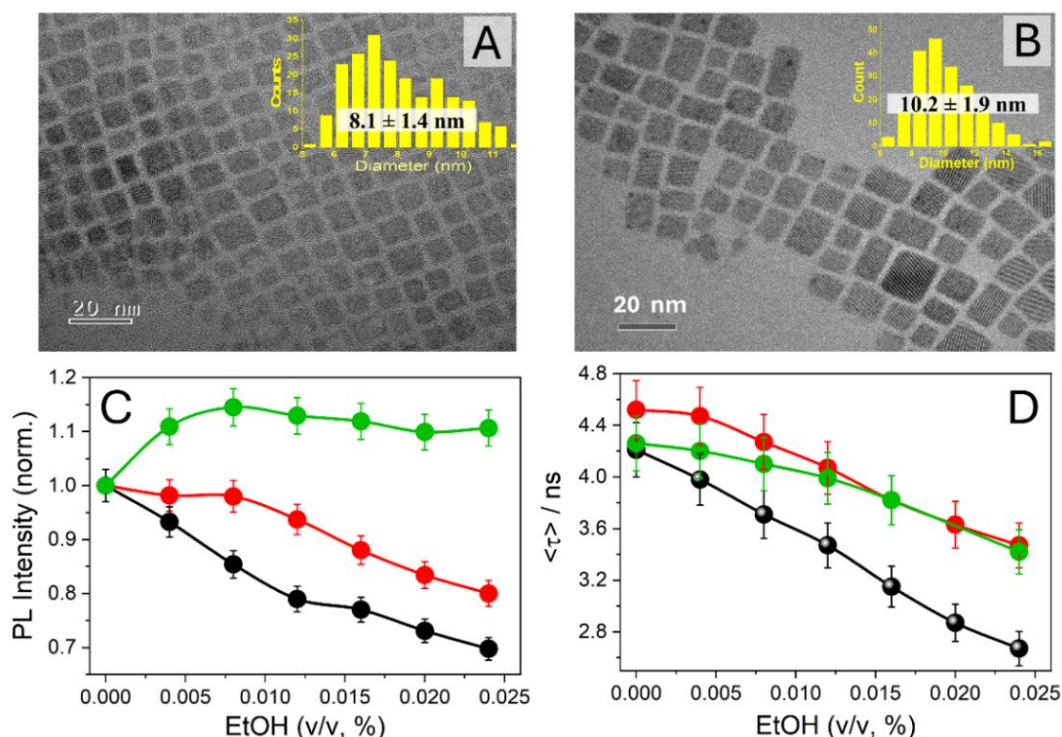
Figure 5.1: HRTEM image of— **[A]** pristine PNC, and **[B]** Ni:PNC. *Inset:* size distribution of synthesized perovskite nanocrystals. [C] Photoluminescence intensity of—pristine PNC (red circle), Ni:PNC (black circle), Ni:PNC-RhB (green circle) [D] TRPL decay profile of Ni:PNC (red circle), pristine PNC (black circle) and Ni:PNC-RhB (green circle) at varied volume percentage of ethanol in acetonitrile.

To build this triad in solution phase, we have first preassembled light-harvester, Ni:PNC–RhB complex. The concentration of RhB has been deliberately kept in micromolar range, 5 μM, whereas that of Ni:PNC in nanomolar range, 32 nM for saturating surface of perovskite nanocrystals in toluene. Moreover, our previous studies suggest that energy transfer efficiency for this concentration range is relatively very high, 94%.[334] Since the stability of this nanocrystal-fluorophore complex is pivotal in unearthing its electron transfer to an acceptor, MV^{+2}, thus we have resolved the modulation of PL dynamics by gradually added binary solvent mixture of acetonitrile-ethanol in toluene. Surprisingly the PL intensity of Ni:PNC—RhB at 510 nm exhibits an increasing trend (Figure 5.1C-D & 5.2). The emission of fluorophore presents in Ni:PNC—RhB monitored at 585 nm follows a generic decreasing trend with

increase in ethanol concentration in ternary solvent (Figure 5.2C). Time-resolved

photoluminescence (TRPL) decays of Ni:PNC—RhB in ternary solvent can be best fitted by

triexponential functions (Table A5.1). Characteristic rise-time component of energy acceptor

in Ni:PNC—RhB complex has been noticed confirming involvement of energy transfer from

Ni:PNC. However, average lifetime of energy donor in Ni:PNC—RhB complex follows the

similar trend as observed for Ni:PNC alone (Figure 5.1D, A5.3).
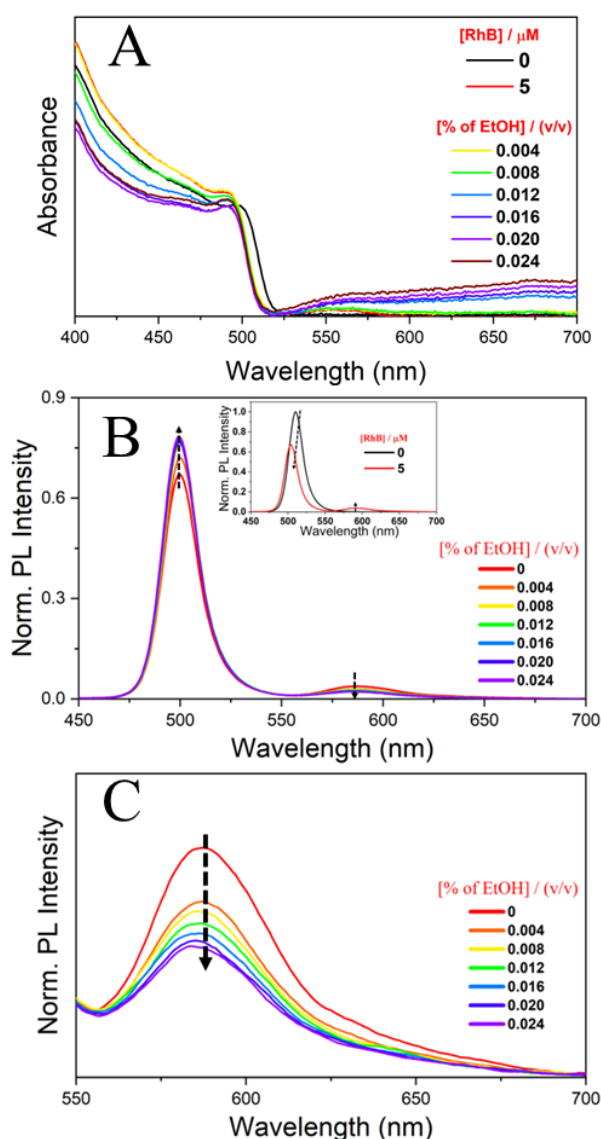
Figure 5.2: Stability of Ni:PNC on gradual addition of EtOH **[A]** Absorbance spectra, **[B]** Photoluminescence spectra of Ni:PNC (510 nm) and Rhodamine B (585 nm). Inset: showing the PL spectra of Ni:PNC (black line) and after addition of 5 μM of RhB (red line). **[C]** Zoomed in PL spectra of Rhodamine B at 585 nm on gradual addition of EtOH.

Contrasting trends observed between photoluminescence intensity and lifetime of Ni:PNC—

RhB complex is often indicative of ground state dynamics—ethanol-induced perturbation of

bound-free equilibrium of RhB in ternary solvents by populating free RhB in solution. This

hypothesis has been elucidated here by reversing the addition of donor and acceptor in solution.

In a typical experiment, the concentration of RhB has been kept fixed (5 μM) in toluene while

the concentration of Ni:PNC is varied (Figure 5.3). The photoluminescence of free RhB is

monitored by keeping the excitation wavelength at 530 nm.
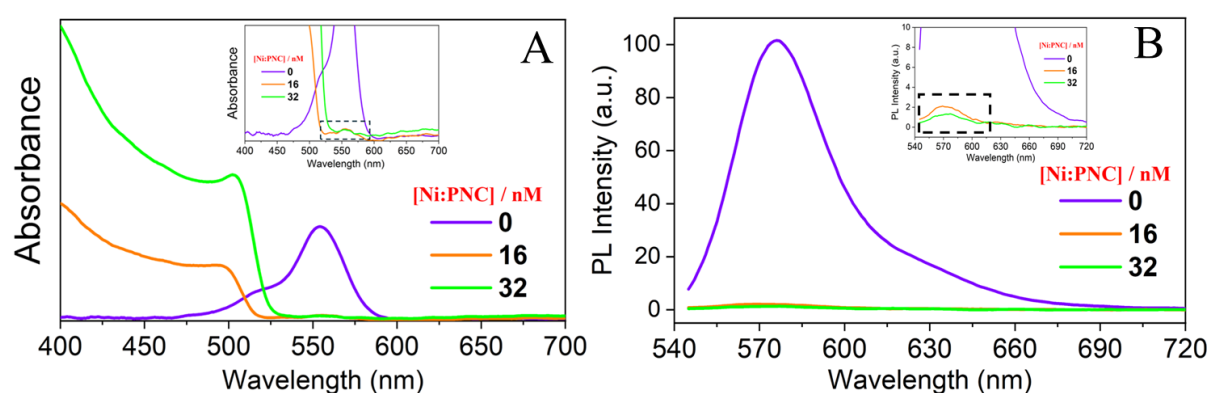
Figure 5.3: [A] Absorbance spectra of Rhodamine B after gradual addition of Ni:PNC (up to
32 nm), **[B]** Photoluminescence spectra of Rhodamine B (λ_{exc}=530 nm) on addition of Ni:PNC,
Inset: showing the zoomed in PL spectra at 585 nm.

Rhodamine B in toluene displays its characteristic absorption (553 nm) and relatively high

fluorescence with a peak centered at 580 nm. However, upon addition of just 16 nM of Ni:PNC

the absorbance and fluorescence (Figure 5.3A-B) of RhB get dramatically dropped indicating

its strong interaction with nano-surface. Upon further increase of Ni:PNC concentration, the

spectral features of RhB remain almost unaltered. It therefore suggests that RhB remains in

bound state. The increasing trend of photoluminescence intensity of donor in Ni:PNC—RhB

complex may thus be attributed to repositioning of RhB around nanosurface in ternary solvent.

5.2.2 Photoluminescence Quenching of Ni:PNC–RhB in presence of an Electron Acceptor, MV^{+2}:

It is expected that competitive binding is bound to take place between energy acceptor, RhB and electron acceptor, MV^{+2} in solution. Binding constant of analyte with PNC plays a decisive role on its accessibility to nano-surface. The apparent association constant (k_{app}) of methyl viologen (MV^{+2}) with CsPbBr$_3$ nanocrystals is on the order of 10^6, which is significantly higher than that of RhB, which is in the order of 10^5 (Figure A5.7).
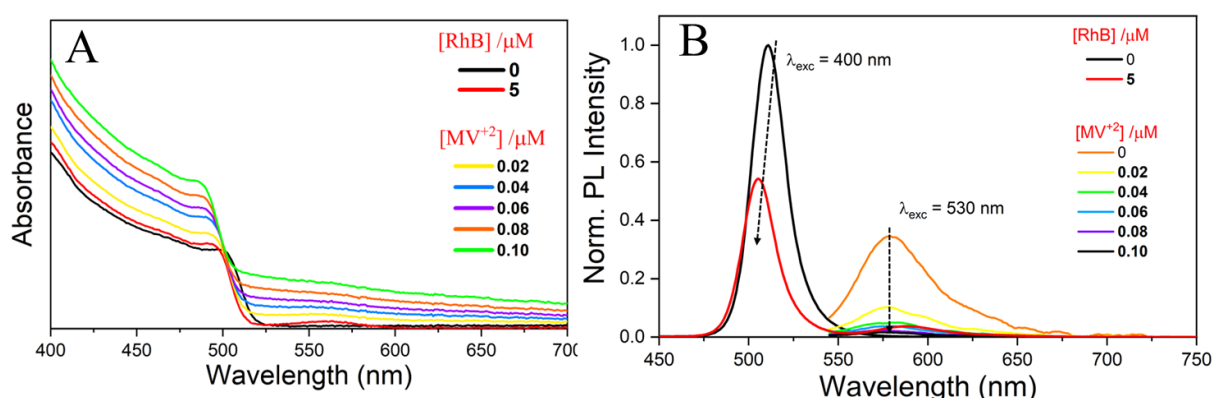
Figure 5.4: [A] Absorbance spectra of Ni:PNC_RhB complex on successive addition of MV^{+2}. **[B]** Photoluminescence spectra of Ni:PNC_RhB complex excited at 530 nm to investigate the detachment process of RhB from the nanocrystal surface after progressive addition of MV^{+2}

It can be hypothesized that preferential binding of MV^{+2} will increase the population of free RhB and its fluorescence will gradually increase upon titration with MV^{2+}. To resolve the issue on preferential binding MV^{+2} over RhB to the Ni:PNC, the emission of RhB has been probed. In contrary, addition of MV^{+2} does not result in an increase in fluorescence of RhB, rather a rapid decline has been noticed (Figure 5.4B). These findings indicate that RhB molecules remain firmly bound to the nanocrystal surface and do not get displaced by the MV^{+2}.

Secondly, we have investigated the efficacy of RhB in electron transfer to MV^{+2} as it is essential for elucidating the electron transfer dynamics of triad, Ni:PNC—RhB—MV^{+2}. To probe this interaction, MV^{+2} has been gradually introduced to a solution of RhB (5 µM) in

toluene in the absence of Ni:PNC. As shown in Figures A5.5, the addition of merely 0.04 μM

MV^{+2} led to complete quenching of RhB fluorescence (K_D = 156.47 μM^{-1}). Additionally, the

average fluorescence lifetime of RhB is decreased from 3.1 ns to 1.1 ns (Table A5.2). Upon

addition of MV^{+2}, an ultrafast component continues to surge, perhaps originating from the

formation of RhB– MV^{+2} ion pair. This result clearly suggests that electron transfer from RhB

to MV^{+2} occurs at ultrafast timescale.

Energy transfer-coupled with electron transfer remains the cornerstone of natural

photosynthetic system.[335–337] Moreover, the photocatalytic activity of PNC is guided by the

efficient extraction of electron from conduction band. Hence, the dynamics of electron transfer

from PNC–fluorophore assembly to MV^{+2} has been investigated in detail. First, Ni:PNC–RhB

light harvester has been assembled in toluene by keeping the donor concentration at 32 nM and

acceptor concentration at 5μM. The process of energy-coupled electron transfer (ECET) has

been investigated by gradual addition of MV^{+2} (0-0.12 μM) in Ni:PNC–RhB solution.

Photoluminescence of Ni:PNC and fluorescence of RhB have been gauged to resolve the

intricacies of ECET dynamics.

Singlet energy transfer from Ni:PNC to RhB takes place because of the significant overlap

between the acceptor absorbance and the donor's emission.[57] The energy transfer results in a

concurrent emission of acceptor at 585 nm in photoluminescence spectra (Figure 5.5A) and

emergence of a rise time in acceptor TRPL decay (Table A5.3). The energy transfer efficiency

is measured to be 88%. The emission of donor, Ni:PNC and acceptor, RhB get gradually

quenched upon addition of MV^{+2} (Figure 5.5A-B). About 88% of the donor's emission and

90% of the acceptor emission has been quenched. The decreasing trend has also been noticed

in excited state properties of Ni:PNC–RhB complex (Figure 5.5C-D). The average emission

lifetime of the Ni:PNC at 510 nm gets reduced by 74% (Table S4) and that of RhB monitored

at 585 nm shows a comparable reduction of about 66% (Table A5.3). Furthermore, it can be

noticed that the rise time component and long component of RhB get gradually diminished whereas a very short component (0.2 ns) has emerged with successive addition of MV^{+2}.
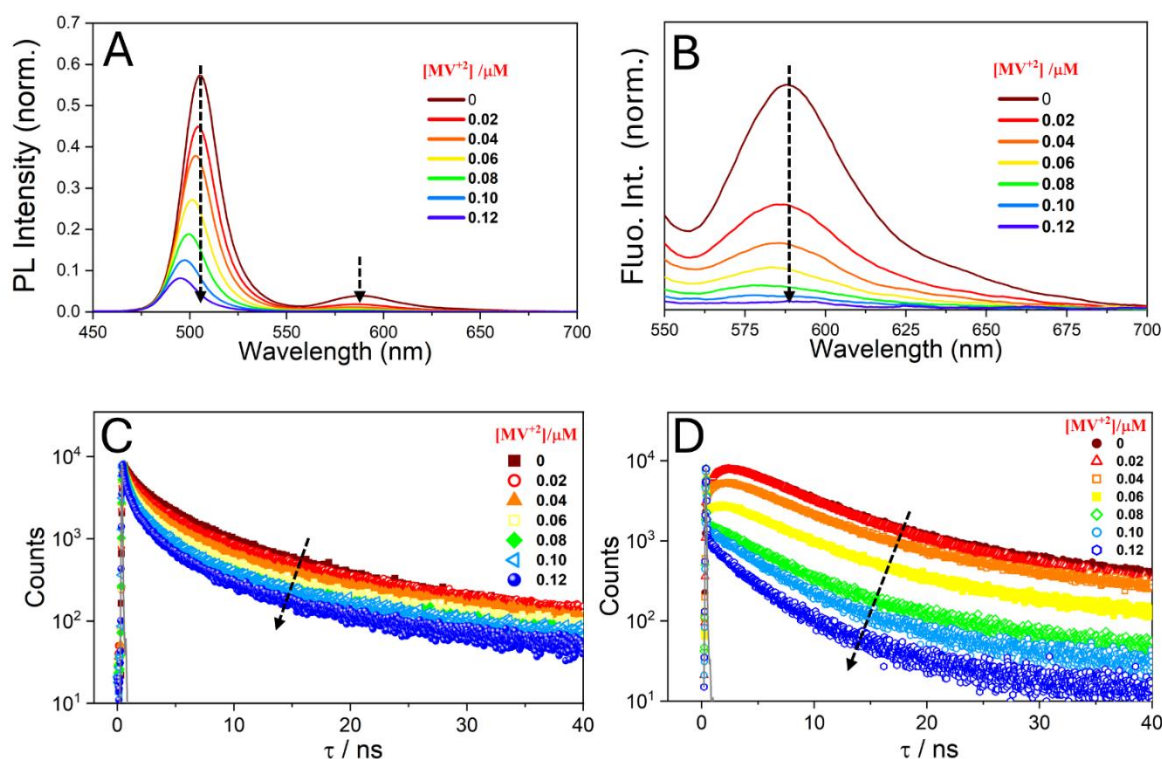
Figure 5.5: Photoluminescence quenching of Donor– **[A]** Ni:PNC and acceptor **[B]** Rhodamine B with successive addition of methyl viologen. Time-resolved photoluminescence decays at λ_{ems} = 510 nm of **[C]** Ni:PNC (donor) **[D]** Time-resolved photoluminescence decays at λ_{ems} = 585 nm of.acceptor RhB on successive addition of methyl viologen.

The relative changes in emission intensity (I_0/I) and emission lifetime (τ_0/τ) of donor and acceptor in Ni:PNC—RhB complex, in the absence (I_0 and τ_0) and presence of MV^{+2} (I and τ) are plotted against the quencher concentration (Figures 5.6). Steady state Stern–Volmer (SV) plots exhibit remarkable nonlinearity, characterized by a positive curvature at higher concentrations of MV^{+2} (Figure 5.6A). We have also constructed Stern–Volmer (SV) plots for photoluminescence quenching of Ni:PNC (without RhB) with gradual addition of MV^{+2}. As expected, photoluminescence quenching of Ni:PNC with MV^{+2} is markedly higher than that of Ni:PNC—RhB complex, suggesting shielding action of RhB. Notably, Stern–Volmer (SV) plot

of Ni:PNC in ternary solvent (without RhB and MV^{+2}) clearly indicates its good colloidal stability. The observed nonlinear (exponential) behaviour of donor, Ni:PNC can be elucidated within the framework of Perrin formalism (equation 5.1).[264]

$$\frac{I_0}{I} = e^{\frac{(Q \times V \times N)}{1000}}$$ (eqn. 5.1)

where V is the volume of sphere, Q is the quencher constant, N is the Avogadro's number. I_0 and I are the PL intensity of donor in absence and in presence of quencher, respectively. Stern-Volmer quenching constant, K_D for the dual "static and dynamic" fluorescence quenching has also been calculated by using equation 5.2.

$$\frac{\tau_0}{\tau} = 1 + k_q \tau_0 [Q] = 1 + K_D [Q]$$ (eqn. 5.2)

τ_0 and τ are the average lifetime of donor in absence and in presence of quencher respectively, and k_q is the dynamic quenching constant. The quenching constants and volume of sphere have been summarized in Table 5.1.

The Steady state Stern Volmer plot for acceptor, RhB is suggestive of two distinct quenching mechanisms, depending upon the concentration range of MV^{+2} (Figure 5.6B). However, time resolved Stern Volmer plots at 510 nm for Ni:PNC—RhB complex and Ni:PNC exhibit a commonly observed linear trend with quencher concentrations (Figure 5.6C). The dynamic quenching constant, k_q at 510 nm for Ni:PNC—RhB complex remains relatively lower than that for Ni:PNC (Table 5.1). On the other hand, the dynamic quenching constant, k_q at 585 nm for Ni:PNC—RhB complex is about 2 times lower than that at 510 nm.
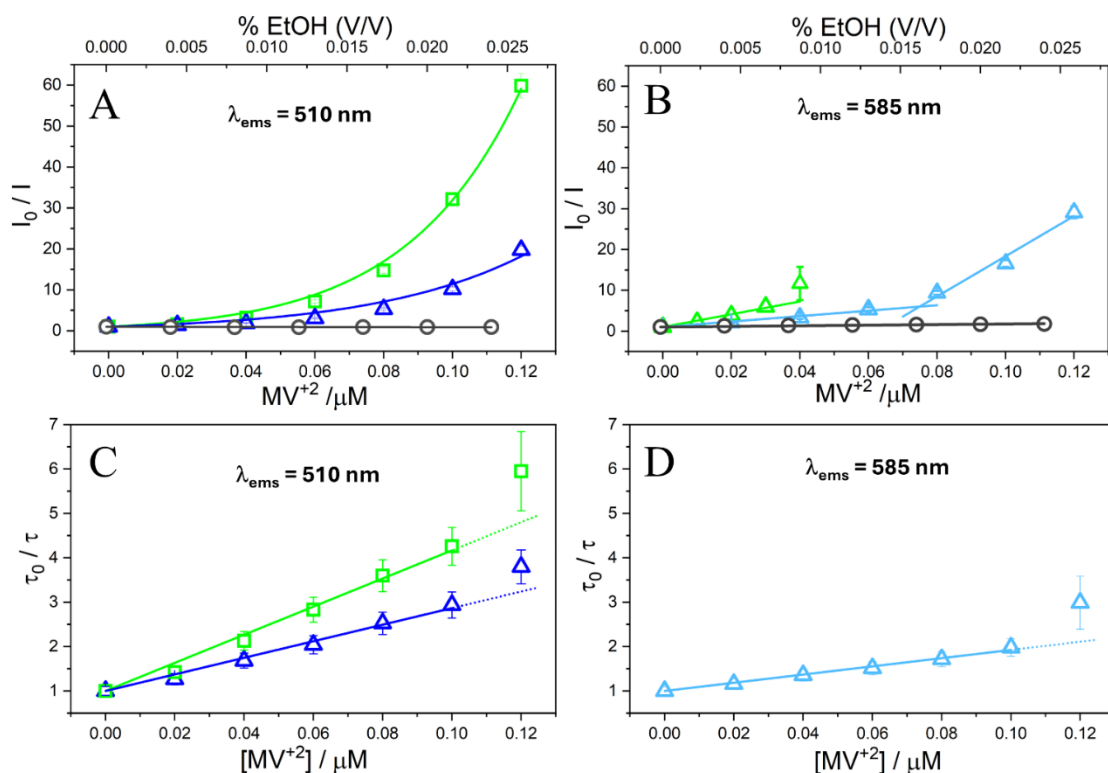
Figure 5.6: [A] Steady state Stern-Volmer quenching kinetics of Ni:PNC on graduall addition of MV^{+2} (green square), quenching kinetics of preassembled Ni:PNC-RhB on successive addition of MV^{+2} (deep blue triangle), quenching kinetics of Ni:PNC-RhB on successive addition of EtOH (grey circle). **[B]** Steady state Ster-Volmer quenching kinetics of RhB on graduall addition of MV^{+2} (green triangle), quenching kinetics of RhB at 585 nm in Ni:PNC-RhB on successive addition of MV^{+2} (light blue triangle), quenching kinetics of RhB at 585 nm in Ni:PNC-RhB on successive addition of EtOH (grey circle). **[C]** Time-resolved Stern-Volmer quenching kinetics of Ni:PNC on graduall addition of MV^{+2} (green square), time-resolved quenching kinetics of Ni:PNC-RhB at 510 nm on successive addition of MV^{+2} (deep blue triangle). **[D]** Time-resolved Stern-Volmer quenching kinetics of RhB at 585 nm in Ni:PNC-RhB on successive addition of MV^{+2} (light blue triangle).

According to Perin Formalism, the estimation volume of the quenching sphere (V) is based on the dynamic quenching constant (K_D), obtained from time-resolved photoluminescence measurements of the donor in the presence of the acceptor (eqn 5.2). When MV^{+2} is introduced to interact directly with Ni:PNC, the volume of sphere, V is estimated to be 5.6×10^{-14} cm^3, whereas when MV^{+2} is allowed to interact with Ni:PNC—RhB complex, it is decreased to 4.1×10^{-14} cm^3. This change in the volume of sphere suggests that MV^{+2} is not directly attached to

the Ni:PNC surface in the presence of RhB; instead, it remains in the solution state and interacts from a more distal position, likely at the outer region of the preassembled Ni:PNC–RhB complex. These findings support a change in quenching geometry and accessibility of the nanocrystal surface by MV^{+2} upon RhB incorporation. Moreover, the dual quenching constant, K_D at 510 nm is 18.66 μM^{-1} for Ni:PNC—RhB complex, whereas that for Ni:PNC is 31.67 μM^{-1}. This reduced value of quenching constant for Ni:PNC—RhB complex further implies that RhB resides near nanocrystal surface.

Table 5.1: Values of K_D, k_q and Volume of Sphere (V) obtained from steady state and time resolved experiments.

Sample	λ_{ems} (nm)	τ_0 (ns)	$k_q \times 10^9$ ($\mu M^{-1} s^{-1}$)	K_D (μM^{-1})	Volume of sphere (cm^3)
Ni:PNC–RhB–MV^{+2}	510	4.14	4.50± 0.50	18.66 ± 0.50	4.1×10^{-14}
Ni:PNC–MV^{+2}	510	4.64	6.82± 0.85	31.67 ± 0.85	5.6×10^{-14}
Ni:PNC–RhB–MV^{+2}	585	4.75	1.94± 0.23	9.24± 0.23	
RhB–MV^{+2}	585	–	–	156.47 ±7.7*	–

5.2.3 Resolving Electron Transfer Dynamics of Ni:PNC-RhB-MV^{+2} system:

To investigate the kinetics of charge carrier recombination and charge transfer for Ni:PNC–MV^{+2} and Ni:PNC–RhB–MV^{+2}, we have employed femtosecond pump–probe transient absorption spectroscopy. Excitation has been performed using a 400 nm laser pulse with a FWHM of 75 fs. Both systems exhibit a pronounced excitonic bleach centered at 496 nm (Figure 5.7A-B). Transient absorption spectra for Ni:PNC and Ni:PNC–RhB complex and kinetics of bleach recovery are presented in Figure 5.8.
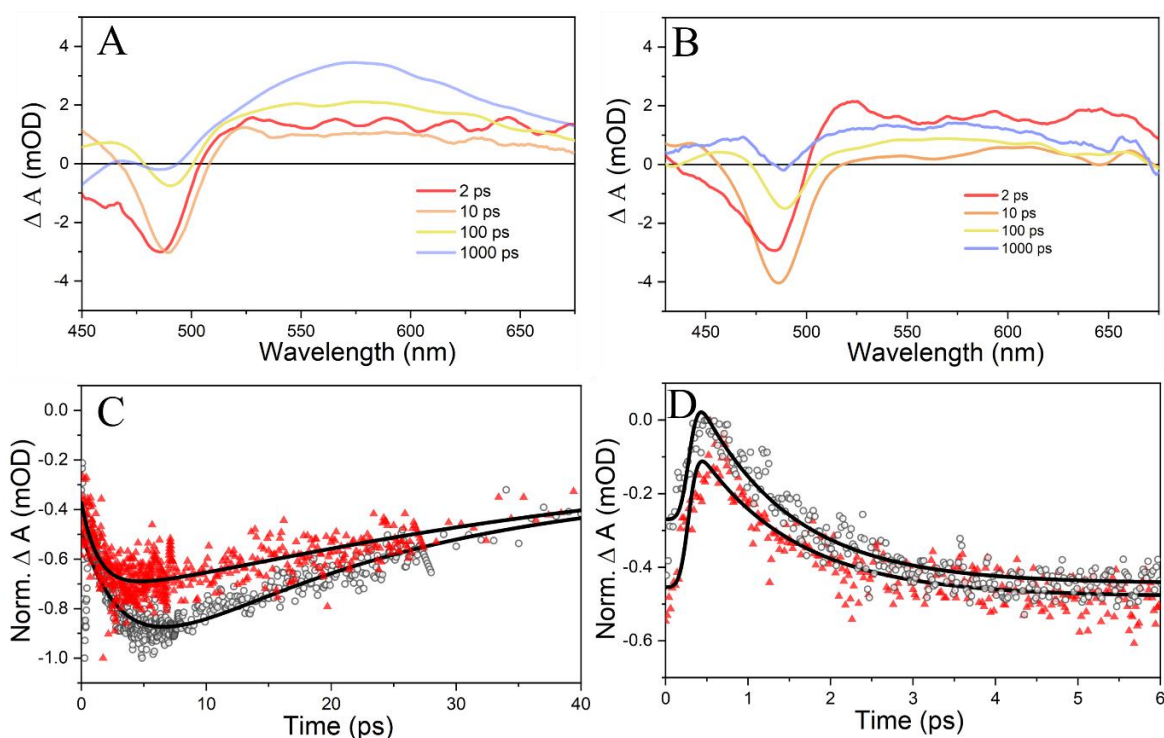
Figure 5.7: Transient absorption spectra recorded after 400 nm laser pulse excitation for **[A]** Ni:PNC with MV^{+2}. **[B]** preassembled Ni:PNC-RhB with MV^{+2}. Comparison of the kinetics of bleach decay probed at 496 nm. **[C]** between Ni:PNC and MV^{+2} (red triangle) and between preassembled Ni:PNC-RhB and MV^{+2} (grey dots). Comparison of the decay kinetics of $MV^{+\bullet}$ radical cation probed at 580 nm **[D]** between Ni:PNC and MV^{+2} (red triangle) and between preassembled Ni:PNC-RhB and MV^{+2} (grey dots).

In the preassembled Ni:PNC–RhB system, the addition of RhB to Ni:PNC facilitates singlet energy transfer from Ni:PNC to RhB, as evident by accelerated bleach recovery at 496 nm. Upon subsequent addition of MV^{+2}, further acceleration in bleach recovery has also been noticed (Figure 5.8 C-D), indicating efficient electron transfer from RhB to MV^{+2}, following initial energy transfer from Ni:PNC to RhB.

The formation of the $MV^{+\bullet}$ radical cation, indicative of successful electron transfer, is confirmed by the appearance of a broad transient absorption feature spanning 550–650 nm (Figures 5.7A and 5.7B).
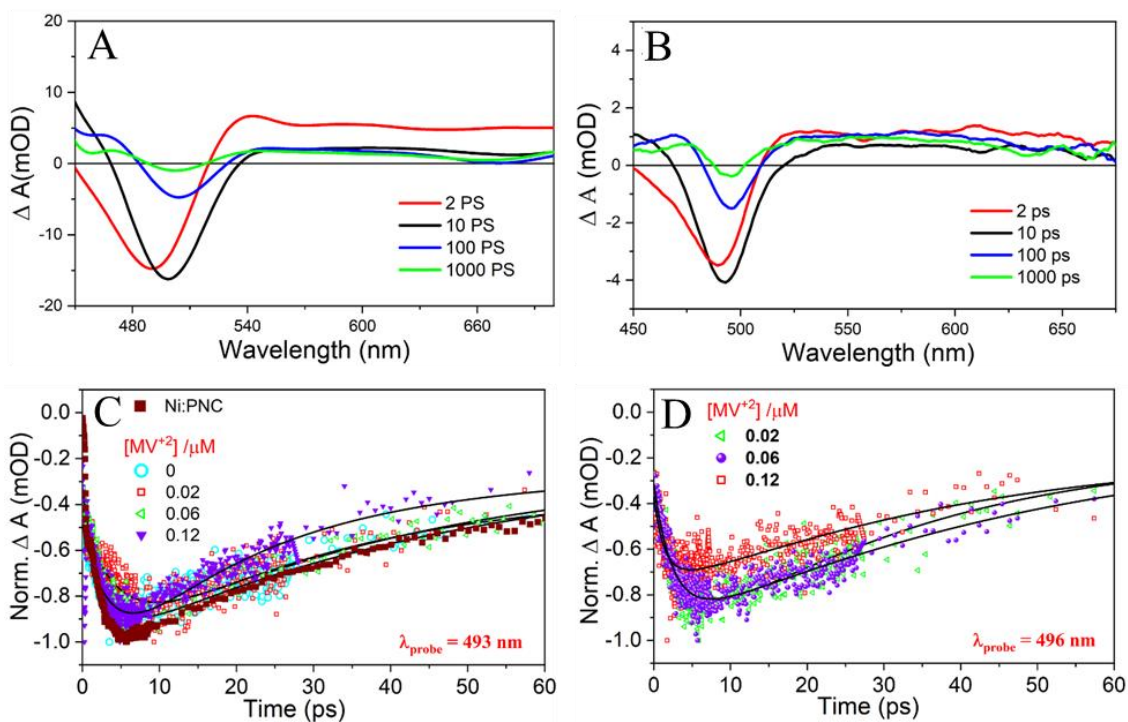
Figure 5.8: Transient difference absorption spectra recorded at 400 nm pulsed laser excitation of Ni:PNC interacting with **[A]** 0 µM RhB **[B]** 5 µM RhB. The concentration of Ni:PNC was fixed at 32 nM. **[C]** Kinetics of the 498 nm bleach decay for Ni:PNC (brown line), after addition of 5 µM RhB (cyan line) monitored at 493 nm, then on gradual addition of MV^{+2} up-to 0.12 µM monitored at 493 nm. **[D]** Kinetics of the 496 nm bleach decay for Ni:PNC after successive addition of MV^{+2} up-to 0.12 µM (without RhB).

Notably, in our case both systems exhibited rapid exciton bleach recovery within 1 ns, which may be attributed to the presence of Ni^{2+}-induced trap states within the bandgap of the perovskite lattice. Prior studies have shown that incorporation of multiple metal cations can introduce structural defects, which can act as recombination centers, thereby facilitating back electron transfer from $MV^{+\bullet}$ to Ni:PNC.[338,339] Based on the maximum bleach and the residual absorbance after 1.0 ns, we have estimated the charge separation efficiency, Φ by using following equation-

$$\Phi = (\Delta A_{(t=1.0\ ns)}/\Delta A_{(t=0)}) \times 100 \qquad \text{(eqn 5.3)}$$

The charge separation efficiency for metal-doped PNC, Ni:PNC is measured to be about 17%, whereas that for Ni:PNC–RhB complex gets reduced to 14%. This indicates that RhB engages

in electron transfer on roughly the same time scale. The decay kinetics (Figure 5.7C-D) are well fitted by bi-exponential fits, and the extracted lifetime parameters are summarized in Table 5.2. The bi-exponential fitting consists of a fast component (τ_1) and a longer component (τ_2). The first component is assigned to shallow trap caused by surface defects, a longer one for electron transfer. Electron transfer rate constants (k_{et}) have been determined using longer component, τ_2 in the presence and absence of the quencher, according to the following equations:

$$k_{et} = \frac{1}{\tau_{2,Ni:PNC-RhB-MV^{+2}}} - \frac{1}{\tau_{2,Ni:PNC-RhB}} \qquad \text{(eqn. 5.4)}$$

$$k_{et} = \frac{1}{\tau_{2,Ni:PNC-MV^{+2}}} - \frac{1}{\tau_{2,Ni:PNC}} \qquad \text{(eqn. 5.5)}$$

A more rapid decay of the bleach signal is observed for the Ni:PNC– MV^{+2} system, yielding a higher electron transfer rate ($k_{et} = 2.1 \times 10^{10}$ s^{-1}), compared to the Ni:PNC–RhB– MV^{+2} system ($k_{et} = 1.7 \times 10^{10}$ s^{-1}).

Table 5.2 Biexponential decay fitting parameters for the transient absorption decay traces of Ni:PNC-RhB and Ni:PNC and electron transfer rate constants (**k_{et}**).

Sample	[MV^{+2}] / μM	τ_1 (a1) /ps	τ_2 (a2) /ps	$<\tau>$ /ps	k_{et} / s^{-1}
Ni:PNC	0	4.47 (0.48)	77.16 (0.52)	42.26	–
Ni:PNC–RhB–MV^{+2}	0	3.84 (0.46)	63.00 (0.54)	35.78	2.9×10^9
	0.02	2.97 (0.47)	57.13 (0.53)	31.67	4.5×10^9
	0.06	2.02 (0.49)	45.62 (0.51)	24.25	8.9×10^9
	0.12	1.18 (0.45)	33.35 (0.55)	18.87	1.7×10^{10}
Ni:PNC–RhB	0.02	2.41(0.48)	56.01 (0.52)	30.28	4.8×10^9
	0.06	2.62 (0.49)	44.72 (0.51)	24.09	9.4×10^9
	0.12	1.51 (0.53)	29.84 (0.47)	14.82	2.1×10^{10}

This reduction in electron transfer rate suggests that RhB modulates the charge transfer pathway. Kinetic traces at 580 nm (Figure 5.7D) revealed that $MV^{+\bullet}$ forms on a sub-picosecond timescale (within 10 ps), followed by partial decay due to recombination with holes localized in mid-gap trap states. A fraction of the charge-separated species persists, governed by the dynamic equilibrium between forward and back electron transfer (Scheme 5.2).
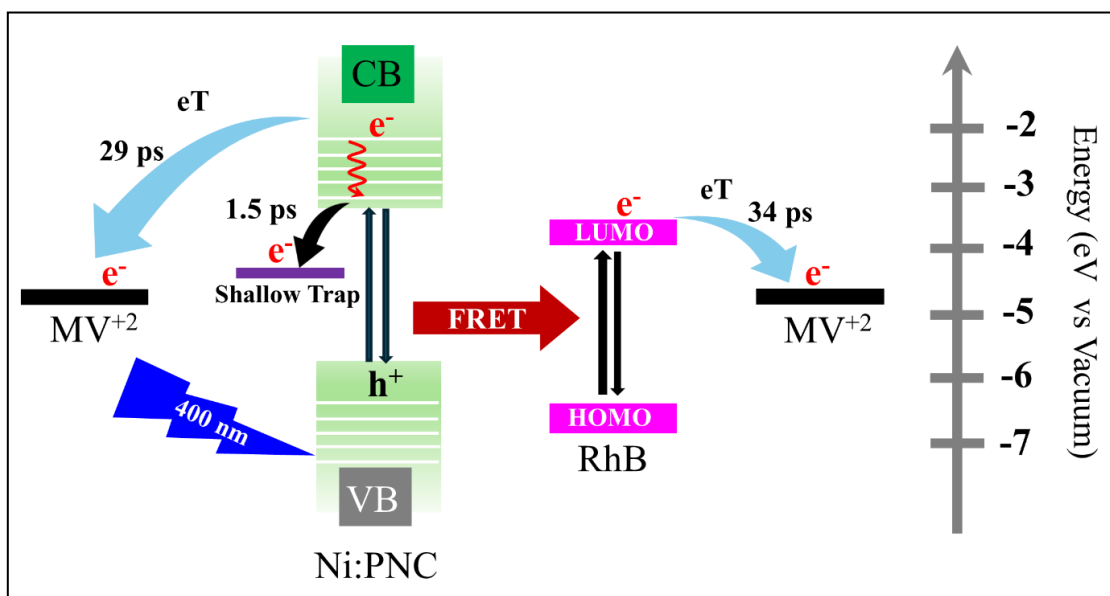
Scheme-5.2: Schematic representation of the energy transfer coupled with electron transfer in the triad, Ni:PNC–RhB–MV^{+2} for the excitation of the donor, Ni:PNC.

5.3 Conclusions:

This study presents a systematic investigation into the photophysical dynamics of a triadic light-harvesting assembly composed of Ni-doped $CsPbBr_3$ perovskite nanocrystals (Ni:PNCs), Rhodamine B (RhB), and methyl viologen (MV^{+2}), elucidating the interplay between resonance energy transfer (RET) and photoinduced electron transfer (PET). The incorporation of Ni^{2+} into the perovskite lattice not only enhances the structural integrity and ethanol tolerance of the nanocrystals but also introduces mid-gap states that modulate charge carrier recombination dynamics. Preassembly of the Ni:PNC–RhB complex facilitates efficient Förster resonance energy transfer (FRET), as evidenced by steady-state and time-resolved photoluminescence studies, while the subsequent introduction of MV^{+2} enables directional electron transfer from

the excited donor–acceptor complex. The competitive interaction between MV^{+2} and RhB highlights the importance of binding affinities in dictating surface accessibility. Femtosecond transient absorption spectroscopy reveals that electron transfer to MV^{+2} occurs on a picosecond timescale, with the presence of RhB modulating the kinetics and spatial distribution of charge-separated states. The observed dual quenching behavior and reduced volume of the quenching sphere in the Ni:PNC–RhB– MV^{+2} system further corroborate the existence of an energy-mediated electron transfer mechanism.

Chapter 6

Summary and Future Scope

6.1. Summary:

Cesium lead halide perovskite nanocrystals ($CsPbX_3$; X = Cl, Br, I) are emerging as leading candidates for optoelectronic applications due to their outstanding photoluminescence, bandgap tunability, and solution-processability. However, their operational instability under ambient conditions continues to limit their practical implementation. Additionally, the influence of specific crystal facets on light-harvesting efficiency and charge transfer dynamics remains inadequately understood. At the same time, emulating natural photosynthesis through artificial light-harvesting assemblies remains an ongoing challenge. The design of perovskite–multi-acceptor systems capable of directional energy or electron transfer, analogous to photosynthetic antenna complexes, is largely unexplored. This thesis aims to address these gaps by developing synthesis, stabilization, and halide exchange properties of cesium lead bromide ($CsPbBr_3$) nanocrystals using a polymer-guided approach with polyvinylidene fluoride (PVDF). We develop a room-temperature, antisolvent-based method that leverages PVDF's hydrophobic nature to direct the formation of nanocrystals, resulting in both orthorhombic Cs_4PbBr_6 and monoclinic $CsPbBr_3$ phases. Encapsulation of these nanocrystals within PVDF significantly influences their optical properties, with a bathochromic shift in emission maxima, indicating structural reorganization. Time-resolved photoluminescence measurements reveal multiple decay components, and importantly, encapsulation enhances the overall PL lifetime, suggesting suppressed non-radiative pathways and more efficient emission. The PVDF matrix also imparts remarkable stability to the nanocrystals, enabling them to be unaffected in water exposure for over a week and facilitating rapid, reversible halide exchange reactions with hydroiodic acid. This reversible ion exchange, combined with the improved stability and tunable emission, points to promising applications in optoelectronics, photocatalysis, and hydrogen production. Overall, the research demonstrates that PVDF not only guides and

stabilizes perovskite nanocrystals at room temperature but also enhances their optical performance and environmental resilience, opening new pathways for their practical deployment.

Furthermore, the next study offers significant insights into the role of crystal facet engineering in modulating Förster resonance energy transfer (FRET) efficiency within doped cesium lead bromide ($CsPbBr_3$) nanocrystals. By doping with trace amounts of Ni^{+2} and Co^{+2} ions, two structurally distinct nanocrystal systems were developed: Ni:PNC, exhibiting a cubic morphology predominantly exposing {100} facets, and Ni:Co:PNC, which formed an elongated dodecahedral shape with dominant {111}/{002} facets. These structural differences were rigorously characterized through Rietveld refinement, TEM imaging, and crystallographic analysis. A key observation was the dramatic difference in FRET efficiency when rhodamine B (RhB) was used as an energy acceptor. The {100}-faceted Ni:PNC demonstrated a high FRET efficiency of 94%, while the {111}-faceted Ni:Co:PNC exhibited a significantly lower efficiency of only 21%. Importantly, these variations occurred despite comparable photoluminescence quantum yields and spectral overlap integrals. This suggests that the efficiency of energy transfer in such systems is not primarily dictated by spectral factors, but rather by nanoscale spatial and chemical interactions at the donor–acceptor interface.

Binding affinity studies and FTIR spectroscopy provided compelling evidence that the {100} facet, rich in Cs^+ surface ions, facilitates stronger interaction with the carboxylate group of RhB, thus reducing donor–acceptor distance (R_{DA}) and enhancing energy transfer. Conversely, the presence of Pb^{+2} in facet {111} enforces specific adhesion with oleyamine due to the chelation/metal–ligand type of interactions and hence blocks the access of rhodamine B to the Ni:Co:PNC nanocrystal.

The comparison between solution-phase and thin-film configurations further revealed that physical confinement significantly enhances energy transfer rates. In thin films, reduced molecular diffusion and closer spatial proximity between donor and acceptor components enabled more efficient FRET, reinforcing the role of nanoscale architecture in guiding energy transfer pathways.

Overall, this work underscores the importance of crystallographic facet exposure and surface composition in directing energy flow in perovskite nanocrystals. The findings suggest that beyond conventional considerations like spectral overlap and quantum yield, facet-specific binding chemistry and dopant-induced structural reorganization are pivotal in determining the efficiency of nonradiative energy transfer processes. These insights have broad implications for the design of perovskite-based optoelectronic devices and photocatalysts. In particular, tailoring nanocrystal facets via controlled doping strategies can serve as a powerful approach for engineering directional energy transfer, improving device performance, and enhancing the functional integration of perovskite materials with organic fluorophores, dyes, or catalytic centers.

In addition to that, the next study explores the energy and electron transfer dynamics in a triadic nanohybrid system comprising nickel-doped $CsPbBr_3$ perovskite nanocrystals (Ni:PNCs), Rhodamine B (RhB), and methyl viologen (MV^{+2}). Leveraging the inherent photophysical advantages of $CsPbBr_3$ such as high absorption, defect tolerance, and bright photoluminescence, the work examines its potential for constructing artificial photosynthetic assemblies via Förster Resonance Energy Transfer (FRET) and Photoinduced Electron Transfer (PET).

The Ni:PNCs demonstrate improved ethanol tolerance due to lattice contraction from Ni^{+2} doping, which enhances stability for hybrid assembly in ternary solvent systems. A high energy

transfer efficiency (~88%) from Ni:PNC to RhB is confirmed through steady-state and time-resolved photoluminescence (TRPL) studies. Ethanol-induced modulation of photoluminescence in the Ni:PNC–RhB complex highlights dynamic equilibrium between bound and free RhB species, influenced by solvent polarity.

The introduction of MV^{+2} as an electron acceptor into the Ni:PNC–RhB system reveals significant emission quenching of both Ni:PNC and RhB, indicating efficient electron transfer. Stern–Volmer analyses suggest reduced accessibility of MV^{+2} to the nanocrystal surface when RhB is present, altering the quenching geometry and implying indirect electron transfer pathways. TRPL and absorption studies demonstrate that electron transfer from RhB to MV^{+2} occurs ultrafast, without displacing RhB from the PNC surface.

Transient absorption spectroscopy provides insight into charge separation kinetics. Ni:PNC–RhB exhibits accelerated exciton bleach recovery and generation of $MV^{+}\bullet$ upon MV^{+2} addition. Despite slightly reduced charge separation efficiency (14%) in the triad compared to Ni:PNC–MV^{+2} (17%), the results confirm sequential energy transfer from Ni:PNC to RhB followed by electron transfer to MV^{+2}. The electron transfer rate (k_{et}) in the triad is slightly slower, affirming RhB's role in modulating the pathway.

In conclusion, the Ni:PNC–RhB–MV^{+2} triad serves as a functional model for exploring energy-coupled electron transfer systems, with potential applications in photocatalysis and artificial photosynthesis. The findings highlight the importance of surface chemistry, binding dynamics, and sequential transfer mechanisms in optimizing hybrid nanomaterials for solar energy conversion.

6.2. Future Scope:

Perovskite research continues to offer excellent opportunities across optoelectronics, energy conversion, and photocatalysis. Future efforts will likely focus on enhancing ambient stability through compositional engineering, surface passivation, and polymer encapsulation strategies. The development of lead-free or low-toxicity alternatives is critical for environmentally sustainable and biomedical applications. Furthermore, integrating perovskite nanocrystals into multi-acceptor energy transfer networks or magnetically responsive composites holds promise for advanced light-harvesting architectures and spintronic photocatalysis. Realizing scalable, long-term stable, and application-specific perovskite platforms will be pivotal in translating laboratory-scale breakthroughs into commercial technologies.

Some of the Immediate scope of this thesis work would be-

(i) Photocatalysis using the Combination of Perovskite nanoparticles with a multi-acceptor system for augmented catalytic activity.

(ii) Biomass valorisation and organic pollutant degradation using perovskite nanoparticles as a catalyst.

(iii) Ambient light-driven photocatalysis through the incorporation of ferromagnetism in the perovskite matrix.

(iv) Dark photocatalysis using perovskite nanocrystals as an electron donor.

(v) Highly efficient lead-free perovskite synthesis for commercial viability and bio medical applications.

Appendix:
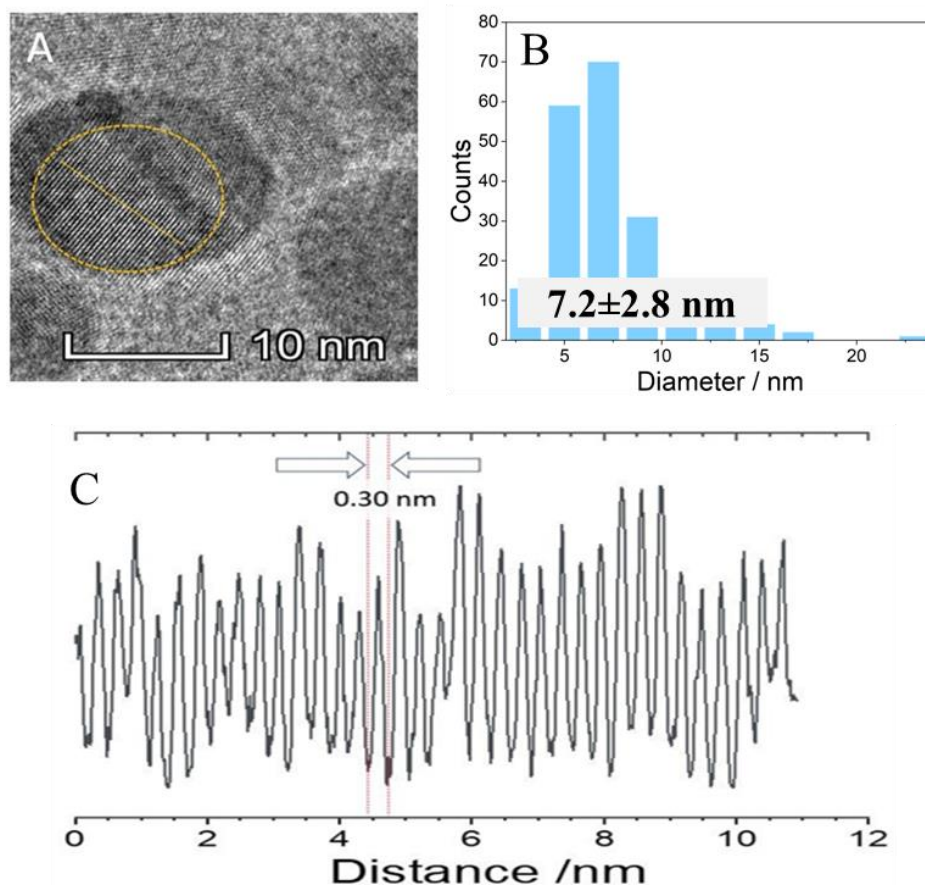
Figure A3.1: [A] HRTEM image of halide perovskite crystal, HPC-2 **[B]** Particle size-distribution of HPC-2 **[C]** lattice spacing (0.30 nm) of HPC-2
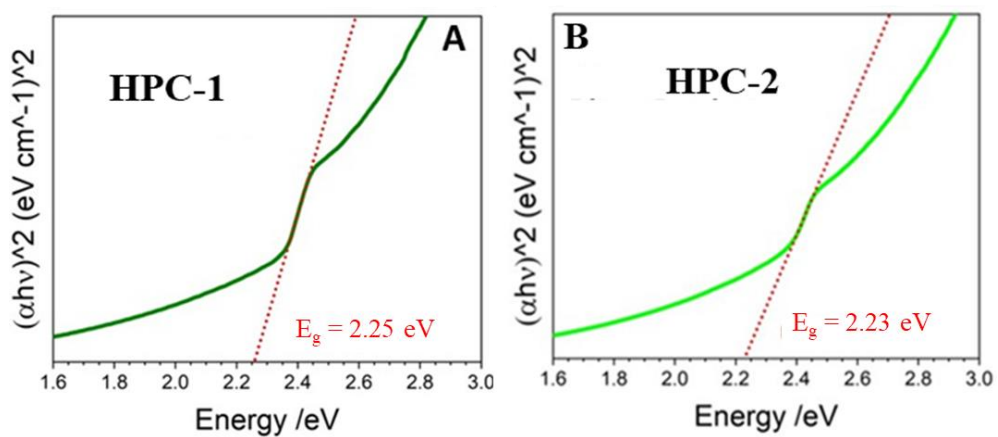
Figure A3.2: [A] Direct bandgap of HPC-1**[B]** Direct bandgap of HPC-2
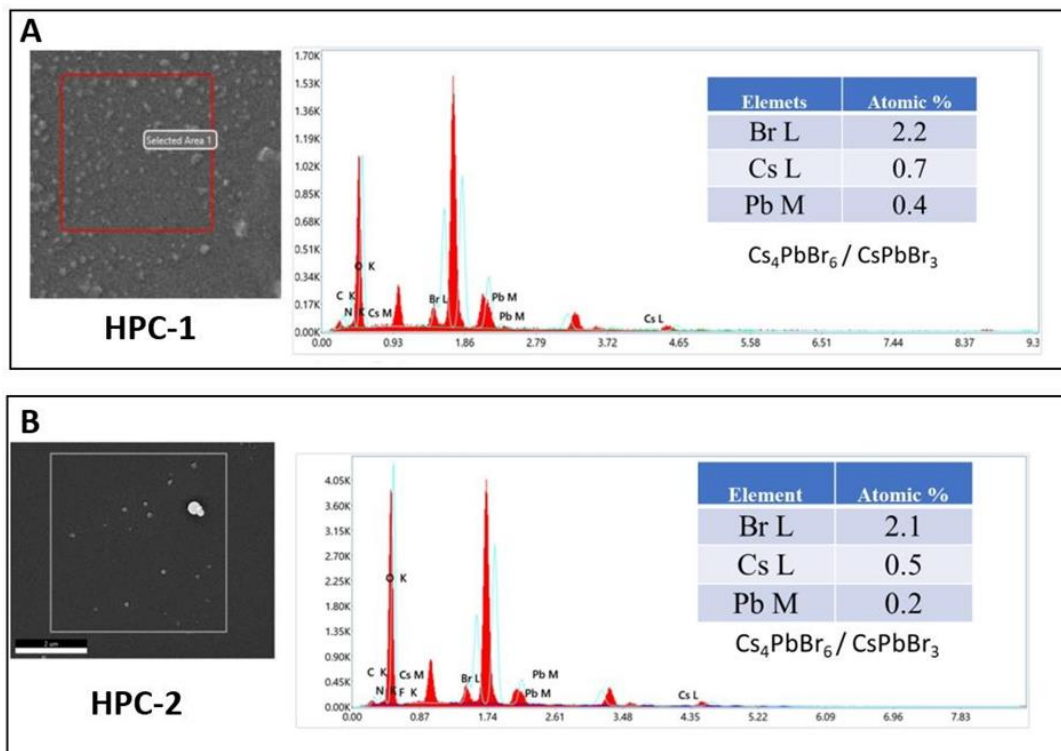
Figure A3.3: FE-SEM imaging and EDS analysis of halide perovskite crystals-**[A]** HPC-1 and **[B]** HPC-2
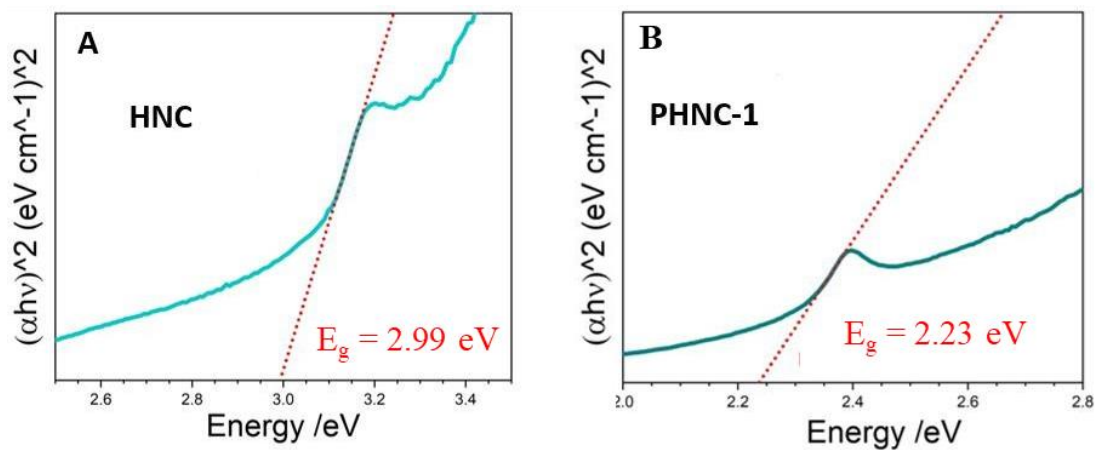
Figure A3.4: [A] Direct bandgap of halide nanocrystal (HNC) **[B]** Direct bandgap of polymer-doped halide nanocrystal (PHNC-1)
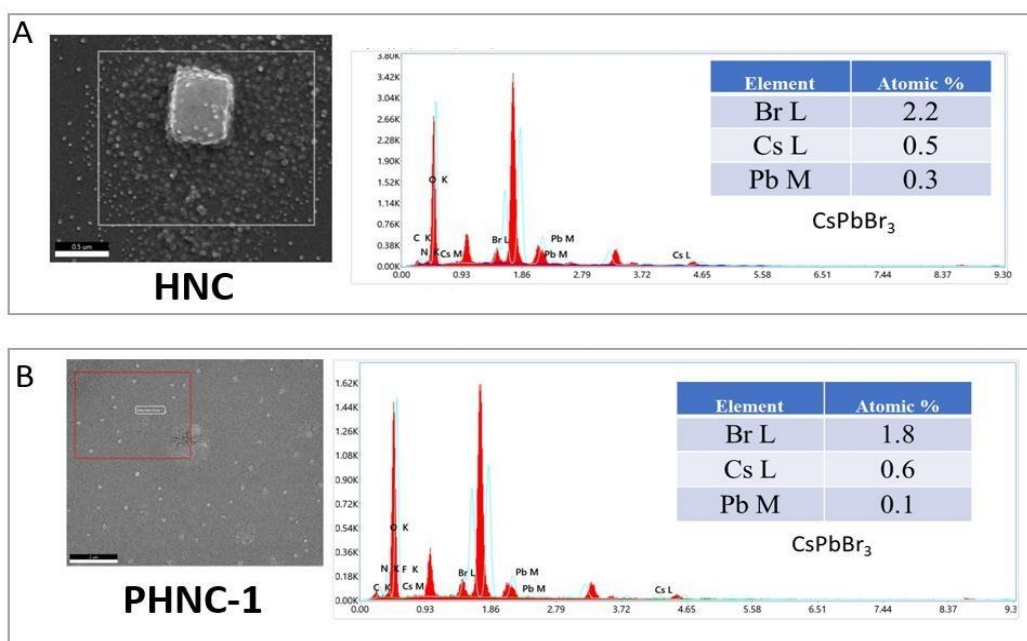
Figure A3.5: FE-SEM imaging and EDS analysis of **[A]** HNC and **[B]** PHNC-1
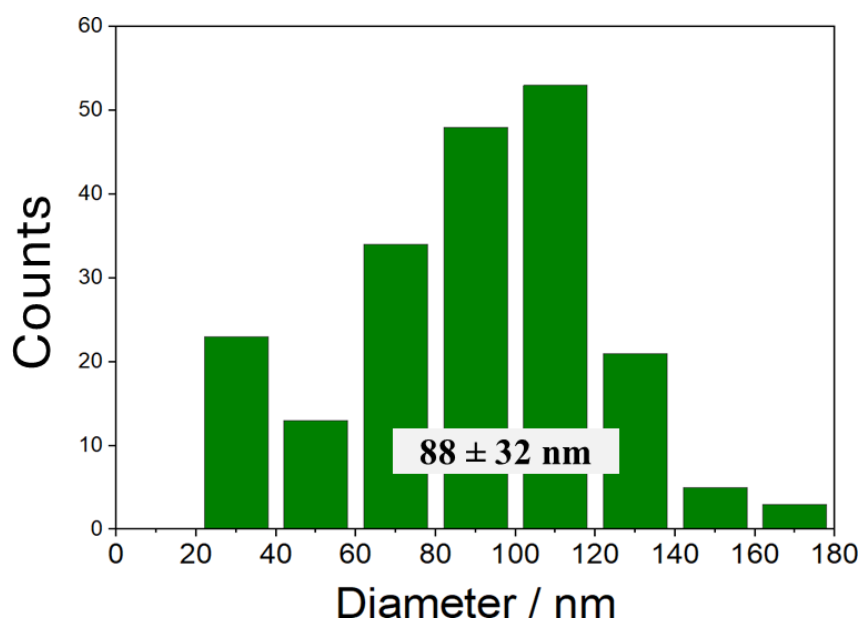
Figure A3.6: Particle size-distribution of polymer-doped nanocrystal, PHNC-1
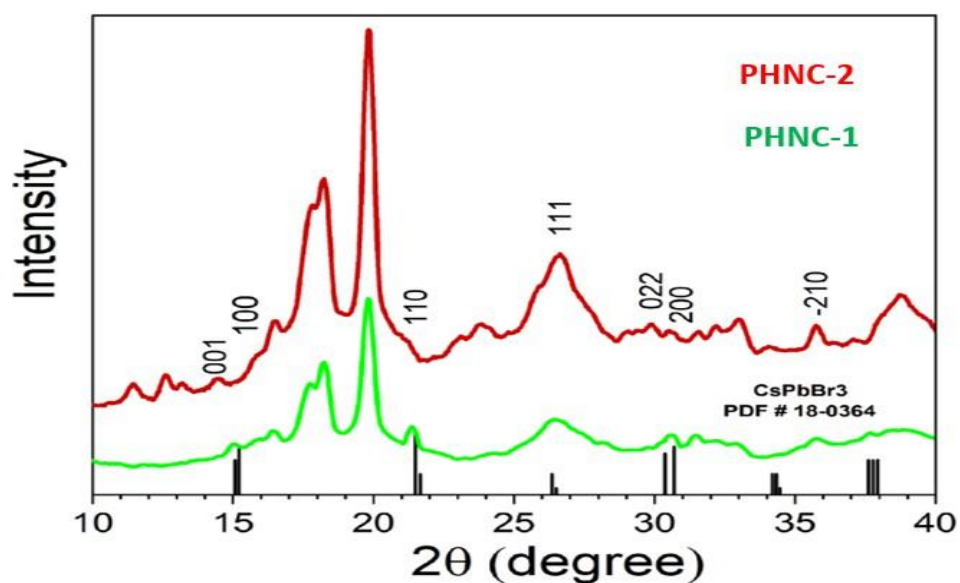
Figure A3.7: XRD pattern of polymer doped nanocrystal films- green emitting PHNC-1 (green) and red-emitting PHNC-2 (red) with the standard reference of monoclinic $CsPbBr_3$, JCPDS no. 18-0364 (black line).
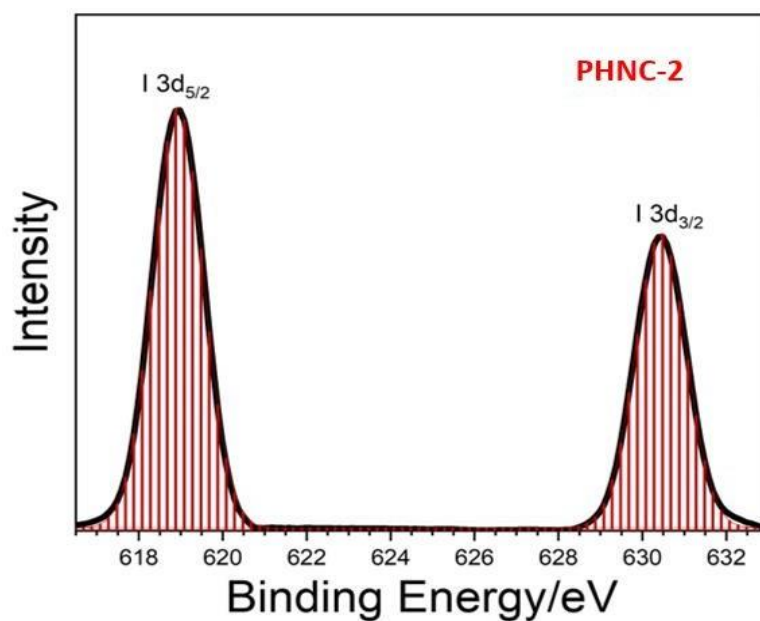
Figure A3.8: High resolution XPS spectrum of Iodine in polymer-doped nanocrystal, PHNC-2.
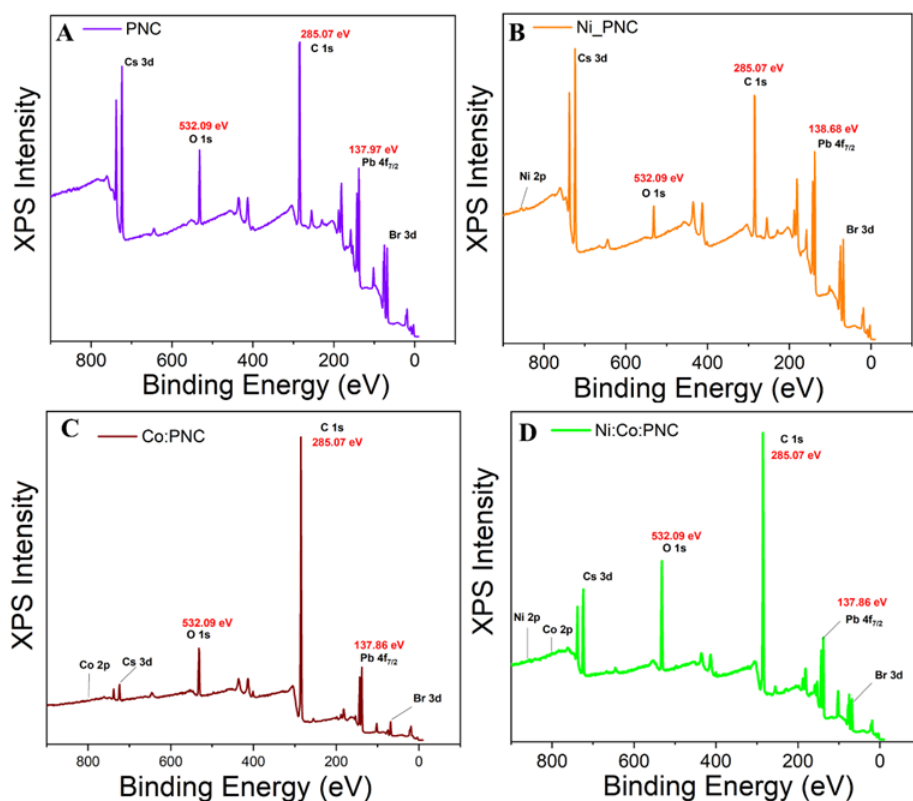
Figure A4.1: High resolution XPS spectrum of— **[A]** pristine PNC (*violet line*), **[B]** Ni:PNC (*orange line*), **[C]** Co:PNC (*red line*) and **[D]**Ni:Co:PNC (*green line*).
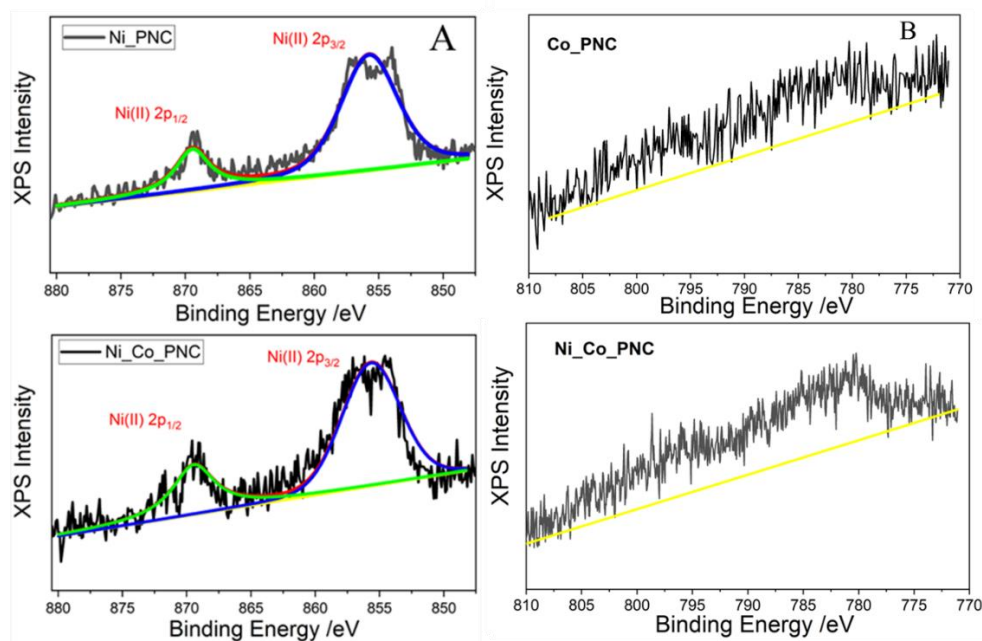
Figure A4.2: High resolution XPS spectra of Ni (II) for— **[A]** Ni:PNC and Ni:Co:PNC. **[B]** High resolution XPS spectra of Co (II) for Co:PNC and Ni:Co:PNC.
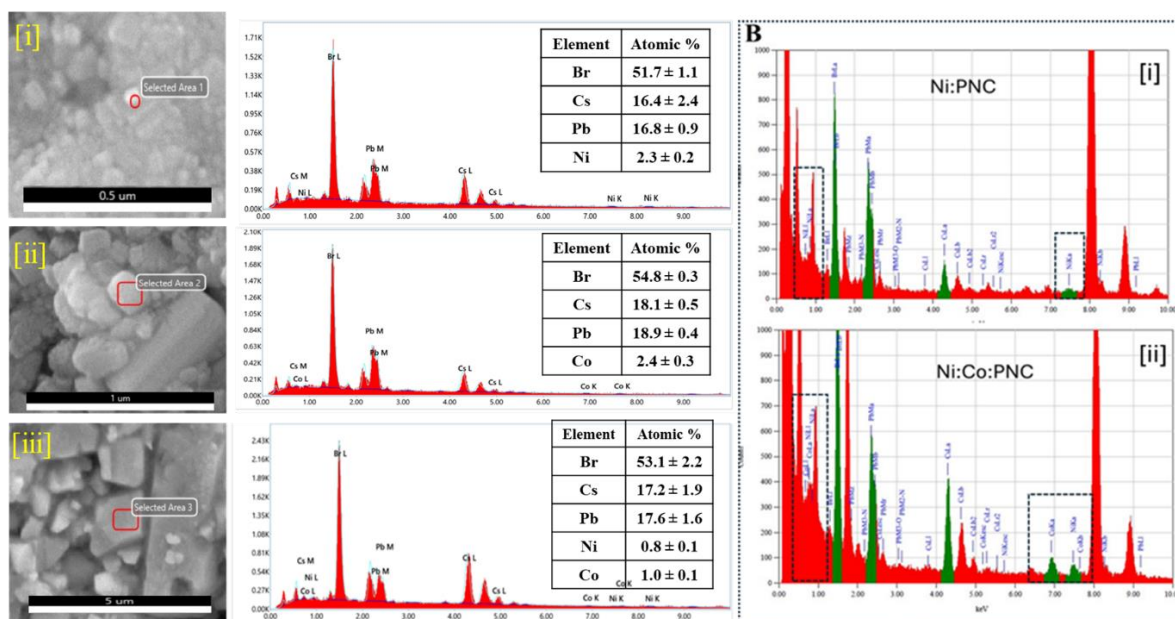
Figure A4.3: **[A]** FESEM image (left panel), energy dispersive X-ray spectra (centre) and K-line & L-line of **[i]** Ni:PNC, **[ii]** Co:PNC, **[iii]** Ni:Co:PNC respectively. **[B]** Energy dispersive X-ray spectra recorded using HRTEM of **[i]** Ni:PNC, **[ii]** Ni:Co:PNC respectively. K-line & L-line of Ni and Co are demarcated.
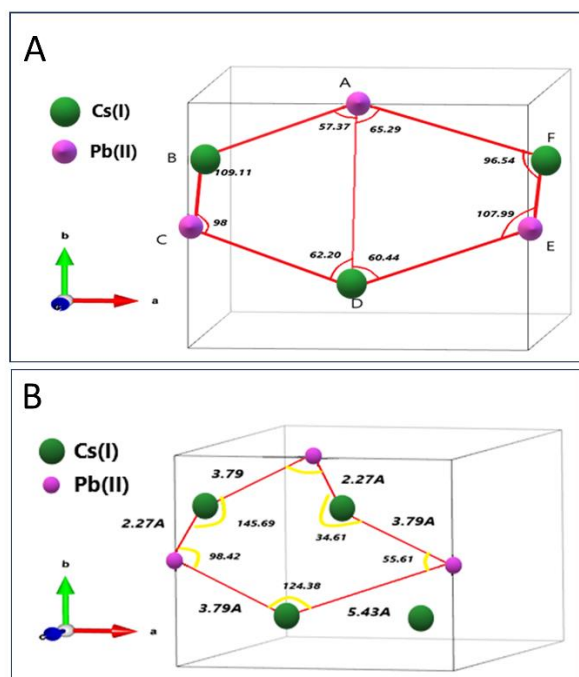
Figure A4.4: Positioning of Cs and Pb atom for the crystal lattice of Ni:PNC and Ni:Co:PNC. Front surface on ab plane of- **[A]** Ni:Co:PNC, **[B]** Ni:PNC. Crystal lattice having Cs(I) and Pb(II) ions only.
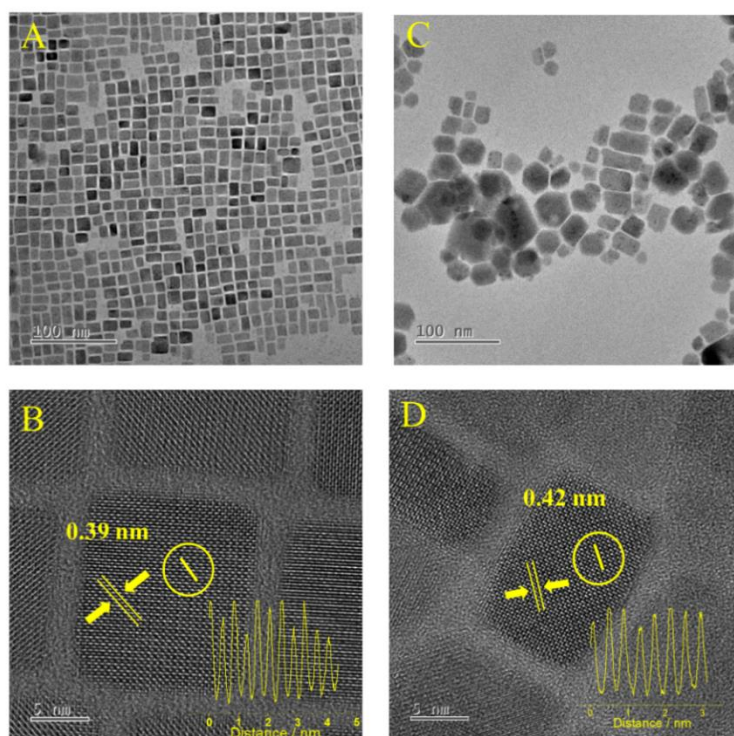
Figure A4.5: HR TEM Image of **[A]** Ni:PNC **[B]** Interplanar spacing of Ni:PNC **[C]** HR TEM Image of Ni:Co:PNC. **[D]** Interplanar spacing of Ni:Co:PNC
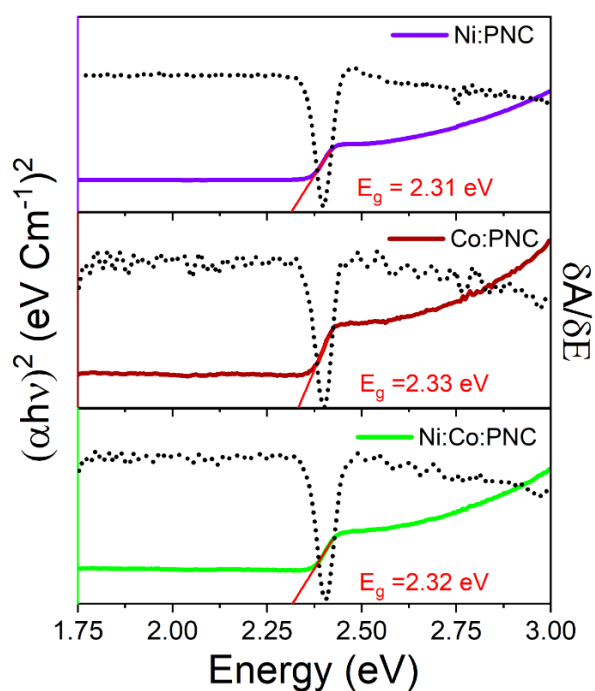
Figure A4.6: Direct Band gap and first order derivative of the absorbance with respect to energy for- [*top*] Ni:PNC , [*centre*] Co:PNC, and [*bottom*] Ni:Co:PNC respectively in solvent hexane
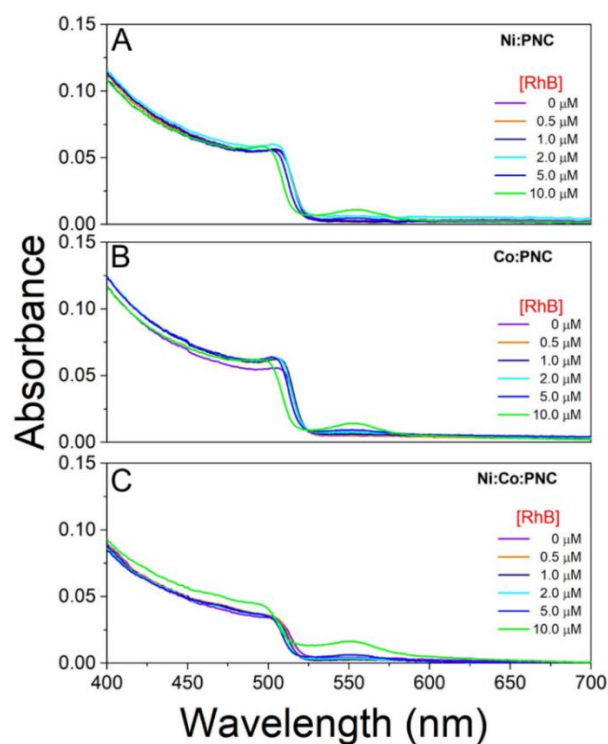
Figure A4.7: Absorbance spectra of **[A]** Ni:PNC, **[B]** Co:PNC, and **[C]** Ni:Co:PNC with the successive addition of Rhodamine B in toluene.
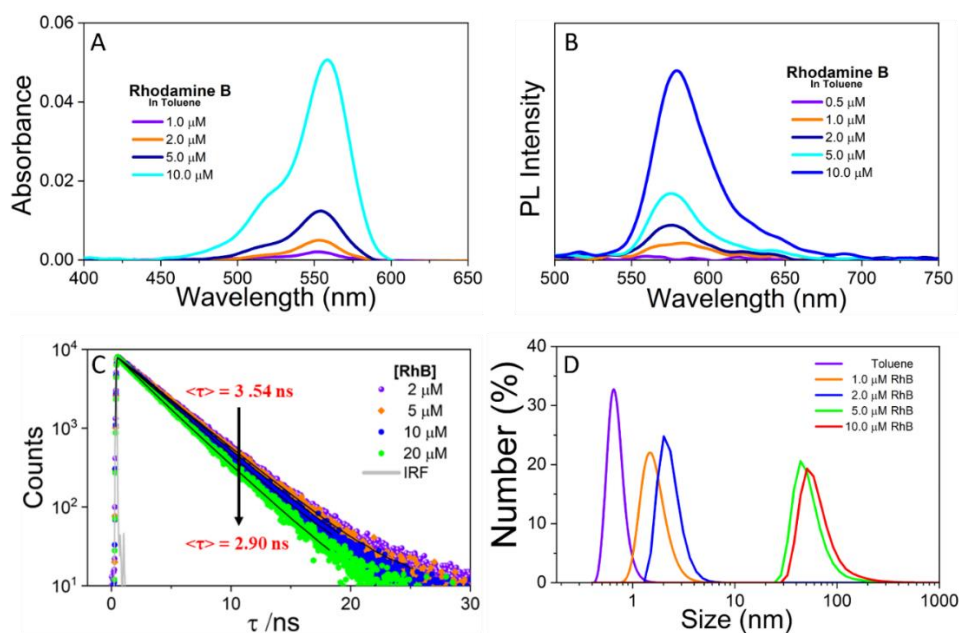
Figure A4.8: Absorbance spectra of **[A]** Rhodamine B in toluene (without donor)**[B]** PL spectra of Rhodamine B in toluene (without donor) **[C]** PL decay traces of Rhodamine B in toluene (without donor) **[D]** Hydrodyanamic diameter of Rhodamine B measured by dyanamic light scattering in toluene.

131
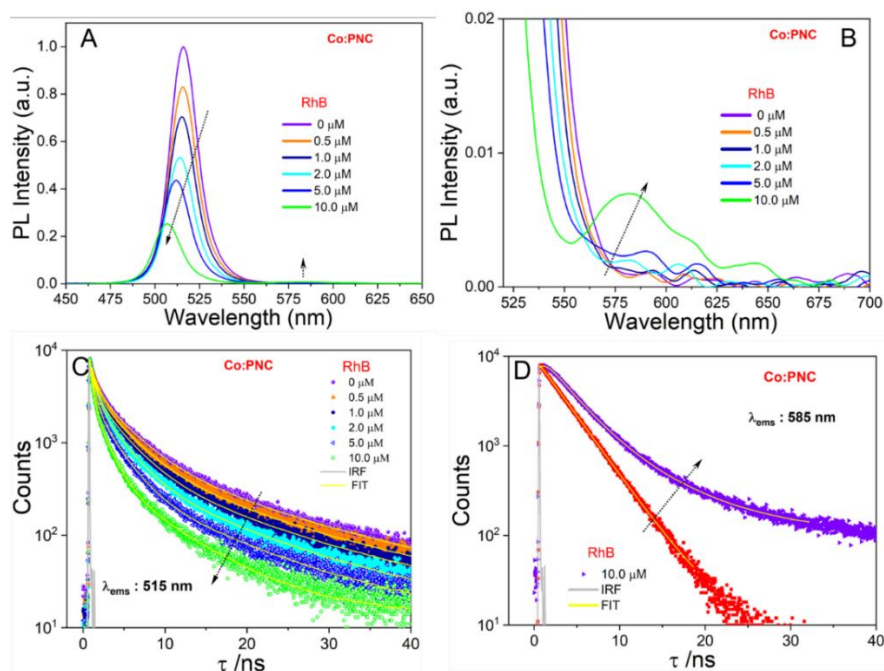
Figure A4.9: Photoluminescence spectra of **[A]** Co:PNC (donor) and **[B]** Rhodamine B (acceptor) on gradual addition of RhB in toluene PL decay traces of **[C]** Donor Co:PNC (λ_{ems} =515 nm) in presence of acceptor RhB and PL decay traces of acceptor **[D]** Rhodamine B (λ_{ems} = 585 nm) in presence of donor Co:PNC
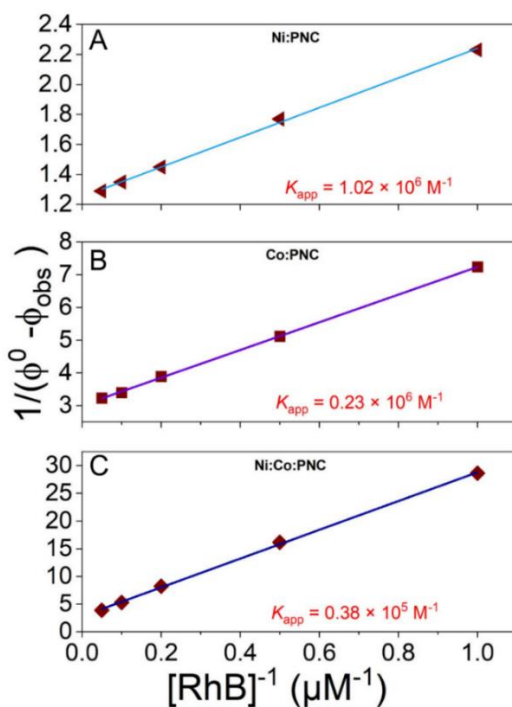
Figure A4.10: Double reciprocal plot of the PL quenching data for **[A]** Ni:PNC, **[B]** Co:PNC, and **[C]** Ni:Co:PNC. All the samples were excited at 400 nm.

Table A4.1: PL decay parameters of donor, Ni:PNC in presence of acceptor, RhB

[RhB]	τ_1 /ns (a$_1$)	τ_2 /ns (a$_2$)	τ_3/ns (a$_3$)	$<\tau>$/ns	χ^2
0 µM	1.01 (0.39)	4.24 (0.51)	20.36 (0.11)	4.68	1.06
0.5 µM	0.55 (0.68)	3.25 (0.26)	17.03 (0.06)	2.27	1.1
1.0 µM	0.53 (0.66)	3.20 (0.27)	16.62 (0.07)	2.36	1.1
2.0 µM	0.49 (0.67)	3.13 (0.27)	16.71 (0.06)	2.25	1.1
5.0 µM	0.45 (0.71)	2.87 (0.24)	15.72 (0.05)	1.83	1.08
10.0 µM	0.28 (0.75)	1.47 (0.20)	6.98 (0.05)	0.83	1.08

λ_{exc} = 405 nm, λ_{ems} =515 nm IRF= 180 ps; Luminescence lifetimes, $<\tau> = \Sigma\, a_i\tau_i{}^2/\Sigma\, a_i\tau_i$

Table A4.2: PL decay parameters of donor, Ni:Co:PNC in presence of acceptor, RhB

[RhB]	τ_1 /ns (a$_1$)	τ_2 /ns (a$_2$)	τ_3/ns (a$_3$)	$<\tau>$/ns	χ^2
0 µM	0.76 (0.27)	4.70 (0.48)	11.83 (0.25)	5.47	1.03
0.5 µM	0.77 (0.25)	4.57 (0.47)	11.51 (0.28)	5.60	1.03
1.0 µM	0.80 (0.24)	4.67 (0.49)	11.55 (0.27)	5.57	1.00
2.0 µM	0.91 (0.26)	4.72 (0.49)	11.53 (0.25)	5.43	1.06
5.0 µM	0.84 (0.29)	4.52 (0.53)	11.50 (0.18)	4.68	1.04
10.0 µM	0.81 (0.32)	4.27 (0.52)	11.60 (0.16)	4.37	1.12

λ_{exc} = 405 nm, λ_{ems} =515 nm IRF= 180 ps; Luminescence lifetimes, $<\tau> = \Sigma\, a_i\tau_i{}^2/\Sigma\, a_i\tau_i$

Table A4.3: PL decay parameters of acceptor, RhB in presence of donor, Ni:PNC

[RhB]	τ_1 /ns (a$_1$)	τ_2 /ns (a$_2$)	τ_3/ns (a$_3$)	$<\tau>$/ns	χ^2
0.5 μM	2.97 (-0.48)	3.09 (0.49)	13.71 (0.02)	3.28	1.07
1.0 μM	1.19 (-0.43)	5.53 (0.40)	15.75 (0.17)	5.44	1.1
2.0 μM	0.90 (-0.48)	5.02 (0.38)	14.72 (0.13)	4.33	1.13
5.0 μM	0.59 (-0.53)	4.16 (0.38)	12.59 (0.09)	2.98	1.11
10.0 μM	0.31 (-0.43)	2.45 (0.48)	7.52 (0.09)	1.99	1.06

λ_{exc} = 405 nm, λ_{ems} = 585 nm IRF= 180 ps; Luminescence lifetimes, $<\tau> = \Sigma a_i \tau_i^2 / \Sigma a_i \tau_i$

Table A4.4: PL decay parameters of acceptor, RhB in presence of donor, Ni:Co:PNC

[RhB]	τ_1 /ns (a$_1$)	τ_2 /ns (a$_2$)	τ_3/ns (a$_3$)	$<\tau>$/ns	χ^2
1.0 μM	0.60 (0.42)	3.89 (0.39)	10.88 (0.19)	3.84	1.07
2.0 μM	0.66 (0.38)	3.80 (0.43)	10.77 (0.19)	3.97	1.02
5.0 μM	0.51 (0.40)	3.38 (0.45)	10.32 (0.15)	3.30	1.12
10.0 μM	0.25 (0.45)	2.10 (0.30)	5.51 (0.25)	2.13	1.09

λ_{exc} = 405 nm, λ_{ems} = 585 nm IRF= 180 ps; Luminescence lifetimes, $<\tau> = \Sigma a_i \tau_i^2 / \Sigma a_i \tau_i$

Table A4.5: PL decay parameters of donor, Co:PNC in presence of acceptor, RhB

[RhB]	τ_1 /ns (a$_1$)	τ_2 /ns (a$_2$)	τ_3/ns (a$_3$)	$<\tau>$/ns	χ^2
0 μM	0.69 (0.60)	3.58 (0.32)	13.41 (0.07)	2.57	1.09
0.5 μM	0.67 (0.63)	3.45 (0.31)	13.26 (0.06)	2.30	1.17
1.0 μM	0.62 (0.66)	3.19 (0.28)	12.52 (0.05)	1.97	1.18
2.0 μM	0.56 (0.68)	2.87 (0.28)	11.85 (0.04)	1.70	1.2
5.0 μM	0.50 (0.04)	2.52 (0.22)	10.78 (0.03)	1.27	1.12
10.0 μM	0.33 (0.69)	1.58 (0.27)	6.98 (0.04)	0.96	1.12

λ_{exc} = 405 nm, λ_{ems} = 515 nm IRF= 180 ps; Luminescence lifetimes, $<\tau> = \Sigma a_i \tau_i^2 / \Sigma a_i \tau_i$

Table A4.6: PL decay parameters of acceptor, RhB in presence of donor, Co:PNC

[RhB]	τ_1 /ns (a$_1$)	τ_2 /ns (a$_2$)	τ_3/ns (a$_3$)	$<\tau>$/ns	χ^2
5.0 µM	0.13 (0.76)	3.36 (0.22)	11.05 (0.03)	1.13	1.10
10.0 µM	0.75 (-0.30)	3.13 (0.57)	7.55 (0.13)	2.99	1.11
20.0 µM	0.39 (-0.22)	3.30 (0.74)	16.29 (0.04)	3.24	1.04

λ_{exc} = 405 nm, λ_{ems} =585 nm IRF= 180 ps; Luminescence lifetimes, $<\tau> = \Sigma\, a_i \tau_i^2 / \Sigma\, a_i \tau_i$

Table A4.7: PL decay parameters of donor, Ni:PNC in presence of acceptor, RhB in thin film.

[RhB]	τ_1 /ns (a$_1$)	τ_2 /ns (a$_2$)	τ_3/ns (a$_3$)	$<\tau>$/ns	χ^2
0 µM	1.25 (0.27)	4.65 (0.60)	15.25 (0.12)	5.05	1.06
0.5 µM	0.95 (0.33)	3.99 (0.59)	11.52 (0.08)	3.61	1.05
1.0 µM	0.71 (0.41)	3.39 (0.52)	10.01 (0.08)	2.81	1.07

λ_{exc} = 405 nm, λ_{ems} =512 nm IRF= 180 ps; Luminescence lifetimes, $<\tau> = \Sigma\, a_i \tau_i^2 / \Sigma\, a_i \tau_i$

Table A4.8: PL decay parameters of acceptor, RhB in presence of donor, Ni:PNC in thin film.

[RhB]	τ_1 /ns (a$_1$)	τ_2 /ns (a$_2$)	τ_3/ns (a$_3$)	$<\tau>$/ns	χ^2
0.5 µM	1.48 (-0.43)	6.92 (0.46)	28.73 (0.11)	7.07	1.06
1.0 µM	0.93 (-0.42)	4.93 (0.53)	21.90 (0.05)	4.07	1.06

λ_{exc} = 405 nm, λ_{ems} =570 nm IRF= 180 ps; Luminescence lifetimes, $<\tau> = \Sigma\, a_i \tau_i^2 / \Sigma\, a_i \tau_i$
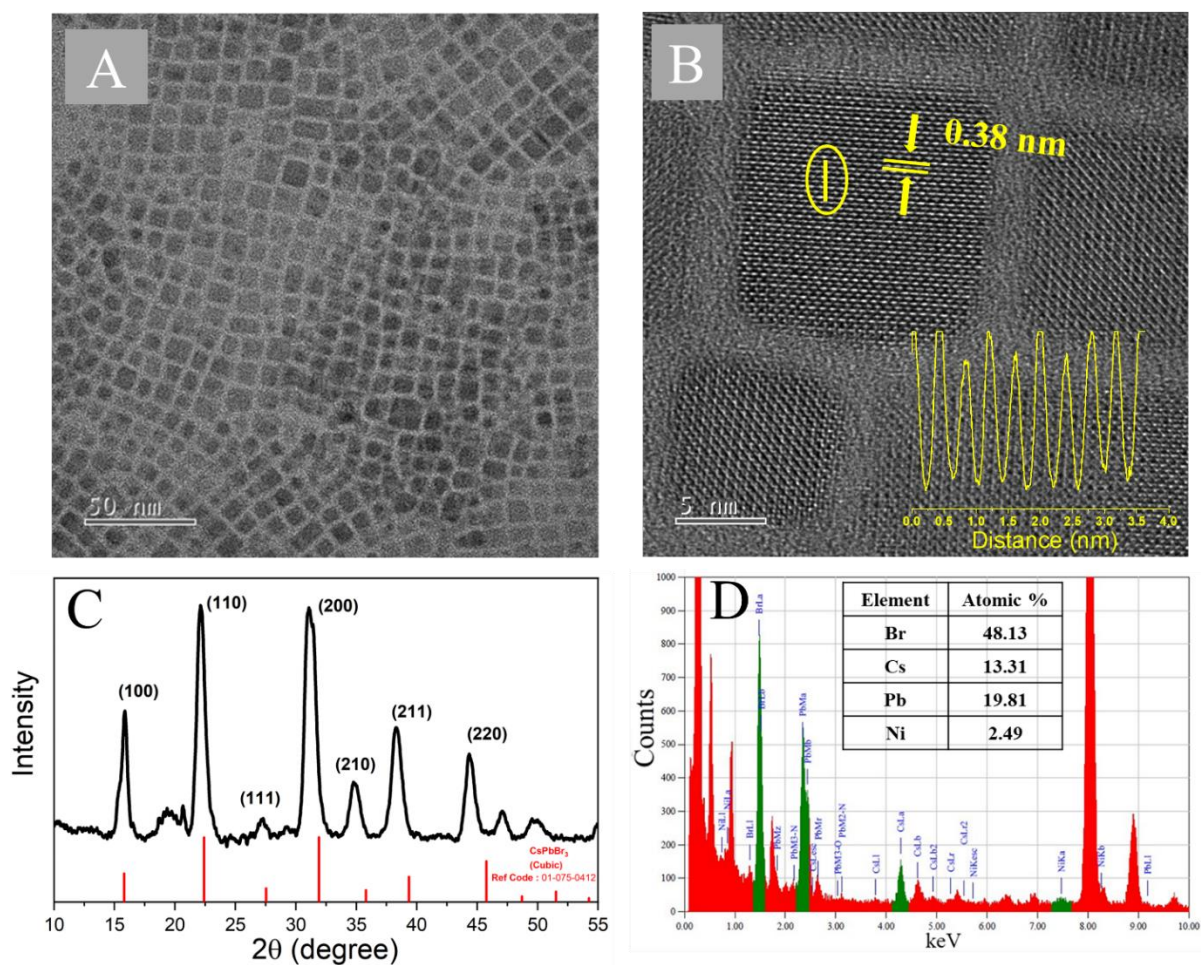
Figure A5.1: HR TEM Image of **[A]** Ni:PNC **[B]** Interplanar spacing of Ni:PNC **[C]** X-ray diffraction pattern of Ni:PNC, the planes are matched with the cubic lattice structure (JCPDS card no – 01-075-0412). **[D]** Energy dispersive X-ray spectra of Ni:PNC recorded using HRTEM , Inset : showing the atomic composition, confirming that Ni^{+2} ion is doped in $CsPbBr_3$
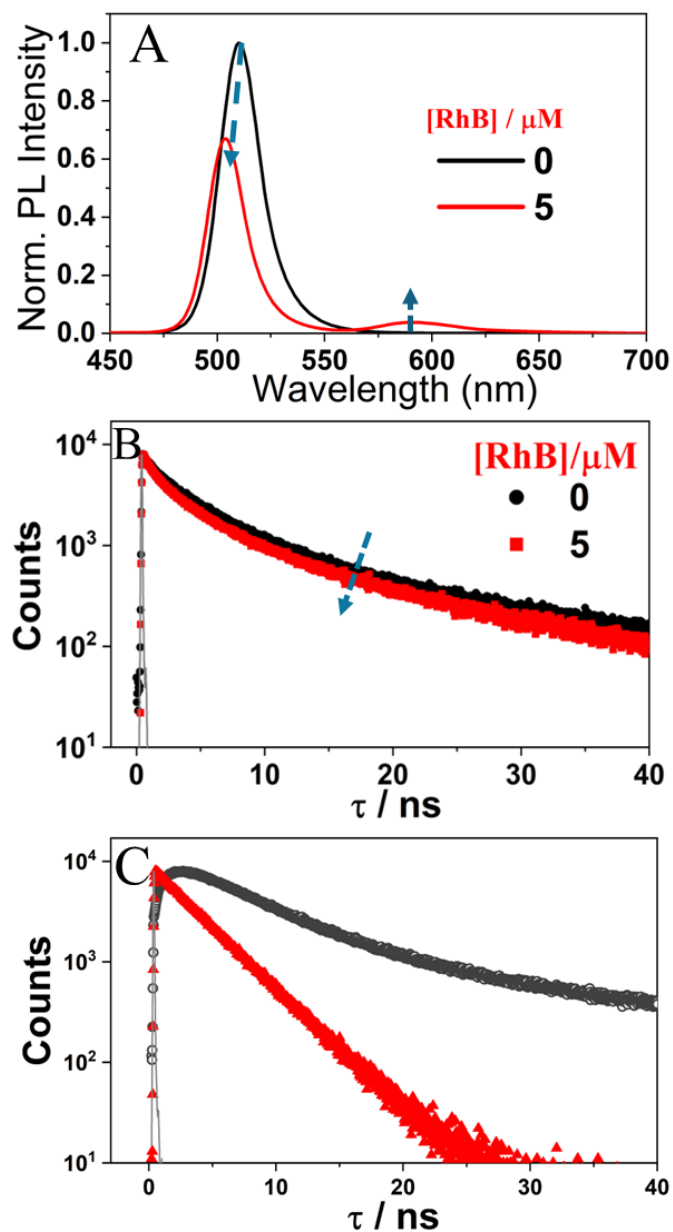
Figure A5.2: Photoluminescence quenching of **[A]** Ni:PNC before (black line) and after (red line) addition of 5 µM of RhB. Time-resolved photoluminescence decays at λ_{ems} = 510 nm of Ni:PNC **[B]** before (black line) and after (red line) addition of 5 µM of RhB. **[C]** Time-resolved photoluminescence decay at λ_{ems} = 585 nm of RhB in the absence of Ni:PNC (red triangle) and RhB in the presence of Ni:PNC (grey circle).
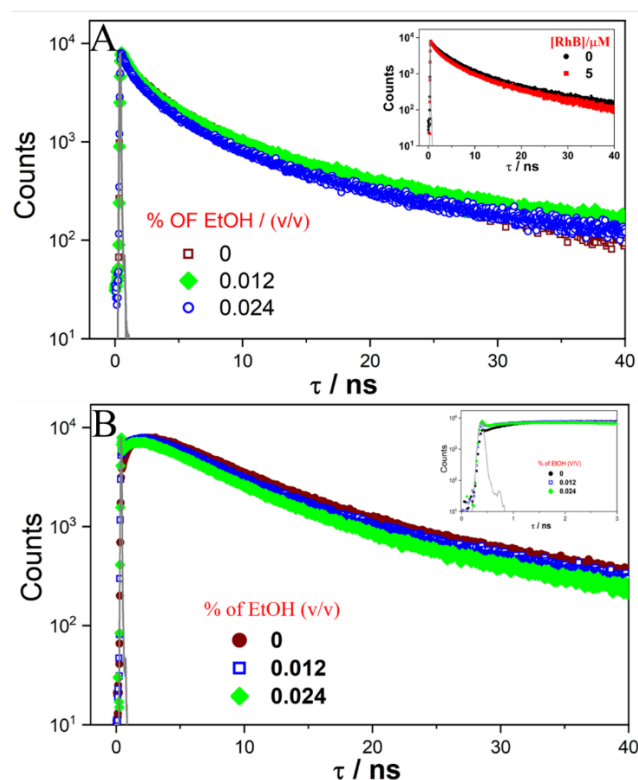
Figure A5.3: [A] Photoluminescence decay of Ni:PNC_RhB complex on gradual addition of EtOH monitored at 510 nm, Inst : showing the PL decay of Ni:PNC (black line), and after addition of 5 µM of RhB (red line). **[B]** Photoluminescence decay of Ni:PNC_RhB complex on gradual addition of EtOH monitored at 585 nm, Inst : showing the retention of rise time component after addition of EtOH through zoomed in portion of PL decay at 585 nm.
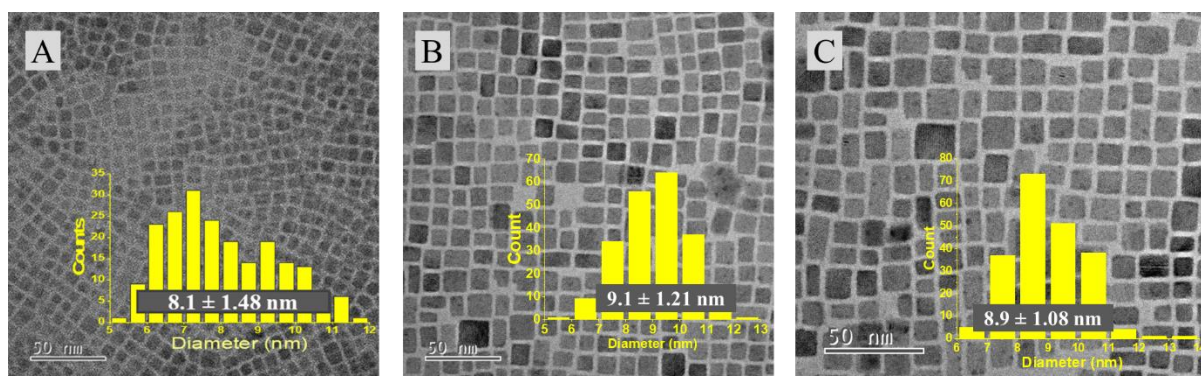
Figure A5.4: HR-TEM image of— **[A]** Ni:PNC **[B]** Ni:PNC—RhB **[C]** Ni:PNC—RhB—MV^{+2}. Inset showing the particle size distribution of all the systems, suggesting the average particle size remain unaltered after addition of different quenchers in ternary solvent
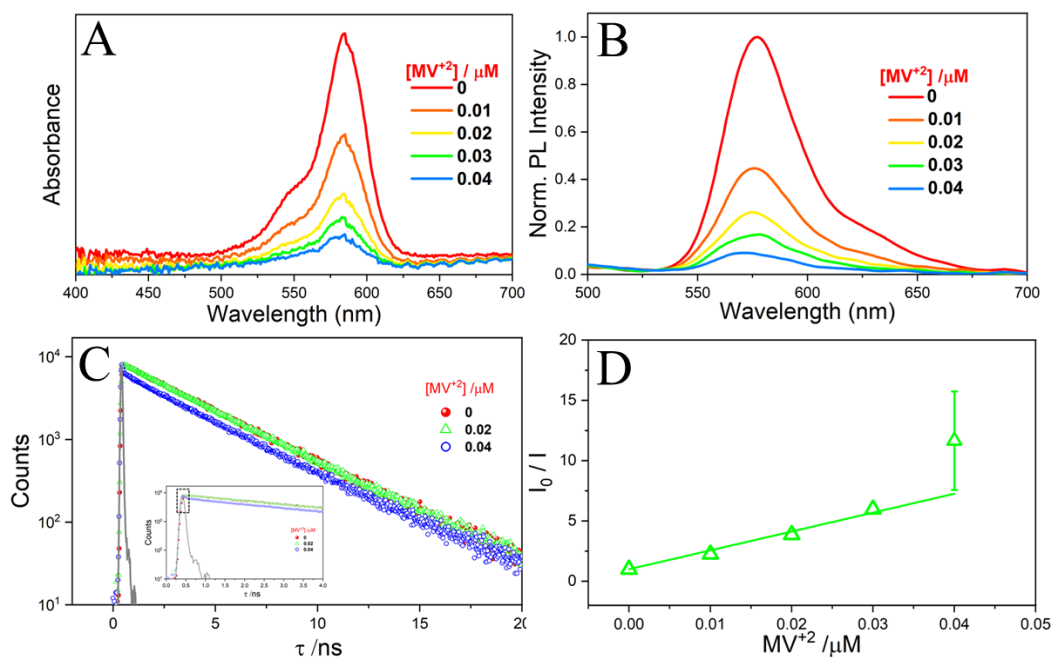
Figure A5.5: Control study: using Rhodamine B on successive addition of MV^{+2} (without Ni:PNC) **[A]** Absorbance spectra **[B]** Photoluminescence spectra **[C]** Photoluminescence decay profile monitored at 585 nm. Inset: showing the arising of shortest component in the demarked area after addition of 0.04 µM MV^{+2}. **[D]** Steady state Ster-Volmer quenching kinetics of RhB on gradual addition of MV^{+2}
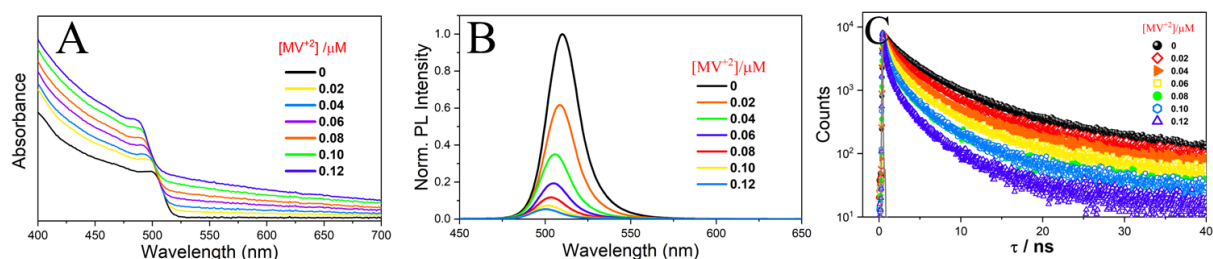
Figure A5.6: Control study: using Ni:PNC on successive addition of MV^{+2} (without RhB) **[A]** Absorbance spectra (each spectra was recorded in the interval of 30 minutes).**[B]** Photoluminescence spectra. (each spectra was recorded in the interval of 30 minutes) **[C]** Photoluminescence decay monitored at 510 nm. (each spectra was recorded in the interval of 30 minutes).
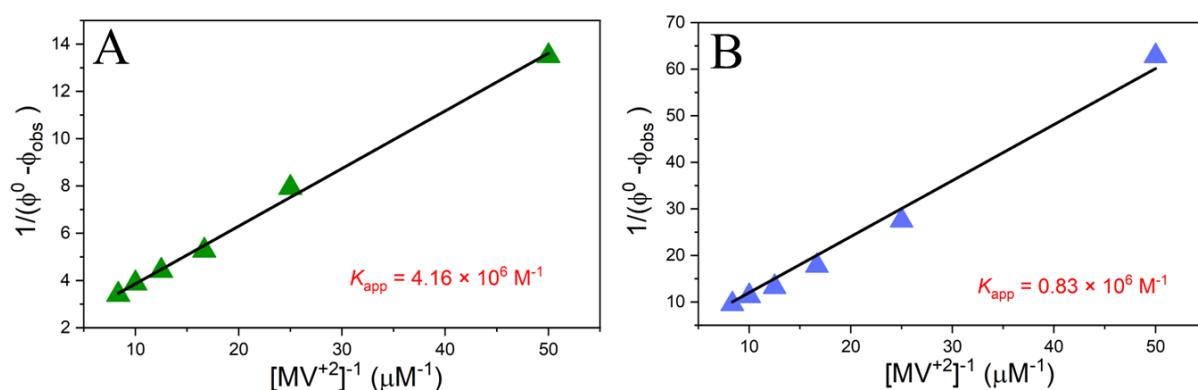
Figure A5.7: Double reciprocal plot of the PL quenching data for **[A]** Ni:PNC–MV^{+2}, **[B]** Ni:PNC–RhB–MV^{+2}. All the samples were excited at 400 nm.

Table A5.1: PL decay parameters of donor, Ni:PNC (510 nm) and acceptor RhB (585 nm) in presence of 5 µM RhB after gradual addition of ACN:EtOH mixture.

λ_{exc} = 405 nm IRF= 180 ps; Luminescence lifetimes, $<\tau> = \Sigma a_i \tau_i{}^2/\Sigma a_i \tau_i$

λ_{ems} (nm)	% of EtOH (v/v)	τ_1 /ns (a$_1$)	τ_2 /ns (a$_2$)	τ_3/ns (a$_3$)	$<\tau>$/ns	χ^2
510	0	1.15 (0.48)	4.53 (0.43)	18.50 (0.10)	4.26	1.12
	0.012	1.11 (0.52)	4.58 (0.39)	18.67 (0.09)	3.99	1.14
	0.024	0.94 (0.55)	4.14 (0.38)	17.42 (0.08)	3.42	1.14
λ_{ems} (nm)	% of EtOH (v/v)	τ_1 /ns (a$_1$)	τ_2 /ns (a$_2$)	τ_3/ns (a$_3$)	$<\tau>$/ns	χ^2
585	0	1.33 (-0.47)	5.47 (0.43)	16.47 (0.10)	4.63	1.09
	0.012	1.34 (-0.41)	4.47 (0.41)	11.69 (0.18)	4.47	1.14
	0.024	1.22 (-0.43)	4.55 (0.40)	11.33 (0.16)	4.22	1.08

Table A5.2: PL decay parameters RhB after gradual addition of MV^{+2} in absence of Ni:PNC

$[MV^{+2}]/\mu M$	λ_{ems} (nm)	τ_1 /ns (a$_1$)	τ_2 /ns (a$_2$)	$<\tau>$/ns	χ^2
0	585	0.46 (0.05)	3.50 (0.95)	3.13	1.10
0.02	585	0.03 (0.34)	3.39 (0.66)	2.26	1.06
0.04	585	0.03 (0.72)	3.24 (0.28)	1.11	1.20

λ_{exc} = 405 nm, IRF= 180 ps; Luminescence lifetimes, $<\tau> = \Sigma a_i \tau_i^2/\Sigma a_i \tau_i$

Table A5.3: PL decay parameters of acceptor RhB, after gradual addition of MV^{+2} (in presence of Ni:PNC)

$[MV^{+2}]/\mu M$	λ_{ems} (nm)	τ_1 /ns (a$_1$)	τ_2 /ns (a$_2$)	τ_3/ns (a$_3$)	$<\tau>$/ns	χ^2
0	585	1.22 (-0.44)	5.71 (0.49)	21.28 (0.07)	4.75	1.06
0.02	585	1.27 (-0.46)	5.32 (0.45)	16.42 (0.09)	4.10	1.12
0.04	585	1.51 (-0.43)	3.18 (0.31)	8.50 (0.25)	3.50	1.04
0.06	585	2.06 (-0.44)	2.82 (0.44)	9.22 (0.12)	3.14	1.01
0.08	585	2.85 (-0.40)	2.86 (0.52)	10.16 (0.08)	2.77	1.01
0.10	585	2.66 (-0.31)	2.66 (0.56)	8.26 (0.13)	2.40	1.15
0.12	585	0.17 (0.52)	1.63 (0.34)	5.34 (0.14)	1.59	1.03

λ_{exc} = 405 nm, IRF= 180 ps; Fluorescence lifetime, $<\tau> = \Sigma a_i \tau_i^2/\Sigma a_i \tau_i$

Table A5.4: PL decay parameters of donor, Ni:PNC after gradual addition of MV^{+2} in presence of 5 μM RhB.

[MV^{+2}]/μM	λ_{ems} (nm)	τ_1 /ns (a$_1$)	τ_2 /ns (a$_2$)	τ_3/ns (a$_3$)	$<\tau>$/ns	χ^2
0	510	1.01 (0.44)	4.05 (0.44)	15.13 (0.12)	4.14	1.14
0.02	510	0.89 (0.53)	3.79 (0.37)	14.85 (0.10)	3.27	1.15
0.04	510	0.69 (0.58)	3.31 (0.34)	14.03 (0.08)	2.46	1.09
0.06	510	0.60 (0.68)	3.14 (0.27)	13.81 (0.06)	2.03	1.07
0.08	510	0.49 (0.72)	2.62 (0.23)	12.39 (0.05)	1.64	1.15
0.10	510	0.45 (0.73)	2.66 (0.22)	12.81 (0.04)	1.41	1.14
0.12	510	0.38 (0.79)	2.39 (0.18)	12.21 (0.03)	1.09	1.08

λ_{exc} = 405 nm IRF= 180 ps; Luminescence lifetimes, $<\tau> = \Sigma\, a_i \tau_i^{\,2}/\Sigma\, a_i \tau_i$

Table A5.5: PL decay parameters of donor, Ni:PNC after gradual addition of MV^{+2} in absence of RhB.

[MV^{+2}]/μM	λ_{ems} (nm)	τ_1 /ns (a$_1$)	τ_2 /ns (a$_2$)	τ_3/ns (a$_3$)	$<\tau>$/ns	χ^2
0	510	1.55 (0.44)	4.82 (0.48)	17.94 (0.08)	4.64	1.10
0.02	510	0.86 (0.45)	3.89 (0.48)	15.95 (0.07)	3.26	1.12
0.04	510	0.83 (0.60)	3.62 (0.35)	15.30 (0.05)	2.18	1.09
0.06	510	0.68 (0.69)	3.39 (0.28)	14.88 (0.03)	1.64	1.17
0.08	510	0.50 (0.78)	2.66 (0.19)	12.06 (0.02)	1.29	1.18
0.10	510	0.45 (0.77)	2.60 (0.21)	11.84 (0.02)	1.09	1.14
0.12	510	0.34 (0.86)	2.09 (0.13)	10.00 (0.01)	0.78	1.08

λ_{exc} = 405 nm, IRF= 180 ps; Luminescence lifetimes, $<\tau> = \Sigma\, a_i \tau_i^{\,2}/\Sigma\, a_i \tau_i$

Reference:

(1) Chuang, C. H. M.; Brown, P. R.; Bulović, V.; Bawendi, M. G. Improved Performance and Stability in Quantum Dot Solar Cells through Band Alignment Engineering. *Nature Materials*, **2014**, *13*, 796–801.

(2) Li, Q.; Wu, K.; Zhu, H.; Yang, Y.; He, S.; Lian, T. Charge Transfer from Quantum-Confined 0D, 1D, and 2D Nanocrystals. *Chemical Reviews*, **2024**, *124*, 5695–5763.

(3) Lu, H.; Huang, Z.; Martinez, M. S.; Johnson, J. C.; Luther, J. M.; Beard, M. C. Transforming Energy Using Quantum Dots. *Energy & Environmental Science*, **2020**, *13*, 1347–1376.

(4) Wang, Y.; Li, X.; Song, J.; Xiao, L.; Zeng, H.; Sun, H. All-Inorganic Colloidal Perovskite Quantum Dots: A New Class of Lasing Materials with Favorable Characteristics. *Advanced Materials*, **2015**, *27*, 7101–7108.

(5) Grätzel, M. The Rise of Highly Efficient and Stable Perovskite Solar Cells. *Accounts of Chemical Research*, **2017**, *50*, 487–491.

(6) Gong, X.; Yang, Z.; Walters, G.; Comin, R.; Ning, Z.; Beauregard, E.; Adinolfi, V.; Voznyy, O.; Sargent, E. H. Highly Efficient Quantum Dot Near-Infrared Light-Emitting Diodes. *Nature Photonics*, **2016**, *10*, 253–257.

(7) Kjaergaard, C. Photocatalysis: HI-Time for Perovskites. *Nature Energy*, **2025**, *2*, 16205.

(8) Lozano, G. The Role of Metal Halide Perovskites in Next-Generation Lighting Devices. *Journal of Physical Chemistry Letters*, **2018**, *9*, 3987–3997.

(9) Kojima, A.; Teshima, K.; Shirai, Y.; Miyasaka, T. Organometal Halide Perovskites as Visible-Light Sensitizers for Photovoltaic Cells. *Journal of the American Chemical Society*, **2009**, *131*, 6050–6051.

(10) Lee, M. M.; Teuscher, J.; Miyasaka, T.; Murakami, T. N.; Snaith, H. J. Efficient Hybrid Solar Cells Based on Meso-Superstructured Organometal Halide Perovskites. *Science*, **2012**, *338*, 643–647.

(11) Protesescu, L.; Yakunin, S.; Bodnarchuk, M. I.; Krieg, F.; Caputo, R.; Hendon, C. H.; Yang, R. X.; Walsh, A.; Kovalenko, M. V. Nanocrystals of Cesium Lead Halide Perovskites ($CsPbX_3$, X = Cl, Br, and I): Novel Optoelectronic Materials Showing Bright Emission with Wide Color Gamut. *Nano Letters*, **2015**, *15*, 3692–3696.

(12) Rosales, B. A.; Mundt, L. E.; Allen, T. G.; Moore, D. T.; Prince, K. J.; Wolden, C. A.; Rumbles, G.; Schelhas, L. T.; Wheeler, L. M. Reversible Multicolor Chromism in Layered Formamidinium Metal Halide Perovskites. *Nature Communications*, **2020**, *11*, 1–12.

(13) Walsh, A.; Zunger, A. Instilling Defect Tolerance in New Compounds. *Nature Materials*, **2017**, *16*, 964–967.

(14) Stranks, S. D.; Burlakov, V. M.; Leijtens, T.; Ball, J. M.; Goriely, A.; Snaith, H. J. Recombination Kinetics in Organic-Inorganic Perovskites: Excitons, Free Charge, and Subgap States. *Physical Review Applied*, **2014**, *2*, 034007.

(15) Fan, Q.; Biesold-McGee, G. V.; Ma, J.; Xu, Q.; Pan, S.; Peng, J.; Lin, Z. Lead-Free Halide Perovskite Nanocrystals: Crystal Structures, Synthesis, Stabilities, and Optical Properties. *Angewandte Chemie International Edition*, **2020**, *59*, 1030–1046.

(16) Zhu, D.; Zito, J.; Pinchetti, V.; Dang, Z.; Olivati, A.; Pasquale, L.; Tang, A.; Zaffalon, M. L.; Meinardi, F.; Infante, I.; De Trizio, L.; Manna, L.; Brovelli, S. Compositional Tuning of Carrier Dynamics in $Cs_2Na_{1-x}Ag_xBiCl_6$ Double-Perovskite Nanocrystals. *ACS Energy Letters*, **2020**, *5*, 1840–1847.

(17) Green, M. A.; Ho-Baillie, A.; Snaith, H. J. The Emergence of Perovskite Solar Cells. *Nature Photonics*, **2014**, *8*, 506–514.

(18) Saliba, M.; Orlandi, S.; Matsui, T.; Aghazada, S.; Cavazzini, M.; Correa-Baena, J. P.; Gao, P.; Scopelliti, R.; Mosconi, E.; Dahmen, K. H.; De Angelis, F.; Abate, A.; Hagfeldt, A.; Pozzi, G.; Graetzel, M.; Nazeeruddin, M. K. A Molecularly Engineered Hole-Transporting Material for Efficient Perovskite Solar Cells. *Nature Energy*, **2016**, *1*, 1–7.

(19) Dou, L.; Wong, A. B.; Yu, Y.; Lai, M.; Kornienko, N.; Eaton, S. W.; Fu, A.; Bischak, C. G.; Ma, J.; Ding, T.; Ginsberg, N. S.; Wang, L. W.; Alivisatos, A. P.; Yang, P. Atomically Thin Two-Dimensional Organic-Inorganic Hybrid Perovskites. *Science*, **2015**, *349*, 1518–1521.

(20) Quan, L. N.; Yuan, M.; Comin, R.; Voznyy, O.; Beauregard, E. M.; Hoogland, S.; Buin, A.; Kirmani, A. R.; Zhao, K.; Amassian, A.; Kim, D. H.; Sargent, E. H. Ligand-Stabilized Reduced-Dimensionality Perovskites. *Journal of the American Chemical Society*, **2016**, *138*, 2649–2655.

(21) Mitzi, D. B.; Feild, C. A.; Harrison, W. T. A.; Guloy, A. M. Conducting Tin Halides with a Layered Organic-Based Perovskite Structure. *Nature*, **1994**, *369*, 467–473.

(22) Ishihara, T.; Takahashi, J.; Goto, T. Optical Properties Due to Electronic Transitions in Two-Dimensional Semiconductors. *Physical Review B*, **1990**, *42*, 11099–11107.

(23) Mitzi, D. B.; Wang, S.; Feild, C. A.; Chess, C. A.; Guloy, A. M. Conducting Layered Organic-Inorganic Halides Containing 〈110〉-Oriented Perovskite Sheets. *Science*, **1995**, *267*, 1473–1476.

(24) Myae Soe, C. M.; Nagabhushana, G. P.; Shivaramaiah, R.; Tsai, H.; Nie, W.; Blancon, J. C.; Melkonyan, F.; Cao, D. H.; Traoré, B.; Pedesseau, L.; Kepenekian, M.; Katan, C.; Even,

J.; Marks, T. J.; Navrotsky, A.; Mohite, A. D.; Stoumpos, C. C.; Kanatzidis, M. G. Structural and Thermodynamic Limits of Layer Thickness in 2D Halide Perovskites. *Proceedings of the National Academy of Sciences of the USA*, **2019**, *116*, 58–66.

(25) Ciccioli, A.; Latini, A. Thermodynamics and the Intrinsic Stability of Lead Halide Perovskites CH₃NH₃PbX₃. *Journal of Physical Chemistry Letters*, **2018**, *9*, 3756–3765.

(26) Nagabhushana, G. P.; Shivaramaiah, R.; Navrotsky, A. Direct Calorimetric Verification of Thermodynamic Instability of Lead Halide Hybrid Perovskites. *Proceedings of the National Academy of Sciences of the USA*, **2016**, *113*, 7717–7721.

(27) Myae Soe, C. M.; Nagabhushana, G. P.; Shivaramaiah, R.; Tsai, H.; Nie, W.; Blancon, J. C.; Melkonyan, F.; Cao, D. H.; Traoré, B.; Pedesseau, L.; Kepenekian, M.; Katan, C.; Even, J.; Marks, T. J.; Navrotsky, A.; Mohite, A. D.; Stoumpos, C. C.; Kanatzidis, M. G. Structural and Thermodynamic Limits of Layer Thickness in 2D Halide Perovskites. *Proceedings of the National Academy of Sciences of the USA*, **2019**, *116*, 58–66.

(28) Wei, M.; de Arquer, F. P. G.; Walters, G.; Yang, Z.; Quan, L. N.; Kim, Y.; Sabatini, R.; Quintero-Bermudez, R.; Gao, L.; Fan, J. Z.; Fan, F.; Gold-Parker, A.; Toney, M. F.; Sargent, E. H. Ultrafast Narrowband Exciton Routing within Layered Perovskite Nanoplatelets Enables Low-Loss Luminescent Solar Concentrators. *Nature Energy*, **2019**, *4*, 197–205.

(29) Shamsi, J.; Kubicki, D.; Anaya, M.; Liu, Y.; Ji, K.; Frohna, K.; Grey, C. P.; Friend, R. H.; Stranks, S. D. Stable Hexylphosphonate-Capped Blue-Emitting Quantum-Confined CsPbBr₃ Nanoplatelets. *ACS Energy Lett* **2020**, *5*, 1900–1907.

(30) Bertolotti, F.; Nedelcu, G.; Vivani, A.; Cervellino, A.; Masciocchi, N.; Guagliardi, A.; Kovalenko, M. V. Crystal Structure, Morphology, and Surface Termination of Cyan-Emissive, Six-Monolayers-Thick CsPbBr₃ Nanoplatelets from X-Ray Total Scattering. *ACS Nano* **2019**, *13*, 14294–14307.

(31) Weidman, M. C.; Seitz, M.; Stranks, S. D.; Tisdale, W. A. Highly Tunable Colloidal Perovskite Nanoplatelets through Variable Cation, Metal, and Halide Composition. *ACS Nano* **2016**, *10*, 7830–7839.

(32) Zhang, Y.; Liu, J.; Wang, Z.; Xue, Y.; Ou, Q.; Polavarapu, L.; Zheng, J.; Qi, X.; Bao, Q. Synthesis, Properties, and Optical Applications of Low-Dimensional Perovskites. *Chemical Communications* **2016**, *52*, 13637–13655.

(33) Qiu, T.; Hu, Y.; Xu, F.; Yan, Z.; Bai, F.; Jia, G.; Zhang, S. Recent Advances in One-Dimensional Halide Perovskites for Optoelectronic Applications. *Nanoscale* **2018**, *10*, 20963–20989.

(34) Stranks, S. D.; Eperon, G. E.; Grancini, G.; Menelaou, C.; Alcocer, M. J. P.; Leijtens, T.; Herz, L. M.; Petrozza, A.; Snaith, H. J. Electron-Hole Diffusion Lengths Exceeding 1 Micrometer in an Organometal Trihalide Perovskite Absorber. *Science* **2013**, *342*, 341–344.

(35) Deng, W.; Huang, L.; Xu, X.; Zhang, X.; Jin, X.; Lee, S. T.; Jie, J. Ultrahigh-Responsivity Photodetectors from Perovskite Nanowire Arrays for Sequentially Tunable Spectral Measurement. *Nano Lett* **2017**, *17*, 2482–2489.

(36) Xiao, R.; Hou, Y.; Fu, Y.; Peng, X.; Wang, Q.; Gonzalez, E.; Jin, S.; Yu, D. Photocurrent Mapping in Single-Crystal Methylammonium Lead Iodide Perovskite Nanostructures. *Nano Lett* **2016**, *16*, 7710–7717.

(37) Saidaminov, M. I.; Haque, M. A.; Almutlaq, J.; Sarmah, S.; Miao, X. H.; Begum, R.; Zhumekenov, A. A.; Dursun, I.; Cho, N.; Murali, B.; Mohammed, O. F.; Wu, T.; Bakr, O. M. Inorganic Lead Halide Perovskite Single Crystals: Phase-Selective Low-Temperature Growth, Carrier Transport Properties, and Self-Powered Photodetection. *Adv Opt Mater* **2017**, *5*, 1600704.

(38) Saidaminov, M. I.; Abdelhady, A. L.; Murali, B.; Alarousu, E.; Burlakov, V. M.; Peng, W.; Dursun, I.; Wang, L.; He, Y.; MacUlan, G.; Goriely, A.; Wu, T.; Mohammed, O. F.; Bakr, O. M. High-Quality Bulk Hybrid Perovskite Single Crystals within Minutes by Inverse Temperature Crystallization. *Nature Communications* **2015**, *6*, 1–6.

(39) Kim, Y.; Yassitepe, E.; Voznyy, O.; Comin, R.; Walters, G.; Gong, X.; Kanjanaboos, P.; Nogueira, A. F.; Sargent, E. H. Efficient Luminescence from Perovskite Quantum Dot Solids. *ACS Appl Mater Interfaces* **2015**, *7*, 25007–25013.

(40) Akkerman, Q. A.; Abdelhady, A. L.; Manna, L. Zero-Dimensional Cesium Lead Halides: History, Properties, and Challenges. *Journal of Physical Chemistry Letters* **2018**, *9*, 2326–2337.

(41) Zhang, Y.; Saidaminov, M. I.; Dursun, I.; Yang, H.; Murali, B.; Alarousu, E.; Yengel, E.; Alshankiti, B. A.; Bakr, O. M.; Mohammed, O. F. Zero-Dimensional Cs_4PbBr_6 Perovskite Nanocrystals. *Journal of Physical Chemistry Letters* **2017**, *8*, 961–965.

(42) Katan, C.; Mercier, N.; Even, J. Quantum and Dielectric Confinement Effects in Lower-Dimensional Hybrid Perovskite Semiconductors. *Chem Rev* **2019**, *119*, 3140–3192.

(43) Saidaminov, M. I.; Almutlaq, J.; Sarmah, S.; Dursun, I.; Zhumekenov, A. A.; Begum, R.; Pan, J.; Cho, N.; Mohammed, O. F.; Bakr, O. M. Pure Cs_4PbBr_6: Highly Luminescent Zero-Dimensional Perovskite Solids. *ACS Energy Lett* **2016**, *1*, 840–845.

(44) Elbanna, A.; Chaykun, K.; Lekina, Y.; Liu, Y.; Febriansyah, B.; Li, S.; Pan, J.; Shen, Z. X.; Teng, J. Perovskite-Transition Metal Dichalcogenides Heterostructures: Recent Advances and Future Perspectives. *Opto-Electronic Science* **2022**, *1*.

(45) Lin, H.; Zhou, C.; Tian, Y.; Siegrist, T.; Ma, B. Low-Dimensional Organometal Halide Perovskites. *ACS Energy Lett* **2018**, *3*, 54–62.

(46) Akkerman, Q. A.; Rainò, G.; Kovalenko, M. V.; Manna, L. Genesis, Challenges and Opportunities for Colloidal Lead Halide Perovskite Nanocrystals. *Nat Mater* **2018**, *17*, 394–405.

(47) Gao, G.; Xi, Q.; Zhou, H.; Zhao, Y.; Wu, C.; Wang, L.; Guo, P.; Xu, J. Novel Inorganic Perovskite Quantum Dots for Photocatalysis. *Nanoscale* **2017**, *9*, 12032–12038.

(48) Congreve, D. N.; Weidman, M. C.; Seitz, M.; Paritmongkol, W.; Dahod, N. S.; Tisdale, W. A. Tunable Light-Emitting Diodes Utilizing Quantum-Confined Layered Perovskite Emitters. *ACS Photonics* **2017**, *4*, 476–481.

(49) Protesescu, L.; Yakunin, S.; Bodnarchuk, M. I.; Krieg, F.; Caputo, R.; Hendon, C. H.; Yang, R. X.; Walsh, A.; Kovalenko, M. V. Nanocrystals of Cesium Lead Halide Perovskites ($CsPbX_3$, X = Cl, Br, and I): Novel Optoelectronic Materials Showing Bright Emission with Wide Color Gamut. *Nano Lett* **2015**, *15*, 3692–3696.

(50) Huang, H.; Polavarapu, L.; Sichert, J. A.; Susha, A. S.; Urban, A. S.; Rogach, A. L. Colloidal Lead Halide Perovskite Nanocrystals: Synthesis, Optical Properties and Applications. *NPG Asia Mater* **2016**, *8*, e328.

(51) Noh, J. H.; Im, S. H.; Heo, J. H.; Mandal, T. N.; Seok, S. Il. Chemical Management for Colorful, Efficient, and Stable Inorganic-Organic Hybrid Nanostructured Solar Cells. *Nano Lett* **2013**, *13*, 1764–1769.

(52) Shamsi, J.; Urban, A. S.; Imran, M.; De Trizio, L.; Manna, L. Metal Halide Perovskite Nanocrystals: Synthesis, Post-Synthesis Modifications, and Their Optical Properties. *Chem Rev* **2019**, *119*, 3296–3348.

(53) Schmidt, L. C.; Pertegás, A.; González-Carrero, S.; Malinkiewicz, O.; Agouram, S.; Mínguez Espallargas, G.; Bolink, H. J.; Galian, R. E.; Pérez-Prieto, J. Nontemplate Synthesis of $CH_3NH_3PbBr_3$ Perovskite Nanoparticles. *J Am Chem Soc* **2014**, *136*, 850–853.

(54) Kundu, S.; Patra, A. Nanoscale Strategies for Light Harvesting. *Chem Rev* **2017**, *117*, 712–757.

(55) Jiang, Y.; Weiss, E. A. Colloidal Quantum Dots as Photocatalysts for Triplet Excited State Reactions of Organic Molecules. *J Am Chem Soc* **2020**, *142*, 15219–15229.

(56) Dubose, J. T.; Kamat, P. V. Energy Versus Electron Transfer: Managing Excited-State Interactions in Perovskite Nanocrystal-Molecular Hybrids. *Chem Rev* **2022**, *122*, 12475–12494.

(57) Dubose, J. T.; Kamat, P. V. Directing Energy Transfer in Halide Perovskite-Chromophore Hybrid Assemblies. *J Am Chem Soc* **2021**, *143*, 19214–19223.

(58) Luo, X.; Han, Y.; Chen, Z.; Li, Y.; Liang, G.; Liu, X.; Ding, T.; Nie, C.; Wang, M.; Castellano, F. N.; Wu, K. Mechanisms of Triplet Energy Transfer across the Inorganic Nanocrystal/Organic Molecule Interface. *Nat Commun* **2020**, *11*, 1–10.

(59) Förster, T. H. Mechanisms of Energy Transfer. *Comprehensive Biochemistry* **1967**, *22*, 61–80.

(60) Sudha, K.; Sundharamurthi, S.; Karthikaikumar, S.; Abinaya, K.; Kalimuthu, P. Switching of Förster to Dexter Mechanism of Short-Range Energy Transfer in Meso-Anthrylporphyrin. *The Journal of Physical Chemistry C* **2017**, *121*, 5941–5948.

(61) Skourtis, S. S.; Liu, C.; Antoniou, P.; Virshup, A. M.; Beratan, D. N. Dexter Energy Transfer Pathways. *Proc Natl Acad Sci U S A* **2016**, *113*, 8115–8120.

(62) Dexter, D. L. A Theory of Sensitized Luminescence in Solids. *J Chem Phys* **1953**, *21*, 836–850.

(63) Abdelhady, A. L.; Saidaminov, M. I.; Murali, B.; Adinolfi, V.; Voznyy, O.; Katsiev, K.; Alarousu, E.; Comin, R.; Dursun, I.; Sinatra, L.; Sargent, E. H.; Mohammed, O. F.; Bakr, O. M. Heterovalent Dopant Incorporation for Bandgap and Type Engineering of Perovskite Crystals. *Journal of Physical Chemistry Letters* **2016**, *7*, 295–301.

(64) Fehr, A. M. K.; Agrawal, A.; Mandani, F.; Conrad, C. L.; Jiang, Q.; Park, S. Y.; Alley, O.; Li, B.; Sidhik, S.; Metcalf, I.; Botello, C.; Young, J. L.; Even, J.; Blancon, J. C.; Deutsch, T. G.; Zhu, K.; Albrecht, S.; Toma, F. M.; Wong, M.; Mohite, A. D. Integrated Halide Perovskite Photoelectrochemical Cells with Solar-Driven Water-Splitting Efficiency of 20.8%. *Nature Communications* **2023**, *14*, 1–12.

(65) Kasparavičius, E.; Franckevičius, M.; Driukas, S.; Gulbinas, V. Charge Carrier Dynamics at the Perovskite Interface with Self-Assembled Monolayers. *ACS Appl Mater Interfaces* **2024**, *16*, 59477–59487.

(66) Dong, Z.; Li, B.; Zhu, Y.; Guo, W. Metal Halide Perovskites for CO_2 Photoreduction: Recent Advances and Future Perspectives. *EES Catalysis* **2024**, *2*, 448–474.

(67) Bienkowski, K.; Solarska, R.; Trinh, L.; Widera-Kalinowska, J.; Al-Anesi, B.; Liu, M.; Grandhi, G. K.; Vivo, P.; Oral, B.; Yılmaz, B.; Yıldırım, R. Halide Perovskites for Photoelectrochemical Water Splitting and CO_2 Reduction: Challenges and Opportunities. *ACS Catalysis* **2024**, *14*, 6603–6622.

(68) Ganji, P.; Chowdari, R. K.; Likozar, B. Photocatalytic Reduction of Carbon Dioxide to Methanol: Carbonaceous Materials, Kinetics, Industrial Feasibility, and Future Directions. *Energy and Fuels* **2023**, *37*, 7577–7602.

(69) Shyamal, S.; Dutta, S. K.; Pradhan, N. Doping Iron in $CsPbBr_3$ Perovskite Nanocrystals for Efficient and Product Selective CO_2 Reduction. *Journal of Physical Chemistry Letters* **2019**, *10*, 7965–7969.

(70) Chen, Z.; Hu, Y.; Wang, J.; Shen, Q.; Zhang, Y.; Ding, C.; Bai, Y.; Jiang, G.; Li, Z.; Gaponik, N. Boosting Photocatalytic CO_2 Reduction on $CsPbBr_3$ Perovskite Nanocrystals by Immobilizing Metal Complexes. *Chemistry of Materials* **2020**, *32*, 1517–1525.

(71) Mosconi, E.; Azpiroz, J. M.; De Angelis, F. Ab Initio Molecular Dynamics Simulations of Methylammonium Lead Iodide Perovskite Degradation by Water. *Chemistry of Materials* **2015**, *27*, 4885–4892.

(72) Christians, J. A.; Miranda Herrera, P. A.; Kamat, P. V. Transformation of the Excited State and Photovoltaic Efficiency of $CH_3NH_3PbI_3$ Perovskite upon Controlled Exposure to Humidified Air. *J Am Chem Soc* **2015**, *137*, 1530–1538.

(73) Dualeh, A.; Gao, P.; Seok, S. Il; Nazeeruddin, M. K.; Grätzel, M. Thermal Behavior of Methylammonium Lead-Trihalide Perovskite Photovoltaic Light Harvesters. *Chemistry of Materials* **2014**, *26*, 6160–6164.

(74) Kulbak, M.; Gupta, S.; Kedem, N.; Levine, I.; Bendikov, T.; Hodes, G.; Cahen, D. Cesium Enhances Long-Term Stability of Lead Bromide Perovskite-Based Solar Cells. *Journal of Physical Chemistry Letters* **2016**, *7*, 167–172.

(75) Zu, F. S.; Amsalem, P.; Salzmann, I.; Wang, R. Bin; Ralaiarisoa, M.; Kowarik, S.; Duhm, S.; Koch, N. Impact of White Light Illumination on the Electronic and Chemical Structures of Mixed Halide and Single Crystal Perovskites. *Adv Opt Mater* **2017**, *5*, 1700139.

(76) Lang, F.; Shargaieva, O.; Brus, V. V.; Neitzert, H. C.; Rappich, J.; Nickel, N. H. Influence of Radiation on the Properties and the Stability of Hybrid Perovskites. *Advanced Materials* **2018**, *30*, 1702905.

(77) Wang, A.; Guo, Y.; Muhammad, F.; Deng, Z. Controlled Synthesis of Lead-Free Cesium Tin Halide Perovskite Cubic Nanocages with High Stability. *Chemistry of Materials* **2017**, *29*, 6493–6501.

(78) Jellicoe, T. C.; Richter, J. M.; Glass, H. F. J.; Tabachnyk, M.; Brady, R.; Dutton, S. E.; Rao, A.; Friend, R. H.; Credgington, D.; Greenham, N. C.; Böhm, M. L. Synthesis and Optical Properties of Lead-Free Cesium Tin Halide Perovskite Nanocrystals. *J Am Chem Soc* **2016**, *138*, 2941–2944.

(79) Leng, M.; Chen, Z.; Yang, Y.; Li, Z.; Zeng, K.; Li, K.; Niu, G.; He, Y.; Zhou, Q.; Tang, J. Lead-Free, Blue Emitting Bismuth Halide Perovskite Quantum Dots. *Angewandte Chemie - International Edition* **2016**, *55*, 15012–15016.

(80) Leng, M.; Yang, Y.; Zeng, K.; Chen, Z.; Tan, Z.; Li, S.; Li, J.; Xu, B.; Li, D.; Hautzinger, M. P.; Fu, Y.; Zhai, T.; Xu, L.; Niu, G.; Jin, S.; Tang, J. All-Inorganic Bismuth-Based Perovskite Quantum Dots with Bright Blue Photoluminescence and Excellent Stability. *Adv Funct Mater* **2018**, *28*, 1704446.

(81) Vybornyi, O.; Yakunin, S.; Kovalenko, M. V. Polar-Solvent-Free Colloidal Synthesis of Highly Luminescent Alkylammonium Lead Halide Perovskite Nanocrystals. *Nanoscale* **2016**, *8*, 6278–6283.

(82) Akkerman, Q. A.; Park, S.; Radicchi, E.; Nunzi, F.; Mosconi, E.; De Angelis, F.; Brescia, R.; Rastogi, P.; Prato, M.; Manna, L. Nearly Monodisperse Insulator Cs_4PbX_6 (X = Cl, Br, I) Nanocrystals, Their Mixed Halide Compositions, and Their Transformation into $CsPbX_3$ Nanocrystals. *Nano Lett* **2017**, *17*, 1924–1930.

(83) Han, C.; Li, C.; Zang, Z.; Wang, M.; Sun, K.; Tang, X.; Du, J. Tunable Luminescent $CsPb_2Br_5$ Nanoplatelets: Applications in Light-Emitting Diodes and Photodetectors. *Photonics Res* **2017**, *5*, 473.

(84) Wang, K. H.; Wu, L.; Li, L.; Yao, H. Bin; Qian, H. S.; Yu, S. H. Large-Scale Synthesis of Highly Luminescent Perovskite-Related $CsPb_2Br_5$ Nanoplatelets and Their Fast Anion Exchange. *Angewandte Chemie - International Edition 2016, 55, 8328–8332.*.

(85) Wei, S.; Yang, Y.; Kang, X.; Wang, L.; Huang, L.; Pan, D. Room-Temperature and Gram-Scale Synthesis of $CsPbX_3$ (X = Cl, Br, I) Perovskite Nanocrystals with 50–85% Photoluminescence Quantum Yields. *Chem Commun* **2016**, *52*, 7265–7268.

(86) Shamsi, J.; Rastogi, P.; Caligiuri, V.; Abdelhady, A. L.; Spirito, D.; Manna, L.; Krahne, R. Bright-Emitting Perovskite Films by Large-Scale Synthesis and Photoinduced Solid-State Transformation of $CsPbBr_3$ Nanoplatelets. *ACS Nano* **2017**, *11*, 10206–10213.

(87) Papavassiliou, G. C.; Pagona, G.; Karousis, N.; Mousdis, G. A.; Koutselas, I.; Vassilakopoulou, A. Nanocrystalline/Microcrystalline Materials Based on Lead-Halide Units. *J Mater Chem* **2012**, *22*, 8271–8280.

(88) Huang, H.; Raith, J.; Kershaw, S. V.; Kalytchuk, S.; Tomanec, O.; Jing, L.; Susha, A. S.; Zboril, R.; Rogach, A. L. Growth Mechanism of Strongly Emitting $CH_3NH_3PbBr_3$ Perovskite Nanocrystals with a Tunable Bandgap. *Nat Commun* **2017**, *8*, 1–9.

(89) Zhai, W.; Lin, J.; Li, Q.; Zheng, K.; Huang, Y.; Yao, Y.; He, X.; Li, L.; Yu, C.; Liu, C.; Fang, Y.; Liu, Z.; Tang, C. Solvothermal Synthesis of Ultrathin Cesium Lead Halide Perovskite

Nanoplatelets with Tunable Lateral Sizes and Their Reversible Transformation into Cs_4PbBr_6 Nanocrystals. *Chem Mater* **2018**, *30*, 3714–3721.

(90) Kesari, Y.; Athawale, A. Ultrasound Assisted Bulk Synthesis of $CH_3NH_3PbI_3$ Perovskite at Room Temperature. *Mater Lett* **2015**, *159*, 87–89.

(91) Bhooshan Kumar, V.; Gouda, L.; Porat, Z.; Gedanken, A. Sonochemical Synthesis of $CH_3NH_3PbI_3$ Perovskite Ultrafine Nanocrystal Sensitizers for Solar Energy Applications. *Ultrason Sonochem* **2016**, *32*, 54–59.

(92) Jancik, J.; Jancik Prochazkova, A.; Scharber, M. C.; Kovalenko, A.; Másilko, J.; Sariciftci, N. S.; Weiter, M.; Krajcovic, J. Microwave-Assisted Preparation of Organo-Lead Halide Perovskite Single Crystals. *Cryst Growth Des* **2020**, *20*, 1388–1393.

(93) Komarneni, S.; Menon, V. C.; Li, Q. H.; Roy, R.; Ainger, F. Microwave-Hydrothermal Processing of $BiFeO_3$ and $CsAl_2PO_6$. *J Am Ceram Soc* **1996**, *79*, 1409–1412.

(94) Joshi, U. A.; Jang, J. S.; Borse, P. H.; Lee, J. S. Microwave Synthesis of Single-Crystalline Perovskite $BiFeO_3$ Nanocubes for Photoelectrode and Photocatalytic Applications. *Appl Phys Lett* **2008**, *92*, 243119.

(95) Pan, Q.; Hu, H.; Zou, Y.; Chen, M.; Wu, L.; Yang, D.; Yuan, X.; Fan, J.; Sun, B.; Zhang, Q. Microwave-Assisted Synthesis of High-Quality "All-Inorganic" $CsPbX_3$ (X = Cl, Br, I) Perovskite Nanocrystals and Their Application in Light Emitting Diodes. *J Mater Chem C* **2017**, *5*, 10947–10954.

(96) Malgras, V.; Tominaka, S.; Ryan, J. W.; Henzie, J.; Takei, T.; Ohara, K.; Yamauchi, Y. Observation of Quantum Confinement in Monodisperse Methylammonium Lead Halide Perovskite Nanocrystals Embedded in Mesoporous Silica. *J Am Chem Soc* **2016**, *138*, 13874–13881.

(97) Demchyshyn, S.; Roemer, J. M.; Groiß, H.; Heilbrunner, H.; Ulbricht, C.; Apaydin, D.; Böhm, A.; Rütt, U.; Bertram, F.; Hesser, G.; Scharber, M. C.; Sariciftci, N. S.; Nickel, B.; Bauer, S.; Głowacki, E. D.; Kaltenbrunner, M. Confining Metal-Halide Perovskites in Nanoporous Thin Films. *Sci Adv* **2017**, *3*, e1700738.

(98) Wang, B.; Zhang, C.; Zheng, W.; Zhang, Q.; Bao, Z.; Kong, L.; Li, L. Large-Scale Synthesis of Highly Luminescent Perovskite Nanocrystals by Template-Assisted Solid-State Reaction at 800 °C. *Chem Mater* **2020**, *32*, 308–314.

(99) Navas, D.; Fuentes, S.; Castro-Alvarez, A.; Chavez-Angel, E. Review on Sol-Gel Synthesis of Perovskite and Oxide Nanomaterials. *Gels* **2021**, *7*, 275.

(100) Bokov, D.; Jalil, A. T.; Chupradit, S.; Suksatan, W.; Ansari, M. J.; Shewael, I. H.; Valiev, G. H.; Kianfar, E. Nanomaterial by Sol-Gel Method: Synthesis and Application. *Adv Mater Sci Eng* **2021**, *2021*, 5102014.

(101) Shlapa, Y.; Solopan, S.; Belous, A. Nanoparticles of $La_{1-x}Sr_xMnO_3$ ($0.23 \leq x \leq 0.25$) Manganite: Features of Synthesis and Crystallochemical Properties. *J Magn Magn Mater* **2020**, *510*, 166902.

(102) Wang, G.; Jia, G.; Wang, J.; Kong, H.; Lu, Y.; Zhang, C. Novel Rare Earth Activator Ions-Doped Perovskite-Type $La_4Ti_3O_{12}$ Phosphors: Facile Synthesis, Structure, Multicolor Emissions, and Potential Applications. *J Alloys Compd* **2021**, *877*, 160217.

(103) Garcia, A. B. S.; Bispo-Jr, A. G.; Lima, S. A. M.; Pires, A. M. Effects of the Pechini's Modified Synthetic Route on Structural and Photophysical Properties of Eu^{3+} or Tb^{3+}-Doped $LaAlO_3$. *Mater Res Bull* **2021**, *143*, 111462.

(104) Grisorio, R.; De Marco, L.; Baldisserri, C.; Martina, F.; Serantoni, M.; Gigli, G.; Suranna, G. P. Sustainability of Organic Dye-Sensitized Solar Cells: The Role of Chemical Synthesis. *ACS Sustain Chem Eng* **2015**, *3*, 770–777.

(105) Bonetti, E.; Del Bianco, L.; Signoretti, S.; Tiberto, P. Synthesis by Ball Milling and Characterization of Nanocrystalline Fe_3O_4 and Fe/Fe_3O_4 Composite System. *J Appl Phys* **2001**, *89*, 1806–1815.

(106) Yi, M.; Shen, Z. A Review on Mechanical Exfoliation for the Scalable Production of Graphene. *J Mater Chem A* **2015**, *3*, 11700–11715.

(107) Protesescu, L.; Yakunin, S.; Nazarenko, O.; Dirin, D. N.; Kovalenko, M. V. Low-Cost Synthesis of Highly Luminescent Colloidal Lead Halide Perovskite Nanocrystals by Wet Ball Milling. *ACS Appl Nano Mater* **2018**, *1*, 1300–1308.

(108) Manukyan, K. V.; Yeghishyan, A. V.; Moskovskikh, D. O.; Kapaldo, J.; Mintairov, A.; Mukasyan, A. S. Mechanochemical Synthesis of Methylammonium Lead Iodide Perovskite. *J Mater Sci* **2016**, *51*, 9123–9130.

(109) Feeney, T.; Schackmar, F.; Donie, Y. D.; Hossain, I. M.; Paetzold, U. W.; Hellmann, T.; Mayer, T.; Abzieher, T.; Schwenzer, J. A.; Powalla, M. From Groundwork to Efficient Solar Cells: On the Importance of the Substrate Material in Co-Evaporated Perovskite Solar Cells. *Adv Funct Mater* **2021**, *31*, 2104482.

(110) Du, P.; Wang, L.; Li, J.; Luo, J.; Ma, Y.; Tang, J.; Zhai, T. Thermal Evaporation for Halide Perovskite Optoelectronics: Fundamentals, Progress, and Outlook. *Adv Opt Mater* **2022**, *10*, 2101770.

(111) Era, M.; Hattori, T.; Taira, T.; Tsutsui, T. Self-Organized Growth of PbI-Based Layered Perovskite Quantum Well by Dual-Source Vapor Deposition. *Chem Mater* **1997**, *9*, 8–10.

(112) Liu, M.; Johnston, M. B.; Snaith, H. J. Efficient Planar Heterojunction Perovskite Solar Cells by Vapour Deposition. *Nature* **2013**, *501*, 395–398.

(113) Wang, Z.; Lyu, M.; Zhang, B. W.; Xiao, M.; Zhang, C.; Han, E. Q.; Wang, L. Thermally Evaporated Metal Halide Perovskites and Their Analogues: Film Fabrication, Applications and Beyond. *Small Methods* **2024**, *9*, 2301633.

(114) Lamberti, F.; Litti, L.; De Bastiani, M.; Sorrentino, R.; Gandini, M.; Meneghetti, M.; Petrozza, A. High-Quality, Ligands-Free, Mixed-Halide Perovskite Nanocrystals Inks for Optoelectronic Applications. *Adv Energy Mater* **2017**, *7*, 1601703.

(115) Rizzo, A.; Lamberti, F.; Buonomo, M.; Wrachien, N.; Torto, L.; Lago, N.; Sansoni, S.; Pilot, R.; Prato, M.; Michieli, N.; Meneghetti, M.; Meneghesso, G.; Cester, A. Understanding Lead Iodide Perovskite Hysteresis and Degradation Causes by Extensive Electrical Characterization. *Solar Energy Materials and Solar Cells* **2019**, *189*, 43–52.

(116) Liang, S. Y.; Liu, Y. F.; Zhang, H. J.; Ji, Z. K.; Xia, H. High-Quality Patterning of $CsPbBr_3$ Perovskite Films through Lamination-Assisted Femtosecond Laser Ablation toward Light-Emitting Diodes. *ACS Applied Materials & Interfaces* **2022**, *14*, 46958–46963.

(117) Abiodun, S. L.; Pellechia, P. J.; Greytak, A. B. Effective Purification of $CsPbBr_3$ Nanocrystals with High Quantum Yield and High Colloidal Stability via Gel Permeation Chromatography. *Journal of Physical Chemistry C* **2021**, *125*, 3463–3471.

(118) Zhou, S. Rapid Separation and Purification of Lead Halide Perovskite Quantum Dots through Differential Centrifugation in Nonpolar Solvent. *RSC Advances* **2021**, *11*, 28410–28419.

(119) De Roo, J.; Ibáñez, M.; Geiregat, P.; Nedelcu, G.; Walravens, W.; Maes, J.; Martins, J. C.; Van Driessche, I.; Kovalenko, M. V.; Hens, Z. Highly Dynamic Ligand Binding and Light Absorption Coefficient of Cesium Lead Bromide Perovskite Nanocrystals. *ACS Nano* **2016**, *10*, 2071–2081.

(120) Chiba, T.; Hoshi, K.; Pu, Y. J.; Takeda, Y.; Hayashi, Y.; Ohisa, S.; Kawata, S.; Kido, J. High-Efficiency Perovskite Quantum-Dot Light-Emitting Devices by Effective Washing Process and Interfacial Energy Level Alignment. *ACS Applied Materials & Interfaces* **2017**, *9*, 18054–18060.

(121) Zhang, Y.; Siegler, T. D.; Thomas, C. J.; Abney, M. K.; Shah, T.; De Gorostiza, A.; Greene, R. M.; Korgel, B. A. A "Tips and Tricks" Practical Guide to the Synthesis of Metal Halide Perovskite Nanocrystals. *Chemistry of Materials* **2020**, *32*, 5410–5423.

(122) Zhang, H.; Sun, C.; Han, J.; Tao, J.; Fan, C.; Liu, X.; Bi, W. Efficient Purification Method for CsPbX₃ Perovskite Quantum Dots. *Journal of Luminescence* **2022**, *250*.

(123) Shen, Y.; Gee, M. Y.; Greytak, A. B. Purification Technologies for Colloidal Nanocrystals. *Chemical Communications* **2017**, *53*, 827–841.

(124) Gomez, L.; De Weerd, C.; Hueso, J. L.; Gregorkiewicz, T. Color-Stable Water-Dispersed Cesium Lead Halide Perovskite Nanocrystals. *Nanoscale* **2017**, *9*, 11992–12001.

(125) Yang, S.; Chen, S.; Mosconi, E.; Fang, Y.; Xiao, X.; Wang, C.; Zhou, Y.; Yu, Z.; Zhao, J.; Gao, Y.; De Angelis, F.; Huang, J. Stabilizing Halide Perovskite Surfaces for Solar Cell Operation with Wide-Bandgap Lead Oxysalts. *Science* **2019**, *365*, 473–478.

(126) Berhe, T. A.; Su, W. N.; Chen, C. H.; Pan, C. J.; Cheng, J. H.; Chen, H. M.; Tsai, M. C.; Chen, L. Y.; Dubale, A. A.; Hwang, B. J. Organometal Halide Perovskite Solar Cells: Degradation and Stability. *Energy & Environmental Science* **2016**, *9*, 323–356.

(127) Cho, H.; Kim, Y. H.; Wolf, C.; Lee, H. D.; Lee, T. W. Improving the Stability of Metal Halide Perovskite Materials and Light-Emitting Diodes. *Advanced Materials* **2018**, *30*, 1704587.

(128) You, J.; Meng, L.; Song, T. B.; Guo, T. F.; Chang, W. H.; Hong, Z.; Chen, H.; Zhou, H.; Chen, Q.; Liu, Y.; De Marco, N.; Yang, Y. Improved Air Stability of Perovskite Solar Cells via Solution-Processed Metal Oxide Transport Layers. *Nature Nanotechnology* **2016**, *11*, 75–81.

(129) Tiep, N. H.; Ku, Z.; Fan, H. J. Recent Advances in Improving the Stability of Perovskite Solar Cells. *Advanced Energy Materials* **2016**, *6*, 1501420.

(130) Kieslich, G.; Sun, S.; Cheetham, A. K. An Extended Tolerance Factor Approach for Organic–Inorganic Perovskites. *Chemical Science* **2015**, *6*, 3430–3433.

(131) Travis, W.; Glover, E. N. K.; Bronstein, H.; Scanlon, D. O.; Palgrave, R. G. On the Application of the Tolerance Factor to Inorganic and Hybrid Halide Perovskites: A Revised System. *Chemical Science* **2016**, *7*, 4548–4556.

(132) Goldschmidt, V. M. Die Gesetze Der Krystallochemie. *Naturwissenschaften* **1926**, *14*, 477–485.

(133) Kieslich, G.; Sun, S.; Cheetham, A. K. Solid-State Principles Applied to Organic–Inorganic Perovskites: New Tricks for an Old Dog. *Chemical Science* **2014**, *5*, 4712–4715.

(134) Wei, Y.; Cheng, Z.; Lin, J. An Overview on Enhancing the Stability of Lead Halide Perovskite Quantum Dots and Their Applications in Phosphor-Converted LEDs. *Chemical Society Reviews* **2019**, *48*, 310–350.

(135) Kovalenko, M. V.; Protesescu, L.; Bodnarchuk, M. I. Properties and Potential Optoelectronic Applications of Lead Halide Perovskite Nanocrystals. *Science* **2017**, *358*, 745–750.

(136) Ren, J.; Dong, X.; Zhang, G.; Li, T.; Wang, Y. Air-Stable and Water-Resistant All-Inorganic Perovskite Quantum Dot Films for White-Light-Emitting Applications. *New Journal of Chemistry* **2017**, *41*, 13961–13967.

(137) Fausia, K. H.; Nharangatt, B.; Vinayakan, R. N.; Ramesh, A. R.; Santhi, V.; Dhandapani, K. R.; Manoj, T. P.; Chatanathodi, R.; Jose, D.; Sandeep, K. Probing the Structural Degradation of $CsPbBr_3$ Perovskite Nanocrystals in the Presence of H_2O and H_2S: How Weak Interactions and HSAB Matter. *ACS Omega* **2023**.

(138) Wang, H. C.; Lin, S. Y.; Tang, A. C.; Singh, B. P.; Tong, H. C.; Chen, C. Y.; Lee, Y. C.; Tsai, T. L.; Liu, R. S. Mesoporous Silica Particles Integrated with All-Inorganic $CsPbBr_3$ Perovskite Quantum-Dot Nanocomposites (MP-PQDs) with High Stability and Wide Color Gamut Used for Backlight Display. *Angewandte Chemie International Edition* **2016**, *55*, 7924–7929.

(139) Huang, H.; Chen, B.; Wang, Z.; Hung, T. F.; Susha, A. S.; Zhong, H.; Rogach, A. L. Water Resistant $CsPbX_3$ Nanocrystals Coated with Polyhedral Oligomeric Silsesquioxane and Their Use as Solid State Luminophores in All-Perovskite White Light-Emitting Devices. *Chemical Science* **2016**, *7*, 5699–5703.

(140) Cha, W.; Kim, H. J.; Lee, S.; Kim, J. Size-Controllable and Stable Organometallic Halide Perovskite Quantum Dots/Polymer Films. *Journal of Materials Chemistry C* **2017**, *5*, 6667–6671.

(141) Minh, D. N.; Eom, S.; Nguyen, L. A. T.; Kim, J.; Sim, J. H.; Seo, C.; Nam, J.; Lee, S.; Suk, S.; Kim, J.; Kang, Y. Perovskite Nanoparticle Composite Films by Size Exclusion Lithography. *Advanced Materials* **2018**, *30*, 1802555.

(142) Song, Y. H.; Yoo, J. S.; Kang, B. K.; Choi, S. H.; Ji, E. K.; Jung, H. S.; Yoon, D. H. Long-Term Stable Stacked $CsPbBr_3$ Quantum Dot Films for Highly Efficient White Light Generation in LEDs. *Nanoscale* **2016**, *8*, 19523–19526.

(143) Ma, K.; Du, X. Y.; Zhang, Y. W.; Chen, S. In Situ Fabrication of Halide Perovskite Nanocrystals Embedded in Polymer Composites via Microfluidic Spinning Microreactors. *Journal of Materials Chemistry C* **2017**, *5*, 9398–9404.

(144) Pathak, S.; Sakai, N.; Wisnivesky Rocca Rivarola, F.; Stranks, S. D.; Liu, J.; Eperon, G. E.; Ducati, C.; Wojciechowski, K.; Griffiths, J. T.; Haghighirad, A. A.; Pellaroque, A.; Friend, R. H.; Snaith, H. J. Perovskite Crystals for Tunable White Light Emission. *Chemistry of Materials* **2015**, *27*, 8066–8075.

(145) Kim, Y.; Yassitepe, E.; Voznyy, O.; Comin, R.; Walters, G.; Gong, X.; Kanjanaboos, P.; Nogueira, A. F.; Sargent, E. H. Efficient Luminescence from Perovskite Quantum Dot Solids. *ACS Applied Materials & Interfaces* **2015**, *7*, 25007–25013.

(146) Hanusch, F. C.; Wiesenmayer, E.; Mankel, E.; Binek, A.; Angloher, P.; Fraunhofer, C.; Giesbrecht, N.; Feckl, J. M.; Jaegermann, W.; Johrendt, D.; Bein, T.; Docampo, P. Efficient Planar Heterojunction Perovskite Solar Cells Based on Formamidinium Lead Bromide. *Journal of Physical Chemistry Letters* **2014**, *5*, 2791–2795.

(147) Swarnkar, A.; Marshall, A. R.; Sanehira, E. M.; Chernomordik, B. D.; Moore, D. T.; Christians, J. A.; Chakrabarti, T.; Luther, J. M. Quantum Dot-Induced Phase Stabilization of α-CsPbI$_3$ Perovskite for High-Efficiency Photovoltaics. *Science (1979)* **2016**, *354*, 92–95.

(148) Chen, K.; Schünemann, S.; Song, S.; Tüysüz, H. Structural Effects on Optoelectronic Properties of Halide Perovskites. *Chemical Society Reviews* **2018**, *47*, 7045–7077.

(149) Amgar, D.; Binyamin, T.; Uvarov, V.; Etgar, L. Near Ultra-Violet to Mid-Visible Band Gap Tuning of Mixed Cation Rb$_x$Cs$_{1-x}$PbX$_3$ (X = Cl or Br) Perovskite Nanoparticles. *Nanoscale* **2018**, *10*, 6060–6068.

(150) Liu, Y.; Pan, G.; Wang, R.; Shao, H.; Wang, H.; Xu, W.; Cui, H.; Song, H. Considerably Enhanced Exciton Emission of CsPbCl$_3$ Perovskite Quantum Dots by the Introduction of Potassium and Lanthanide Ions. *Nanoscale* **2018**, *10*, 14067–14072.

(151) Huang, S.; Wang, B.; Zhang, Q.; Li, Z.; Shan, A.; Li, L. Postsynthesis Potassium-Modification Method to Improve Stability of CsPbBr$_3$ Perovskite Nanocrystals. *Advanced Optical Materials* **2018**, *6*, 1701106.

(152) Zhu, H.; Trinh, M. T.; Wang, J.; Fu, Y.; Joshi, P. P.; Miyata, K.; Jin, S.; Zhu, X. Y. Organic Cations Might Not Be Essential to the Remarkable Properties of Band Edge Carriers in Lead Halide Perovskites. *Advanced Materials* **2017**, *29*, 1603072.

(153) Gangishetty, M. K.; Sanders, S. N.; Congreve, D. N. Mn^{2+} Doping Enhances the Brightness, Efficiency, and Stability of Bulk Perovskite Light-Emitting Diodes. *ACS Photonics* **2019**, *6*, 1111–1117.

(154) Garai, A.; Vishnu, E. K.; Banerjee, S.; Nair, A. A. K.; Bera, S.; Thomas, K. G.; Pradhan, N. Vertex-Oriented Cube-Connected Pattern in CsPbBr$_3$ Perovskite Nanorods and Their Optical Properties: An Ensemble to Single-Particle Study. *Journal of the American Chemical Society* **2023**, *145*, 13989–13999.

(155) Ahmed, G. H.; Liu, Y.; Bravić, I.; Ng, X.; Heckelmann, I.; Narayanan, P.; Fernández, M. S.; Monserrat, B.; Congreve, D. N.; Feldmann, S. Luminescence Enhancement Due to Symmetry Breaking in Doped Halide Perovskite Nanocrystals. *Journal of the American Chemical Society* **2022**, *144*, 15862–15870.

(156) Mondal, N.; De, A.; Samanta, A. Achieving Near-Unity Photoluminescence Efficiency for Blue-Violet-Emitting Perovskite Nanocrystals. *ACS Energy Letters* **2019**, *4*, 32–39.

(157) Zou, S.; Liu, Y.; Li, J.; Liu, C.; Feng, R.; Jiang, F.; Li, Y.; Song, J.; Zeng, H.; Hong, M.; Chen, X. Stabilizing Cesium Lead Halide Perovskite Lattice through Mn(II) Substitution for Air-Stable Light-Emitting Diodes. *Journal of the American Chemical Society* **2017**, *139*, 11443–11450.

(158) Wang, A.; Guo, Y.; Muhammad, F.; Deng, Z. Controlled Synthesis of Lead-Free Cesium Tin Halide Perovskite Cubic Nanocages with High Stability. *Chemistry of Materials* **2017**, *29*, 6493–6501.

(159) Yong, Z. J.; Guo, S. Q.; Ma, J. P.; Zhang, J. Y.; Li, Z. Y.; Chen, Y. M.; Zhang, B. B.; Zhou, Y.; Shu, J.; Gu, J. L.; Zheng, L. R.; Bakr, O. M.; Sun, H. T. Doping-Enhanced Short-Range Order of Perovskite Nanocrystals for Near-Unity Violet Luminescence Quantum Yield. *Journal of the American Chemical Society* **2018**, *140*, 9942–9951.

(160) Liu, M.; Zhong, G.; Yin, Y.; Miao, J.; Li, K.; Wang, C.; Xu, X.; Shen, C.; Meng, H. Aluminum-Doped Cesium Lead Bromide Perovskite Nanocrystals with Stable Blue Photoluminescence Used for Display Backlight. *Advanced Science* **2017**, *4*, 1700335.

(161) Pan, G.; Bai, X.; Yang, D.; Chen, X.; Jing, P.; Qu, S.; Zhang, L.; Zhou, D.; Zhu, J.; Xu, W.; Dong, B.; Song, H. Doping Lanthanide into Perovskite Nanocrystals: Highly Improved and Expanded Optical Properties. *Nano Letters* **2017**, *17*, 8005–8011.

(162) Liu, Y.; Chen, T.; Jin, Z.; Li, M.; Zhang, D.; Duan, L.; Zhao, Z.; Wang, C. Tough, Stable and Self-Healing Luminescent Perovskite-Polymer Matrix Applicable to All Harsh Aquatic Environments. *Nature Communications* **2022**, *13*, 1–11.

(163) Zhou, Q.; Bai, Z.; Lu, W.; Wang, Y.; Zou, B.; Zhong, H. In Situ Fabrication of Halide Perovskite Nanocrystal-Embedded Polymer Composite Films with Enhanced Photoluminescence for Display Backlights. *Advanced Materials* **2016**, *28*, 9163–9168.

(164) Bai, Y.; Liu, C.; Shan, Y.; Chen, T.; Zhao, Y.; Yu, C.; Pang, H. Metal-Organic Frameworks Nanocomposites with Different Dimensionalities for Energy Conversion and Storage. *Advanced Energy Materials* **2022**, *12*, 2100346.

(165) Ma, S.; Yuan, G.; Zhang, Y.; Yang, N.; Li, Y.; Chen, Q. Development of Encapsulation Strategies towards the Commercialization of Perovskite Solar Cells. *Energy & Environmental Science* **2022**, *15*, 13–55.

(166) Lin, C. C.; Jiang, D. H.; Kuo, C. C.; Cho, C. J.; Tsai, Y. H.; Satoh, T.; Su, C. Water-Resistant Efficient Stretchable Perovskite-Embedded Fiber Membranes for Light-Emitting Diodes. *ACS Applied Materials & Interfaces* **2018**, *10*, 2210–2215.

(167) Tsai, P. C.; Chen, J. Y.; Ercan, E.; Chueh, C. C.; Tung, S. H.; Chen, W. C. Uniform Luminous Perovskite Nanofibers with Color-Tunability and Improved Stability Prepared by One-Step Core/Shell Electrospinning. *Small* **2018**, *14*, 1704379.

(168) Li, X.; Wang, Y.; Sun, H.; Zeng, H. Amino-Mediated Anchoring Perovskite Quantum Dots for Stable and Low-Threshold Random Lasing. *Advanced Materials* **2017**, *29*, 1701185.

(169) Tang, X.; Yang, J.; Li, S.; Liu, Z.; Hu, Z.; Hao, J.; Du, J.; Leng, Y.; Qin, H.; Lin, X.; Lin, Y.; Tian, Y.; Zhou, M.; Xiong, Q. Single Halide Perovskite/Semiconductor Core/Shell Quantum Dots with Ultrastability and Nonblinking Properties. *Advanced Science* **2019**, *6*, 1900412.

(170) Huang, H.; Chen, B.; Wang, Z.; Hung, T. F.; Susha, A. S.; Zhong, H.; Rogach, A. L. Water Resistant CsPbX$_3$ Nanocrystals Coated with Polyhedral Oligomeric Silsesquioxane and Their Use as Solid State Luminophores in All-Perovskite White Light-Emitting Devices. *Chemical Science* **2016**, *7*, 5699.

(171) Ravi, V. K.; Saikia, S.; Yadav, S.; Nawale, V. V.; Nag, A. CsPbBr$_3$/ZnS Core/Shell Type Nanocrystals for Enhancing Luminescence Lifetime and Water Stability. *ACS Energy Letters* **2020**, *5*, 1794–1796.

(172) Protesescu, L.; Yakunin, S.; Kumar, S.; Bär, J.; Bertolotti, F.; Masciocchi, N.; Guagliardi, A.; Grotevent, M.; Shorubalko, I.; Bodnarchuk, M. I.; Shih, C. J.; Kovalenko, M. V. Dismantling the "Red Wall" of Colloidal Perovskites: Highly Luminescent Formamidinium and Formamidinium-Cesium Lead Iodide Nanocrystals. *ACS Nano* **2017**, *11*, 3119–3134.

(173) Lu, C. H.; Biesold-Mcgee, G. V.; Liu, Y.; Kang, Z.; Lin, Z. Doping and Ion Substitution in Colloidal Metal Halide Perovskite Nanocrystals. *Chemical Society Reviews* **2020**, *49*, 4953–5007.

(174) Butler, K. T.; Frost, J. M.; Walsh, A. Band Alignment of the Hybrid Halide Perovskites CH$_3$NH$_3$PbCl$_3$, CH$_3$NH$_3$PbBr$_3$ and CH$_3$NH$_3$PbI$_3$. *Materials Horizons* **2015**, *2*, 228–231.

(175) Umebayashi, T.; Asai, K.; Kondo, T.; Nakao, A. Electronic Structures of Lead Iodide Based Low-Dimensional Crystals. *Physical Review B* **2003**, *67*, 155405.

(176) Noh, J. H.; Im, S. H.; Heo, J. H.; Mandal, T. N.; Seok, S. Il. Chemical Management for Colorful, Efficient, and Stable Inorganic-Organic Hybrid Nanostructured Solar Cells. *Nano Letters* **2013**, *13*, 1764–1769.

(177) Filip, M. R.; Eperon, G. E.; Snaith, H. J.; Giustino, F. Steric Engineering of Metal-Halide Perovskites with Tunable Optical Band Gaps. *Nature Communications* **2014**, *5*, 1–9.

(178) Brivio, F.; Walker, A. B.; Walsh, A. Structural and Electronic Properties of Hybrid Perovskites for High-Efficiency Thin-Film Photovoltaics from First-Principles. *APL Materials* **2013**, *1*.

(179) Borriello, I.; Cantele, G.; Ninno, D. Ab Initio Investigation of Hybrid Organic-Inorganic Perovskites Based on Tin Halides. *Physical Review B* **2008**, *77*, 235214.

(180) Tao, S.; Schmidt, I.; Brocks, G.; Jiang, J.; Tranca, I.; Meerholz, K.; Olthof, S. Absolute Energy Level Positions in Tin- and Lead-Based Halide Perovskites. *Nature Communications* **2019**, *10*, 1–10.

(181) Xing, G.; Mathews, N.; Sun, S.; Lim, S. S.; Lam, Y. M.; Grätzel, M.; Mhaisalkar, S.; Sum, T. C. Long-Range Balanced Electron-and Hole-Transport Lengths in Organic-Inorganic $CH_3NH_3PbI_3$. *Science (1979)* **2013**, *342*, 344–347.

(182) Johnston, M. B.; Herz, L. M. Hybrid Perovskites for Photovoltaics: Charge-Carrier Recombination, Diffusion, and Radiative Efficiencies. *Accounts of Chemical Research* **2016**, *49*, 146–154.

(183) Motta, C.; El-Mellouhi, F.; Kais, S.; Tabet, N.; Alharbi, F.; Sanvito, S. Revealing the Role of Organic Cations in Hybrid Halide Perovskite $CH_3NH_3PbI_3$. *Nature Communications* **2015**, *6*.

(184) Herz, L. M. Charge-Carrier Dynamics in Organic-Inorganic Metal Halide Perovskites. *Annual Review of Physical Chemistry* **2016**, *67*, 65–89.

(185) Herz, L. M. Charge-Carrier Mobilities in Metal Halide Perovskites: Fundamental Mechanisms and Limits. *ACS Energy Letters* **2017**, *2*, 1539–1548.

(186) Aneesh, J.; Swarnkar, A.; Ravi, V. K.; Sharma, R.; Nag, A.; Adarsh, K. V. Ultrafast Exciton Dynamics in Colloidal $CsPbBr_3$ Perovskite Nanocrystals: Biexciton Effect and Auger Recombination. *Journal of Physical Chemistry C* **2017**, *11*, 36.

(187) Mondal, N.; De, A.; Das, S.; Paul, S.; Samanta, A. Ultrafast Carrier Dynamics of Metal Halide Perovskite Nanocrystals and Perovskite-Composites. *Nanoscale* **2019**, *11*, 9796–9818.

(188) Akkerman, Q. A.; Rainò, G.; Kovalenko, M. V.; Manna, L. Genesis, Challenges and Opportunities for Colloidal Lead Halide Perovskite Nanocrystals. *Nature Materials* **2018**, *17*, 394–405.

(189) Huang, H.; Bodnarchuk, M. I.; Kershaw, S. V.; Kovalenko, M. V.; Rogach, A. L. Lead Halide Perovskite Nanocrystals in the Research Spotlight: Stability and Defect Tolerance. *ACS Energy Letters* **2017**, *2*, 2071–2083.

(190) Ten Brinck, S.; Zaccaria, F.; Infante, I. Defects in Lead Halide Perovskite Nanocrystals: Analogies and (Many) Differences with the Bulk. *ACS Energy Letters* **2019**, *4*, 2739–2747.

(191) Ten Brinck, S.; Infante, I. Surface Termination, Morphology, and Bright Photoluminescence of Cesium Lead Halide Perovskite Nanocrystals. *ACS Energy Letters* **2016**, *1*, 1266–1272.

(192) Alstrum-Acevedo, J. H.; Brennaman, M. K.; Meyer, T. J. Chemical Approaches to Artificial Photosynthesis. 2. *Inorganic Chemistry* **2005**, *44*, 6802–6827.

(193) Kamat, P. V. Photochemistry and Light Energy Conversion. *ACS Energy Letters* **2017**, *2*, 2157–2158.

(194) Scholes, G. D.; Fleming, G. R.; Olaya-Castro, A.; Van Grondelle, R. Lessons from Nature about Solar Light Harvesting. *Nature Chemistry* **2011**, *3*, 763–774.

(195) van der Meer, B. W.; C. E. G. Resonance Energy Transfer: Theory and Data. *(No Journal Title Specified)*.

(196) Ed. Of This Book. *Molecular Quantum Mechanics*, 3. *Quantum* **1997**, *935702*.

(197) Dexter, D. L. A Theory of Sensitized Luminescence in Solids. *Journal of Chemical Physics* **1953**, *21*, 836–850.

(198) Luo, X.; Han, Y.; Chen, Z.; Li, Y.; Liang, G.; Liu, X.; Ding, T.; Nie, C.; Wang, M.; Castellano, F. N.; Wu, K. Mechanisms of Triplet Energy Transfer across the Inorganic Nanocrystal/Organic Molecule Interface. *Nature Communications* **2020**, *11*, 1–10.

(199) Dubose, J. T.; Kamat, P. V. Directing Energy Transfer in Halide Perovskite-Chromophore Hybrid Assemblies. *Journal of the American Chemical Society* **2021**, *143*, 19214–19223.

(200) Mongin, C.; Garakyaraghi, S.; Razgoniaeva, N.; Zamkov, M.; Castellano, F. N. Direct Observation of Triplet Energy Transfer from Semiconductor Nanocrystals. *Science (1979)* **2016**, *351*, 369–372.

(201) Smith, M. B.; Michl, J. Singlet Fission. *Chemical Reviews* **2010**, *110*, 6891–6936.

(202) Khnayzer, R. S.; Blumhoff, J.; Harrington, J. A.; Haefele, A.; Deng, F.; Castellano, F. N. Upconversion-Powered Photoelectrochemistry. *Chemical Communications* **2011**, *48*, 209–211.

(203) He, S.; Han, Y.; Guo, J.; Wu, K. Long-Lived Delayed Emission from $CsPbBr_3$ Perovskite Nanocrystals for Enhanced Photochemical Reactivity. *ACS Energy Letters* **2021**, *6*, 2786–2791.

(204) Jiang, Y.; Yang, M.; Wu, Y.; López-Arteaga, R.; Rogers, C. R.; Weiss, E. A. Chemo- and Stereoselective Intermolecular [2 + 2] Photocycloaddition of Conjugated Dienes Using Colloidal Nanocrystal Photocatalysts. *Chem Catalysis* **2021**, *1*, 106–116.

(205) Jiang, Y.; Wang, C.; Rogers, C. R.; Kodaimati, M. S.; Weiss, E. A. Regio- and Diastereoselective Intermolecular [2+2] Cycloadditions Photocatalysed by Quantum Dots. *Nature Chemistry* **2019**, *11*, 1034–1040.

(206) Chemmangat, A.; Murray, S.; Kamat, P. V. Steering Energy Transfer Pathways through Mn-Doping in Perovskite Nanocrystals. *Journal of the American Chemical Society* **2025**, *147*, 40.

(207) Mikhnenko, O. V.; Blom, P. W. M.; Nguyen, T. Q. Exciton Diffusion in Organic Semiconductors. *Energy & Environmental Science* **2015**, *8*, 1867–1888.

(208) Luo, X.; Lai, R.; Li, Y.; Han, Y.; Liang, G.; Liu, X.; Ding, T.; Wang, J.; Wu, K. Triplet Energy Transfer from CsPbBr$_3$ Nanocrystals Enabled by Quantum Confinement. *Journal of the American Chemical Society* **2019**, *141*, 4186–4190.

(209) Sanehira, E. M.; Marshall, A. R.; Christians, J. A.; Harvey, S. P.; Ciesielski, P. N.; Wheeler, L. M.; Schulz, P.; Lin, L. Y.; Beard, M. C.; Luther, J. M. Enhanced Mobility CsPbI$_3$ Quantum Dot Arrays for Record-Efficiency, High-Voltage Photovoltaic Cells. *Science Advances* **2017**, *3*.

(210) Hoffman, J. B.; Zaiats, G.; Wappes, I.; Kamat, P. V. CsPbBr$_3$ Solar Cells: Controlled Film Growth through Layer-by-Layer Quantum Dot Deposition. *Chemistry of Materials* **2017**, *29*, 9767–9774.

(211) Gebre, S. T.; Kiefer, L. M.; Guo, F.; Yang, K. R.; Miller, C.; Liu, Y.; Kubiak, C. P.; Batista, V. S.; Lian, T. Amine Hole Scavengers Facilitate Both Electron and Hole Transfer in a Nanocrystal/Molecular Hybrid Photocatalyst. *Journal of the American Chemical Society* **2023**, *145*, 3238–3247.

(212) Dubose, J. T.; Kamat, P. V. Probing Perovskite Photocatalysis. Interfacial Electron Transfer between CsPbBr$_3$ and Ferrocene Redox Couple. *Journal of Physical Chemistry Letters* **2019**, *10*, 6074–6080.

(213) Kobosko, S. M.; Dubose, J. T.; Kamat, P. V. Perovskite Photocatalysis. Methyl Viologen Induces Unusually Long-Lived Charge Carrier Separation in CsPbBr$_3$ Nanocrystals. *ACS Energy Letters* **2020**, *5*, 221–223.

(214) De, A.; Das, S.; Samanta, A. Hot Hole Transfer Dynamics from CsPbBr$_3$ Perovskite Nanocrystals. *ACS Energy Letters* **2020**, *5*, 2246–2252.

(215) Shynkarenko, Y.; Bodnarchuk, M. I.; Bernasconi, C.; Berezovska, Y.; Verteletskyi, V.; Ochsenbein, S. T.; Kovalenko, M. V. Direct Synthesis of Quaternary Alkylammonium-Capped Perovskite Nanocrystals for Efficient Blue and Green Light-Emitting Diodes. *ACS Energy Letters* **2019**, *4*, 2703–2711.

(216) Bodnarchuk, M. I.; Boehme, S. C.; Ten Brinck, S.; Bernasconi, C.; Shynkarenko, Y.; Krieg, F.; Widmer, R.; Aeschlimann, B.; Günther, D.; Kovalenko, M. V.; Infante, I. Rationalizing and Controlling the Surface Structure and Electronic Passivation of Cesium Lead Halide Nanocrystals. *ACS Energy Letters* **2019**, *4*, 63–74.

(217) Pan, J.; Quan, L. N.; Zhao, Y.; Peng, W.; Murali, B.; Sarmah, S. P.; Yuan, M.; Sinatra, L.; Alyami, N. M.; Liu, J.; et al. Highly Efficient Perovskite-Quantum-Dot Light-Emitting Diodes by Surface Engineering. *Advanced Materials* **2016**, *28*, 8718–8725.

(218) Dubose, J. T.; Kamat, P. V. Surface Chemistry Matters. How Ligands Influence Excited State Interactions between CsPbBr$_3$ and Methyl Viologen. *Journal of Physical Chemistry C* **2020**, *124*, 12990–12998.

(219) Palabathuni, M.; Akhil, S.; Singh, R.; Mishra, N. Charge Transfer in Photoexcited Cesium-Lead Halide Perovskite Nanocrystals: Review of Materials and Applications. *ACS Applied Nano Materials* **2022**, *5*, 10097–10117.

(220) Bonifacio, R.; Lugiato, L. A. Cooperative Radiation Processes in Two-Level Systems: Superfluorescence. *Physical Review A* **1975**, *11*, 1507.

(221) Dicke, R. H. Coherence in Spontaneous Radiation Processes. *Physical Review* **1954**, *93*, 99.

(222) Patton, B.; Langbein, W.; Woggon, U. Trion, Biexciton, and Exciton Dynamics in Single Self-Assembled CdSe Quantum Dots. *Physical Review B* **2003**, *68*, 125316.

(223) Malik, S.; Le Ru, E. C.; Childs, D.; Murray, R. Time-Resolved Studies of Annealed InAs/GaAs Self-Assembled Quantum Dots. *Physical Review B* **2001**, *63*, 155313.

(224) Macovei, M.; Keitel, C. H. Laser Control of Collective Spontaneous Emission. *Physical Review Letters* **2003**, *91*, 123601.

(225) Biolatti, E.; Iotti, R. C.; Zanardi, P.; Rossi, F. Quantum Information Processing with Semiconductor Macroatoms. *Physical Review Letters* **2000**, *85*, 5647.

(226) Imamoglu, A.; Awschalom, D. D.; Burkard, G.; DiVincenzo, D. P.; Loss, D.; Sherwin, M.; Small, A. Quantum Information Processing Using Quantum Dot Spins and Cavity QED. *Physical Review Letters* **1999**, *83*, 4204.

(227) Park, Y. S.; Guo, S.; Makarov, N. S.; Klimov, V. I. Room Temperature Single-Photon Emission from Individual Perovskite Quantum Dots. *ACS Nano* **2015**, *9*, 10386–10393.

(228) Nakahara, S.; Tahara, H.; Yumoto, G.; Kawawaki, T.; Saruyama, M.; Sato, R.; Teranishi, T.; Kanemitsu, Y. Suppression of Trion Formation in $CsPbBr_3$ Perovskite Nanocrystals by Postsynthetic Surface Modification. *Journal of Physical Chemistry C* **2018**, *122*, 22188–22193.

(229) Green, M. A.; Dunlop, E. D.; Hohl-Ebinger, J.; Yoshita, M.; Kopidakis, N.; Ho-Baillie, A. W. Y. Solar Cell Efficiency Tables (Version 55). *Progress in Photovoltaics: Research and Applications* **2020**, *28*, 3–15.

(230) Green, M. A.; Emery, K.; Hishikawa, Y.; Warta, W.; Dunlop, E. D. Solar Cell Efficiency Tables (Version 42). *Progress in Photovoltaics: Research and Applications* **2013**, *21*, 827–837.

(231) Guo, Z.; Wan, Y.; Yang, M.; Snaider, J.; Zhu, K.; Huang, L. Long-Range Hot-Carrier Transport in Hybrid Perovskites Visualized by Ultrafast Microscopy. *Science (1979)* **2017**, *356*, 59–62.

(232) Palabathuni, M.; Akhil, S.; Singh, R.; Mishra, N. Charge Transfer in Photoexcited Cesium-Lead Halide Perovskite Nanocrystals: Review of Materials and Applications. *ACS Applied Nano Materials* **2022**, *5*, 10097–10117.

(233) Dey, A.; Ye, J.; De, A.; Debroye, E.; Ha, S. K.; Bladt, E.; et al. State of the Art and Prospects for Halide Perovskite Nanocrystals. *ACS Nano* **2021**, *15*, 10775–10981.

(234) Tong, Y.; Yao, E.-P.; Manzi, A.; Bladt, E.; Wang, K.; Döblinger, M.; et al. Spontaneous Self-Assembly of Perovskite Nanocrystals into Electronically Coupled Supercrystals: Toward Filling the Green Gap. *Advanced Materials* **2018**, *30*, 1801117.

(235) Li, X.; Wu, Y.; Zhang, S.; Cai, B.; Gu, Y.; Song, J.; Zeng, H. $CsPbX_3$ Quantum Dots for Lighting and Displays: Room-Temperature Synthesis, Photoluminescence Superiorities, Underlying Origins and White Light-Emitting Diodes. *Advanced Functional Materials* **2016**, *26*, 2435–2445.

(236) Chiba, T.; Hayashi, Y.; Ebe, H.; Hoshi, K.; Sato, J.; Sato, S.; et al. Anion-Exchange Red Perovskite Quantum Dots with Ammonium Iodine Salts for Highly Efficient Light-Emitting Devices. *Nature Photonics* **2018**, *12*, 681–687.

(237) Lin, K.; Xing, J.; Quan, L. N.; de Arquer, F. P. G.; Gong, X.; Lu, J.; Xie, L.; Zhao, W.; Zhang, D.; Yan, C.; et al. Perovskite Light-Emitting Diodes with External Quantum Efficiency Exceeding 20 per Cent. *Nature* **2018**, *562*, 245–248.

(238) Khamgaonkar, S. S.; Leudjo Taka, A.; Maheshwari, V. Engineering and Design of Halide Perovskite Photoelectrochemical Cells for Solar-Driven Water Splitting. *Advanced Functional Materials* **2024**, *34*, 2405414.

(239) Huang, Y.; Fang, M.; Zou, G.; Zhang, B.; Wang, H. Monochromatic and Electrochemically Switchable Electrochemiluminescence of Perovskite CsPbBr$_3$ Nanocrystals. *Nanoscale* **2016**, *8*, 18734–18739.

(240) Cardenas-Morcoso, D.; Gualdrón-Reyes, A. F.; Ferreira Vitoreti, A. B.; García-Tecedor, M.; Yoon, S. J.; Solis De La Fuente, M.; Mora-Seró, I.; Gimenez, S. Photocatalytic and Photoelectrochemical Degradation of Organic Compounds with All-Inorganic Metal Halide Perovskite Quantum Dots. *Journal of Physical Chemistry Letters* **2019**, *10*, 630–636.

(241) Xu, J. J.; Xu, D.; Wang, Z. L.; Wang, H. G.; Zhang, L. L.; Zhang, X. B. Synthesis of Perovskite-Based Porous La$_{0.75}$Sr$_{0.25}$MnO$_3$ Nanotubes as a Highly Efficient Electrocatalyst for Rechargeable Lithium-Oxygen Batteries. *Angewandte Chemie International Edition* **2013**, *52*, 3887–3890.

(242) Perovskite Devices Power Up. *Nature Electronics* **2023**, *6*, 545.

(243) Durai, L.; Badhulika, S. Current Challenges and Developments in Perovskite-Based Electrochemical Biosensors for Effective Theragnostics of Neurological Disorders. *ACS Omega* **2022**, *7*, 39491–39497.

(244) Zhou, Y.; Gu, Q.; Li, Y.; Tao, L.; Tan, H.; Yin, K.; Zhou, J.; Guo, S. Cesium Lead Bromide Perovskite-Based Lithium-Oxygen Batteries. *Nano Letters* **2021**, *21*, 4861–4867.

(245) Alom, M. S.; Kananke-Gamage, C. C. W.; Ramezanipour, F. Perovskite Oxides as Electrocatalysts for Hydrogen Evolution Reaction. *ACS Omega* **2022**, *7*, 7444–7451.

(246) Beall, C. E.; Fabbri, E.; Schmidt, T. J. Perovskite Oxide Based Electrodes for the Oxygen Reduction and Evolution Reactions: The Underlying Mechanism. *ACS Catalysis* **2021**, *11*, 3094–3114.

(247) Deeksha; Kour, P.; Ahmed, I.; Sunny; Sharma, S. K.; Yadav, K.; Mishra, Y. K. Transition Metal-Based Perovskite Oxides: Emerging Electrocatalysts for Oxygen Evolution Reaction. *ChemCatChem* **2023**, *15*, e202300040.

(248) Yuan, S.; Chen, D.; Li, X.; Zhong, J.; Xu, X. In Situ Crystallization Synthesis of CsPbBr$_3$ Perovskite Quantum Dot-Embedded Glasses with Improved Stability for Solid-State Lighting and Random Upconverted Lasing. *ACS Applied Materials & Interfaces* **2018**, *10*, 18918–18926.

(249) Jia, Y.; Kerner, R. A.; Grede, A. J.; Brigeman, A. N.; Rand, B. P.; Giebink, N. C. Diode-Pumped Organo-Lead Halide Perovskite Lasing in a Metal-Clad Distributed Feedback Resonator. *Nano Letters* **2016**, *16*, 4624–4629.

(250) Tian, C.; Tong, G.; Zhao, S.; Zhai, W.; Ge, C.; Ran, G. Low-Threshold Room-Temperature Continuous-Wave Optical Lasing of Single-Crystalline Perovskite in a Distributed Reflector Microcavity. *RSC Advances* **2019**, *9*, 35984–35989.

(251) Lin, C. H.; Zeng, Q.; Lafalce, E.; Yu, S.; Smith, M. J.; Yoon, Y. J.; Chang, Y.; Jiang, Y.; Lin, Z.; Vardeny, Z. V.; Tsukruk, V. V. Large-Area Lasing and Multicolor Perovskite Quantum Dot Patterns. *Advanced Optical Materials* **2018**, *6*, 1800474.

(252) Xu, Y.; Chen, Q.; Zhang, C.; Wang, R.; Wu, H.; Zhang, X.; Xing, G.; Yu, W. W.; Wang, X.; Zhang, Y.; Xiao, M. Two-Photon-Pumped Perovskite Semiconductor Nanocrystal Lasers. *Journal of the American Chemical Society* **2016**, *138*, 3761–3768.

(253) Pradhan, N. Growth of Lead Halide Perovskite Nanocrystals: Still in Mystery. *ACS Physical Chemistry Au* **2022**, *2*, 268–276.

(254) Correa-Baena, J. P.; Saliba, M.; Buonassisi, T.; Grätzel, M.; Abate, A.; Tress, W.; Hagfeldt, A. Promises and Challenges of Perovskite Solar Cells. *Science (1979)* **2017**, *358*, 739–744.

(255) Rosales, B. A.; Hanrahan, M. P.; Boote, B. W.; Rossini, A. J.; Smith, E. A.; Vela, J. Lead Halide Perovskites: Challenges and Opportunities in Advanced Synthesis and Spectroscopy. *ACS Energy Letters* **2017**, *2*, 906–914.

(256) Zhou, P.; Chen, H.; Chao, Y.; Zhang, Q.; Zhang, W.; Lv, F.; et al. Single-Atom Pt–I_3 Sites on All-Inorganic Cs_2SnI_6 Perovskite for Efficient Photocatalytic Hydrogen Production. *Nature Communications* **2021**, *12*, 1–8.

(257) Bai, Y.; Liu, C.; Shan, Y.; Chen, T.; Zhao, Y.; Yu, C.; Pang, H. Metal-Organic Frameworks Nanocomposites with Different Dimensionalities for Energy Conversion and Storage. *Advanced Energy Materials* **2022**, *12*, 2100346.

(258) Imran, M.; Mai, B. T.; Goldoni, L.; Cirignano, M.; Jalali, H. B.; Di Stasio, F.; Pellegrino, T.; Manna, L. Switchable Anion Exchange in Polymer-Encapsulated $APbX_3$ Nanocrystals Delivers Stable All-Perovskite White Emitters. *ACS Energy Letters* **2021**, *6*, 2844–2853.

(259) Ahmed, T.; Seth, S.; Samanta, A. Boosting the Photoluminescence of $CsPbX_3$ (X = Cl, Br, I) Perovskite Nanocrystals Covering a Wide Wavelength Range by Postsynthetic Treatment with Tetrafluoroborate Salts. *Chemistry of Materials* **2018**, *30*, 3633–3637.

(260) Chen, M.; Yang, S.; Yuan, Y.; Shen, X.; Liu, Y.; Wang, Q.; Cao, D.; Xu, C. Thermal Quenching and Antiquenching of Photoluminescence in Solution-Grown Cs_4PbBr_6 Perovskite Single Crystals. *Journal of Physical Chemistry C* **2021**, *125*, 11278–11284.

(261) Chen, M.; Yuan, Y.; Wang, Z.; Shen, X.; Liu, Y.; Cao, D. Optical Property Behaviors of $CsPbBr_3$ Colloidal Nanoparticles in a Ligand-Assisted Reprecipitation Process. *Crystal Growth & Design* **2020**, *20*, 4855–4860.

(262) Pal, P.; Saha, S.; Banik, A.; Sarkar, A.; Biswas, K. All-Solid-State Mechanochemical Synthesis and Post-Synthetic Transformation of Inorganic Perovskite-Type Halides. *Chemistry – A European Journal* **2018**, *24*, 1811–1815.

(263) Koscher, B. A.; Swabeck, J. K.; Bronstein, N. D.; Alivisatos, A. P. Essentially Trap-Free CsPbBr$_3$ Colloidal Nanocrystals by Postsynthetic Thiocyanate Surface Treatment. *Journal of the American Chemical Society* **2017**, *139*, 6566–6569.

(264) Lakowicz, J. R. *Principles of Fluorescence Spectroscopy*. **2006**, 1–954.

(265) Cha, J. H.; Han, J. H.; Yin, W.; Park, C.; Park, Y.; Ahn, T. K.; Cho, J. H.; Jung, D. Y. Photoresponse of CsPbBr$_3$ and Cs$_4$PbBr$_6$ Perovskite Single Crystals. *Journal of Physical Chemistry Letters* **2017**, *8*, 565–570.

(266) Saidaminov, C. I.; Almutlaq, M. I.; Sarmah, J. P.; Dursun, S.; Zhumekenov, I. A. Pure Cs$_4$PbBr$_6$: Highly Luminescent Zero-Dimensional Perovskite Solids. *ACS Energy Letters* **2016**, *1*, 840–845.

(267) Zeng, P.; Wei, L.; Zhao, H.; Zhang, R.; Chen, H.; Liu, M. Crystalline Phase-Controlled Synthesis of Regular and Stable Endotaxial Cesium Lead Halide Nanocrystals. *Journal of Materials Chemistry C* **2020**, *8*, 9358–9365.

(268) Jing, Q.; Xu, Y.; Su, Y.; Xing, X.; Lu, Z. A Systematic Study of the Synthesis of Cesium Lead Halide Nanocrystals: Does Cs$_4$PbBr$_6$ or CsPbBr$_3$ Form? *Nanoscale* **2019**, *11*, 1784–1789.

(269) Rakita, Y.; Kedem, N.; Gupta, S.; Sadhanala, A.; Kalchenko, V.; Böhm, M. L.; Kulbak, M.; Friend, R. H.; Cahen, D.; Hodes, G. Low-Temperature Solution-Grown CsPbBr$_3$ Single Crystals and Their Characterization. *Crystal Growth & Design* **2016**, *16*, 5717–5725.

(270) Xuan, T.; Lou, S.; Huang, J.; Cao, L.; Yang, X.; Li, H.; Wang, J. Monodisperse and Brightly Luminescent CsPbBr$_3$/Cs$_4$PbBr$_6$ Perovskite Composite Nanocrystals. *Nanoscale* **2018**, *10*, 9840–9844.

(271) Xu, L.; Li, J.; Fang, T.; Zhao, Y.; Yuan, S.; Dong, Y.; Song, J. Synthesis of Stable and Phase-Adjustable CsPbBr$_3$@Cs$_4$PbBr$_6$ Nanocrystals via Novel Anion–Cation Reactions. *Nanoscale Advances* **2019**, *1*, 980–988.

(272) Lin, J.; Lai, M.; Dou, L.; Kley, C. S.; Chen, H.; Peng, F.; Sun, J.; Lu, D.; Hawks, S. A.; Xie, C.; et al. Thermochromic Halide Perovskite Solar Cells. *Nature Materials* **2018**, *17*, 261–267.

(273) Pradhan, N. Why Do Perovskite Nanocrystals Form Nanocubes and How Can Their Facets Be Tuned? A Perspective from Synthetic Prospects. *ACS Energy Letters* **2021**, *6*, 92–99.

(274) Mondal, N.; Samanta, A. Complete Ultrafast Charge Carrier Dynamics in Photo-Excited All-Inorganic Perovskite Nanocrystals (CsPbX$_3$). *Nanoscale* **2017**, *9*, 1878–1885.

(275) Tanaka, T.; Kozako, M.; Fuse, N.; Ohki, Y. Proposal of a Multi-Core Model for Polymer Nanocomposite Dielectrics. *IEEE Transactions on Dielectrics and Electrical Insulation* **2005**, *12*, 669–681.

(276) Møller, C. K. Crystal Structure and Photoconductivity of Cæsium Plumbohalides. *Nature* **1958**, *182*, 1436.

(277) Dastidar, S.; Egger, D. A.; Tan, L. Z.; Cromer, S. B.; Dillon, A. D.; Liu, S.; Kronik, L.; Rappe, A. M.; Fafarman, A. T. High Chloride Doping Levels Stabilize the Perovskite Phase of Cesium Lead Iodide. *Nano Letters* **2016**, *16*, 3563–3570.

(278) Jena, A. K.; Kulkarni, A.; Miyasaka, T. Halide Perovskite Photovoltaics: Background, Status, and Future Prospects. *Chemical Reviews* **2019**, *119*, 3036–3103.

(279) Huang, H.; Verhaeghe, D.; Weng, B.; Ghosh, B.; Zhang, H.; Hofkens, J.; Steele, J. A.; Roeffaers, M. B. J. Metal Halide Perovskite Based Heterojunction Photocatalysts. *Angewandte Chemie International Edition* **2022**, *61*, e202203261.

(280) Fu, Y.; Zhu, H.; Chen, J.; Hautzinger, M. P.; Zhu, X. Y.; Jin, S. Metal Halide Perovskite Nanostructures for Optoelectronic Applications and the Study of Physical Properties. *Nature Reviews Materials* **2019**, *4*, 169–188.

(281) Fiuza-Maneiro, N.; Sun, K.; López-Fernández, I.; Gómez-Graña, S.; Müller-Buschbaum, P.; Polavarapu, L. Ligand Chemistry of Inorganic Lead Halide Perovskite Nanocrystals. *ACS Energy Letters* **2023**, *8*, 1152–1191.

(282) Zhang, Y.; Siegler, T. D.; Thomas, C. J.; Abney, M. K.; Shah, T.; De Gorostiza, A.; Greene, R. M.; Korgel, B. A. A "Tips and Tricks" Practical Guide to the Synthesis of Metal Halide Perovskite Nanocrystals. *Chemistry of Materials* **2020**, *32*, 5410–5423.

(283) Ma, C.; Eickemeyer, F. T.; Lee, S. H.; Kang, D. H.; Kwon, S. J.; Grätzel, M.; Park, N. G. Unveiling Facet-Dependent Degradation and Facet Engineering for Stable Perovskite Solar Cells. *Science (1979)* **2023**, *379*, 173–178.

(284) Ma, J. P.; Chen, J. K.; Yin, J.; Zhang, B. B.; Zhao, Q.; Kuroiwa, Y.; Moriyoshi, C.; Hu, L.; Bakr, O. M.; Mohammed, O. F.; et al. Doping Induces Structural Phase Transitions in All-Inorganic Lead Halide Perovskite Nanocrystals. *ACS Materials Letters* **2020**, *2*, 367–375.

(285) Pradhan, N. Tips and Twists in Making High Photoluminescence Quantum Yield Perovskite Nanocrystals. *ACS Energy Letters* **2019**, *4*, 1634–1638.

(286) Chen, J. K.; Ma, J. P.; Guo, S. Q.; Chen, Y. M.; Zhao, Q.; Zhang, B. B.; Li, Z. Y.; Zhou, Y.; Hou, J.; Kuroiwa, Y.; et al. High-Efficiency Violet-Emitting All-Inorganic Perovskite Nanocrystals Enabled by Alkaline-Earth Metal Passivation. *Chemistry of Materials* **2019**, *31*, 3974–3983.

(287) He, Z.; Liang, X.; Xiang, W. High-Efficiency Ca^{2+} Doping All-Inorganic Nanocrystals ($CsPbBr_3$ and $CsPbBr_1I_2$) Encapsulated in a Superhydrophobic Aerogel Inorganic Matrix for White Light-Emitting Diodes. *Chemical Engineering Journal* **2022**, *427*, 130964.

(288) Das, S.; De, A.; Samanta, A. Ambient Condition Mg^{2+} Doping Producing Highly Luminescent Green-and Violet-Emitting Perovskite Nanocrystals with Reduced Toxicity and Enhanced Stability. *Journal of Physical Chemistry Letters* **2020**, *11*, 1178–1188.

(289) Garai, A.; Vishnu, E. K.; Banerjee, S.; Nair, A. A. K.; Bera, S.; Thomas, K. G.; Pradhan, N. Vertex-Oriented Cube-Connected Pattern in $CsPbBr_3$ Perovskite Nanorods and Their Optical Properties: An Ensemble to Single-Particle Study. *Journal of the American Chemical Society* **2023**, *145*, 13989–13999.

(290) Seth, S.; Ahmed, T.; De, A.; Samanta, A. Tackling the Defects, Stability, and Photoluminescence of $CsPbX_3$ Perovskite Nanocrystals. *ACS Energy Letters* **2019**, *4*, 1610–1618.

(291) Gray, H. B. Powering the Planet with Solar Fuel. *Nature Chemistry* **2009**, *1*, 7.

(292) Huang, H.; Pradhan, B.; Hofkens, J.; Roeffaers, M. B. J.; Steele, J. A. Solar-Driven Metal Halide Perovskite Photocatalysis: Design, Stability, and Performance. *ACS Energy Letters* **2020**, *5*, 1107–1123.

(293) Manna, A.; Dinda, T. K.; Ghosh, S.; Mal, P. $CsPbBr_3$ in the Activation of the C–Br Bond of $CBrX_3$ (X = Cl, Br) under Sunlight. *Chemistry of Materials* **2023**, *35*, 628–637.

(294) Gao, M.; Fan, J.; Li, X.; Wang, Q.; Li, D.; Feng, J.; Duan, X. A Carbon-Negative Hydrogen Production Strategy: CO_2 Selective Capture with H_2 Production. *Angewandte Chemie International Edition* **2023**, *62*, e202216527.

(295) Shyamal, S.; Dutta, S. K.; Das, T.; Sen, S.; Chakraborty, S.; Pradhan, N. Facets and Defects in Perovskite Nanocrystals for Photocatalytic CO_2 Reduction. *Journal of Physical Chemistry Letters* **2020**, *11*, 3608–3614.

(296) Zhang, P.; Yang, X.; Du, S.; Yin, L.; Wang, J.; Liu, P.; Hou, W. Insight into the Crystal Facet Effect of {101} and {100} Facets of $CeVO_4$ in the Photochemical Property and Photocatalysis. *Journal of Physical Chemistry Letters* **2022**, *13*, 10432–10438.

(297) Kamat, P. V. Semiconductor Surface Chemistry as Holy Grail in Photocatalysis and Photovoltaics. *Accounts of Chemical Research* **2017**, *50*, 527–531.

(298) Bi, C.; Wang, S.; Li, Q.; Kershaw, S. V.; Tian, J.; Rogach, A. L. Thermally Stable Copper(II)-Doped Cesium Lead Halide Perovskite Quantum Dots with Strong Blue Emission. *Journal of Physical Chemistry Letters* **2019**, *10*, 943–952.

(299) Xu, Y. F.; Yang, M. Z.; Chen, H. Y.; Liao, J. F.; Wang, X. D.; Kuang, D. Bin. Enhanced Solar-Driven Gaseous CO_2 Conversion by $CsPbBr_3$ Nanocrystal/Pd Nanosheet Schottky-Junction Photocatalyst. *ACS Applied Energy Materials* **2018**, *1*, 5083–5089.

(300) Barak, Y.; Meir, I.; Dehnel, J.; Horani, F.; Gamelin, D. R.; Shapiro, A.; Lifshitz, E. Uncovering the Influence of Ni^{2+} Doping in Lead-Halide Perovskite Nanocrystals Using Optically Detected Magnetic Resonance Spectroscopy. *Chemistry of Materials* **2022**, *34*, 1686–1698.

(301) Behera, R. K.; Dutta, A.; Ghosh, D.; Bera, S.; Bhattacharyya, S.; Pradhan, N. Doping the Smallest Shannon Radii Transition Metal Ion Ni(II) for Stabilizing α-$CsPbI_3$ Perovskite Nanocrystals. *Journal of Physical Chemistry Letters* **2019**, *10*, 7916–7921.

(302) Maity, P.; Dana, J.; Ghosh, H. N. Multiple Charge Transfer Dynamics in Colloidal $CsPbBr_3$ Perovskite Quantum Dots Sensitized Molecular Adsorbate. *Journal of Physical Chemistry C* **2016**, *120*, 18348–18354.

(303) Choi, H.; Nicolaescu, R.; Paek, S.; Ko, J.; Kamat, P. V. Supersensitization of CdS Quantum Dots with a Near-Infrared Organic Dye: Toward the Design of Panchromatic Hybrid-Sensitized Solar Cells. *ACS Nano* **2011**, *5*, 9238–9245.

(304) Aggarwal, P.; Halder, A.; Neelakshi, N.; Ramapanicker, R.; Govind Rao, V. Energy Funneling from Water-Dispersed Perovskites to Chromophores. *ACS Energy Letters* **2023**, *8*, 1520–1528.

(305) DuBose, J. T.; Kamat, P. V. How Pendant Groups Dictate Energy and Electron Transfer in Perovskite-Rhodamine Light Harvesting Assemblies. *Journal of the American Chemical Society* **2023**, *145*, 4601–4612.

(306) Boulesbaa, A.; Huang, Z.; Wu, D.; Lian, T. Competition between Energy and Electron Transfer from CdSe QDs to Adsorbed Rhodamine B. *Journal of Physical Chemistry C* **2010**, *114*, 962–969.

(307) Lu, H.; Long, R. Spin-Orbit Coupling Notably Retards Non-Radiative Electron-Hole Recombination in Methylammonium Lead Triiodide Perovskites. *Journal of Physical Chemistry Letters* **2023**, *14*, 2715–2721.

(308) Kim, H.; Bae, S. R.; Lee, T. H.; Lee, H.; Kang, H.; Park, S.; Jang, H. W.; Kim, S. Y. Enhanced Optical Properties and Stability of $CsPbBr_3$ Nanocrystals Through Nickel Doping. *Advanced Functional Materials* **2021**, *31*, 2102770.

(309) Runčevski, T.; Brown, C. M. The Rietveld Refinement Method: Half of a Century Anniversary. *Crystal Growth & Design* **2021**, *21*, 4821–4822.

(310) Bertolotti, F.; Protesescu, L.; Kovalenko, M. V.; Yakunin, S.; Cervellino, A.; Billinge, S. J. L.; Terban, M. W.; Pedersen, J. S.; Masciocchi, N.; Guagliardi, A. Coherent Nanotwins and Dynamic Disorder in Cesium Lead Halide Perovskite Nanocrystals. *ACS Nano* **2017**, *11*, 3819–3831.

(311) Bera, S.; Behera, R. K.; Pradhan, N. α-Halo Ketone for Polyhedral Perovskite Nanocrystals: Evolutions, Shape Conversions, Ligand Chemistry, and Self-Assembly. *Journal of the American Chemical Society* **2020**, *142*, 20865–20874.

(312) Rohatgi-Mukherjee, K. K. Mechanism of Absorption and Emission of Radiation of Photochemical Interest. *Fundamentals of Photochemistry* **1978**, *79*.

(313) Saini, S.; Srinivas, G.; Bagchi, B. Distance and Orientation Dependence of Excitation Energy Transfer: From Molecular Systems to Metal Nanoparticles. *Journal of Physical Chemistry B* **2009**, *113*, 1817–1832.

(314) Singh, H.; Bagchi, B. Non-Forster Distance and Orientation Dependence of Energy Transfer and Applications of Fluorescence Resonance Energy Transfer to Polymers and Nanoparticles: How Accurate Is the Spectroscopic Ruler with $1/R^6$ Rule? **2005**.

(315) Peterson, M. D.; Jensen, S. C.; Weinberg, D. J.; Weiss, E. A. Mechanisms for Adsorption of Methyl Viologen on CdS Quantum Dots. *ACS Nano* **2014**, *8*, 2826–2837.

(316) Wu, X.; Xie, S.; Liu, C.; Zhou, C.; Lin, J.; Kang, J.; Zhang, Q.; Wang, Z.; Wang, Y. Ligand-Controlled Photocatalysis of CdS Quantum Dots for Lignin Valorization under Visible Light. *ACS Catalysis* **2019**, *9*, 8443–8451.

(317) DuBose, J. T.; Kamat, P. V. How Pendant Groups Dictate Energy and Electron Transfer in Perovskite-Rhodamine Light Harvesting Assemblies. *Journal of the American Chemical Society* **2023**, *145*, 4601–4612.

(318) Yanagi, R.; Zhao, T.; Solanki, D.; Pan, Z.; Hu, S. Charge Separation in Photocatalysts: Mechanisms, Physical Parameters, and Design Principles. *ACS Energy Letters* **2022**, *7*, 432–452.

(319) Steiner, A. M.; Lissel, F.; Fery, A.; Lauth, J.; Scheele, M. Prospects of Coupled Organic–Inorganic Nanostructures for Charge and Energy Transfer Applications. *Angewandte Chemie International Edition* **2021**, *60*, 1152–1175.

(320) Lee, Y. M.; Nam, W.; Fukuzumi, S. Redox Catalysis via Photoinduced Electron Transfer. *Chemical Science* **2023**, *14*, 4205–4218.

(321) Li, X.; Slyker, L. W.; Nichols, V. M.; Pau, G. S. H.; Bardeen, C. J.; Tang, M. L. Ligand Binding to Distinct Sites on Nanocrystals Affecting Energy and Charge Transfer. *Journal of Physical Chemistry Letters* **2015**, *6*, 1709–1713.

(322) Wu, K.; Liang, G.; Shang, Q.; Ren, Y.; Kong, D.; Lian, T. Ultrafast Interfacial Electron and Hole Transfer from CsPbBr$_3$ Perovskite Quantum Dots. *Journal of the American Chemical Society* **2015**, *137*, 12792–12795.

(323) Flaucher, I.; van der Laan, M.; Huisman, J.; Schall, P. Spectral Shaping by Radiative Energy Transfer in CsPbBr$_3$ Nanocrystal-Dye Mixtures. *ACS Applied Optical Materials* **2025**, *28*, 32.

(324) Cortés-Villena, A.; Bellezza, D.; Cunha, C.; Rosa-Pardo, I.; Seijas-Da Silva, Á.; Pina, J.; Abellán, G.; Seixas de Melo, J. S.; Galian, R. E.; Pérez-Prieto, J. Engineering Metal Halide Perovskite Nanocrystals with BODIPY Dyes for Photosensitization and Photocatalytic Applications. *Journal of the American Chemical Society* **2024**, *146*, 14479–14492.

(325) Rocha-Ortiz, J. S.; Wu, J.; Wenzel, J.; Bornschlegl, A. J.; Perea, J. D.; Leon, S.; Barabash, A.; Wollny, A. S.; Guldi, D. M.; Zhang, J.; Insuasty, A.; Lüer, L.; Ortiz, A.; Hirsch, A.; Brabec, C. J. Enhancing Planar Inverted Perovskite Solar Cells with Innovative Dumbbell-Shaped HTMs: A Study of Hexabenzocoronene and Pyrene-BODIPY-Triarylamine Derivatives. *Advanced Functional Materials* **2023**, *33*, 2304262.

(326) Yang, J.; Sheng, W.; Xiao, S.; Liu, G.; Lin, Z.; Tan, L.; Chen, Y. Directional Crystallization by Floating Self-Assembly for Efficient and Stable Tin-Based Perovskite Solar Cells. *Chemistry of Materials* **2021**, *33*, 4362–4372.

(327) Peterson, M. D.; Jensen, S. C.; Weinberg, D. J.; Weiss, E. A. Mechanisms for Adsorption of Methyl Viologen on CdS Quantum Dots. *ACS Nano* **2014**, *8*, 2826–2837.

(328) Dworak, L.; Matylitsky, V. V.; Breus, V. V.; Braun, M.; Basché, T.; Wachtveitl, J. Ultrafast Charge Separation at the CdSe/CdS Core/Shell Quantum Dot/Methylviologen Interface: Implications for Nanocrystal Solar Cells. *Journal of Physical Chemistry C* **2011**, *115*, 3949–3955.

(329) Wang, Y. F.; Wang, H. Y.; Li, Z. S.; Zhao, J.; Wang, L.; Chen, Q. D.; Wang, W. Q.; Sun, H. B. Electron Extraction Dynamics in CdSe and CdSe/CdS/ZnS Quantum Dots Adsorbed with Methyl Viologen. *Journal of Physical Chemistry C* **2014**, *118*, 17240–17246.

(330) Sekhar, M. C.; Paul, S.; De, A.; Samanta, A. An Ultrafast Transient Absorption Study of Charge Separation and Recombination Dynamics in CdSe QDs and Methyl Viologen: Dependence on Surface Stoichiometry. *ChemistrySelect* **2018**, *3*, 2675–2682.

(331) DuBose, J. T.; Kamat, P. V. Surface Chemistry Matters. How Ligands Influence Excited State Interactions between CsPbBr₃ and Methyl Viologen. *Journal of Physical Chemistry C* **2020**, *124*, 12990–12998.

(332) Trimpl, M. J.; Wright, A. D.; Schutt, K.; Buizza, L. R. V.; Wang, Z.; Johnston, M. B.; Snaith, H. J.; Müller-Buschbaum, P.; Herz, L. M. Charge-Carrier Trapping and Radiative Recombination in Metal Halide Perovskite Semiconductors. *Advanced Functional Materials* **2020**, *30*, 2004312.

(333) Grzyb, J.; Slawski, J.; Bialek, R.; Burdzinski, G.; Gibasiewicz, K.; Worch, R. Competition between Photoinduced Electron Transfer and Resonance Energy Transfer in an Example of Substituted Cytochrome C-Quantum Dot Systems. *Journal of Physical Chemistry B* **2021**, *125*, 3307–3320.

(334) Panda, S.; Roy, G.; Basu, T.; Panda, D. Facet {100} Fosters Resonance Energy Transfer in Ni/Co-Doped CsPbBr₃ Nanocrystals. *ACS Applied Energy Materials* **2024**, *7*, 10179–10188.

(335) Bouduban, M. E. F.; Burgos-Caminal, A.; Ossola, R.; Teuscher, J.; Moser, J. E. Energy and Charge Transfer Cascade in Methylammonium Lead Bromide Perovskite Nanoparticle Aggregates. *Chemical Science* **2017**, *8*, 4371–4380.

(336) Luo, X.; Liang, G.; Han, Y.; Li, Y.; Ding, T.; He, S.; Liu, X.; Wu, K. Triplet Energy Transfer from Perovskite Nanocrystals Mediated by Electron Transfer. *Journal of the American Chemical Society* **2020**, *142*, 11270–11278.

(337) DuBose, J. T.; Kamat, P. V. Energy Versus Electron Transfer: Managing Excited-State Interactions in Perovskite Nanocrystal-Molecular Hybrids. *Chemical Reviews* **2022**, *122*, 12475–12494.

(338) Mukherjee, M.; Chemmangat, A.; Kamat, P. V. Hole Trapping in Lead Halide Perovskite Nanocrystal-Viologen Hybrids and Its Impact on Back Electron Transfer. *ACS Nano* **2025**, *19*, 10549–10557.

(339) Thomas, A.; Sandeep, K.; Somasundaran, S. M.; Thomas, K. G. How Trap States Affect Charge Carrier Dynamics of CdSe and InP Quantum Dots: Visualization through Complexation with Viologen. *ACS Energy Letters* **2018**, *3*, 2368–2375.

Research Publication:

__S. Panda,__ G. Roy, T. Basu, D. Panda*, Facet {100} Fosters Resonance Energy Transfer in Ni/Co-Doped $CsPbBr_3$ Nanocrystals.

ACS Applied Energy Materials 2024, 7, 10179−10188

__S. Panda,__ A. Soni, V. Gupta, R. Niranjan, D. Panda*, PVDF-directed synthesis, stability and anion exchange of cesium lead bromide nanocrystals.

Methods and Applications in Fluorescence 2022 10, 044005.
(Institute of Physics) IOP Publishing, Special Issue: Fluorescence Research in India

S. K. Pal, M. Parashar, B.B. Kanrar, __S. Panda__, N. Roy, P. Paira, D. Panda*, N-doped yellow-emissive carbon nanodots from Gallic acid: reaction engineering, stimuli-responsive red emission, and intracellular localization.

Journal of Physical Chemistry C 125 (2021) 5748–5759

__S. Panda,__ A. Kumar, D. Panda*, Electron Transfer in Ni-Doped $CsPbBr_3$ Nanocrystal– Fluorophore Light Harvester 2025 (Manuscript Communicated)

__S. Panda,__ D. Panda*, Impact of Metal ions on Energy and Electron Transfer efficiency in a Metal doped $CsPbBr_3$ system 2025 (Manuscript under preparation).

Conference participation:

Presented Poster in Recent Trends in Chemical Sciences (RTCS-2022) organized by IIT (ISM) Dhanbad, 16-18th December, 2022.

Title – *PVDF directed Synthesis, Stability, Anion Exchange of Cesium Lead Bromide Nanocrystals*

Presented Poster in Inaugural conference of Society of Physical Chemistry (SoPhyc-2023) organized by IIT Kanpur, 29-31st October 2023.

Title – *Fluorescence Resonance Energy Transfer from Ni/Co-doped Perovskite Nanocrystals to Rhodamine B: Unearthing the Role of Crystal Facets.*